THE ROLE OF OXYGEN AND NITROGEN IN TITANIUM ALLOYS FOR AEROSPACE APPLICATIONS



Hazel Mary Gardner

Trinity College,

University of Oxford

Supervised by Professor David Armstrong,

Dr Paul Bagot and Professor Michael Moody.

A thesis submitted for the degree of

Doctor of Philosophy

HILARY TERM, 2020

ABSTRACT

This thesis aims to improve the fundamental understanding of the mechanisms and effects underpinning oxygen embrittlement and high-temperature oxidation of titanium alloys. This has been accomplished by using Atom Probe Tomography (APT) and Electron Probe Microanalysis (EPMA) to quantify oxygen segregation on the micro and nanoscale, linking changes in composition, crystal orientation and microstructure to the local mechanical properties using nanoindentation.

The current literature reports that oxygen can embrittle titanium alloys by encouraging the formation of the intermetallic α_2 phase, but the formation mechanism is not known. In this work, APT has mapped the interaction of oxygen and nitrogen with the α_2 precipitates formed in both Ti-7Al model alloys and Ti-64, resulting in the proposal of an α_2 precipitate formation mechanism. The interstitial elements are also mapped in detail within these microstructures to answer the question of where oxygen and nitrogen reside. Nanoindentation studies have determined that α_2 precipitates are not the dominant hardening mechanism upon ageing, but suggest that oxygen ordering can cause significant hardening, highlighting the importance of controlling the cooling rate during alloy processing.

Current models for *α case* depth prediction often do not incorporate the effect of microstructure. In this thesis, oxygen ingress on an *in-service* TIMETAL 834 compressor disc has been shown to be affected by microstructure on both the micron and nanoscale, and reinforces the importance of orientation of α/ β interfaces on oxygen diffusion. The relative contributions of oxygen concentration, crystal orientation and microstructure to the hardness of the oxygen-rich surface layer have been measured using a novel analysis protocol. It has been found that the hardening effects of microstructure and crystal orientation are only significant at very low oxygen concentrations, whereas interstitial solid solution hardening dominates by order of magnitude for higher oxygen concentrations.

In this thesis, a deeper understanding of the processes of oxygen embrittlement and high-temperature oxidation has been developed through careful mapping and quantification of oxygen and nitrogen and their effect on mechanical properties. This will enable these processes to be better accounted for in decisions about material processing and aeroengine component life predictions.

PREFACE

The work presented in this doctoral thesis has been carried out at the Department of Materials, University of Oxford from October 2016 to March 2020, under the supervision of Professor David Armstrong, Dr Paul Bagot and Professor Michael Moody. All of the research carried out for this thesis is original, and where the work of others has been included it has been clearly referenced and acknowledged. No part of this thesis has been submitted for a degree at this, or any other university. Some of the work has been published in peer-reviewed journals and presented at conferences and seminars as detailed below:

Journal Articles:

A study of the interaction of oxygen with the α_2 phase in the model alloy Ti-7 wt. % Al.
H. M. Gardner, A. Radecka, D. Rugg, D. E. J. Armstrong, M. P. Moody and P. A. J. Bagot, *Scripta Materialia*, vol. 185, pp. 111-116, 2020.

The role of oxygen and nitrogen in titanium alloys for aerospace applications
H. M. Gardner, A. Radecka, D. Rugg, D. E. J. Armstrong, M. P. Moody and P. A. J. Bagot*, MATEC Web Conf*, 2020.

A More Holistic Characterisation Of Internal Interfaces In A Variety of Materials via Complementary Use Of Transmission Kikuchi Diffraction and Atom Probe Tomography.
B. M. Jenkins, J. O. Douglas, **H. Gardner**, D. Tweddle, A. Kareer, P. S. Karamached, N. Riddle, J. M. Hyde, P. A.J. Bagot, G. R. Odette, M. P. Moody, *Applied Surface Science*, vol. 528, 2020.

An in-situ approach for preparing atom probe tomography specimens by xenon plasma focused ion beam milling
J.E. Halpin, R. Webster, **H. Gardner**, M.P. Moody, P.A.J. Bagot, D.A. MacLaren, *Ultramicroscopy*, vol. 202, pp. 121–127, 2019.

Characterizing solute hydrogen and hydrides in pure and alloyed titanium at the atomic scale
Y. Chang, A. J. Breen, Z. Tarzimoghadam, P. Kürnsteiner, **H. Gardner**, A. Ackerman, A. Radecka, P.A.J. Bagot, W. Lu, T. Li, E. A. Jägle, M. Herbig, L. T. Stephenson, M.P. Moody, D. Rugg, D. Dye, D. Ponge, D. Raabe, B. Gault, *Acta Mater.,* vol. 150, pp. 273–280, 2018.

Conferences:

H. M. Gardner, A. Radecka, D. Rugg, D. E. J. Armstrong, M. P. Moody and P. A. J. Bagot. Nanoindentation, EPMA and Atom Probe Tomography Characterisation of Oxygen-rich Layer formed on a Titanium Jet Engine Component. Microscopy and Microanalysis, 4^{th}-8^{th} August 2019, Portland, Oregon, US (Poster Presentation).

H. M. Gardner, A. Radecka, D. Rugg, D. E. J. Armstrong, M. P. Moody and P. A. J. Bagot
The role of oxygen and nitrogen in titanium alloys for aerospace applications. 14^{th} World Conference on Titanium, 10^{th}-14^{th} June 2019, Nantes, France (Oral Presentation).

H. M. Gardner, A. Radecka, D. Rugg, D. E. J. Armstrong, M. P. Moody and P. A. J. Bagot. Investigating the Effects of Oxygen and Nitrogen on Titanium alloys for Turbine Engine applications. Atom Probe Tomography and Microscopy Symposium, 10^{th} – 15^{th} June 2018, National Institute for Standards and Technology, Gaithersburg, US (Oral Presentation).

H.M. Gardner, M.P. Moody, D.E.J. Armstrong, P.A.J. Bagot. The role of oxygen in formation of the α_2

phase in titanium alloys for aerospace. 7th European Atom Probe Workshop, 2nd- 5th October 2017, Gullmarsstrand, Sweden (Oral Presentation).

H. Gardner, S. Pedrazzini, P.A.J. Bagot, M.P. Moody. APT studies of the microstructural evolution of Nickel Superalloy Inconel 625 during ageing. 6th European Atom Probe Workshop, 20th-23rd September 2016, University of Oxford, UK (Poster Presentation).

Hazel M. Gardner. The role of oxygen and nitrogen in titanium alloys for aerospace applications. 2nd August, 2019. Pacific Northwest National Laboratory, US (Oral Presentation, Invited Speaker).

Hazel M. Gardner. Investigating the Effects of Oxygen and Nitrogen on Titanium alloys for Turbine Engine applications. 18th June, 2018. Northwestern University, US (Oral Presentation, Invited Speaker).

ACKNOWLEDGEMENTS

This thesis and the work it contains was made possible by the support of a great number of people. Firstly, I would like to extend my sincere thanks to my supervisors Dr Paul Bagot, Prof. Michael Moody and Prof. David Armstrong. Your guidance and encouragement has enabled me to reach this point, and has formed me into the researcher that I am today.

I am grateful to Prof. David Rugg for his boundless enthusiasm for the project and for generously sharing his time and vast titanium knowledge with me. I thank Dr Anna Radecka for organising industrial placements and visits- I have benefitted so much from seeing how my work fits into "the big picture." I also thank Anna for her help training me on the FIB and for making me feel welcome whenever I was up at Derby. A big thank you to Dave Collins and the rest of the team at Rolls-Royce Materials for helpful discussions and multiple enjoyable placements. Thank you to Dr Kate Fox, Dave Collins, Felicity Dear and Prof. David Dye for providing samples for this work, to Dr Matt Thomas and the team at TIMET for LECO chemical analysis, and to the team at Loughborough Surface Analysis Ltd for the DSIMS measurements.

I owe a huge debt of thanks to everyone in the Oxford Atom Probe group. You have provided a supportive and fun working environment and I feel privileged to be a part of the group. Special mentions go to Anne, James and Meg for being the best office mates I could have asked for. Thanks are also due to Dr James Douglas for his advice and scientific insight, for being generous with his time, for his endless puns and for all of his help on the FIB. Thanks to Dr Daniel Haley and Dr Andrew London for patiently helping me with my many coding and statistics related queries- I have learnt so much from you. Thank you to Chris Magazzeni for introducing me to and helping me with the nanoindentation mapping. Dr Philip Gopon, thank you for all your help with the EPMA and for the opportunity to analyse (a very small part of) the Moon.

I am very thankful for my friends and support network in Oxford, including the postgraduate community at St Ebbes Church. To my library study buddies- thank you for making thesis writing so much more enjoyable. I also thank my housemates, Olly and Lucy, for their continued friendship- we made it!

To my family, thank you for always being there and for getting me through the tough times. I could not have done this without you.

Dominus Illuminatio Mea – The Lord is my light.

The Lord has sustained me through my DPhil and this work has been conducted by His grace, for His glory.

CONTENTS

1 Introduction 1
2 Literature Review 5
2.1 Engineering relevance 5
2.2 Introduction to titanium 9
2.3 The titanium-aluminium phase diagram 11
2.4 Alloy classification 16
2.4.1 α alloys 18
2.4.2 α+β alloys 18
2.4.3 β alloys 21
2.4.4 Effect of alloying additions 21
2.5 Deformation behaviour of titanium 24
2.6 Hardening mechanisms in titanium alloys 26
2.7 Interstitial elements 27
2.7.1 Effect on deformation behaviour 32
2.7.2 Effect on mechanical properties 33
2.7.3 Effect on microstructure 35
2.8 α2 phase 37
2.9 Dwell fatigue 47
2.10 α case 51
2.10.1 Industrial relevance 52
2.10.2 Effect of α *case* on mechanical properties 53
2.10.3 Formation of α *case* 55
2.11 Summary 62
3 Materials and Methods 63
3.1 Materials 63
3.1.1 Trace levels of oxygen and nitrogen 63
3.1.2 High levels of oxygen 66
3.2 Quantifying oxygen 67
3.3 Atom Probe Tomography 68
3.3.1 Principles 68
3.3.2 APT sample preparation 69
3.3.3 Selection of APT analysis conditions 70
3.3.4 Mass spectrum ranging and peak overlaps 74
3.3.5 Identifying and extracting precipitates 77
3.3.6 Precipitate morphology 78
3.4 Electron Probe Microanalysis (EPMA) 80

3.4.1 Principles 80
3.4.2 Sample requirements 82
3.4.3 Selection of EPMA analysis conditions 83
3.5 Nanoindentation 89
3.5.1 Principles 89
3.5.2 Experimental details 90
3.6 Electron microscopy based techniques 91
4 Mapping oxygen and nitrogen within the microstructure of titanium alloys 94
4.1 Introduction 94
4.2 Mapping oxygen at grain boundaries 95
4.3 Oxygen and the α_2 phase 97
4.4 Mapping nitrogen 103
4.5 Discussion 109
4.5.1 Segregation at α-α grain boundaries 109
4.5.2 Role of oxygen in the formation of the α_2 phase 109
4.5.3 Comparison of the behaviour of oxygen and nitrogen with respect to α_2 112
4.5.4 Partitioning behaviour of nitrogen with respect to β phase 113
4.6 Conclusions 114
5 Characterisation of the α_2 phase and its effect on mechanical properties 116
5.1 Introduction 116
5.2 Characterisation of the α_2 phase 116
5.2.1 Composition 117
5.2.2 Morphology 119
5.3 Hardness as a function of ageing time and interstitial content 125
5.3.1 Effect of crystal orientation on hardness 128
5.4 Discussion 129
5.4.1 Characterisation of the α_2 phase 129
5.4.2 Evaluation of hardening mechanisms 130
5.5 Conclusions 135
6 Characterisation of the *oxygen-rich layer* 136
6.1 Introduction 136
6.2 Characterisation of bulk TIMETAL 834 material 136
6.3 *In-service* compressor disc 140
6.3.1 Oxygen concentration 140
6.3.2 Nanohardness measurements 143
6.4 *Lab-controlled* sample 146
6.5 Discussion 152
6.6 Conclusions 156

7 Understanding the relationship between crystal orientation, microstructure, oxygen ingress and hardness 158
7.1 Introduction 158
7.2 Data collection and processing 158
7.3 Discussion 166
7.3.1 Mechanisms underpinning hardness changes 167
7.3.2 Interplay between crystal orientation, microstructure, oxygen content, and hardness 168
7.3.3 Effect of crystal orientation and microstructure on oxygen ingress 169
7.4 Conclusions 170
8 Summary and conclusions 172
8.1 Introduction 172
8.2 Conclusions 172
8.3 Future work 174
8.4 Concluding remarks 174
9 References 176

1 INTRODUCTION

Air passenger traffic is forecast to increase by 5.2% p.a. over the next 20 years [1]. New engine architecture solutions, more durable materials and improved predictive capability for *in-service* behaviour are required for an engine manufacturer to meet increased demand while remaining commercially competitive. Additionally, the 2050 emissions targets of the Advisory Council for Aeronautics Research in Europe must be met, which includes reducing overall CO_2 emissions per passenger kilometre by 75%, relative to values in the year 2000 [2].

Use of titanium alloys in an engine instead of denser alternatives can help achieve both the environmental and commercial requirements by decreasing total engine weight and thus reducing specific fuel consumption (SFC). Decreased SFC reduces CO_2 at the airframe level and also provides commercial benefits to both engine operators and engine manufacturers [3].

In a jet engine, titanium alloys are mainly used in fan blades, compressor discs and compressor blades. However, for the use of titanium alloys to be successful, there are some materials science challenges that must be met. For example, although making compressor discs from titanium alloys instead of nickel superalloys reduces engine weight, it also results in operating titanium alloys in hotter parts of the engine. Moreover, the drive towards increased propulsive efficiency further increases the temperature experienced by titanium alloy compressor discs. Temperatures can exceed 600^{o}C at the back of the compressor and operating titanium alloys at these temperatures can lead to significant oxygen ingress [3], resulting in a brittle surface layer that is often referred to as *α case*. The high oxygen contents within this layer significantly reduce ductility, degrading fatigue performance by increasing the probability of crack initiation and propagation [4].

Several studies have been carried out modelling diffusion of oxygen and nitrogen to predict *α case* depth, and to predict the effect of *α case* depth on mechanical properties [4–9]. These predictions are often validated with experimental data. However, there is variation in the

accuracy of techniques used to measure oxygen ingress, and the effect of crystal orientation and microstructure on oxygen ingress is not typically accounted for. Some work has been done showing the effect of α colony lath orientation on oxygen ingress [10], and accounting for the different diffusivities in basketweave compared to lamellar microstructures [11], but further studies on a wider range of microstructures are needed.

Another materials science challenge facing titanium alloys is cold dwell fatigue. This occurs when titanium components, such as fan blades, operate at low temperature (less than 100^{o}C) and experience periods of relatively low-level stress for extended hold periods [12]. Under these conditions, "cold creep" [13–15] can enable load redistribution from soft to hard α grains [13], resulting in facet crack nucleation and growth [16]. As a result, periodic inspections of the fan disk and blades during service, and the replacement of cracked rotor components, is required. Cold dwell fatigue also leads to the over-design of disks and blades, with a consequent increase in the rate of SFC.

The ordered, intermetallic α_2 (Ti_3Al) phase has a modified hexagonal (DO_{19}) crystal structure and promotes planar slip [17], encouraging strain localisation and making the alloy more susceptible to low cycle fatigue, notch high cycle fatigue and cold dwell fatigue. Oxygen is known to promote α_2 formation [18], but the mechanism by which it does this is not well understood.

Further work is needed to understand the role of oxygen and nitrogen in both compressor disc oxidation and cold dwell fatigue. For example, the location of oxygen and nitrogen within the microstructure of titanium alloys must be determined, along with the role of oxygen and nitrogen in α_2 formation and the effect of oxygen, nitrogen and α_2 on mechanical properties. The relationship between crystallography, microstructure and oxygen content, and their effect on hardness with the *α case,* must be understood.

Cold dwell fatigue and compressor disc oxidation are driven by activity on the nanoscale. The unique combination of high spatial resolution and chemical sensitivity, in particular the ability to

detect and quantify light elements, makes atom probe tomography (APT) ideally suited for an improved understanding of these processes. Complementary electron microscopy techniques contextualise the APT results, and nanohardness measurements relate changes in composition to mechanical properties. This thesis uses these experimental techniques to gain a more in-depth insight into cold dwell fatigue and compressor disc oxidation, providing experimental information to improve component life prediction models and enabling safe use of titanium in hotter parts of the jet engine, ultimately reducing engine weight.

An introduction to titanium alloys is given in Chapter 2, along with an overview of their use in jet engines. Current knowledge of the α_2 phase is summarised along with an outline of the current understanding of cold dwell fatigue. The formation of *α case* and its known effects on mechanical properties are also described. The base materials used in this thesis are the model alloy Ti-7Al alloy, supplied by Timet plc, and Ti-6Al-4V (Ti-64) fan blade plate material, supplied by Rolls-Royce plc, both with controlled levels of oxygen and nitrogen added. Ageing treatments were applied to each of these alloys to form α_2, as detailed in Chapter 3. A section of TIMETAL 834 compressor disc that had experienced *in-service* temperatures and exposure, also provided by Rolls-Royce Plc, was used to study compressor disc oxidation. My work used APT to map and quantify oxygen and nitrogen, alongside complementary EPMA, nanoindentation and electron microscopy techniques. Chapter 4 maps oxygen and nitrogen at both phase boundaries and grain boundaries, with the aim of understanding the role of oxygen and nitrogen in the formation of α_2 precipitates. Chapter 5 goes on to characterise the α_2 phase in depth and evaluates the hardening mechanisms at work in the quenched and aged alloys. Higher levels of oxygen contamination are studied in Chapter 6. This Chapter aims to quantify oxygen ingress at the surface of a compressor disc and use complementary nanoindentation and EBSD measurements to study the effects of microstructure and crystal orientation on hardness. A new analysis protocol is developed in Chapter 7 allowing the correlative study of hardness, crystal orientation, microstructure and oxygen concentration at

the surface of the compressor disc, to give new insights into the interrelation of these factors. The significant findings of the thesis and suggestions for further work are provided in Chapter 8.

2 LITERATURE REVIEW

2.1 ENGINEERING RELEVANCE

Demand for air travel increased by 6.3% in 2016 compared to 2015 [19] and is set to double over the next 20 years, according to the International Air Transport Association [20]. Leading aircraft manufacturer Airbus forecast that 34,170 additional passenger aircraft will be required to meet this demand [21]. With the number of aircraft increasing at such a rate, environmental impact must be minimised and it is important to minimise operating costs to produce greater numbers efficiently. As can be seen from Figure 2.1, Boeing estimates that approximately 25% of operating costs are accounted for by fuel and maintenance. Although exact figures will vary from aircraft to aircraft, this highlights the need to reduce maintenance and fuel costs.

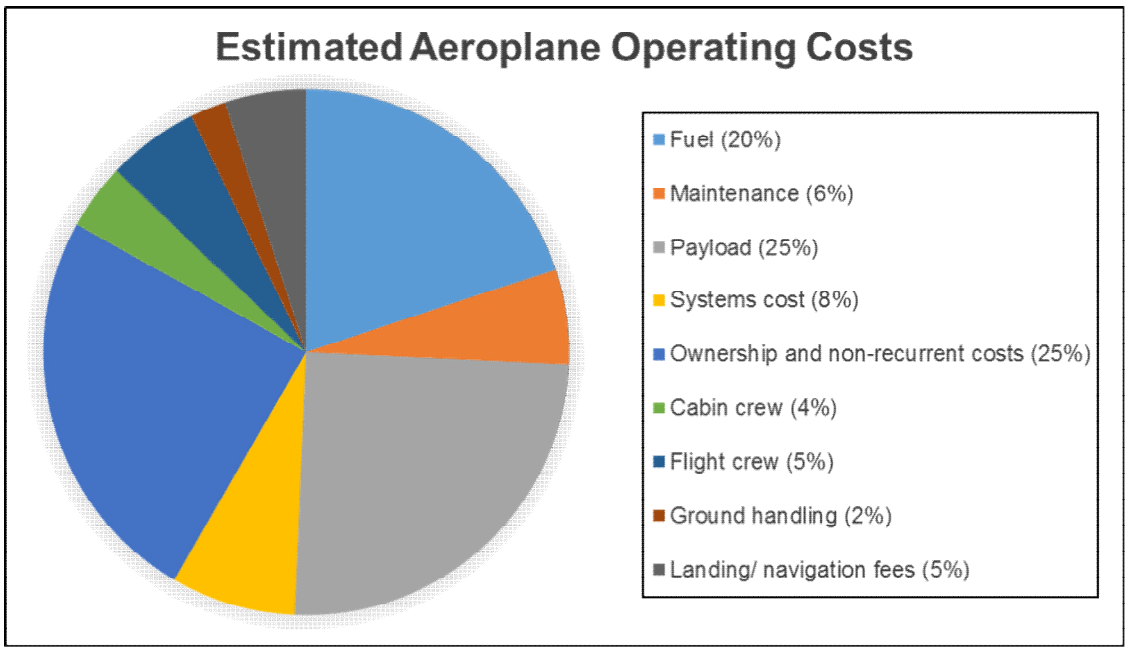


Figure 2.1: Pie chart showing the contributing factors to the total operating cost of an aeroplane, as estimated by Boeing using their Integrated Cost Analysis System. Data taken from [22].

24% of total maintenance costs is accounted for by replacement and maintenance of components [23]. Thus extending the lifetime of components is economically desirable since it reduces the frequency of costly maintenance checks as well as reducing component costs.

In a civil aeroengine, safety critical components that require regular inspection are the titanium fan blades and compressor discs. These are rotating components in the engine. The titanium alloy fan blades at the front of an aeroengine draw air into the compressor, also made of titanium alloy. Airflow through the engine is indicated by the arrows in Figure 2.2. The compressor increases the pressure of the air before it is mixed with fuel in the combustion chamber and ignited.

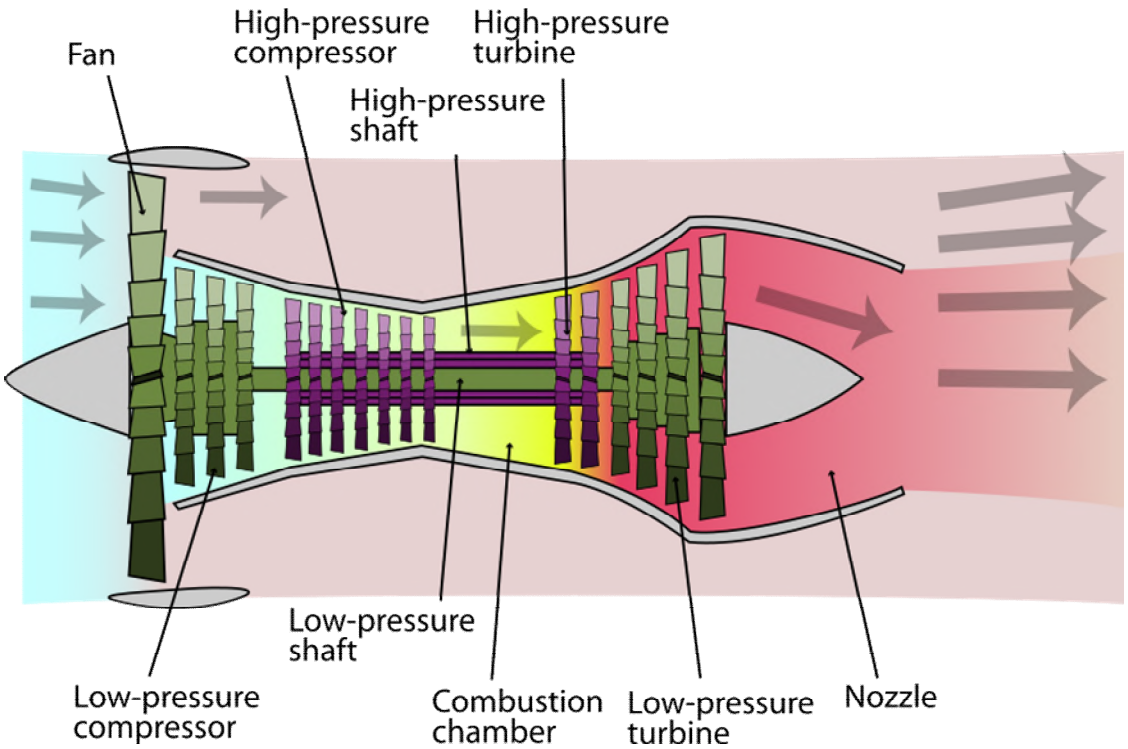


Figure 2.2: Schematic diagram of a turbofan engine, adapted from [24].

High-temperature, high-pressure combustion gases, shown in red on Figure 2.2, expand through nickel superalloy turbines, causing them to rotate and drive the compressors and the fan. After passing through the turbines, exhaust gases are expelled from the nozzle. In a turbojet, all of the thrust is provided by expulsion of hot exhaust gases whereas in a turbofan, 30-70% of the thrust is provided by the lower temperature, by-pass air [25].

A jet engine is approximately 35% titanium by mass [26], with other components being made from steel, nickel, aluminium and composites, as shown in Figure 2.3. Titanium alloys are selected

for use in the fan and compressor because of their high strength-to-weight ratio and good corrosion resistance. Competing materials for lower temperature applications include carbon fibre-based composites owing to their higher fatigue resistance and lower weight [27]. However, composites are less resilient to foreign object damage than titanium [28], and so composite fan blades use titanium leading edges. Additionally, the development and manufacture of composite fan blades is expensive, since automating the process is non-trivial. Titanium is also used at higher temperatures in the compressor, where temperatures can reach up to ~600°C [3], and studies are needed on the behaviour of titanium at these temperatures to improve component life predictions. Thus, research into titanium is an important topic of study.

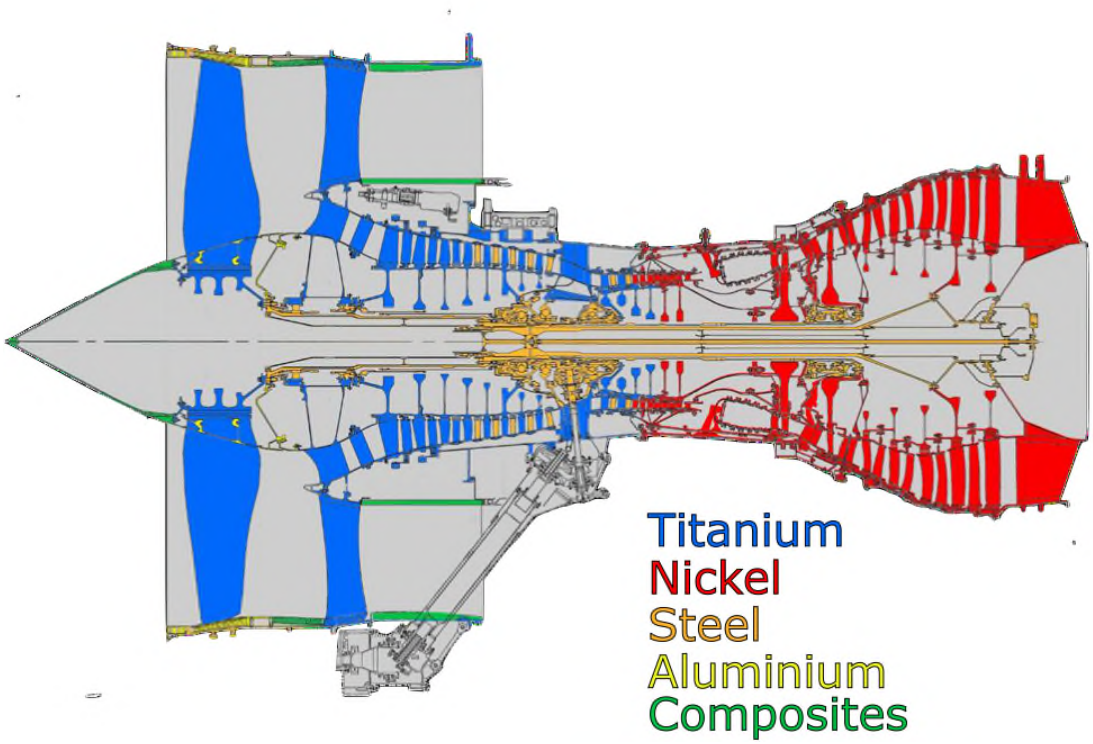


Figure 2.3: Diagram illustrating the materials used in a Rolls-Royce jet engine. Titanium alloys are highlighted in blue. Image adapted from [29].

One of the key failure mechanisms for fan blades is cold dwell fatigue [30], which results in component failure at stresses much lower than their tensile strength [31]. Fan blades are susceptible to cold dwell fatigue because they operate at low temperature (less than 100°C) and experience periods of relatively low-level stress for extended hold periods. The problem of cold

dwell fatigue will be discussed in more detail in section 2.9. A better understanding of the fundamental mechanisms underpinning cold dwell fatigue will increase the accuracy of life predictions, enable maintenance checks to be scheduled less frequently, reduce the need for overdesign, and thus reduce engine weight while increasing fuel efficiency.

With the number of aircraft in a fleet increasing at such a rapid rate, it has become more important than ever to keep fuel consumption to a minimum to maximise the profit made and minimise environmental impact. Boeing predict that fuel accounts for 20% of the operating costs of an aeroplane [22], meaning that any savings made would have a significant benefit to profits. The environmental savings are also substantial; approximately 3.15 tonnes of CO_2 emissions are avoided for each tonne of fuel saved [32].

Fuel consumption can be reduced by reducing aircraft weight. One way of achieving this is reducing overdesign, as mentioned previously. An additional solution is to maximise the number of engine components made from titanium since it has a high strength-to-weight ratio. However, above ~480°C the increased rate of oxygen diffusion enables oxygen embrittlement and leads to oxidation [5]. Titanium discs are therefore limited to a maximum operating temperature of ~600°C, which is approached in the high-pressure compressor [29]. Thus components beyond the compressor, i.e. turbine components, are made from heavier nickel alloys, which have excellent high-temperature properties [33]. By better understanding the high-temperature oxidation behaviour of titanium alloys, their use can be safely justified at hotter operating temperatures, thus keeping engine weight to a minimum.

In summary, the fundamental mechanisms that lead to component failure and high-temperature degradation must be better understood since they will ultimately reduce the cost to industry of inspections, component replacement and overdesign, and decrease fuel consumption.

2.2 INTRODUCTION TO TITANIUM

The high-temperature strength, low density and corrosion resistance of titanium make it useful in a range of applications, including medical implants [34,35] and marine components [36]. However, the largest user of titanium is the aerospace industry, which accounted for approximately 77% of titanium metal consumption in 2015 [37].

Pure titanium undergoes an allotropic phase transformation at 882°C. Above this temperature it exists as the body centred cubic (BCC) β phase and below it exists as the hexagonal close packed (HCP) α phase. From Table 2.1, it can be seen that the yield stress of titanium is comparable to that of Fe-based alloys and nickel superalloys, but that the density of titanium is much lower. It is this combination of properties that makes titanium an attractive choice for use in the aerospace industry, where weight saving is of primary importance.

The corrosion resistance of titanium is superior to that of Fe-based alloys or nickel superalloys. This is partly due to the high reactivity of titanium with oxygen, which results in the formation of a thin, protective surface layer of TiO_2. The grade of the titanium also plays a role in corrosion resistance. Commercially pure (CP) titanium (grades 1-4) is used in industrial applications where its high corrosion resistance is of greater importance than mechanical properties, e.g. chemical processing equipment. Higher titanium grades also have good corrosion resistance but are often used in applications where mechanical properties are also important. For example, pumps used to handle acidic fluids on oilfields must withstand vibrations and high mean stresses in addition to being corrosion resistant. For this reason, they are made from medium-strength alloys such as grades 25, 28 and 29 [38]. A list of commonly used titanium grades can be found in the following reference [39].

Oxygen content in titanium alloys must be controlled to prevent embrittlement [39]. The reactivity of titanium with oxygen is therefore a significant contributor to the high price of

titanium since titanium production must occur in an inert atmosphere/ under vacuum to minimise dissolved oxygen. Other factors that contribute to the high price are the high energy costs associated with titanium production and the high cost of reducing naturally occurring titanium dioxide to titanium metal via the Kroll process [40].

Another disadvantage of the high reactivity of titanium with oxygen is that it limits the high-temperature use of titanium alloys. Above 480^{o}C, the rate of oxygen diffusion through the surface oxide is increased such that excessive oxide growth and embrittlement of the sub-oxide layer occurs [5]. Consequentially, nickel superalloys are often used in place of titanium in high-temperature applications as a result of their higher oxidation limit, which can be seen in Table 2.1.

Table 2.1: Comparison of the properties of titanium alloys with other materials. Data from [39,41–45]

	Ti-64	Fe-based alloys	Nickel superalloys
Melting temperature (^{o}C)	1605-1720	1425 - 1540	1320-1425
Density (g/cm^{3})	~4.4	~8	~8.9
Modulus (GPa)	96.8-153	200	200-220
Tensile strength (MPa)	380-1150	295 - 2400	800-1080
Oxidation limit (^{o}C)	600	870-1150	850-1080
Relative corrosion resistance	Very high	Low	Medium
Relative reactivity with oxygen	Very high	Low	Low
Comparative price of metal	Very high	Low	High

2.3 THE TITANIUM-ALUMINIUM PHASE DIAGRAM

The titanium-aluminium binary phase diagram is of fundamental importance since aluminium is a major alloying element in a wide range of commercial titanium-based alloys. However, establishing the equilibrium phase diagram has proved difficult. For example, early work faced challenges due to the formation of hydrides upon etching and the presence of only weak X-ray superlattice reflections from the Ti-Al system, both of which hindered phase identification [46]. Additionally, the movement of equilibrium phase boundaries as a result of the presence of trace oxygen has made the exact location of phase boundaries hard to determine [18].

The first Ti-Al phase diagram to be widely accepted by the titanium community was produced by Blackburn [46] using transmission electron microscopy (TEM) and X-ray studies, and can be seen in Figure 2.4. It focusses on the Ti-rich end of the phase diagram ($<$ 30 wt.% Al). The diagram shows a hatched region of short range order (SRO) between the α and α + α_2 phase boundary, and also between the α + α_2 and α_2 phase fields where anomalous antiphase contrast is seen in TEM. These regions of uncertainty highlight the difficulty of determining the equilibrium phase boundaries involving α_2.

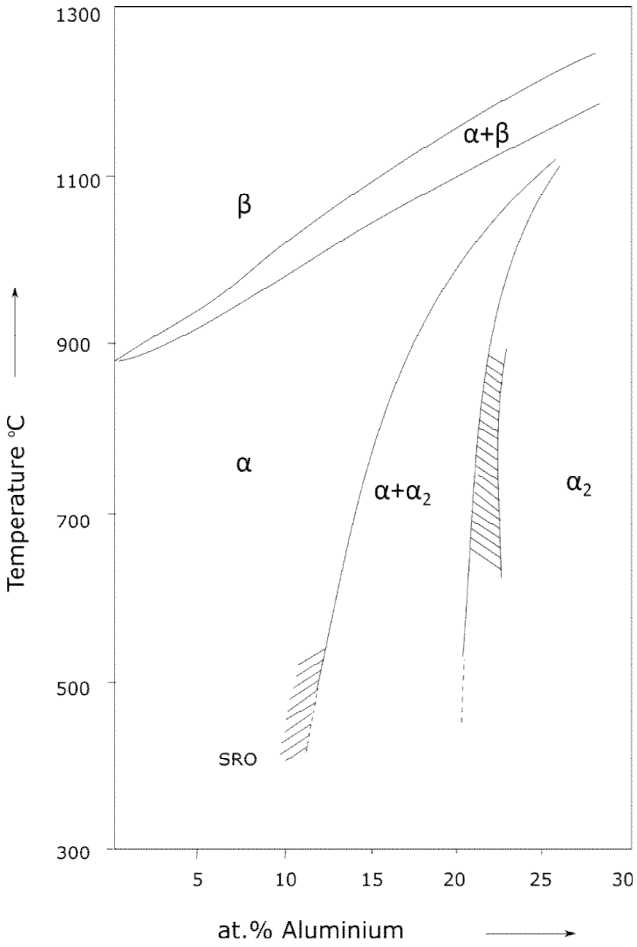


Figure 2.4: Ti-rich end of the Ti-Al phase diagram according to Blackburn, redrawn from [46].

The α / α + α_2 phase boundary of Blackburn's diagram agrees with X-ray diffraction and electrical resistivity data taken by Clark et al. [47]. However, Figure 2.4 conflicts with the work of Ence and Margolin [48], who propose the presence of both Ti_3Al and Ti_2Al in the region where Blackburn propose single phase Ti_3Al . Blackburn's interpretation is currently accepted. The width of the α_2 phase field on Figure 2.4 is due to the lattice parameter of the Ti_3Al phase varying as a result of changing Al content.

A review of the literature performed by Murray [49] resulted in the publication of the phase diagram displayed in Figure 2.5. Initially, Murray reported the formation of the ordered α_2 phase either by precipitation from supersaturated α or via the eutectoid reaction $\alpha \rightarrow \alpha_2 + \gamma$. Shull et al. [50] confirmed the eutectoid reaction in 1985, which can be seen in Figure 2.5.

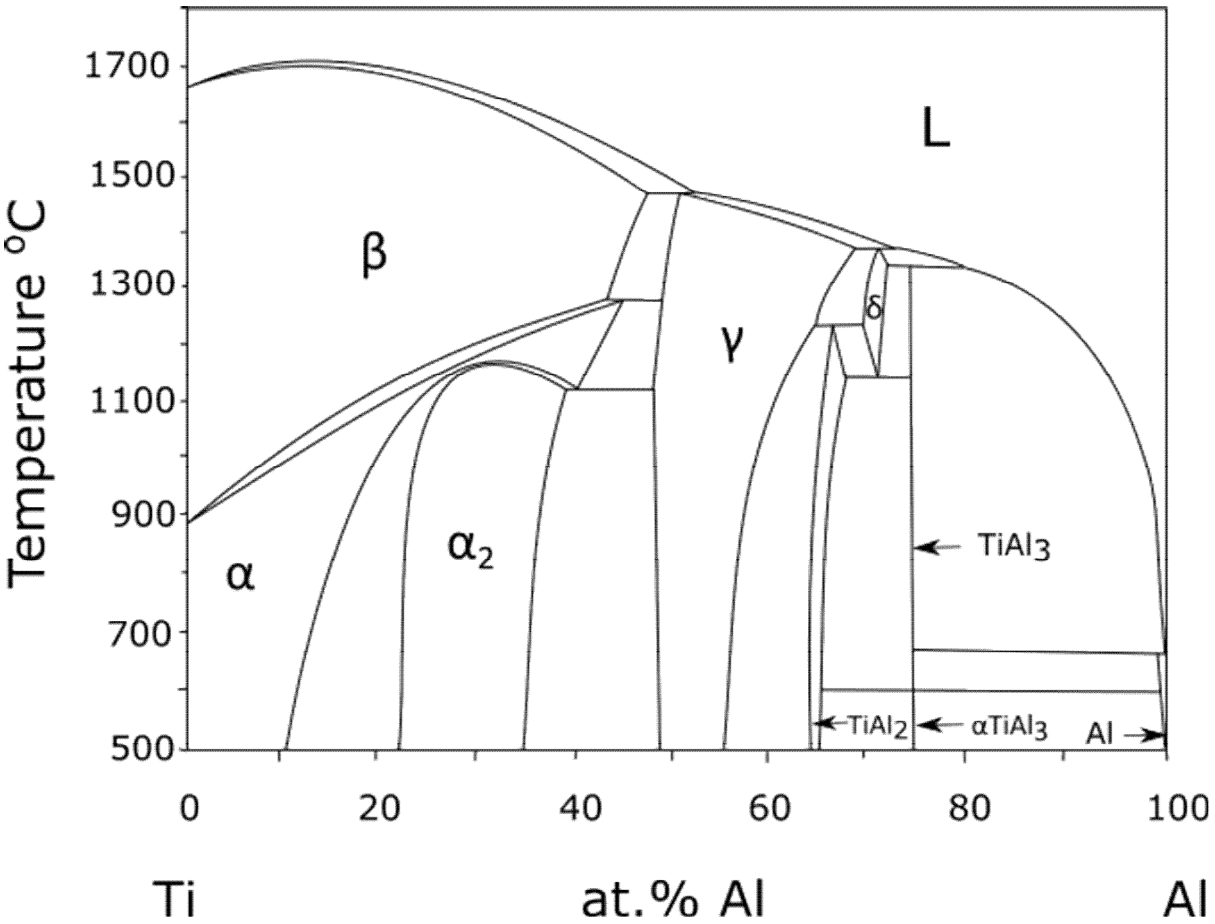


Figure 2.5: Ti-Al phase diagram according to Murray, redrawn from [51].

Further uncertainty centred on the higher aluminium region of the diagram. Two alternative diagrams for this region were proposed and are displayed schematically in Figure 2.6. Figure 2.6 (a) represents the original diagram submitted by Murray [49] and (b) represents the alternative version proposed by Valencia et al. [52]. Microstructural evolution during solidification was studied by Valencia et al. [52], and the results led to the conclusion that Murray's diagram [49] needed to be modified to include a stable L + α phase field. The revised version of the diagram is shown in Figure 2.6 (b) and concurs with the work of Ence et al. [48], which proposed the presence of two peritectics. The presence of two peritectics has since been confirmed by Kainuma et al. [53] using diffusion couple experiments, and others [54,55]

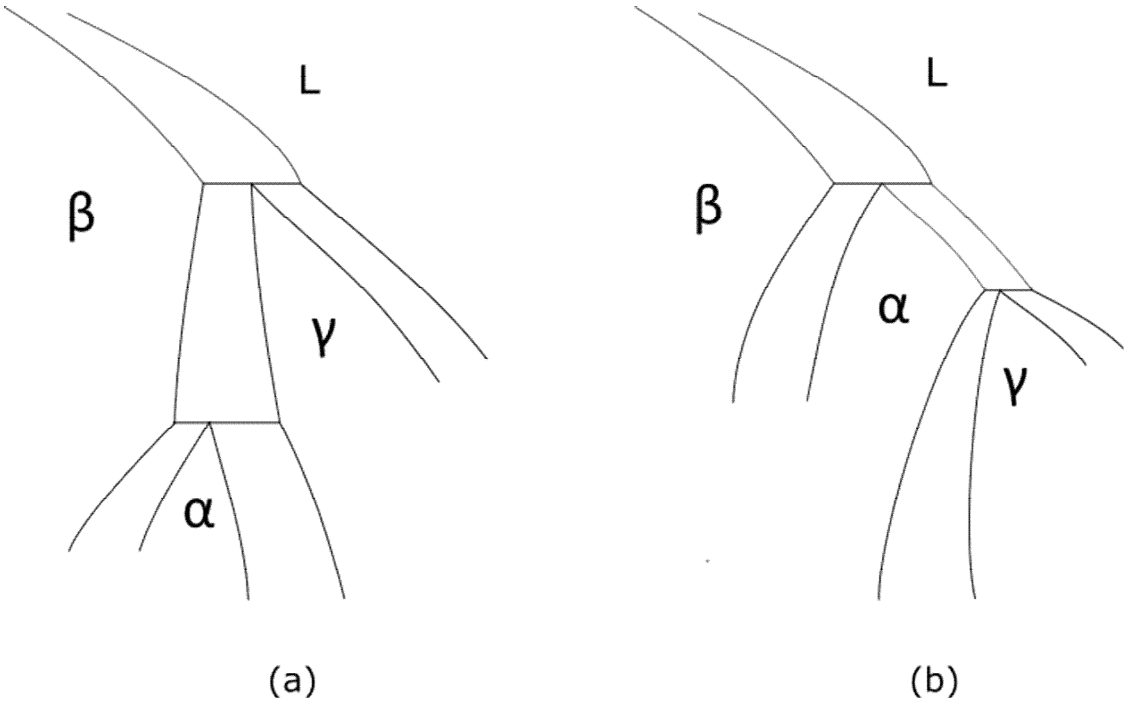


Figure 2.6: Schematic drawings of two potential configurations of the high Al end of the Ti-Al binary phase diagram (~30-80 at.%Al), according to (a) Murray [49] *and (b) McCullough* [54] *and others* [48][53][55].

Much discussion has arisen around the α_2/ SRO region of the Ti-Al phase diagram. SRO refers to the chemical ordering of solutes in an alloy such that the atoms of one type are surrounded by unlike atoms [56], and typically occurs on the length scale of the first or second nearest neighbour [57]. As mentioned above, Blackburn first indicated the presence of SRO on his phase diagram in 1967 [46]. Later work by Swartzendruber [58] proposed a position for the α_2 / $\alpha + \alpha_2$ phase boundary based on magnetic susceptibility measurements, and Namboodhiri [59] provided further information about the SRO boundary by taking electrical resistivity measurements. This resulted in the section of the phase diagram reproduced in Figure 2.7.

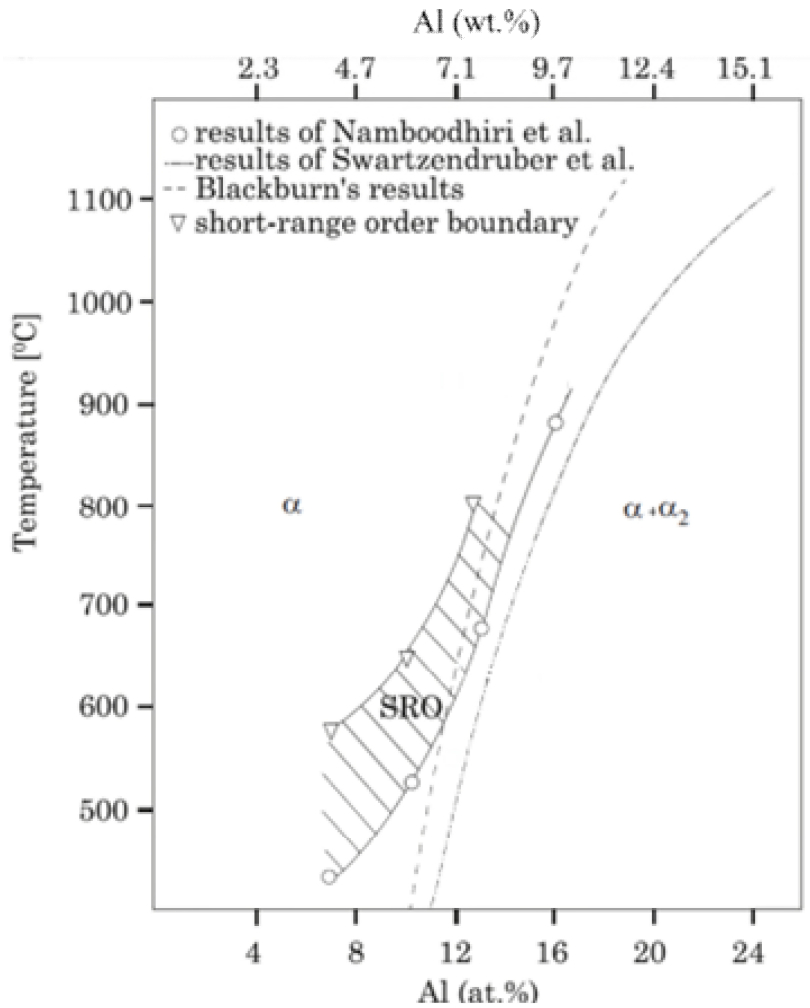


Figure 2.7: Titanium-rich end of the Ti-Al binary phase diagram showing contributions by Blackburn [46]*, Namboodhiri* [59] *and Swartzendruber* [58]*. After* [60]*.*

The exact positioning of the SRO region is still an open topic of discussion in the current literature. However, the updated Ti-Al binary phase diagram produced by Radecka et al. [60], and displayed in Figure 2.8, is a useful reference point.

A final version of the Ti-Al phase diagram that is worthy of note is the diagram calculated using thermodynamics by Kattner et al. [61]. The principal reactions in the calculated diagram agree with the diagram of McCullough et al. [62] and, after being modified to make it agree with existing thermodynamic data, it was published as a revised version of the Murray diagram [41], and can be seen in Figure 2.8. The Kattner diagram will be taken to be the best current version of the Ti-Al phase diagram and will be used for reference throughout the rest of this work.

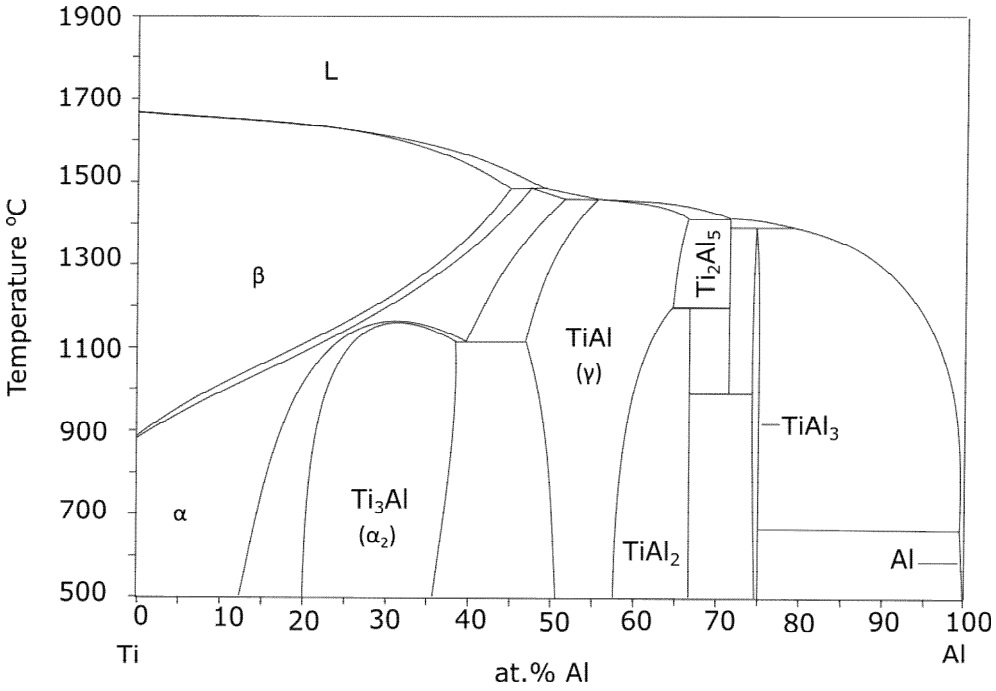


Figure 2.8: Calculated Ti-Al binary phase diagram redrawn from [61].

2.4 ALLOY CLASSIFICATION

Small additions of alloying elements can significantly change the properties of titanium alloys by changing the temperature of the $\alpha \rightarrow \beta$ transition. This enables the alloy properties to be tailored to the engine environment in which they are situated. For example, alloying additions to titanium alloys for use in compressor discs, where temperatures can approach 600°C, are carefully controlled to optimise high-temperature strength. Zr and Sn are present in the compressor disc alloy TIMETAL 834 for this reason [63].

Alloying additions can be classified into two groups; α stabilisers (e.g. Al, O, N), which partition preferentially to the α phase, stabilising it to higher temperatures and β stabilisers (e.g. V, Mo, Fe and Cr), which partition to β, expanding the β phase field. Al and O also suppress twinning [34]. β stabilisers can be further broken down into β isomorphic (e.g. Mo and V) and β eutectoid (e.g. Fe, Cr, Si and H). The former are completely soluble in β-Ti whereas the latter form intermetallic compounds via eutectoid decomposition. Neutral elements (e.g. Zr, Hf) do not significantly

stabilise either α or β but are added to increase strength and hardness [64]. The effect of alloying elements can be seen graphically in Figure 2.9.

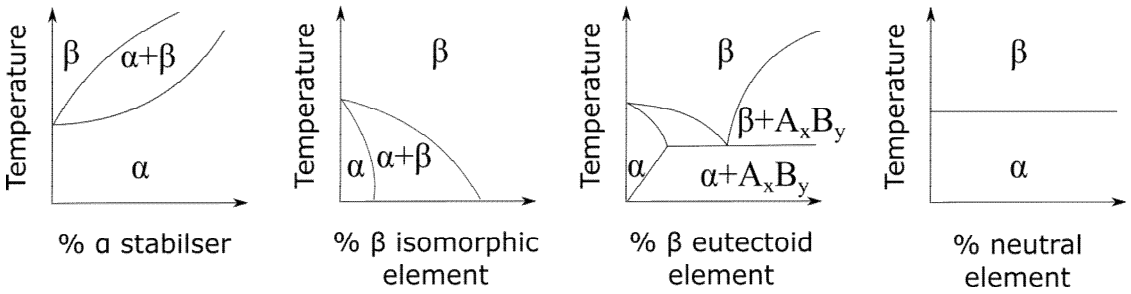


Figure 2.9: Schematic binary phase diagrams illustrating the effect of alloying additions, after [39].

The total α stabiliser content is measured as an equivalent Al content, as described in Equation 2.1, which is an empirically derived equation.

$$Al_{eq} = [Al] + 0.17[Zr] + 0.33[Sn] + 10[O] \qquad \textit{Equation 2.1}$$

An upper limit of $[Al]_{eq} \sim 9$ at.% is placed on α alloying additions to avoid embrittlement via formation of the intermetallic α_2 phase.

Pure titanium has an HCP crystal structure below $882^{\circ}C$ (α phase) but has a BCC crystal structure at temperatures above $882^{\circ}C$ (β phase). Titanium alloys are classified as either α, β or $\alpha + \beta$, depending on the concentration of β-stabiliser present, as illustrated in Figure 2.10.

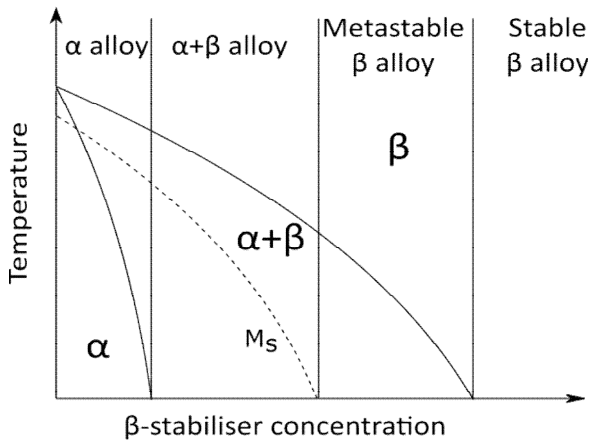


Figure 2.10: Schematic diagram of a pseudo-binary section through isomorphous phase diagram, after [39].

2.4.1 α alloys

Single-phase α alloys contain alloying additions which stabilise the α phase, such as Al and O. Examples include commercially pure titanium, Ti-5Al-2Sn-ELI[1] and Ti-8Al-1Mo-1V. They are non-heat treatable, meaning their strength derives primarily from solid solution strengthening and not age hardening, which results in good weldability. The hexagonal crystal structure of the α phase limits slip, reducing alloy formability [65]. The high corrosion resistance of α alloys results in their use in heat exchangers and chemical processing equipment.

Alloys containing no more than $\sim$2 at.% β stabilising elements (e.g. Mo or V) are often termed 'near-α'. The amount of β-stabilising elements present is measured as a molybdenum equivalence, as illustrated in Equation 2.2.

$$\mathrm{Mo_{eq}} = [\mathrm{Mo}] + 0.6[\mathrm{V}] + 0.44[\mathrm{W}] + 0.28[\mathrm{Nb}] + 0.22[\mathrm{Ta}] + 1.25[\mathrm{Cr}] + 1.25[\mathrm{Ni}] + 1.7[\mathrm{Co}] + 2.5[\mathrm{Fe}] \quad \textit{Equation 2.2}$$

Near-α alloys are used in high-temperature aeroengine components since they have superior high-temperature mechanical properties to other α alloys and are significantly lighter than steels. Examples include TIMETAL 834, Ti-6Al-2Sn-4Zr-2Mo (Ti-6242), Ti-5Al-5Sn-2Zr-2Mo, TIMETAL 685 and Ti 1100[2]. However, like all α alloys, they are susceptible to cold dwell fatigue owing to the formation of the ordered Ti_3Al phase and, depending on alloy composition, may also be susceptible to stress corrosion cracking [39].

2.4.2 α+β alloys

Alloys containing both α and β phases in varying proportions are known as α+β alloys. Applications of $\alpha + \beta$ alloys are split according to their strength and the temperature range in

[1] Extra Low Interstitials

[2] Al5.9-Sn2.6- Zr4.0-Mo0.4-Si0.42

which they operate. Ti-64 is the most widely used $\alpha + \beta$ alloy, used in the fan blades and low-temperature compressor of aeroengines owing to its combination of high tensile strength and good fatigue properties [66]. It contains a greater volume fraction of α than β and has high yield strength (~1000 MPa), good ductility and toughness, and good fatigue properties. Figure 2.11 shows a partial isothermal section for the Ti-Al-V ternary system at 600°C, and it can be seen that Ti-64 lies in the $\alpha + \beta$ phase field.

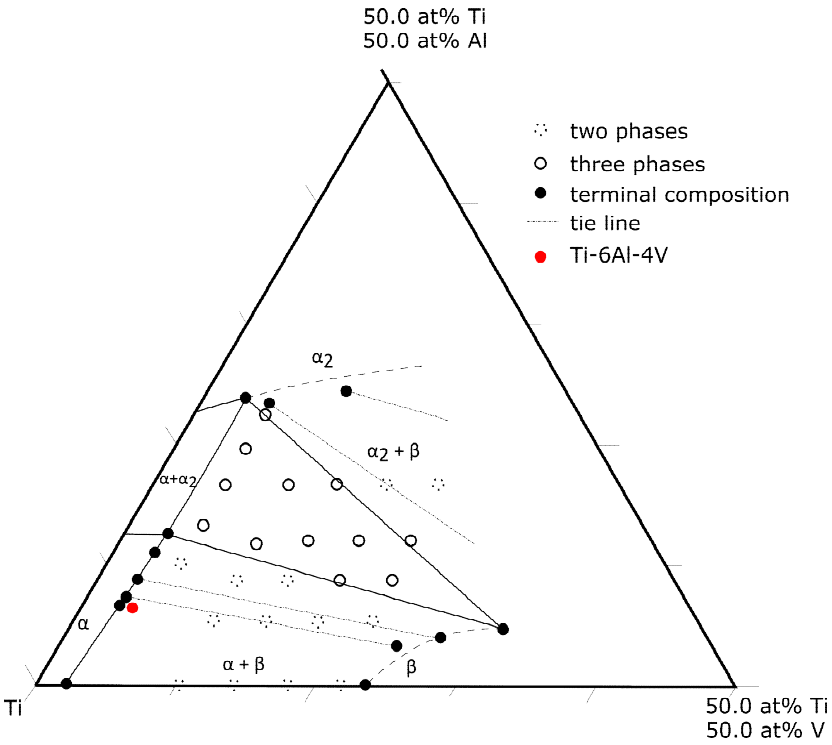


Figure 2.11: Titanium-rich corner of the isothermal section at 600°C. Composition of the alloy Ti-64 is shown in red. Circles indicate the points at which electron microscopy techniques were used to verify the two-phase ($\alpha + \beta$) and ($\alpha_2 + \beta$) phase fields, as well as the three-phase ($\alpha + \alpha_2 + \beta$) triangle and tie line end compositions. Redrawn from [67].

Ti-6Al-2Sn-4Zr-6Mo (Ti-6246) is a higher temperature $\alpha + \beta$ alloy that is used in the compressor of an aeroengine. The combination of high temperature creep strength, and high fatigue strength-to-weight ratio makes Ti-6246 better suited to this application than higher density nickel superalloys.

The properties of both high temperature and high strength α+β alloys are strongly dependent on processing. For example, a fully lamellar microstructure, seen in Figure 2.12 (a), can be achieved

by recrystallising above the α/β transformation temperature after deformation in the $\alpha + \beta$ phase field. The rate of cooling after recrystallisation is crucial since it controls the size of the α colonies that are produced. Alloys that are cooled faster have a smaller colony size and thus a shorter slip length. This results in higher yield strength and improved low cycle fatigue strength [66]. Alternatively, a bimodal microstructure of α and transformed β is achieved by recrystallising below the transformation temperature after deformation, as seen in Figure 2.12 (b). If the cooling rate after recrystallisation is sufficiently slow, an equiaxed microstructure is obtained since only primary α grains grow, and no α lamellae form. An equiaxed microstructure is also obtained for very low recrystallisation temperatures, and can be seen in Figure 2.12 (c).

When comparing the properties of a fully lamellar microstructure to that of a bimodal microstructure (assuming that the cooling rates after recrystallisation are the same), the bimodal structure should have higher yield stress and higher low cycle fatigue strength. This is a result of the small β grain size in the bimodal structure, which leads to small α colony size and therefore, small slip length [66].

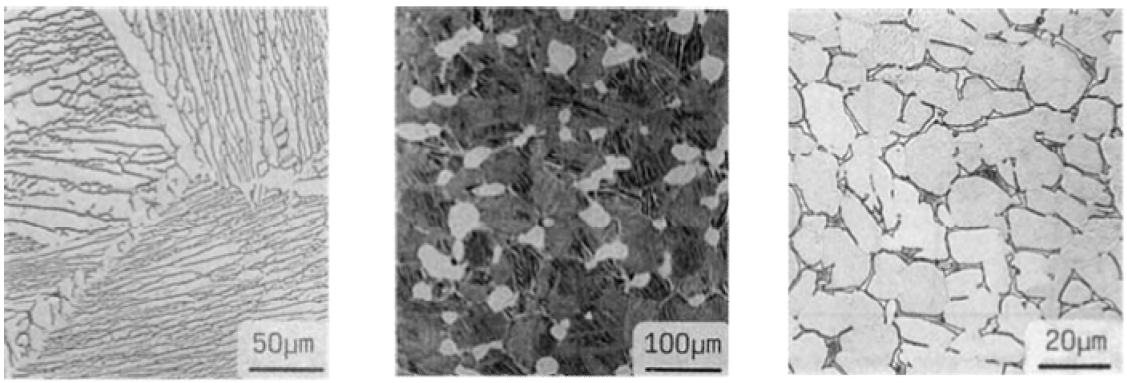


Figure 2.12: Micrographs showing the dependence of microstructure of $\alpha + \beta$ alloys on processing. (a) Lamellar microstructure in Ti-6242; (b) Bi-modal microstructure in TIMETAL 834; (c) Equiaxed microstructure in Ti-6242 [66].

2.4.3 β alloys

There is a minimum amount of β-stabiliser required such that upon quenching to room temperature, the β phase is retained without transforming to martensite. Alloys which meet these criteria are defined as β alloys. Examples include Ti-10V-2Fe-3Al, Ti-13V-11Cr-3Al, Ti-8Mo-8V-2Fe-3Al and Ti-15-3. They are the highest strength class of titanium alloys since they benefit from both solid solution strengthening and age hardening; strengthening α-Ti particles and ω phase particles can both form upon ageing [68]. This results in their use in aircraft landing gear, power plants and sporting goods. They also have excellent forgeability but are heavier than α+β alloys due to the heavy β stabilisers.

This thesis focusses on α, near-α and $\alpha + \beta$ alloys.

2.4.4 Effect of alloying additions

It can be seen from Table 2.2 that a wide range of compositions exist for high temperature titanium alloys. This is a result of the alloys being designed for different applications. For example, the near-α alloy Ti-6242 was designed to have high creep strength and therefore contains a higher α stabiliser content than the α+β alloy Ti-6246. This increases the volume fraction of α phase in Ti-6242, which improves creep performance since the rate of self-diffusion in α-Ti is several orders of magnitude slower than in β [39]. The addition of 0.1 wt.% silicon to this alloy creates Ti-6242S, which further improves creep strength owing to the ability of silicon to impede dislocation motion via solute drag [69,70]. Figure 2.13 illustrates that adding 0.1 wt.% Si to Ti-6242 reduces creep deformation [71].

Table 2.2: Temperature range and chemical composition of high temperature titanium alloys, listed in order of introduction [72].

Alloy name	Year of introduction	Maximum useful operating temperature (°C)	Composition (wt.%)							
			Al	Sn	Zr	Mo	Nb	V	Si	Ti
Ti-64	1954	300	6	-	-	-	-	4	-	Bal.
TIMETAL 550	1956	425	4	2	-	4	-	-	0.5	Bal.
Ti-811	1961	400	8	-	-	1	-	1	-	Bal.
TIMETAL 679	1961	450	2	11	5	1	-	-	0.2	Bal.
Ti-6246	1966	450	6	2	4	6	-	-	-	Bal.
Ti-6242	1967	450	6	2	4	2	-	-	-	Bal.
TIMETAL 685	1969	520	6	-	5	0.5	-	-	0.25	Bal.
Ti-6242S	1974	520	6	2	4	2	-	-	0.1	Bal.
TIMETAL 829	1976	580	5.5	3.5	3	0.3	1	-	0.3	Bal.
TIMETAL 834	1984	590	5.8	4	3.5	0.5	0.7	-	0.3	Bal.

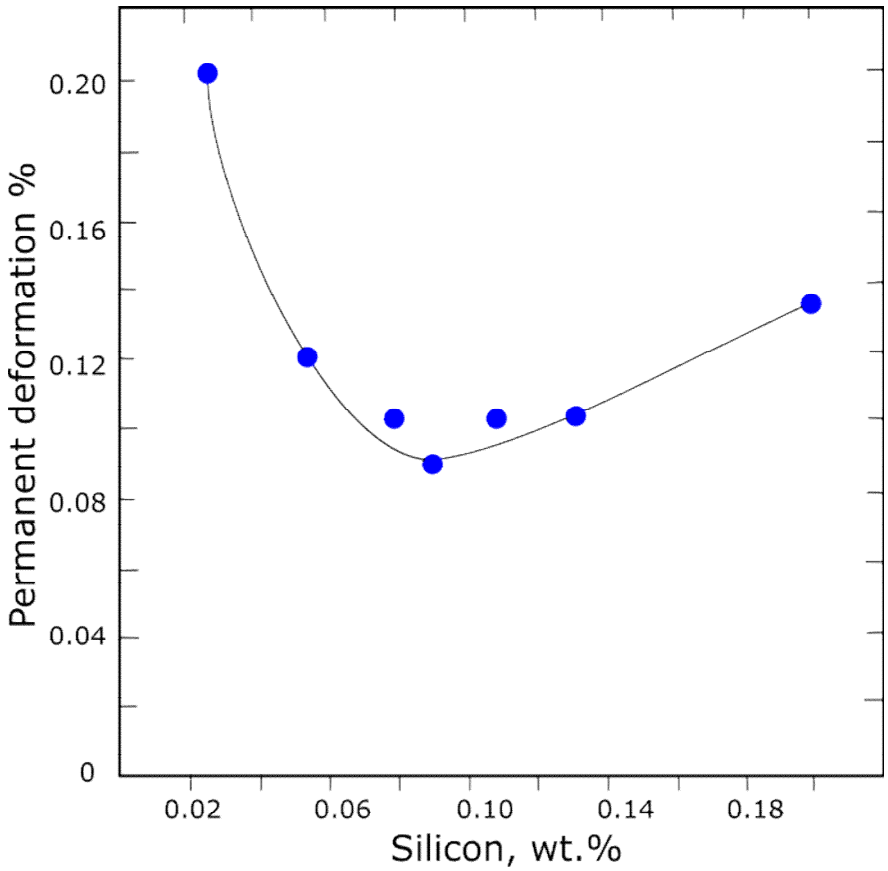


Figure 2.13: Effect of silicon on creep deformation of Ti-6242 after heat treatment at 510°C for 100h at 240 MPa, redrawn from [71].

Additions of aluminium to titanium increases tensile strength, with the most significant strength increase achieved between 4 and 5 wt.% added aluminium [73]. Hardness also increases as aluminium is added to titanium, with peak hardness achieved at 26 wt.% Al, as can be seen in Figure 2.14. This corresponds to the maximum solubility of aluminium in α-Ti. Hardness then decreases through the two phase $\alpha + \gamma$ two phase region until a minimum is reached with the formation of the γ phase [73]. Aluminium additions also reduce alloy density [72]. However, when more than ~5 wt.% Al is added, the formation of the embrittling α_2 phase is encouraged [39]. This is reflected in the alloy compositions in Table 2.2, which all contain less than 7 wt.% Al (except Ti-811). Tin, another α stabiliser, is often added in conjunction with aluminium to further increase strength without causing embrittlement. However, tin is generally not used as the primary α stabiliser since it increases alloy weight whereas aluminium reduces alloy weight. Zirconium is added for further solid solution strengthening but levels are kept below ~5 wt.% to

minimise loss in ductility and creep strength. Molybdenum is added as a β stabiliser and increases strength and hardness in quenched and aged material. However, molybdenum reduces weldability and so molybdenum content is kept low in high long-term creep strength materials. Niobium is also a β stabiliser, and improves high temperature oxidation resistance [72].

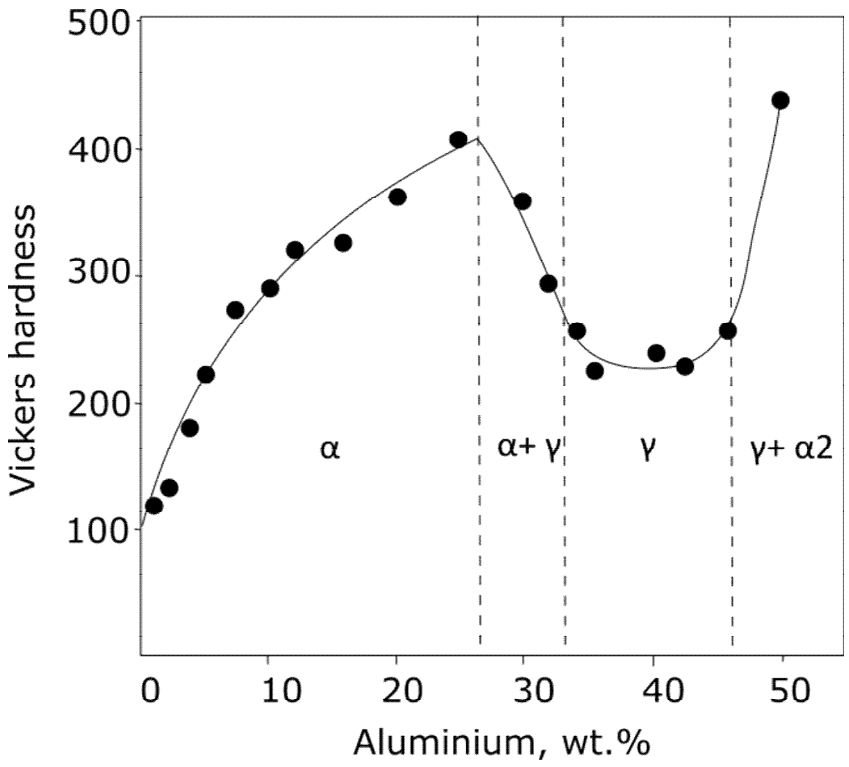


Figure 2.14: Effect of aluminium content on Vickers hardness of titanium, redrawn from [73].

2.5 DEFORMATION BEHAVIOUR OF TITANIUM

Titanium can deform by either twinning or slip. Both these processes occur via plastic shear. After slip has occurred, the sheared region has the same lattice structure as the original lattice. However, the lattice of the sheared region formed after deformation twinning is the mirror image of the original crystal [74].

The low-temperature ductility of α titanium is a result of activation of twinning modes. Twinning is especially important when the applied stress direction is parallel to the c-axis, as illustrated in Figure 2.15 since this prevents slip of dislocations with a basal Burgers vector from relieving the

stress. However, even small alloying additions of elements such as Al, O or N cause twinning to be suppressed [39]. Thus, dislocation slip is considered the primary deformation mechanism in titanium alloys.

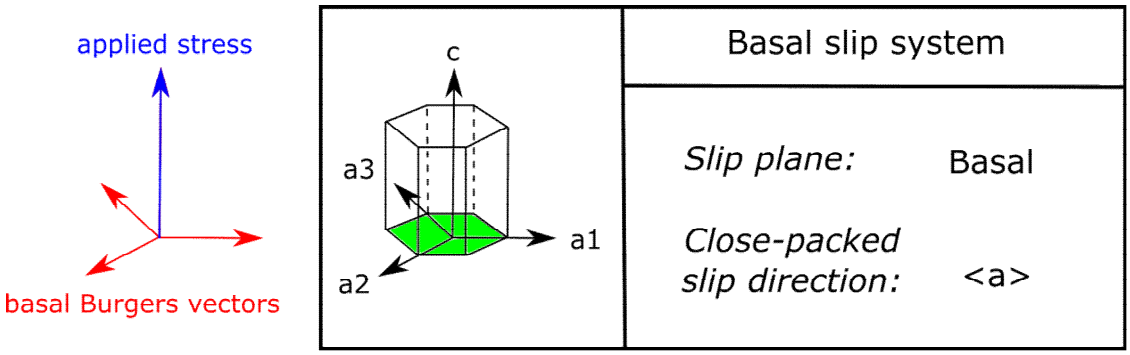


Figure 2.15: Diagram to illustrate that when stress is applied parallel to the c-axis of titanium, the stress cannot be relieved by slip of dislocations with a basal Burgers vector since these slip directions are perpendicular to the applied stress. Redrawn from [75].

Churchman [76] identified the slip systems to be $\{10\bar{1}0\}\langle 11\bar{2}0\rangle$, $\{10\bar{1}1\}\langle 11\bar{2}0\rangle$, $(0001)\langle 11\bar{2}0\rangle$, which corresponds to slip in the close-packed directions on the prismatic, pyramidal and basal slip planes, respectively.

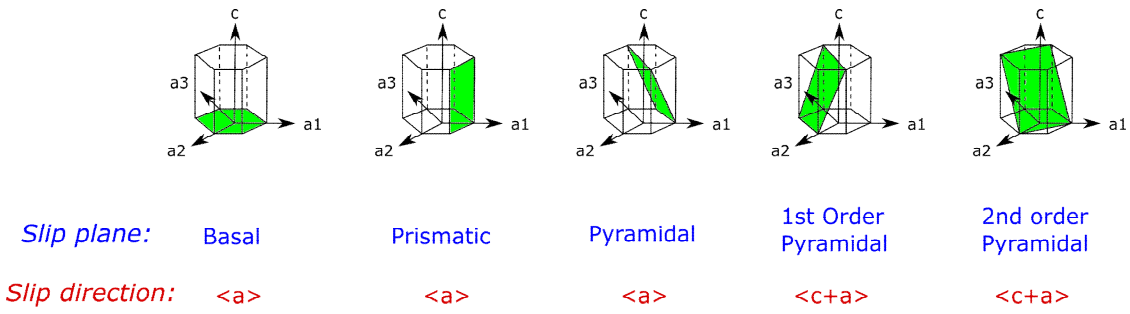


Figure 2.16: Slip systems available in HCP single-crystal titanium. Slip planes are described in blue and slip directions are represented in red. Redrawn from [75].

The combinations of slip planes and corresponding close-packed slip directions result in 12 slip systems in total, displayed in Figure 2.16, but this is reduced to 4 independent slip systems [39]. This number of slip systems is insufficient to satisfy the Von Mises criterion[3] for a polycrystalline

[3] The Von Mises criterion states that 5 independent slip systems must exist for a polycrystalline material to undergo homogeneous plastic deformation [237].

material to undergo homogeneous plastic deformation. Thus a twinning system or a slip system containing a <c+a> Burgers vector must operate for plastic deformation to occur. Twinning is almost entirely suppressed in alloys containing greater than 5 wt.% aluminium, and thus deformation in such alloys is dependent on the slip of <c+a> dislocations, which have been observed in TEM [39].

2.6 HARDENING MECHANISMS IN TITANIUM ALLOYS

A number of mechanisms can cause hardening in α-type titanium alloys. Britton et al. [77] demonstrated, using commercially pure titanium (CP-Ti), that hardness depends on crystal orientation. Declination angle is the angle between the indentation direction and the c-axis of the hexagonal titanium crystal structure, which is equal to the second Euler angle. As the declination angle decreases, hardness increases. The dependence of hardness on crystal orientation stems from the difference in critical resolved shear stress on each of the slip systems involved in the deformation. The hexagonal symmetry of the α phase titanium means that, in order to satisfy the Von Mises criterion, slip that creates displacement out of the basal plane, i.e. <c+a> slip, is required in addition to basal <a> type slip [78]. The closer that the direction of the applied indentation load is to the c-axis, the greater the amount of <c+a> slip that is needed to enable plastic deformation to occur [77]. <c+a> type dislocations are energetically less favourable than <a> type dislocations, making <c+a> slip three times harder to initiate than <a> slip [77,78]. Thus the critical resolved shear stress is higher on the <c+a> type slip systems, meaning the material is harder when indented closer to the c-axis.

Britton et al. [77] measure a small variation in hardness of ~1.5 GPa due to changes in declination angle in CP-Ti. Precipitation of α_2 (see section 2.8) and intrinsic lattice flow stress also have a minor contribution to hardening of the α phase [79]. However, more major hardness contributions are provided by work hardening, boundary hardening and solid solution hardening, including hardening due to interstitial oxygen atoms [79], which will be described in greater detail

in section 2.7.2. Ordering of interstitial oxygen atoms can cause hardening at temperatures below 427-577°C [79–81].

Microstructure can also affect hardness. For example, grain size affects hardness through the Hall-Petch effect [82,83]. In near-α alloys, such as TIMETAL 834, the typical processing treatment of homogenisation in the α + β phase field, followed by quenching from the α phase field, leads to the formation of large α grains with fine lath regions of transformed β, as seen in Figure 2.12 (b). The two different microstructural features have different mechanical properties; the lath regions are harder than the large α grains [84].

2.7 INTERSTITIAL ELEMENTS

Oxygen and nitrogen are interstitial impurities that dissolve preferentially in the α phase of titanium [85]. The maximum solubility of nitrogen in the α phase is 19 at.%, whereas the binary Ti-O phase diagram reveals the solubility limit of oxygen in α to be 34 at.% [51]. Both elements are considered α stabilisers and therefore raise the β transus, as can be seen from Figure 2.17.

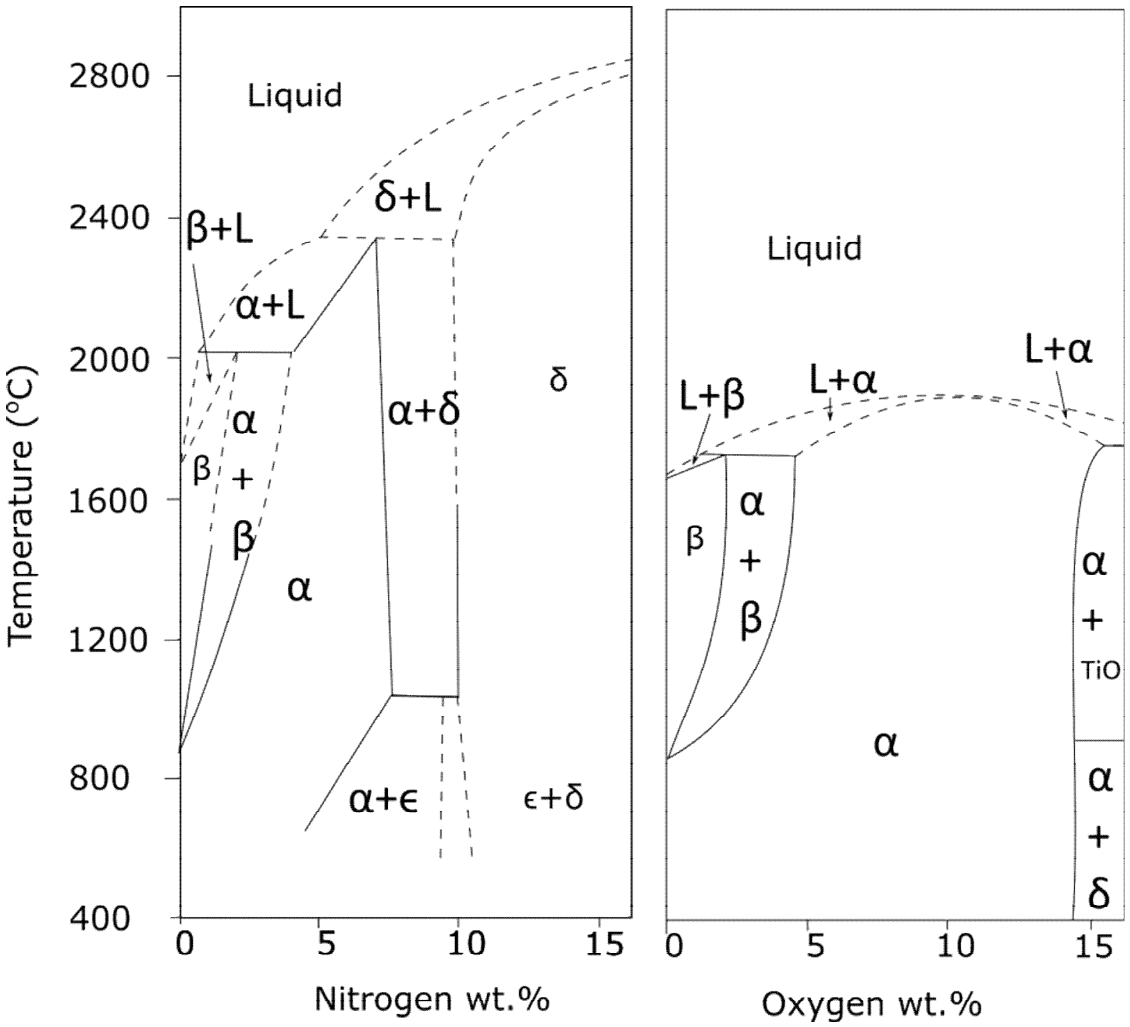


Figure 2.17: Titanium-rich ends of the binary systems Ti-O and Ti-N, showing the α-stabilising effect of oxygen and nitrogen, redrawn from [85].

While these interstitial elements have a strengthening effect at low temperatures, this benefit is outweighed by their highly detrimental impact on ductility. For example, addition of 0.2 wt.% nitrogen to α titanium almost triples the tensile strength but more than halves the percentage elongation [86]. Consequently, oxygen and nitrogen levels are carefully controlled during alloy processing to minimise their effect on mechanical properties. For example, much of the processing is carried out in an inert atmosphere/ under vacuum to minimise oxygen and nitrogen pickup from the air.

Additionally, triple vacuum arc remelting is now routinely used in titanium processing. Dissolved oxygen and nitrogen are removed from the molten titanium by the vacuum, thus increasing alloy

quality. Use of the cold hearth melting technique [87] dissolves low-density inclusions, which are hard regions of brittle, interstitially-stabilised α phase that originate from high concentrations of oxygen and nitrogen in titanium sponge [88].

Pickup of nitrogen and oxygen can occur during fabrication and forming, but can also occur during service. For example, work by Shimojo et al. [89] has shown that nitrogen is absorbed onto fresh fracture surfaces produced during cyclic loading, and then enters the plastic zone during subsequent loading. At temperatures above 480^{o}C, oxygen from the environment diffuses through the passivating surface oxide layer forming a subsurface layer known as the α case. This will be discussed in more detail in section 2.10.

Oxygen and nitrogen sit in interstitial sites, preferring to occupy the octahedral hole in the HCP crystal structure [88]. The HCP α phase has one octahedral interstitial per titanium atom whereas the BCC β phase has three. Consequently, the interstitial sites in the α phase are larger, and thus solubility of interstitial atoms is higher in α than β [90]. Interstitial oxygen results in a volume expansion of the unit cell of 1.3x10^{-3} nm^{3} per at.% O [91] whereas nitrogen results in a larger volume expansion of 1.8x10^{-3} nm^{3} per at.% N on account of its larger atomic radius [92]. Experiments carried out on Ti-64 powder heated to 600^{o}C in commercially pure argon gas showed that expansion increases with temperature due to lattice thermal expansion and absorption of oxygen and nitrogen [93]. Both oxygen and nitrogen interstitials produce a more considerable expansion in the c-axis than the a-axis, resulting in an increase in the c/a ratio of the HCP α phase [92]. This reduces the number of slip and twinning systems available for plastic deformation, reducing hot fabricability [85].

Oxygen has been shown to preferentially occupy octahedral interstitial sites surrounded by six titanium atoms, known as [OTi6] sites [80,94–97]. *Ab initio* studies by Nayak et al. [96] used density functional theory (DFT) to calculate the formation energies of point defects, which reveals that the majority of impurity elements in titanium prefer to occupy substitutional positions. For

these elements, this configuration leads to the lowest supercell volume change, and thus the lowest elastic energy of the system. The exception to this are smaller elements, such as oxygen and nitrogen, which are preferentially located at interstitial positions. These elements have the ability to attract electrons and thus undergo chemical hybridisation with the surrounding host titanium atoms. Gunda et al. [98] describe how introduction of interstitial atoms into α-Ti creates p levels in the density of states, which enables hybridisation of the interstitial p orbitals with the titanium atom d orbitals, producing σ bonds. The effect of hybridisation dominates over the elastic energy savings that would be made by occupying a substitutional site [96].

DFT calculations by Scotti et al. [97] explore the difference in energy between the eight interstitial sites available for oxygen to occupy in α-Ti, seen in Figure 2.18 . They confirm the stability of octahedral sites, but also show that hexahedral, crowdion, and basal crowdion sites are more stable than the tetrahedral sites. This affects the diffusion paths taken by oxygen interstitial atoms, resulting in highly anisotropic oxygen diffusion. This has implications for formation of *α case* layers, which will be discussed in section 2.10.

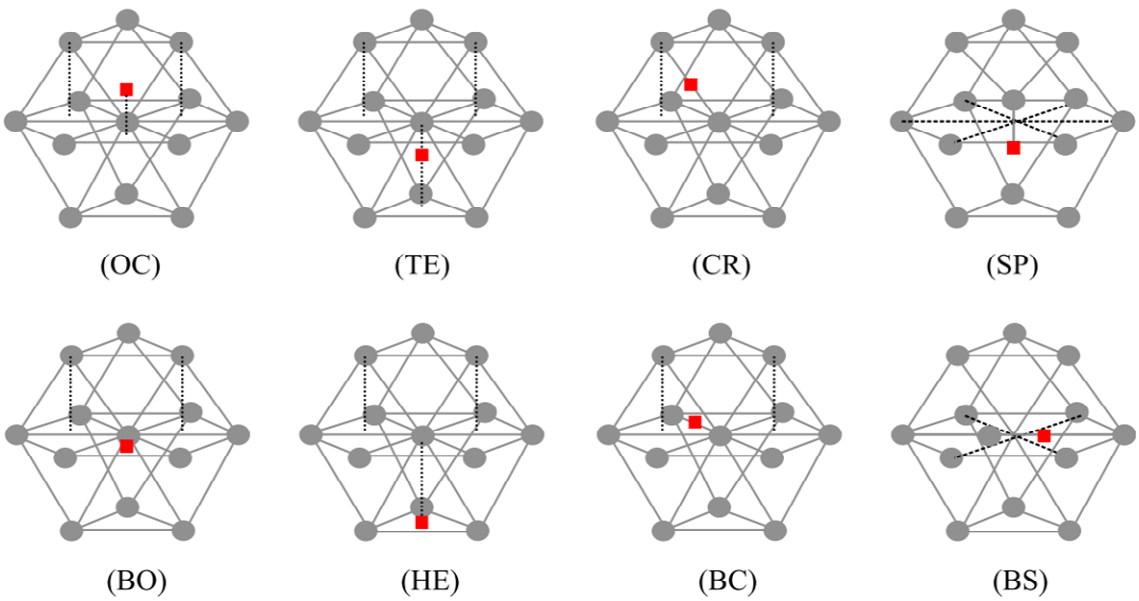


Figure 2.18: Schematic representation of interstitial sites in the HCP crystal (highlighted in red): octahedral (OC), tetrahedral (TE), crowdion (CR), split dumbbells along c axis (SP), basal octahedral (BO), hexahedral (HE), basal crowdion (BC), and split dumbbells in the basal plane (BS) [97].

Interactions between neighbouring interstitial oxygen atoms can occur, as described by Ruban et al. [80] for α-Ti. They find that interstitial-interstitial interactions have chemical and strain contributions, with the chemical contribution giving rise to strong repulsion of nearest neighbour interstitials. The result of these interactions is ordering of oxygen atoms into $TiO_{1/6}$, $TiO_{1/3}$ or $TiO_{1/2}$ phases, depending on oxygen concentration. These phases can be seen in Figure 2.19, and it should be noted that the nearest-neighbour interstitial positions of oxygen atoms are vacant in all phases, due to strong chemical repulsion. Oxygen ordering is also predicted to occur on the oxygen interstitial sublattice of the ordered α_2 phase, based on a discrepancy between predicted and measured oxygen content within this phase [94]. More in depth discussion of the α_2 phase can be found in section 2.8.

Looking at the behaviour of oxygen within the wider microstructure of titanium alloys, Aksyonov et al. [24] have performed *ab initio* DFT calculations to investigate grain boundary segregation in α-Ti. While twin boundaries are favourable for oxygen segregation (due to their symmetrical void shapes), the segregation energies are low suggesting weak enrichment. Attraction of oxygen to twin boundaries in α -Ti has also been shown to be energetically favourable by Ghazisaeidi et al. [25]. However, for general (non-symmetrical) grain boundaries, the non-symmetrical void shape results in repulsion of oxygen from the grain boundary.

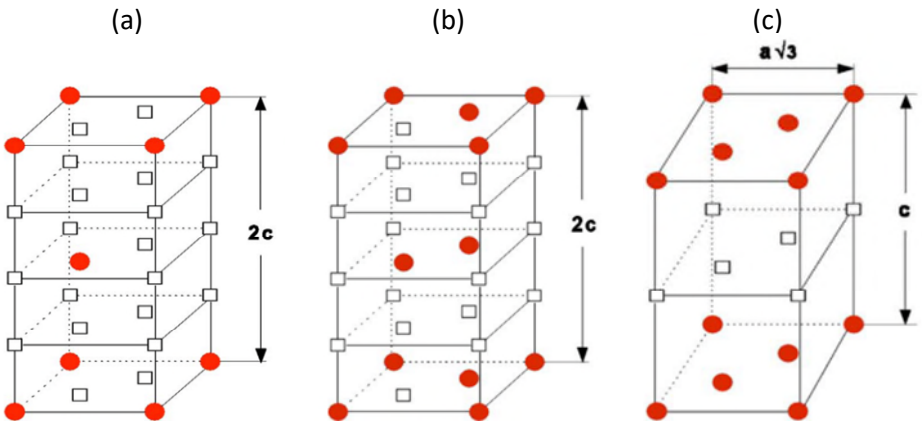


Figure 2.19: The ground-state structures of the (a) TiO1/6, (b) TiO1/3 and (c) TiO1/2 interstitial alloys. Only interstitial positions are shown. Filled symbols are oxygen atoms in the interstitial positions [80].

APT work by Semenova et al. [26] has shown that oxygen, nitrogen and carbon segregate to α - α boundaries in ultra-fine grained commercially pure titanium. The boundary type was not characterised, but subsequent work by Aksyonov [24] show that co-segregation of carbon and oxygen is not favourable and that instead what is being seen by Semenova is competitive segregation of carbon and oxygen.

Whilst segregation of oxygen to non-symmetrical α-α grain boundaries has been calculated to be energetically unfavourable, experimental observations have shown that α- β boundaries can act as fast diffusion paths [10,11]. This will be discussed in more detail in section 2.10.3.2.

2.7.1 Effect on deformation behaviour

Deformation of titanium occurs mainly via slip, as mentioned in section 2.4.4. Slip occurs via glide of dislocations, which can only happen when the component of the applied shear stress acting on the slip plane in the slip direction reaches a critical value known as the critical resolved shear stress (CRSS).

Oxygen and nitrogen have a strong effect on the CRSS of dislocations in titanium, increasing the strength of both basal and prism slip [78]. Oxygen promotes dislocation glide over twinning, which reduces ductility [91]. At oxygen concentrations higher than 0.25 wt.%, cross slip becomes more difficult and slip changes from wavy to planar, as can be seen in Figure 2.20. This indicates strain localisation and results in a loss of formability [39].

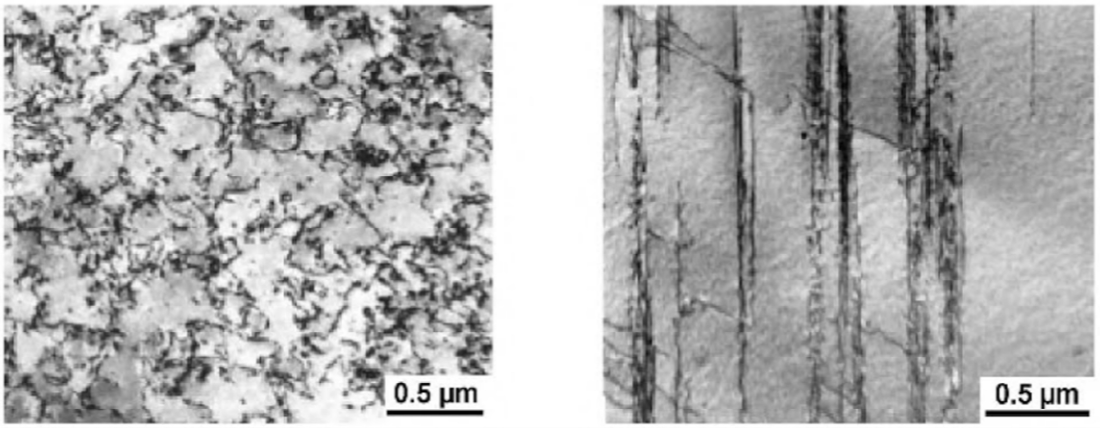


Figure 2.20: TEM micrograph showing effect of oxygen on slip mode in CP-Ti (a) Wavy slip, 0.15% oxygen (b) Planar slip, 0.5 wt.% oxygen [39].

Planar slip bands can indicate the presence of ordering. Planar slip was observed in pure α titanium as oxygen content was increased. This could mean short range ordering of oxygen atoms is causing the planar slip behaviour in pure titanium [81]. This observation has led to investigation of whether short range ordering occurs before the formation of the ordered α_2 phase, which will be discussed in greater depth in section 2.8.1.2.

2.7.2 Effect on mechanical properties

2.7.2.1 Mechanistic understanding

Interstitial solid solution hardening in HCP α-Ti can be caused by interaction of dislocations with non-isotropic strain fields that form around oxygen or nitrogen interstitials due to a greater change in lattice strain in the c-axis compared to the a-axis [93]. However, Yu et al. [99] report that elastic interactions between the lattice strains of interstitial atoms and lattice strains of dislocations is not the dominant hardening mechanism. The level of interstitial solid solution hardening provided by oxygen in titanium alloys is unusually large and originates from strong interactions between interstitial solutes and the core of screw dislocations [99]. The presence of oxygen interstitials near to the core of a screw dislocation gliding on a prismatic plane

in α-Ti may cause local cross slip, resulting in pinning of the dislocation core. Furthermore, passage of a dislocation reduces the size of the octahedral interstitial hole, and may result in the oxygen atom having to occupy the higher energy basal plane sites, also resulting in hardening [99]. These two screw dislocation-interstitial interactions have a greater hardening effect than the strain field interactions described above.

2.7.2.2 Mechanical testing

Liu et al. [79] found that hardness of titanium alloys varies as a function of the square root of oxygen concentration. They performed tensile tests on three Ti-6Al-2V α alloys with 0.07, 0.202 and 0.651 wt.%O, respectively. Total embrittlement occurred at 0.65 wt.% O, well below the solubility limit of oxygen in α. Figure 2.21 further quantifies the effect of oxygen on the hardness of titanium and shows nitrogen is a more potent hardener by weight than oxygen [100]. This is reflected in the lower maximum allowed content of nitrogen compared to oxygen (0.03 wt.% N allowed in Grade 1 Titanium compared to 0.1 wt.% O) [88]. For example, addition of 0.2 wt.% oxygen reduces the elongation of titanium from 40% to 20%, whereas addition of the same weight percentage of nitrogen reduces the elongation to less than 10% [86]. However, the activation energy for the diffusion of nitrogen in α is higher than that for diffusion of oxygen in α [92]. This means nitrogen is less penetrating, and thus the hardening effect is more restricted to the surface.

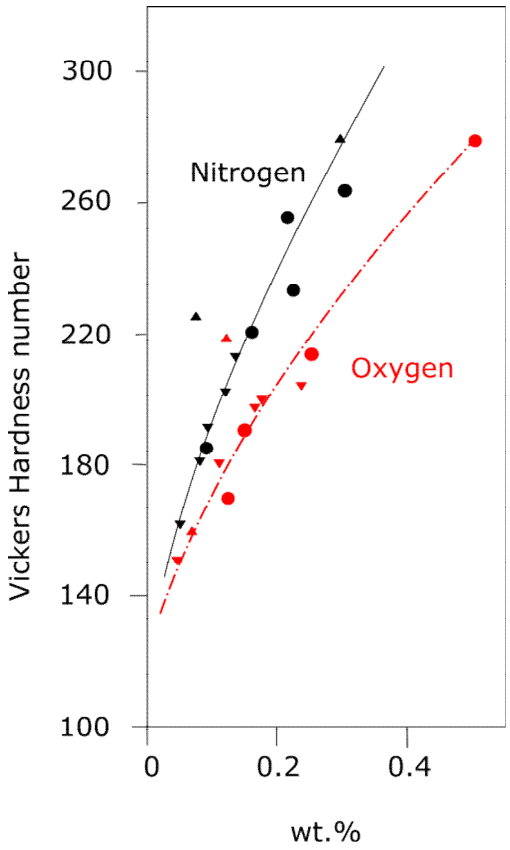


Figure 2.21: Plot showing Vickers hardness increasing with interstitial content in high purity titanium produced by the iodide method, with nitrogen being a more potent hardener than oxygen. Redrawn from [85]. *Data plotted as filled circles are from* [73,101]*, upright triangles are from* [102]*, downward triangles are from* [103].

2.7.3 Effect on microstructure

Oxygen content was found to control the massive martensite transformation [104]. Binary Ti-Al alloys with high O content (>3000 ppm) underwent the $\beta \rightarrow \alpha$ lath transformation whereas alloys with <700 ppm O underwent the massive featureless transformation. Thus, oxygen content can control the microstructure of titanium alloys, although these microstructural changes were not linked to changes in mechanical properties.

A more recent APT/ TEM correlative study linked oxygen embrittlement of Ti-64 to microstructural changes [105]. A high oxygen (Ti-64-0.49O) and low oxygen (Ti-64-0.25O) sample were studied. Three embrittling microstructural changes were highlighted; the formation of acicular α in the β phase, the formation of nanometer α_2 in the α phase and α-β-α layered structures at grain boundaries. Each of these features were only observed in the high oxygen

sample. Nitrogen is also known to promote fine, embrittling acicular microstructures, as can be seen in Figure 2.22, but it is not currently known if nitrogen promotes the formation of the α_2 phase.

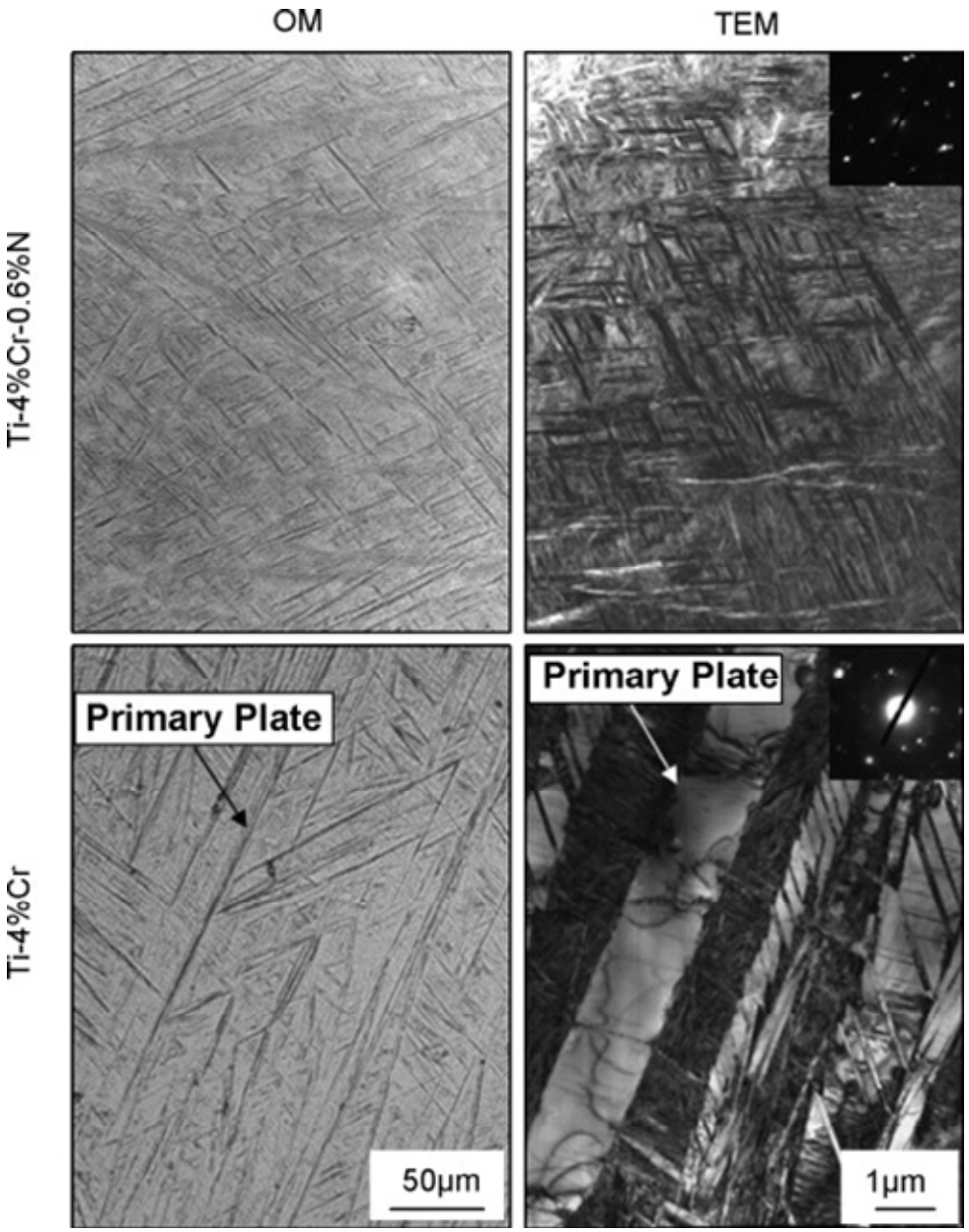


Figure 2.22: Optical micrographs and TEM images of Ti–4%Cr–0.6%N alloy produced by solution nitriding at 1473 K for 21.6 ks and Ti–4%Cr alloy solution-treated at 1473 K for 7.2 ks in a vacuum, followed by water-quenching [106].

2.8 α_2 PHASE

The α_2 phase forms in the α phase of alloys with >5 wt.% Al [39]. It is a coherent, ordered phase with stoichiometry Ti_3Al, and has the DO_{19} crystal structure [39]. Oxygen can encourage the formation of the ordered α_2 phase. In titanium-rich alloys, α_2 forms at lower Al contents and higher temperatures when oxygen content is increased [104]. Oxygen is also observed to encourage α_2 formation in aluminium-rich alloys, where the much higher solubility of oxygen in α_2 compared to the γ phase is thought to be the driving force [95]. The compositions at which α_2 forms at 1100^oC can be seen in Figure 2.23 . Often a range of compositions are reported in literature for Ti_3Al, since both the Ti and Al sublattice can be defective [95]. For example, for the aluminium-rich γ – α_2 system, Donachie [88] reports that α_2 contains 23-25 at.% Al, whereas Jones et al [94] report a composition of 22.5- 39 at.% Al.

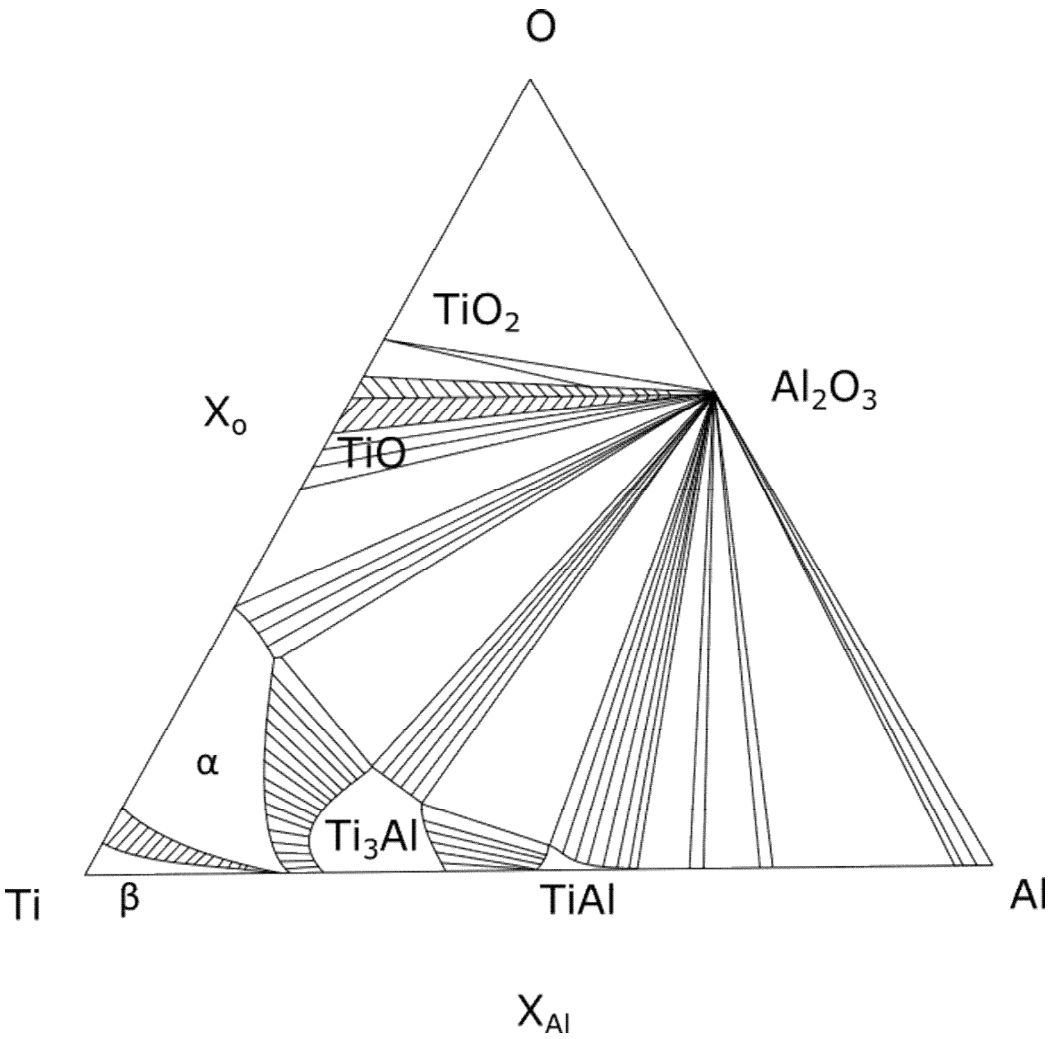


Figure 2.23: Calculated isothermal section of the Ti-Al-O ternary system at 1100^{o}C. Redrawn from [107].

As mentioned in section 2.7, oxygen prefers to occupy octahedral interstitial sites that are surrounded by titanium atoms, known as [OTi6] sites [80,94–97]. Jones et al. [94] provided experimental evidence in the form of neutron diffraction measurements to confirm that this is true for the α_2 phase in addition to the α phase. Moreover, they reported elongation with increasing oxygen content of the Ti-Ti and Ti-Al bonds that are aligned close to the c-axis direction.

Gehlen et al. [108] reported that distortions in the Ti_3Al lattice relative to the α-Ti lattice positions lead to expansion of the octahedral interstitial site where oxygen resides. It has been proposed by Ardakani et al. [104] that this causes oxygen to partition to, and stabilise, the α_2

phase over the α phase. Lim et al. [18] also postulated that oxygen partitions to α_2, based on tests that showed the strength of aged Ti-8wt.% Al does not increase continuously with increasing oxygen as for pure titanium. This suggests that in aged Ti-8wt.% Al, oxygen changes from being in solution in α to being dissolved in α_2. Concentration profiles measured across γ-α_2 interfaces in the high aluminium γ-Ti system using APT show that oxygen partitions to the α_2 phase [109]. However, there has not yet been any direct measurement of oxygen partitioning to the α_2 phase in the low aluminium, $\alpha + \alpha_2$ system.

The intensity of Ti_3Al (α_2) diffraction peaks increase with oxygen content during ageing of Ti-6Al-2V[4] at 550^{o}C [79], indicating an increasing volume fraction of α_2 [18]. The α_2 volume fraction also increases when oxygen content is increased up to 1300 wppm O in the alloy Ti-8wt.% Al, giving an increase in strength but also a marked rise in brittleness [18]. Beyond 1300 wppm O, the volume fraction levels off and does not increase with increasing oxygen content. Additionally, for Ti-8wt.% Al that contains more than 1000 ppm oxygen, there is no net strengthening with increasing oxygen content due to four competing effects balancing out [18]:

- Dissolution of oxygen in α_2
- Increase in the volume fraction of α_2
- Decrease in aluminium content of the matrix
- Dissolution of oxygen in the matrix (minimal)

Thus increasing oxygen content has multiple effects on alloy strength.

Elements other than oxygen also affect the formation of α_2. For example, Sn, Zr, Si and V are thought to increase the kinetics of α_2 formation [110]. During annealing Al, O and Sn partition to the α phase, enriching it in α stabilising elements. α_2 then forms from this phase during ageing,

[4] Ti-6Al-2V simulates the composition of the α phase of Ti-64

nucleating first as spheres but becoming ellipsoidal as ageing progresses, with the major axis aligned along the [0001] direction [39,46,111,112]. Blackburn reports that the precipitates remain spherical in diameter up to a radius of ~50 nm [46]. The change in morphology occurs because the lattice misfit parallel to the c-axis is 0.35% whereas perpendicular, the value is 0.83% [113]. Ardakani et al. [104] report that increased oxygen content causes the α_2 precipitate to become more elongated along the c-axis, but did not affect precipitate size perpendicular to the c-axis.

The presence of superlattice diffraction spots in TEM identifies precipitates as α_2 since the superlattice reflections result from the ordered Ti_3Al structure. α_2 superlattice spots have been observed in multiple titanium alloys, including TIMETAL 834, Ti-64 and Ti-7Al [110,112,114–116]. The development of superlattice spots with increasing ageing time can be seen for the alloy Ti-7Al in Figure 2.24, where arrows indicate superlattice spots.

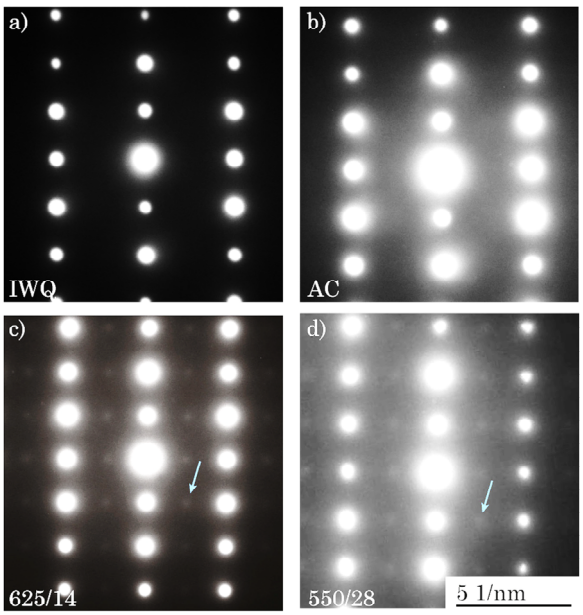


Figure 2.24: Ti-7Al, selected area [$2\bar{1}\bar{1}0$] diffraction patterns in the a) ice water quenched, b) air-cooled, c) aged at 625^{o}C for 14 days and d) aged at 550^{o}C for 28 days samples. The superlattice reflections are marked by arrows [112].

2.8.1.1 Effect of α_2 on mechanical properties

The ordered α_2 phase both hardens and embrittles the alloy in which it forms. However, the extent of embrittlement is controlled by the mechanism of interaction of moving dislocations

with the coherent α_2 precipitates. Dislocations cut small coherent precipitates [117], but as precipitate size increases, a critical radius is reached beyond which dislocations bypass the precipitates [118]. The transition between the cutting mechanism and the bypass mechanism is illustrated schematically in Figure 2.25. When the cutting mechanism operates, dislocations pass through the ordered precipitates, destroying them. This removes an obstacle in the glide plane, making slip favourable on this glide plane. As a result, subsequent slip takes place on this glide plane leading to dislocation pile-up. Stress is concentrated at the head of pile-ups, which favours crack nucleation and thus embrittles the material. However, when the bypass mechanism operates, dislocation loops form around the precipitates, creating further obstacles in the glide plane. This leads to a more homogeneous distribution of dislocations, without the build-up of large stress concentrations, resulting in a more ductile material [119]. For example, in their studies on Ti-Al alloys containing 14.5 to 18.1 at.% aluminium, the highest elongation to fracture produced from microstructures with homogeneously distributed α_2 was $\sim 7\%$. However, the maximum increase in elongation that is achievable is limited because although dislocations on primary slip systems operate via the bypass mechanism, dislocations that subsequently become mobile on secondary slip systems operate via a cutting mechanism, cutting through both the precipitates and the primary slip system dislocations that surround them. The transition between the cutting and bypass mechanisms is controlled by precipitate radius and precipitate spacing. Thus understanding of the formation of the coherent α_2 precipitates is essential to favour the bypass mechanism and therefore maximise alloy ductility.

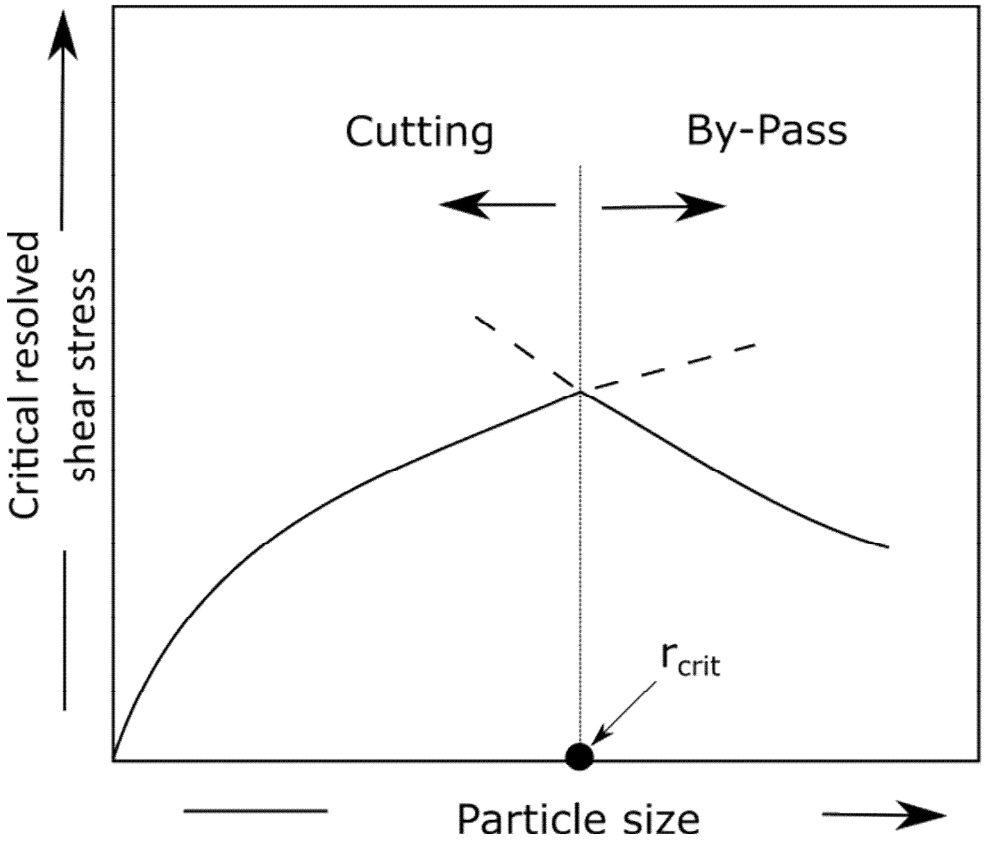


Figure 2.25: Diagram showing the transition from cutting of particles by dislocations to particle by-pass as particle size increases, after [119].

2.8.1.2 α_2 formation

The precipitation characteristics of α_2 are controlled by ageing temperature and alloy composition. For example, higher ageing temperatures result in heterogeneous precipitation at grain boundaries and dislocations, but the likelihood of heterogeneous nucleation is decreased with increasing aluminium content [120]. Higher ageing temperatures accelerate diffusion but reduce the driving force for nucleation. Consequentially, higher ageing temperatures favour heterogeneous nucleation since the interface energy of grain boundaries and dislocations can supply the required driving force. Increasing aluminium content increases the α_2 transformation temperature, meaning that for a fixed ageing temperature, undercooling is increased and thus there is a more significant driving force for homogeneous precipitation.

Work by Weissmann et al. [119] found that samples in the region just below line B in the phase diagram displayed in Figure 2.26 produced microstructures with a homogeneous distribution of α_2 and large inter-precipitate distances that are necessary to promote the bypass mechanism. For example, the alloy compositions and ageing temperatures corresponding to points P and Q on Figure 2.26 resulted in interparticle distances of 800-1200 Å and ~1800 Å, respectively[5] [119]. Homogeneous precipitation occurred easily owing to the low misfit between the α_2 precipitates and the matrix, resulting in a small critical radius for nucleation.

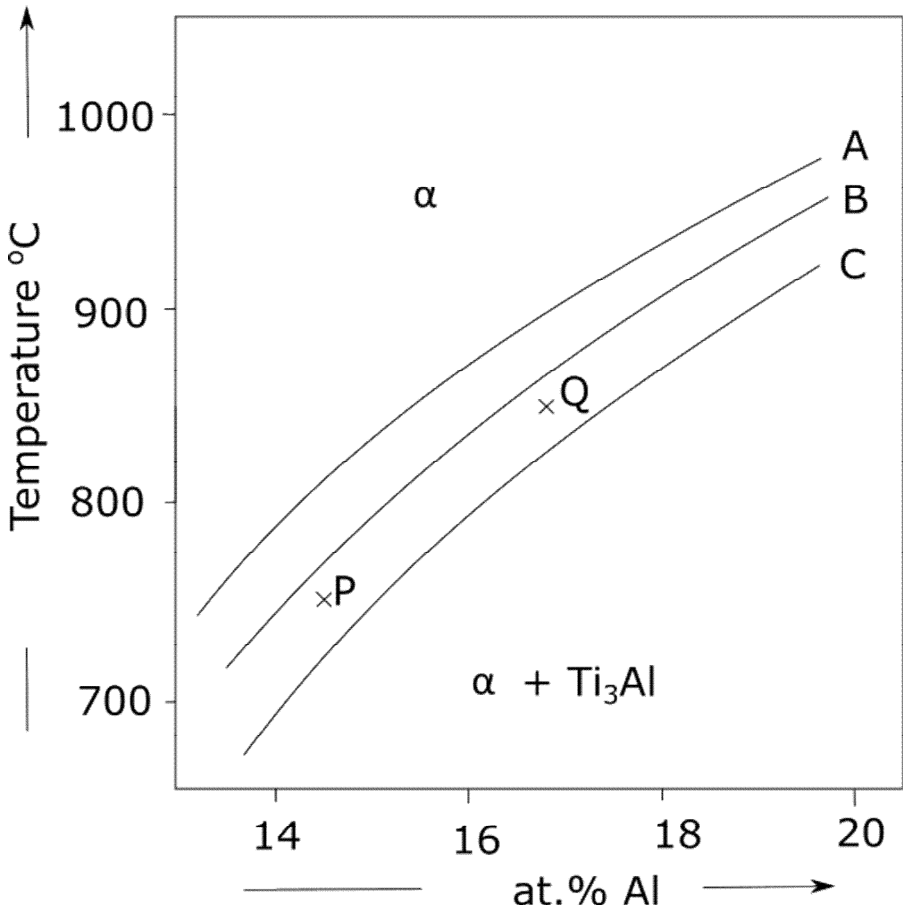


Figure 2.26: Section of the Ti-Al phase diagram demonstrating the nucleation behaviour of the α_2 phase. Region A-B: nucleation only on dislocations and grain boundaries. Region B-C: nucleation preferred on dislocations and boundaries; later throughout the matrix. Region below C: nucleation simultaneously on dislocations and boundaries and throughout the matrix. Region above A: single α phase field. Point P corresponds to the alloy Ti-14.5 at.% Al aged at 750°C. Point Q corresponds to the alloy Ti-16.8 at.% Al aged at 850°C. Redrawn from [119].

[5] Both sets of interparticle distances were achieved after ageing for 100 hours at the respective temperatures.

Ardakani et al. [104] agreed with Weissmann and Lutjering [119], finding the formation of α_2 to be homogeneous except at high oxygen content (~3200 ppm). Heterogeneous nucleation occurred on grain boundaries in the high oxygen content material as a result of enhanced vacancy diffusion.

As mentioned in the previous section, there has been some discussion in the literature as to whether the short range ordering of the α phase occurs before α_2 formation. Work by Lenssen [115] on the commercial alloy TIMETAL 834 used APT and TEM to investigate the formation of α_2. Superlattice diffraction spots corresponding to an ordered phase were observed in the TEM before compositional variations could be detected in the atom probe. Lenssen interpreted this as evidence of the occurrence of a conditional spinodal mechanism, where ordering occurs prior to decomposition into the α and α_2 phase. Wood et al. [116] investigated ordering in the binary alloy Ti-15at.%Al and showed that ordering occurs in the α matrix before compositional phase separation to form α_2. Building on this, Radecka et al. [112] were able to detect aluminium clustering using APT before the appearance of distinct α_2 precipitates in TEM.

2.8.1.3 Growth of α_2

Blackburn [46] noted that the growth rate of the α_2 phase in Ti-13.39 at.% Al is rapid during the first 100 hours of ageing at 500-550°C but becomes slower as ageing progresses. Later work by Namboodhiri et al. [111], using TEM and electrical resistivity measurements, provided some quantification of the α_2 growth kinetics. Electrical resistivity measurements were taken from alloys in the range 14.2 to 19.2 at.% Al. The results, shown in Figure 2.27 for the Ti-16 at.% Al alloy, suggested α_2 growth follows C-curve kinetics, with the maximum growth rate (nose of the time-temperature-transformation (TTT) curve) at 600°C. The corresponding activation energy for α_2 growth at 600°C was found to be 113.0$\pm$8.3kJ. This value is lower than the activation energy for self-diffusion of titanium, which was calculated using the melting point of titanium and found to be 251-285 kJ mol^{-1}. This led Namboodhiri to conclude that precipitation is not controlled by

bulk diffusion [111]. However, Sasano et al. [121] calculated the activation energy for α_2 precipitation to be 104.6 kJ mol^{-1} and deemed this to be close to the activation energy for diffusion of aluminium in titanium calculated by Goold to be 98.3 kJ mol^{-1} [122]. This led Sasano et al. [121] to conclude that the rate-controlling process in α_2 precipitation is aluminium diffusion. The source of the difference in opinion between Sasano and Namboodhiri is the activation energy, as calculated by Goold. Namboodhiri deemed the value to be "anomalously low", in line with similar calculations obtained for Ti, Zr and Hf and so instead chose to estimate the activation energy using the melting point of titanium [123].

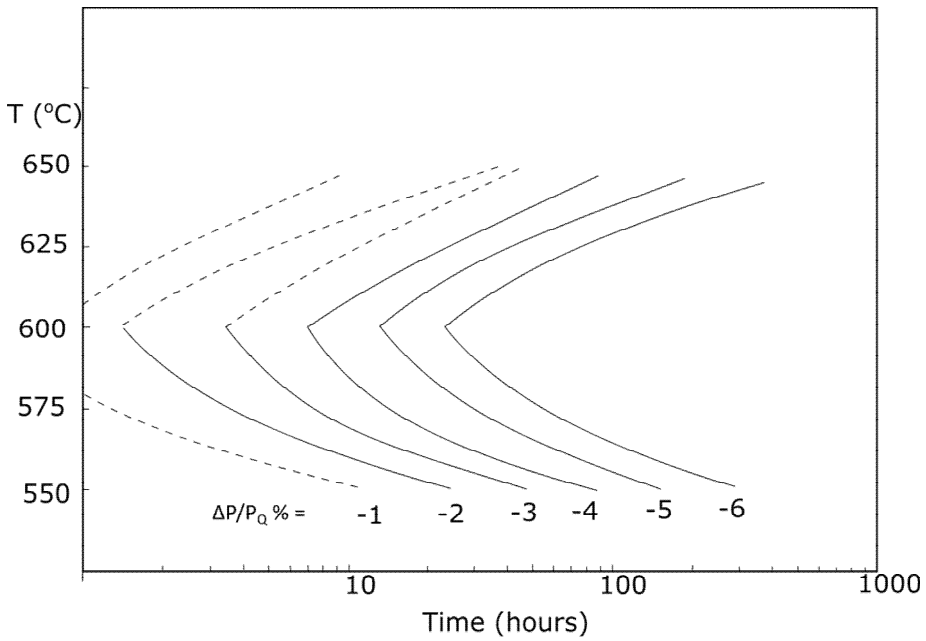


Figure 2.27: Time to fractional change in resistivity vs ageing temperature, Ti-16 at.% Al alloy. Redrawn from [119].

Ardakani et al. [104] studied the kinetics of α_2 formation in Ti-7Al using TEM diffraction patterns and created the TTT curve in Figure 2.28. The nose of the TTT curve is positioned slightly below 600°C. It should be noted that the points on the curve corresponding to shorter ageing times (< 4 hours) were determined on the basis of weak superlatice reflections. When compared with the Namboodhiri TTT curve [111] for alloys in the composition range Ti-8-9wt.% Al, it seems that the nose of the TTT curve moves to higher temperatures with increasing aluminium content. This could be explained by the fact that higher aluminium content increases the α_2 transformation

temperature [124] and thus the temperature at which the maximum rate of α_2 precipitation occurs also increased.

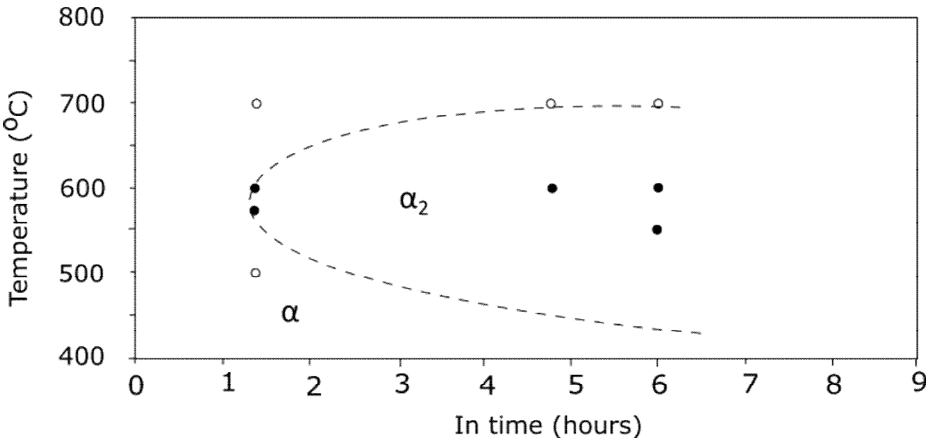


Figure 2.28: TTT curve for Ti_3Al formation in Ti-7Al alloy, redrawn from [104]*. Filled circles represent times and temperatures where α_2 was observed; open circles represent regions where α_2 was not observed.*

Sircar et al. [124] report that ordering kinetics become slower with increasing aluminium content. However, this conclusion was based on a comparison of the kinetics of α_2 nucleation in only two alloys (Ti-19.3 at.% Al and Ti-25.2 at.% Al), and should thus be treated with caution.

Donlon et al. [125] used TEM to investigate the presence of α_2 in three near-α alloys; Ti-1100, Ti-6242S and TIMETAL 834. The TTT curves for these alloys after β processing can be seen in Figure 2.29. The noses of the curves lie within the same 550-650°C temperature range as those of the binary alloys in Figure 2.27 and Figure 2.28.

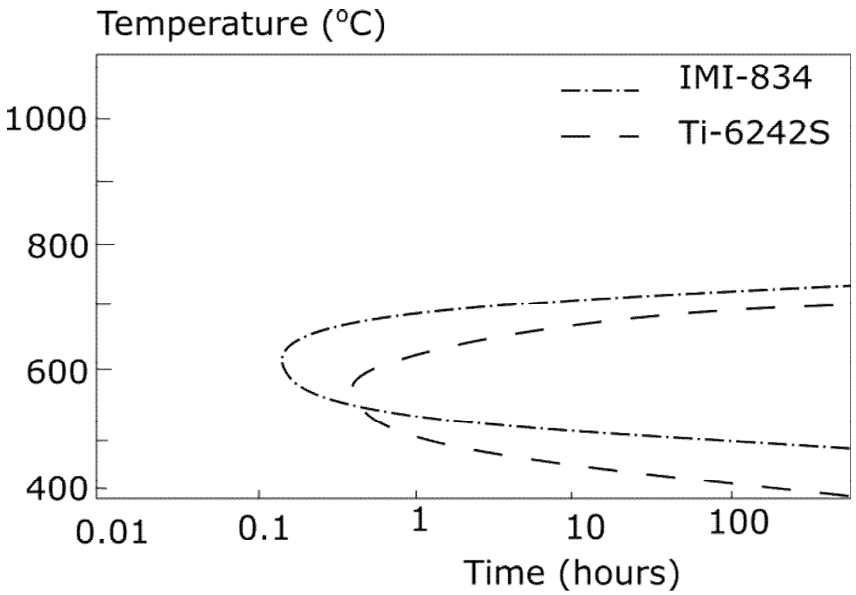


Figure 2.29: TTT curve for Ti_3Al formation in β processed TIMETAL 834 and Ti-6242S, redrawn from [125].

The lattice misfit between the α matrix and α_2 precipitates is small. This means the critical radius for nucleation is small, resulting in a high density of homogeneously nucleated nucleation centres. This leads Lutjering and Weissman [119] to assume that α_2 growth follows Ostwald ripening [126] growth kinetics, with particle radius increasing proportional to (ageing time)$^{\frac{1}{3}}$. However, no systematic study on α_2 coarsening kinetics in binary Ti-Al has been carried out to date.

2.9 DWELL FATIGUE

The presence of the α_2 phase is known to encourage cold dwell fatigue [112]. It has been suggested that ordering of the Ti-Al lattice means that dislocations have to travel in pairs, and may only travel on alternate slip planes [127]. This restriction in dislocation motion results in strain localisation, which can lead to the nucleation of cold dwell fatigue cracks [110]. Planar slip bands containing paired dislocations have been linked with the presence of the ordered α_2 phase in Ti-64 aged for five weeks at 550°C [128].

The stress conditions that an aeroengine experiences during normal operation combined with the other factors, such as the presence of α_2 precipitates, mean that titanium fan blades are susceptible to cold dwell fatigue. During each flight of a civil aircraft, the fan blades are subjected to cyclic loading. Cyclic loading results in fatigue failure of components at a stress below the failure stress reached in a tensile test. A schematic representation of one load cycle is shown in Figure 2.30, and the stress levels experienced at different points in the cycle are indicated. Peak stresses are achieved during take-off and landing. However, during the cruise period, illustrated schematically in Figure 2.30, aeroengine components are also exposed to constant high mean stress, which can cause component failure in a process known as cold dwell fatigue. The word 'cold' refers to the fact that this process occurs in parts of the engine that are at a relatively low temperature ($< 100°$C). Cold dwell fatigue presents a significant problem in the aerospace sector since susceptible components such as the fan blades must be regularly inspected during service, and any components containing cracks must be replaced. Additionally, these components are designed with extra dimensional safety tolerances, which reduces efficiency and ultimately leads to increased fuel consumption. It is a complex problem which is currently unsolved, and much research has been undertaken to provide a better understanding of the metallurgical factors that affect cold dwell fatigue [129–132]. In addition to the knowledge that the presence of α_2 promotes cold dwell fatigue, it is also known that alloys containing a high volume fraction of the α phase, and a low volume fraction of the β phase, are the most susceptible [129]. Within these alloys, those that have a microstructure that consists of clusters of similarly-oriented α grains, known as α colonies, are the most likely to experience cold dwell fatigue [129]. However, once a dwell fatigue crack has nucleated, colony microstructures have been found to be more resistant to dwell fatigue crack growth than equiaxed or Widmanstatten microstructures [130–132].

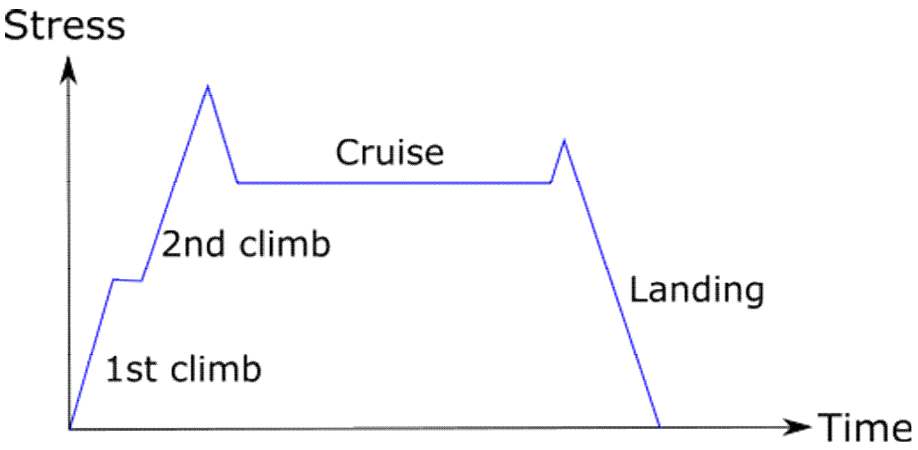


Figure 2.30: Schematic showing a single load cycle for a gas turbine engine. After [133].

The orientation of the α grains plays a vital role in the cold dwell fatigue process. α grains that are oriented with the c-axis at an angle to the tensile axis are said to be 'soft' since they can deform relatively easily by slip on the prism and basal planes. On the other hand, 'hard' grains are defined as grains for which the c-axis is parallel to the tensile axis. Deformation by slip is much harder in these grains since it involves $< c + a >$ dislocations on pyramidal planes, for which the critical resolved shear stress is high. During cold dwell fatigue, stress is redistributed from soft to hard α grains via cold creep. Planar glide of $< a >$-type dislocations in soft grains leads to the load being transferred to the hard grain, with dislocations piling up at the grain boundary between the soft and the hard grain, as shown in Figure 2.31. Stress is concentrated at the grain boundary and cannot be relieved by slip, resulting instead in crack nucleation.

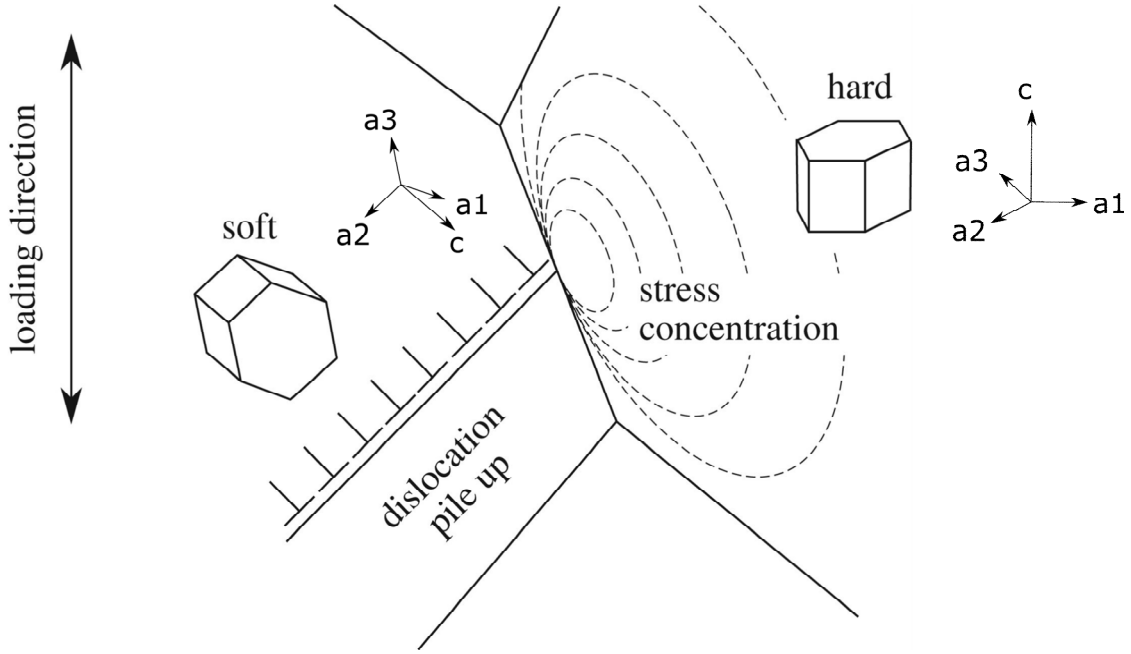


Figure 2.31: Schematic showing slip accumulating in the soft grain at the boundary with a hard grain, resulting in stress concentration in the hard grain and eventual crack nucleation. After [30].

Fracture morphology is also a relevant factor in cold dwell fatigue. Crack initiation is known to be subsurface, and the fracture surface consists of quasi-cleavage[6] facets, which form preferentially on hard grains [16]. The facets form almost parallel to the basal plane of the α phase [78] and the orientation of the basal planes is usually within $\pm 10^{o}$ of the applied stress direction [78]. Work by Cuddihy et al. [16] suggests that macroscopic tensile uniaxial stress state is more damaging than tension-tension biaxial stress state. A jet engine disc experiences multiaxial stress states and Cuddihy et al. [16] report that these remote stress states influence facet formation.

Despite the progress so far, much more work is required to understand the underlying mechanisms that drive cold dwell fatigue. For example, cold dwell fatigue only occurs at temperatures below 200 °C [39], but the reason for this is not well-understood. It is likely that above 200°C, a thermally activated deformation process is triggered which reduces stress concentrations at grain boundaries [30]. Calculations by Ready et al. [30] propose that above 200°C, $< c + a >$ slip is activated in hard α grains because the higher temperature enables

[6] Quasi-cleavage facets form by a mixture of microvoid coalescence and cleavage [238].

formation and migration of kinks. These postulations agree with research by Ghosh and coworkers [134,135]. Further work is needed to understand the temperature dependence of the critical resolved shear stress of prism, basal and $< c + a >$ slip in the α phase. Further work is also needed to characterise the α_2 phase such that its formation can be controlled and more accurate life predictions of α_2-containing components can be made.

2.10 α CASE

The oxidation resistance of titanium is excellent at lower temperatures due to the presence of a protective TiO_2 oxide. However, above 480 °C, oxygen and nitrogen can diffuse through the surface oxide. The high affinity of titanium for oxygen, coupled with the high solubility of oxygen in titanium, lead to the simultaneous formation of TiO_2 oxide scale at the surface and, beneath it, formation of a high oxygen content surface layer. This layer is often referred to as *α case*, since the high levels of oxygen stabilize the α phase. *α case* can have a significant, detrimental effect on mechanical properties [4].

Historically there has been some ambiguity in the language used to describe high oxygen content layers formed on titanium components. Satko et al. [11] provide a helpful distinction between the *oxygen-rich layer* that forms at intermediate temperatures (up to ~600°C) *in-service*, and *α case*, which they define as forming at the higher temperatures experienced during alloy processing (~850-1000°C). Formation of the *oxygen-rich layer* does not result in microstructural change. However, *α case* formation does, in the form of β denudation where the volume fraction of β phase is reduced due to oxygen stabilising the α phase. The term *α case* is often broadly used in industry and in the literature as an umbrella term for both of the phenomena described by Satko et al. [11]. However, the work done in this thesis will use the specific definitions of *oxygen-rich layer* for the *in-service* layer and *α case* for the processing layer, as defined by Satko et al. [11].

2.10.1 Industrial relevance

Surface regions affected by oxygen ingress that form during material processing and component manufacture are usually removed either mechanically or chemically, often by pickling in a mixture of hydrofluoric/ nitric acid [136]. However, this approach is not possible if, for example, the layer forms on an inaccessible surface or *in-service*.

In-service operating temperatures have increased to improve engine efficiency and development of high temperature titanium alloys has enabled the use of titanium, instead of nickel, further back into the compressor, minimising engine weight. As a result, titanium components have been reaching temperatures exceeding 600°C [3]. It is *α case* formation that prevents compressor discs from being operated at even higher temperatures, since the low ductility of the *α case* layer can result in crack formation under tensile loading [4]. This is of particular concern in the rare case that high cycle loading regimes are coincident with *α case* formation since, under these conditions, transient high stresses may be sufficient to nucleate and propagate a HCF crack resulting in lower-than-expected HCF strength [3]. The effect of *α case* on mechanical properties will be explored in more detail in section 2.10.2.

2.10.1.1 Life prediction

Accurate component life predictions are required to both improve jet engine efficiency and prevent *in-service* component failures. While experimental testing under simulated loading conditions is routinely carried out, computer simulations may reduce the high cost associated with this.

Successful component life predictions rely on two types of models; one to predict the oxygen ingress depth under *in-service* conditions and one to predict the effect of the *oxygen-rich layer* thickness on mechanical properties.

Oxygen ingress depth can be determined by modelling diffusion of oxygen and nitrogen through application of Fick's second law of diffusion, calibrated with experimental data, to estimate a

diffusion coefficient. Multiple attempts have been made at this in the literature [4–6], but the effect of crystal orientation and microstructure is not typically accounted for, resulting in variation in the reported diffusion coefficients. For example, McReynolds et al. [4] estimated diffusion coefficient of a Ti-6242S sample with a bimodal microstructure of ~4 X 10^{-3} mm^2/s at 649°C, which is ~20 times higher than the value reported by Shamblen et al. [6] at 639°C.

A variety of models are available to predict the effect of oxygen ingress depth on mechanical properties [7–9]. For example, Parthasarathy et al. [8] predict crack formation in a brittle oxygen rich surface layer of Ti-6242 exposed to *in-service*-like conditions. The crack formation model required accurate prediction of oxygen ingress depth, but the oxygen ingress was calibrated using the diffusion coefficient of oxygen in the β phase, despite the alloy in the model only containing ~10% volume fraction of β. This demonstrates the importance of accurate diffusion coefficients in prediction of both oxygen ingress depth and the effect of *oxygen-rich layer* thickness on mechanical properties.

A number of key barriers to accurate determination of diffusion coefficient are outlined by Satko et al. [11] ; failure to account for the effect of microstructure on diffusion coefficient; variation in reliability of the wide range of techniques used to measure oxygen ingress depth; lack of literature information on the relationship between diffusion coefficients for the α phase, β phase and α - β boundaries; confusion in the use of *α case* terminology, as outlined in section 2.10. These barriers must be overcome to improve model accuracy and ensure accurate life prediction.

2.10.2 Effect of *α case* on mechanical properties

Oxygen and nitrogen stabilise the *α* case layer and provide solid solution strengthening. However, these interstitial elements also have a deleterious effect on mechanical properties as a result of forming the *α case* layer.

Correlation between increased oxygen ingress depth and loss of ductility in Ti-6242 has been observed, with oxygen ingress causing up to 80% reduction in tensile elongation [6,137].

Investigations by Pilchak et al. [138] revealed that this reduction in ductility was a result of the restriction of void growth in areas of high oxygen content, preventing ductile failure and leading instead to fracture via formation of facets, which resulted in cracks propagating along grain boundaries [138].

Leyens et al. [139] found that when the alloy Ti-1100 was annealed in air at 600 °C, an exposure time of 100 hours was required to form strain cracks within the 20 μm thick oxygen-affected area. These cracks then penetrated into the unaffected material, resulting in a macroscopic loss of ductility.

Jia et al. [140] observed that the fracture mode changed from ductile to quasi-cleavage fracture after thermal exposure of the alloy Ti-60, resulting in a loss of fatigue strength. However, they attributed the loss of ductility to α_2 formation, in addition to α case formation [140].

Loss of ductility due to oxygen ingress has a significant impact on fatigue properties [88] because of the ease of microcrack formation within the brittle *oxygen-rich layer* [7]. For example, in Ti-6242, 2 μm α case reduced low cycle fatigue life up to 50% whereas a 10 μm α case caused up to 90% life reduction [141].

As described in section 2.7.2, increased interstitial concentration hardens titanium alloys. This can be exploited to measure oxygen ingress depth. For example, microhardness tests reveal hardness decreases with increasing depth from the sample surface, i.e. decreasing oxygen content, in Ti-64, Ti-Al-2Sn-4Zr-2Mo and TIMETAL 834 [5][142]. Since microhardness is higher in the α case, microhardness measurements can determine α case thickness, and have been found to correlate well with optical measurements [143]. Leyens et al. [139] also measured hardness as a function of distance from the surface. Samples of Ti-1100 with a bimodal microstructure exhibited an abrupt transition in microhardness from the oxygen-penetrated zone to the unaffected material. In contrast, the change in microhardness between the *oxygen-rich layer* and unaffected material in lamellar Ti-100 was more gradual, as can be seen from Figure 2.32. Comparison of Figure 2.32 (a)

and (c) shows that there is a good spatial correlation between the region of high hardness and high oxygen content in the bimodal microstructure.

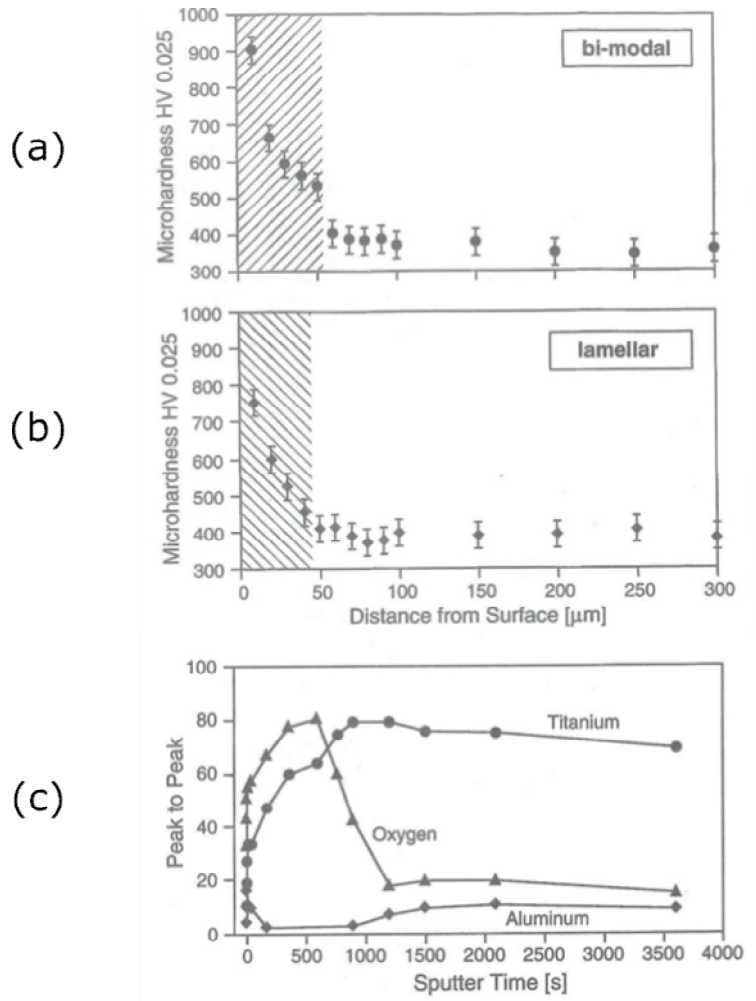


Figure 2.32: Microhardness profiles of Ti-1100 after exposure in air for 1000 hours at 600^{o}C are shown in (a) and (b). The hardness profile for the bimodal microstructure in (a) is much sharper than the hardness profile for the lamellar microstructure in (b). (c) shows the Auger Electron Spectroscopy depth profiles, carried out by Secondary Ion Mass Spectroscopy, of the subsurface zone of the bimodal structure after exposure to air for 1000 hours at 600^{o}C. Good spatial correlation can be seen between the region of high oxygen content and the region of high hardness [139].

2.10.3 Formation of *α case*

The high affinity of titanium for oxygen results in the immediate formation of a thin layer of TiO_2 upon exposure. This oxide layer, which is ~4-5 nm thick, acts as a barrier between the metal and the reacting oxygen [144], preventing further oxidation and slowing down diffusion of oxygen at temperatures below ~480^{o}C degrees [5,145]. However, at higher temperatures, oxygen can

diffuse more readily through the oxide layer and react with titanium at the metal-oxide interface, forming TiO_2 and increasing the oxide layer thickness. Conditions that produce a more continuous oxide layer result in samples with superior oxidation performance [145], since transport of oxygen through the oxide layer and into the metal becomes rate-limiting. Oxygen also simultaneously dissolves in the metal [145], stabilising the α phase and creating a hard and brittle *oxygen-rich layer* below the oxide [146], which is often referred to as *α* case. Higher temperatures and longer exposure times can often lead to a change in the oxidation kinetics, as will be described below.

2.10.3.1 Oxidation behaviour of titanium and titanium alloys

Oxidation rate laws describe change in oxide thickness as a function of time, which in turn controls oxygen ingress and, therefore, *α case* formation. The rate laws followed during oxidation of CP-Ti are temperature dependent, and can be seen schematically in Figure 2.33.

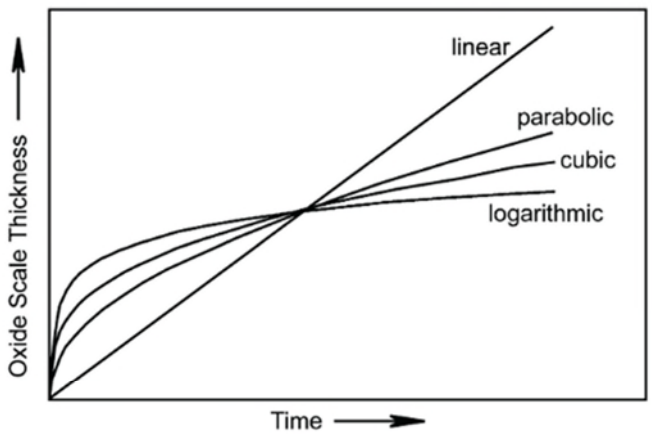


Figure 2.33: Schematic representation of variation of oxide thickness with exposure time according to different rate laws [147].

Oxidation of CP-Ti follows a parabolic rate law between 400-600 °C [145]. Between 600-1000°C, concurrent oxide growth and oxygen dissolution occur which, overall, follow a parabolic rate law [146] while after prolonged exposure, the rate becomes approximately linear [147,148]. Parabolic rate laws are dominant for thicker oxide scales where diffusion through the oxide becomes the

rate-limiting process, and can be described by the Wagner theory of oxidation [149]. However, linear rate laws describe oxidation when diffusion through the oxide scale is fast, perhaps due to thinning of the oxide due to cracking and spallation, and surface reactions or diffusion through a gas phase become rate-controlling [144]. Therefore, growth of TiO_2 controls the oxidation behaviour of CP-Ti at 600-650°C, where the parabolic rate law dominates. However, at higher temperatures, dissolution of oxygen in the metal becomes rate-controlling and a linear rate law is followed [148].

In comparison to CP-Ti, the oxidation laws governing titanium alloys are more complex owing to the effect of microstructure, grain boundaries and phase boundaries, the presence of β phase and alloying elements. In Ti-64, growth of the oxide scale is parabolic up to 700°C, and oxidation rate becomes linear after longer exposures above this temperature due to spalling of the oxide scale.

The aluminium in Ti-64 improves oxidation resistance since aluminium ions incorporated into the rutile layer decrease the rate of oxygen diffusion [150]. Furthermore, aluminium enables formation of Al_2O_3, which is a more stable oxide than TiO_2 below 1400°C [151]. The multilayer TiO_2 and Al_2O_3 structure that forms on Ti-64 can lead to a change in oxidation kinetics. Cracking occurs once a critical oxide thickness is reached, as a result of mismatch in expansion coefficients between the oxide and the metal. This negates the protective effect of the oxide, through which oxygen diffuses at a slower rate, and exposes the metal to higher levels of oxygen, temporarily accelerating oxidation [152]. Microstructure also has a role to play in oxidation kinetics; fine grain Ti-64 has been observed to oxidise at a faster rate than coarser microstructures owing to the higher proportion of grain boundary area in the fine grained material [153].

The alloy Ti-6242 shows similar oxidation kinetics to Ti-64. Parabolic growth occurs at temperatures up to 650°C and beyond this, deviation from the parabolic law is observed as a result of a porous oxide scale [137]. TIMETAL 834 also follows parabolic growth but, unlike Ti-64

and Ti-6242, does not show a change in oxidation kinetics at higher temperatures of prolonged exposures [154–156].

In addition to oxygen, *in-service* components will be exposed to nitrogen from the air. A mechanism for the oxidation of titanium in the presence of nitrogen was proposed by Chaze et al. [157]. During the initial stages of oxidation in air (i.e. in the presence of nitrogen), oxides are more thermodynamically stable than nitrides, as can be seen in Figure 2.34. The kinetics and activation energies are similar for oxidation in oxygen and air [157]. Over time, nitrogen from the atmosphere diffuses inwards, increasing the concentration of nitrogen in the rutile oxide layer. Nitrogen diffuses faster in rutile than oxygen and is slower to dissolve in titanium metal than oxygen. This results in nitrogen accumulation at the oxide-metal interface and the formation of nitrides, including Cr_2N in Ti-Cr(1-19 wt.%)and TiN in Ti-Si(0.25-1.0 wt.%) [157], which can act as a barrier to oxygen diffusion during subsequent oxidation [158]. However, the nitride layer has been observed to be consumed to enable oxide formation during long term exposures [158].

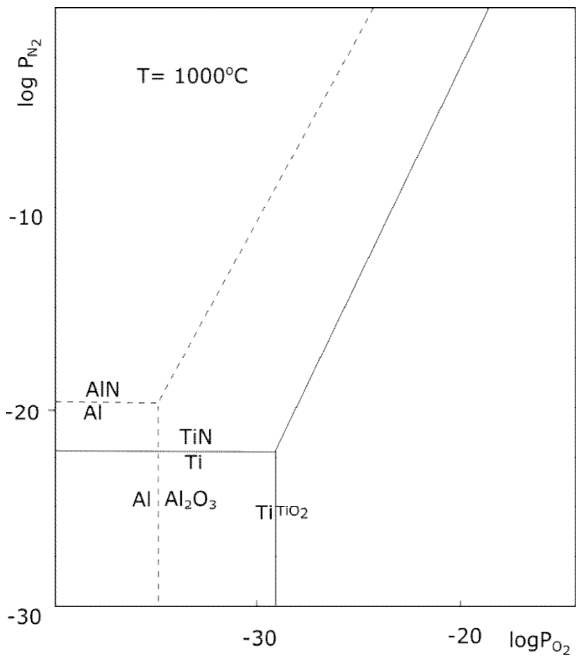


Figure 2.34: Thermodynamic equilibrium diagram for Ti-Al-O-N system. After [157].

2.10.3.2 Diffusion of oxygen and nitrogen

Diffusion of oxygen and nitrogen into the bulk metal controls the α case formation [138]. Oxygen is a stronger α case former than nitrogen as it diffuses more readily [88]. Since the atomic radius for oxygen and nitrogen is sufficiently small, these elements diffuse interstitially, preferentially occupying the octahedral interstitial sites as described in section 2.7.

The driving force for diffusion is the oxygen chemical potential gradient; diffusion occurs down the chemical potential gradient. If the chemical potential gradient is positive, then diffusion occurs in the same direction as the oxygen concentration gradient. However, if the chemical potential gradient is negative, then diffusion occurs against the oxygen concentration gradient. For an ideal solution, concentration gradient is considered in the place of chemical potential gradient. For simplicity, the case of an ideal solution is considered here, although it is recognised that there are scenarios in the current study where diffusion would occur against a concentration gradient e.g. inwards diffusion of oxygen from the surface along β phase (that is acting as a fast diffusion path) into the α phase.

As oxygen diffuses from the surface inwards, the concentration gradient changes with time and is thus a form of non steady state diffusion, and can be approximated by the carburization equation, a specific solution of Fick's second law [159]

$$C(x,t) = C_s - (C_s - C_0)erf(\frac{x}{2\sqrt{Dt}}) \qquad \textit{Equation 2.3}$$

where C_s is the concentration of oxygen at the surface of the material, C_0 is the concentration of oxygen in the bulk material, x is the diffusion depth, D is the diffusion coefficient and t is time. Equation 2.3 is reached by applying the following boundary conditions:

1. $C(x=\infty, t) = C_0$
2. $C(x=0, t) = C_s$

The diffusion coefficient, D, can be described by the Arrhenius law [159]

$$D = D_0 e^{-\frac{Q}{RT}}$$ *Equation 2.4*

where D_0 is the maximal diffusivity, Q is the activation energy for *oxygen-rich layer* formation, R is the gas constant and T is temperature. The activation energy for α case formation in TIMETAL 834 was found to be 160 kJ mol^{-1} [154], which is close to the activation energy for the oxygen diffusion in α (201 kJ mol^{-1} [160]) and corroborates the idea that α case formation is controlled by oxygen ingress.

Accurate calculation of the diffusion coefficient, D, relies on accurate values of D_0. There are a range of values reported in the literature, and a comprehensive survey on diffusivities of oxygen in α-Ti, β-Ti and rutile has been carried out by Liu and Welsch [161]. Variation in the D_0 values reported can be accounted for by considering the difference in experimental and analytical methods used to measure oxygen concentration gradients [162].

The effective diffusion coefficient can also be affected by microstructure. For example, the presence of β phase can have a significant effect on the rate of oxygen diffusion in an alloy since the diffusion rate of oxygen in β is faster than in α [39]. This is proposed to affect the morphology of the *α case* formed [163,164]. For example, a higher fraction of β phase near the surface will diffuse oxygen away from the stabilised *α case* layer faster than it can be replenished by diffusion from the surface, leading to a shallower α-stabilised region and a deeper oxygen diffusion zone. Leyens et al. [139] observed that the depth of the oxygen diffusion zone is greater for bimodal microstructures compared to lamellar microstructures. They attribute this to the larger number of phase boundaries available in the bimodal microstructure, which can act as fast diffusion paths for oxygen. However, more recent work by Satko et al. [11] shows the opposite trend; the largest effective diffusion coefficient (D_{eff}) was observed in a colony microstructure. Tiley et al. [10] report that colonies with α-laths oriented parallel to the oxygen ingress result in the greatest oxygen ingress. Thus it is possible that a large proportion of boundaries in the Leyens [139] lamellar microstructure were unfavourably oriented. Basketweave microstructure showed the

smallest D_{eff}, while D_{eff} was noted to increase as the area fraction of secondary alpha colonies increased in bimodal microstructures [11].

A recent APT study suggests that microstructure plays a role in the morphology of the α_2 phase formed in air-exposed Ti-64 [165]. It is postulated by Bagot et al. [165] that diffusion of oxygen from the surface through β plates in an α/ β colony has enabled growth of the secondary α plates in the colony, until the β is consumed. The secondary α plates would then have a core with lower oxygen content, from which α_2 could precipitate, resulting in the banded structure seen in Figure 2.35 (a).

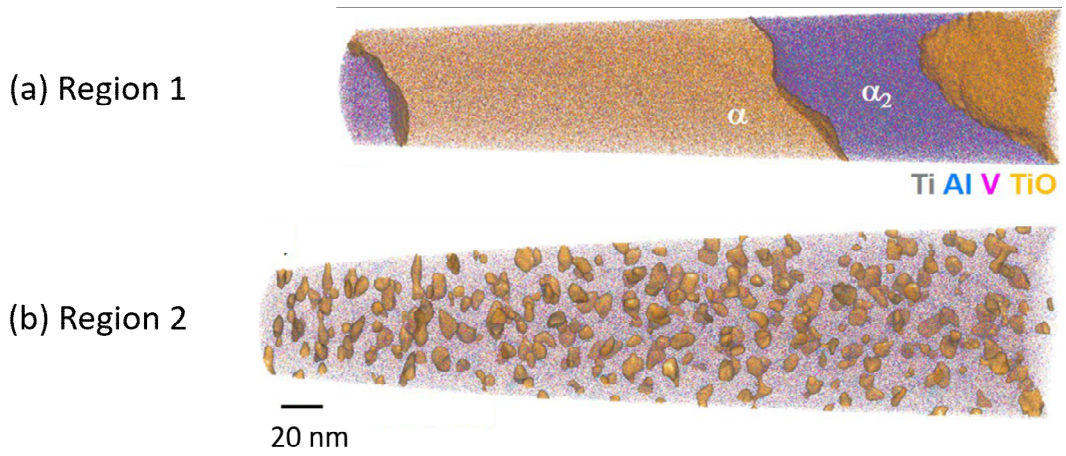


Figure 2.35: APT results showing two different regions of microstructure within the α case of Ti-64, oxidised in air for 24 hours at 800^{o}C. (a) shows banded α_2 regions of composition Ti63.8 -O10.4 -Al20.7 -V5.1 (at.%) and (b) shows α_2 nanospheres of composition Ti66.0 -O10.0 -Al20.8 -V2.8 (at.%) [165].

Bagot et al. [165] suggest that the spherical α_2 precipitates, shown in Figure 2.35, form in primary α grains in which the oxygen content increases more gradually. They propose that the lack of prior α/β interfaces within the grain results in heterogeneous precipitation of the near-spherical α_2 precipitates. Further work is required to confirm and further understand the kinetics, exposure dependence and alloy dependence of these proposed α_2 nucleation mechanisms.

2.11 SUMMARY

Titanium alloys are widely used in the aerospace industry owing to their excellent corrosion resistance and high strength-to-weight ratio. However, even trace amounts of oxygen and nitrogen can affect the mechanical properties of alloys used to make key components such as fan blades. For example, work by Lim et al. [18] demonstrates that increasing oxygen content can have multiple competing effects on the mechanical properties of Ti-8wt.% Al. However, further work is needed to understand the mechanism by which oxygen encourages α_2 formation, and the relative contribution of α_2 precipitation to hardening.

Very high levels of oxygen and nitrogen, such as those reached in the compressor discs of an aeroengine during service, can also affect component performance. Alloy microstructure affects the depth of oxygen ingress on compressor discs *in-service*, which in turn affects the mechanical properties, as demonstrated by Satko [11] and Gaddam [141]. However, there is limited information available on the effect of different microstructures. As microstructural features within the *α case* can be nanoscale [165], analysis techniques with high spatial resolution and chemical sensitivity, such as APT, must be employed to increase understanding of α case formation such that detrimental effects on mechanical properties can be minimised.

Through high-resolution characterisation, using APT complemented by nanoindentation, this thesis aims to determine the location of oxygen and nitrogen within the often nanoscale microstructure of titanium alloys, furthering the understanding of the role of these interstitial elements in formation of the embrittling α_2 phase and revealing the effect of oxygen, nitrogen and α_2 on mechanical properties. Use of complementary EPMA, EBSD, nanoindentation and APT will help expand the limited knowledge of the effect of microstructure on oxygen ingress, linking observations on the nanoscale to the microscale, as well as exploring the interrelationship between crystal orientation, microstructure, oxygen content and hardness.

3 MATERIALS AND METHODS

3.1 MATERIALS

Two sets of materials were used in this thesis; one set to study the effects of trace oxygen and nitrogen and another to study high levels of oxygen. The set of materials used to investigate the role of trace oxygen and nitrogen comprises two alloys; the model alloy Ti-7Al and the commercially used alloy Ti-64. The material for the high oxygen study comprises of a TIMETAL 834 compressor disc that has experienced *in-service* conditions, and control pieces of TIMETAL 834.

3.1.1 Trace levels of oxygen and nitrogen

Ti-7 wt.% Al (Ti-7Al), a single-phase model alloy with a composition similar to that of the α phase of Ti-64 fan blade alloy, was supplied by TIMET Witton, Birmingham, UK. A simple model alloy system was chosen to enable the study of the role of oxygen and nitrogen with minimal complications from microstructure and numerous alloying elements. The Ti-7Al material was melted using an Arc furnace, and controlled amounts of oxygen (500 wppm O or 2500 wppm O) were introduced into the melt via the addition of TiO_2 powder. As mentioned in section 2.7 of the Literature Review, commercially used α-type titanium alloys often have approximately 800- 2000 wppm O added to provide strength, but this comes at the expense of fracture toughness, especially upon ageing [39,79]. In this study, a range of oxygen concentrations has been selected to investigate how the current, industry-permitted levels of oxygen affect embrittlement. The material was rolled at 900°C and then recrystallised at 980°C for 1 hour before being quenched in ice water. Subsamples of each oxygen content were then encapsulated under argon and aged for ten days at 550°C and 49 days at 550°C, respectively. The ageing time has been chosen to form α_2, based on the TTT curve for Ti-7Al from Ardakani et al. [104]. A set of "air-cooled" samples were also made through recrystallization at 980°C followed by an ice water quench, and then ageing for 40 minutes at 550°C before air cooling.

It should be noted that the bulk oxygen content of the Ti-7Al + 2500 wppm O, 49 day aged sample is higher than intended; instead of 0.25 wt.% (0.73 at.%) oxygen, the sample ultimately contained 0.39 wt.% (1.1 at.%) oxygen, as can be seen in Table 3.1.

Table 3.1 : APT-measured bulk compositions of the Ti-7Al samples.

	Ti-7Al + 500 wppm O			Ti-7Al + 2500 wppm O		
Element	**Ice water quenched (IWQ) (at.%)**	**10 day**	**49 day**	**IWQ**	**10 day**	**49 day**
Al	9.35±0.4	10.0±0.4	10.2±0.3	10.6	10.2±0.2	9.4±0.53
Ti	90.0±0.5	89.5±0.2	89.3±0.3	88.3	88.7±0.2	88.8±0.38
O	0.19±0.03	0.16±0.04	0.18±0.02	0.69	0.72±0.02	1.12±0.05
N	0.05±0.003	0.02±0.003	0.04±0.002	0.06	0.06±0.01	0.08±0.01

Ti-64 is an α + β alloy commonly used in the aerospace industry. In this alloy, aluminium is the primary α phase stabiliser while vanadium is the main β phase stabiliser. The material used in this study was re-melted from fan blade plate provided by Rolls-Royce Plc, and nitrogen was added through the addition of TiN powder to achieve levels of nominal N, 500 wppm N, 2000 wppm N and 4000 wppm N. The material was processed according to its nitrogen content, as described in Figure 3.1. Subsamples of each nitrogen content were then aged in a vacuum furnace for 49 days at 550°C to form α_2 precipitates.

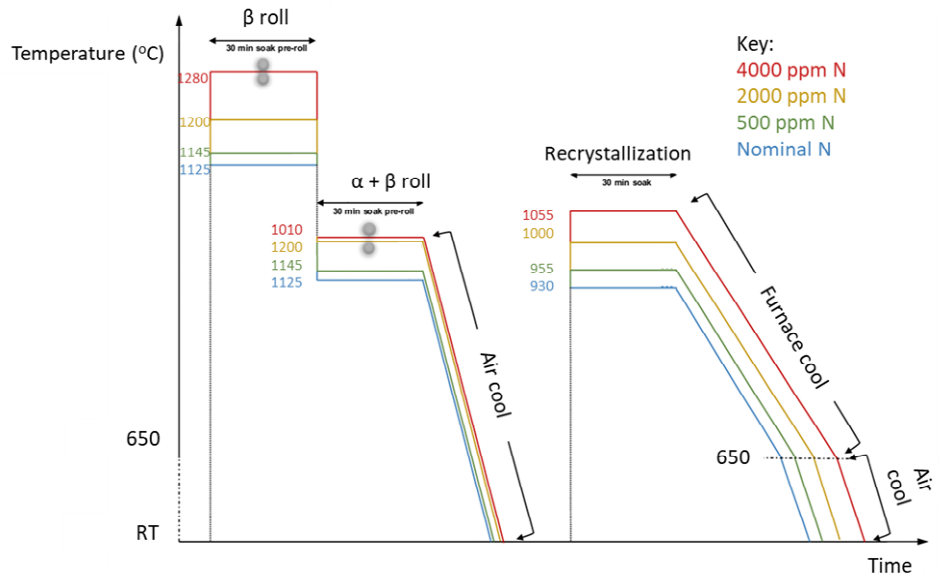


Figure 3.1 : Schematic describing the processing routes of the Ti-64 + N alloy series.

To understand the role of oxygen and nitrogen on the detailed microstructure of these alloys, a technique with high spatial resolution and chemical sensitivity is needed to image the nanoscale α_2 precipitates and determine their composition. Atom Probe Tomography (APT) is a three-dimensional microscopy technique that fills these criteria. APT overcomes some of the challenges that are typically encountered when quantifying light elements, such as oxygen, using electron microscopy techniques. A more detailed description of APT is given in section 3.3.

Nominal, APT-, LECO™ combustion analysis- and Dynamic Secondary Ion Mass Spectrometry (DSIMS)-measured composition for each of the Ti-7Al + O and Ti-64 + N samples can be found in Figure 3.2; there is good agreement between the oxygen and nitrogen APT measurements and the independent DSIMS/ LECO measurements which shows that oxygen and nitrogen can be accurately quantified using APT.

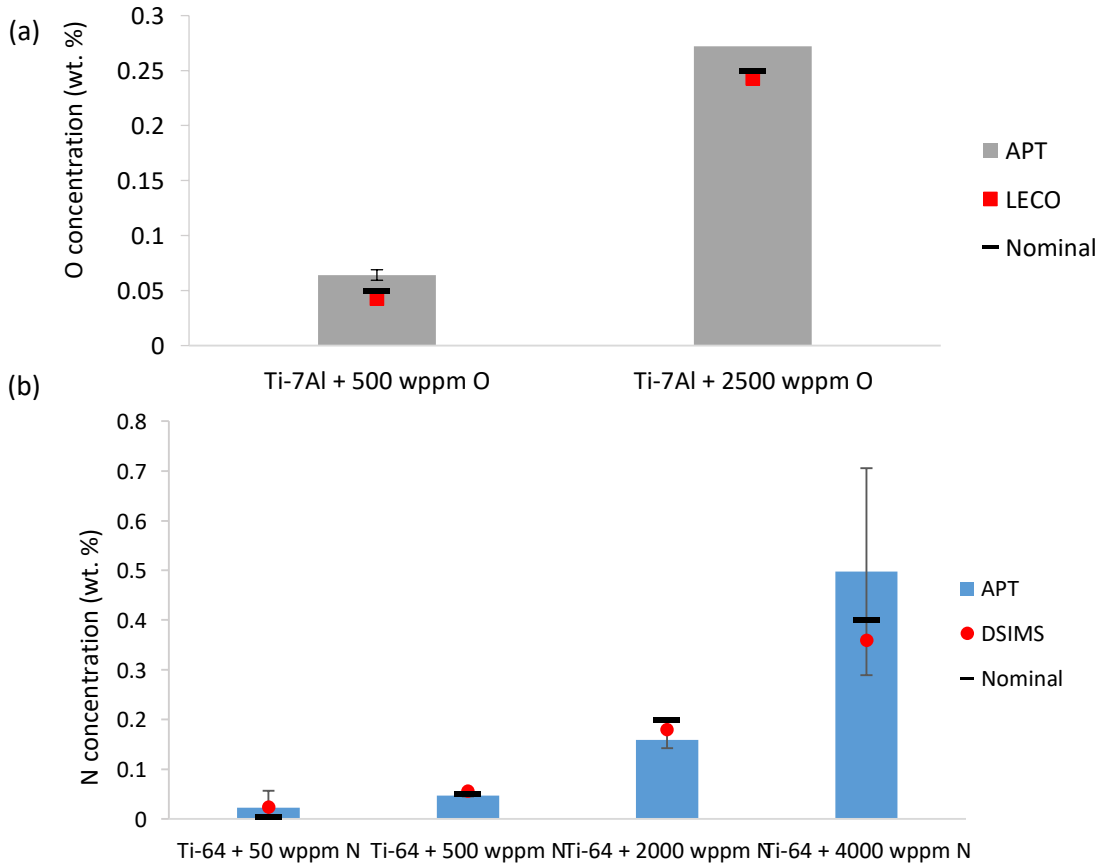


Figure 3.2: Nominal, APT-, LECO- and DSIMS-measured composition for the (a) Ti-7Al + O and (b) Ti-64 + N samples.

Representative SEM micrographs for the Ti-7Al and Ti-64 unaged material can be seen in Figure 3.3. These micrographs highlight the relatively simple microstructures intentionally chosen for this study. It can be seen from Figure 3.3 (a) and (b) that the α grain size in Ti-7Al does not significantly change upon ageing. The volume fraction of the β phase in the Ti-64 material is estimated, using ImageJ [166], to be 20%.

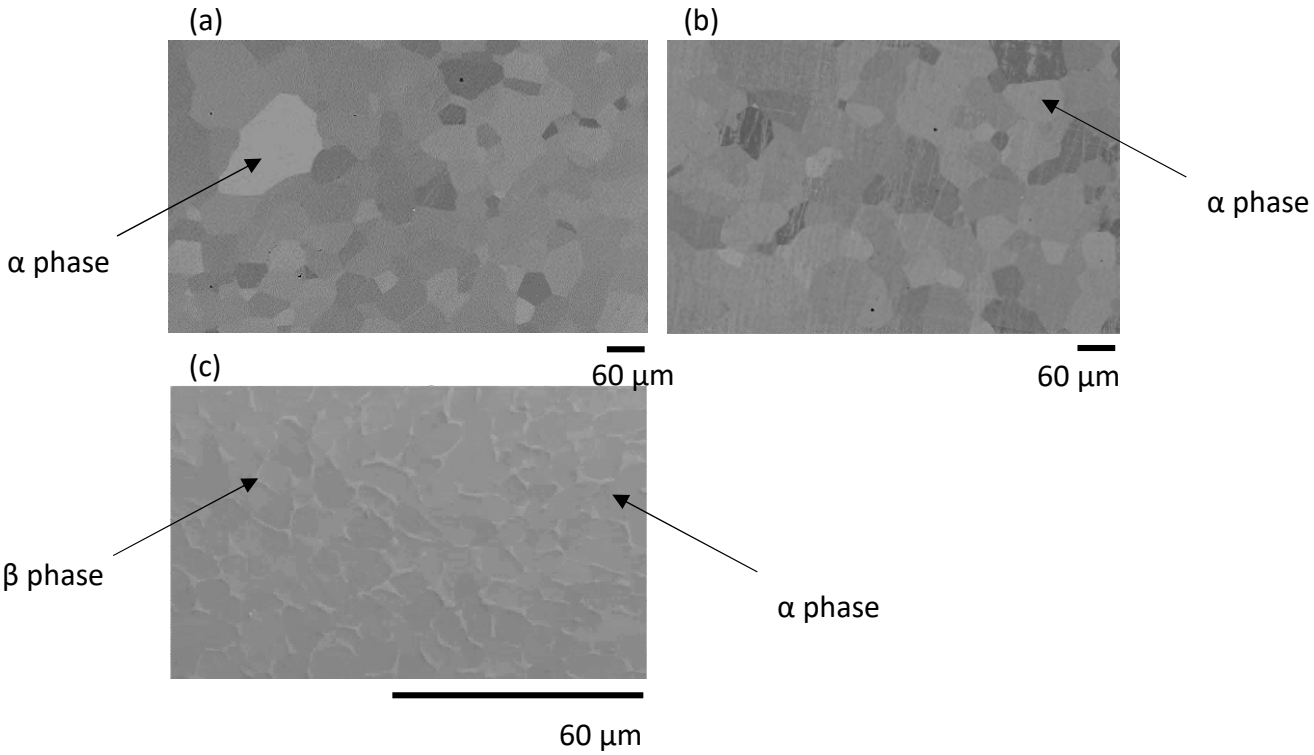


Figure 3.3: Representative SEM micrograph of (a) Ti-7Al + 2500 wppm O, ice water quenched (b) Ti-7Al + 2500 wppm O, 49 day aged, (c) Ti-64 + 4000 wppm N, unaged.

3.1.2 High levels of oxygen

TIMETAL 834 is a near-α-Ti alloy with nominal composition Ti -5.8%Al -4%Sn -3.5%Zr -0.7%Nb -0.5%Mo -0.3%Si. The addition of zirconium and tin improve the high-temperature strength of the alloy, making it suitable for operation at temperatures up to 600°C in components such as compressor discs [63]. A section of TIMETAL 834 compressor disc that has experienced temperatures up to 630°C, for 18,000 hours was provided by Rolls-Royce Plc. After billet forging in the α + β phase field, the alloy was solution treated at 1015°C for 2 hours, oil quenched and then aged at 700°C for 2 hours, before being air-cooled. This resulted in a duplex microstructure

consisting of lamellar grains, containing fine laths of secondary α and retained β, and large primary α grains. An example of this duplex microstructure can be seen in Figure 3.4 (d).

A cross-section of the disc mounted in conductive resin, as shown in Figure 3.4 (c), was ground and polished to a colloidal silica finish. Colloidal silica was neutralised with hydrogen peroxide to prevent pitting during polishing. On a separate piece of non-exposed TIMETAL 834, an *oxygen-rich layer* was also created by ageing in air at 550°C for 1000 hours. This sample will be referred to as the *lab-controlled* sample.

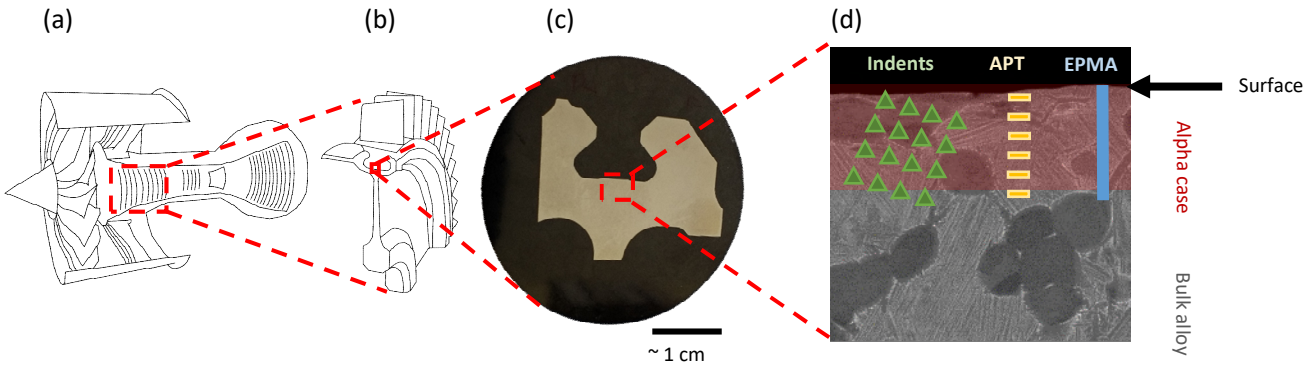


Figure 3.4: A cutaway drawing of a jet engine is shown in (a) and in (b) is shown a cutaway drawing of one-quarter of a compressor disc. (c) shows a photograph of the cross-section of compressor disc used in this study, and (d) shows a schematic of the analysis performed in the current study.

3.2 QUANTIFYING OXYGEN

Previous studies have underlined the importance of accurate quantification of oxygen concentration at the surface of titanium, where oxygen ingress occurs in the top few tens of microns [164,167]. EPMA is sometimes used to measure surface oxygen profiles in titanium [168], but is reliant on suitable standard samples to provide quantitative results; this is discussed in greater depth in section 3.4. Energy dispersive spectroscopy (EDS) also requires reliable standard samples to quantify oxygen, and has reduced spectral resolution compared to EPMA, making it more difficult to isolate the oxygen X-ray line. Attempts have been made to quantify oxygen using Secondary Ion Mass Spectrometry (SIMS) [169]. This is challenging as the interpretation of any

SIMS data again relies on comparison with accurate standard samples. It is non-trivial to find representative standards and to verify the standard oxygen concentration independently. Furthermore, SIMS also has limited lateral spatial resolution since trenches used to collect statistically significant data are on the order of tens of microns in width.

An alternative technique is APT, a 3D microscopy technique with a uniquely powerful combination of very high spatial and chemical resolution. APT does not rely on external standards for quantification unlike SIMS, EDS and EPMA, and this enables use of APT to quantify and map oxygen segregation on the nanoscale, thereby generating new insights into the interaction of microstructure and local oxygen concentration. For example, APT studies have revealed formation of α_2 precipitates of varying morphology within the *α case* layer formed on Ti-64 [170] and have also investigated the relationship between mechanical properties and oxygen concentration in this alloy [171]. APT has also been used to study ordering [60,110,112], oxygen and carbon segregation [172] and fine scale precipitation [173,174] in a range of titanium alloys.

3.3 Atom Probe Tomography

3.3.1 Principles

APT provides excellent spatial and chemical resolution through the highly controlled field evaporation of atoms from a sharp needle-shaped sample made from the material of interest. When a DC voltage is applied, the small radius of the needle-shaped sample (<100 nm) generates the intense electric field required for field evaporation, according to Equation 3.1

$$F = V / k_f R \qquad \textit{Equation 3.1}$$

where F is the electric field at the apex of a tip of radius of curvature, R, which has a voltage, V, applied to it. The field reduction factor, k_f, (which typically has a value of 3-5 [175]) accounts for the tip being non-spherical. The applied DC voltage generates an intense electric field, which is

intentionally kept just below that required for field evaporation. A superimposed voltage or laser pulse enables an atom at the specimen surface to overcome the activation barrier for field ion evaporation, ideally resulting in evaporation of a single atom per pulse. The resultant field-evaporated ion is accelerated by the field towards the detector, as illustrated in Figure 3.5. Nanosecond pulsing enables measurement of the time-of-flight from sample to detector, which allows the mass-to-charge state ratio of the ion to be determined so that each detected ion is chemically identified. The spatial location of the impact of each ion on the detector is also recorded. Computer software can determine the position on the sample from which each detected ion originated. This is achieved with a reverse projection algorithm, along with an assumed (spherical cone) model of specimen geometry, and knowledge of the position of detector hits and evaporation sequence. The result is a 3D virtual reconstruction of the sample, in which the spatial location and chemical identity of each atom are known.

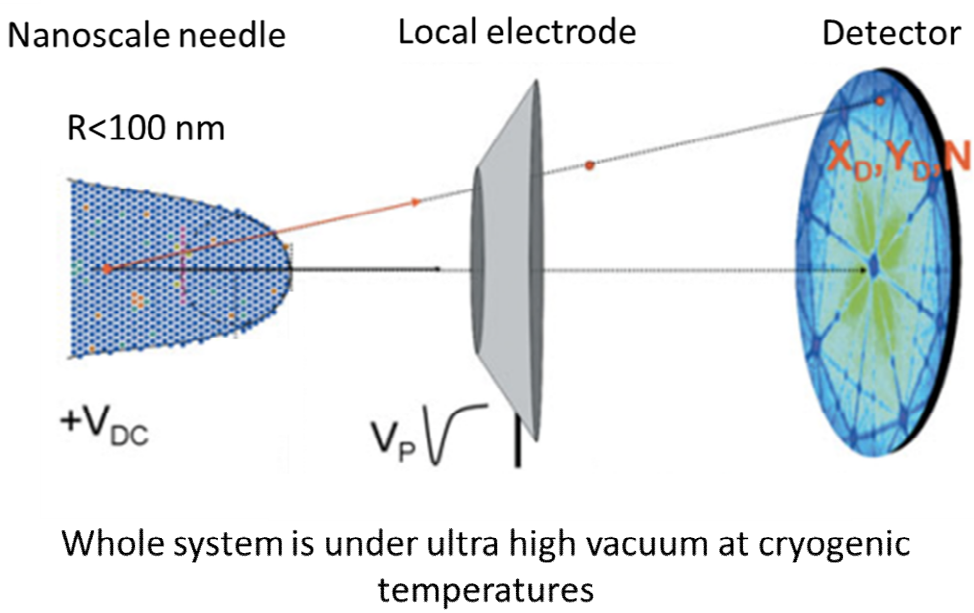


Figure 3.5: Schematic showing the workings of a local electrode atom probe, after [176].

3.3.2 APT sample preparation

APT samples were prepared on a Zeiss NVision 40 FIB-SEM (focussed ion beam scanning electron microscope) or a Zeiss Crossbeam FIB-SEM, using the standard FIB lift-out method [177]. For both

the *lab-controlled* and *in-service* TIMETAL 834 material, APT samples were made at increasing depth from the surface, as shown schematically in in Figure 3.4.

Samples for Transmission Kikuchi Diffraction (TKD) were prepared using the FIB, according to the technique described by Jenkins et al. [178], to enable grain boundaries to be captured within the APT sample. The grain boundaries were difficult to locate accurately in Ti-7Al using secondary electron imaging on an APT sample, owing to the low compositional or orientation-based contrast between the two grains. In order to be captured in the analysis volume of an APT dataset, the grain boundary feature of interest must be located within the top 100 nm of a tip (with radius less than 50 nm). Such precise location of a feature is challenging when the feature cannot be easily seen. Iterative imaging of the material using TKD, and shaping/ polishing using the FIB, enabled fabrication of APT samples containing grain boundaries, the type of which was also successfully characterised, using the protocol as described by Jenkins et al. [178]. Further details of TKD analysis procedure can be found in section 3.6.

3.3.3 Selection of APT analysis conditions

The atom probe was operated in laser mode, and not voltage mode, in order to increase the yield of successful analyses. The thermal energy provided by each laser pulse lowers the effective evaporation field, and the electrostatic stress associated with this field. Although the causes of APT specimen fracture are not fully understood, the reduced electrostatic stress at the surface, combined with the lack of cyclic stress due to voltage pulsing, are thought to contribute to the increased specimen yield in laser mode compared to voltage mode [179].

When using APT, it is necessary to optimise experimental conditions to ensure accurate quantification of all elements, including trace solutes such as oxygen and nitrogen [180]. Experimental conditions affect relative evaporation conditions of each species, as well as their charge state, which in turn affects mass spectrum peak positions.

One such experimental condition is the energy of the laser pulse used to field evaporate ions from the needle. Laser pulse energy can be changed to limit the $^{48}Ti^{+++}$ / $^{16}O^{+}$ peak overlap at 16 Da, which can be seen in Figure 3.6.

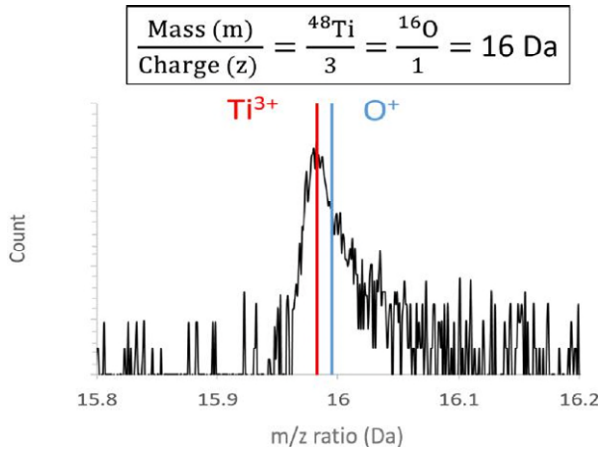


Figure 3.6: Schematic diagram of the mass spectrum of the alloy Ti-7Al illustrating the peak overlap between Ti 3+ and O 1+. The two peaks do not overlap precisely at 16 Da because the measured masses of the two ionic species are accurate to a large number of significant figures, which gives rise to the small difference in mass-to-charge ratio.

At lower laser energy (higher standing field requirement), titanium evaporates in the 3+ charge state, meaning it overlaps with the O+ peak in the mass spectrum. A higher laser energy evaporates titanium in lower charge states (2+ and 1+), avoiding this peak overlap.

Laser energy was varied to minimise the fraction of titanium detected in the 3+ charge state, and it can be seen from Figure 3.7 that the overlap was minimised for laser energies > 100pJ.

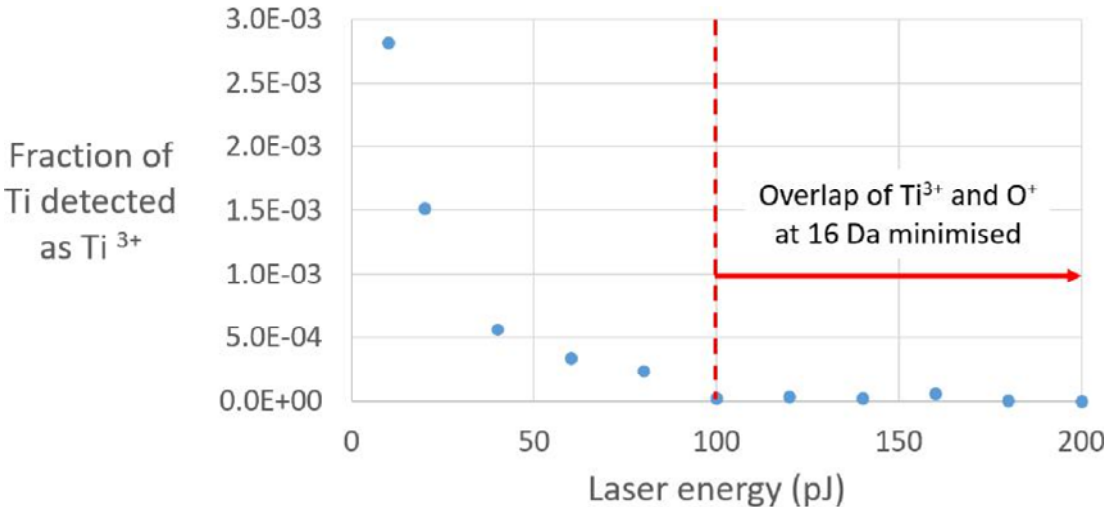


Figure 3.7: Plot of fraction of titanium in 3+ charge state against laser energy. The amount of Ti 3+ located in the 16 Da peak in the mass spectrum is minimised at laser energies above 100 pJ.

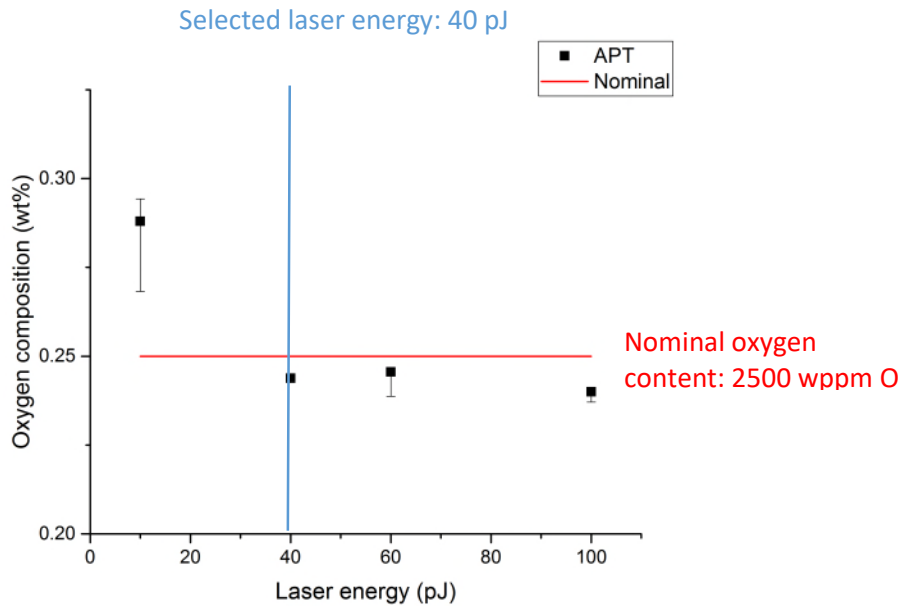


Figure 3.8: Plot of variation in APT-measured oxygen content with laser energy. Except for the oxygen concentration at a laser energy of 10 pJ, the measured oxygen concentration is approximately the same order of magnitude as the nominal value of 2500 wppm.

Upon analysing APT needles using a 100 pJ laser energy in the Cameca local electrode atom probe (LEAP) 5000, non-uniform evaporation behaviour and density variations in the dataset were observed. This suggests that although 100 pJ may be suitable for studying oxygen concentration, since it minimises the mass spectrum peak overlaps containing oxygen, it may also be causing density artefacts in the resulting datasets that will affect accurate precipitate characterisation.

Figure 3.8 shows that the oxygen concentrations measured as a function of laser energy are all in good agreement with the nominal value of 2500 wppm. The exception to this is the higher oxygen concentration measured at 10 pJ, which is likely a consequence of random concentration fluctuations within the small APT sample volume. It should be recognised that lower laser energies are associated with low sample yield due to a higher applied standing voltage requirements [179]. Based on Figure 3.8, a laser energy of 40 pJ was selected, since this gave acceptable sample yield, gave oxygen concentrations close to the independently measured values, and avoided the density artefacts associated with high laser energies.

Another artefact observed in all samples analysed in laser mode can be seen in Figure 3.9. Fluctuations in density can be seen radiating from the core of the tip. This effect has been termed 'feathering', and is only observed in laser mode running (not in voltage mode.) Tips of the same material have been run in both voltage and laser mode, and the analysis compared. Feathering does not affect the composition, as can be seen in Table 3.2. However, density-based cluster identification algorithms are affected by the clustering. For this reason, isoconcentration surfaces were used to identify clusters. Full details of precipitation identification and extraction can be found in section 3.3.5.

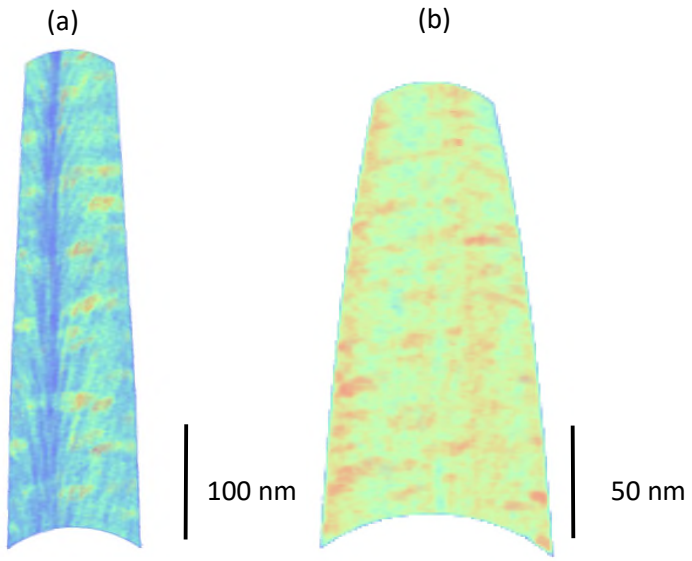


Figure 3.9: Slices through measured density maps of APT datasets of Ti-7Al + 2500 wppm O run in (a) laser mode and (b) voltage mode. Maximum density range is approximately 5-55 ions per nm^3, with blue being low density.

All subsequent APT samples following parameter optimisation were analysed with a CAMECA LEAP 5000 HR system, using a laser energy of 40 pJ, a stage temperature of 50 K and a pulse frequency of 200 kHz. APT data analysis was performed using the commercially available Integrated Visualisation and Analysis Software (IVAS) software package (CAMECA, version 3.8.2) and the open-access 3Depict software [181]. The oxygen content of each APT sample was analysed by solving the mass spectrum peak overlaps using custom Matlab code written by Dr Andrew London [182], which will be discussed in more detail in the next section.

Table 3.2: APT-measured compositions of two representative samples, each measured in voltage and laser mode.

	Ti-7Al + 500 wppm O, 49 day aged		Ti-64 + 2000 wppm N, IWQ	
	Voltage (wt.%)	**Laser**	**Voltage**	**Laser**
Ti	91.0	92.5	89.0	90.3
Al	8.2	6.7	6.9	6.8
O	0.66	0.61	0.41	0.31
N	0.01	0.01	0.18	0.16
V	-	-	3.3	2.3

3.3.4 Mass spectrum ranging and peak overlaps

APT can resolve isotopes of elements. Elements field evaporate from the APT tip in different charge states, and each peak in the mass spectrum corresponds to an isotope in a specific charge state. Ranging the mass spectrum is a process that involves identifying the ionic species contributing to each mass spectrum peak, and defining the minimum and maximum Dalton values that correspond to the peak. Prior knowledge of the material is helpful in assisting in the process of deciding which species are contributing to each peak. This may be obtained, for example, from the nominal composition of the alloy or EDS mapping of the sample. Isotopes help confirm chemical identity, and peak heights represent different isotopic abundances. A further useful aid is the program *weights* [183], which enables the input of the elements contained in the sample together with the Dalton value of the unidentified peak. *Weights* then produces a list of potential ionic species that could be contributing to the peak. Another useful tool, called *rangecheck* [183], checks that range files are rational. For example, it checks that if a side-peak is ranged, then other peaks in the expected distribution are also ranged; if a peak is ranged, its name and mass should match to within a given tolerance; charge states must be contiguous, e.g. 1+ and 3+ states cannot be ranged unless an ion is also ranged at 2+ [183].

Different elements can have the same mass-to-charge state ratio, leading to a mass spectrum peak overlap. This leads to multiple options for the ionic species contributing to a peak when ranging. Peak overlaps can be solved with sufficient knowledge of the possible contributing species present and the isotopic abundances of these species. Once the overlap has been solved,

and the relative contributions of each species to the peak has been determined, accurate compositions can be reported. Furthermore, the peak can be labelled as the species making the most significant contribution to the peak. It should be noted that, while solving mass spectrum overlaps can lead to an accurate composition measurement, it does not determine the chemical identity of individual ions within the dataset with certainty. This may make local composition variations more difficult to observe reliably.

Important peak overlaps in this study include those that involve oxygen-containing species. The majority of oxygen is detected as TiO ions (TiO++ = 67% O and TiO+ = 20% O) whilst the O+ at 16 Da only contributes 8%. The oxygen-containing overlaps are illustrated diagrammatically in Figure 3.10. The bubbles on the diagram represent ionic species, while the lines between them represent the overlaps. The thickness of these lines represent the computational difficulty associated with solving the overlaps, and the Dalton value corresponding to the overlap is written on the line.

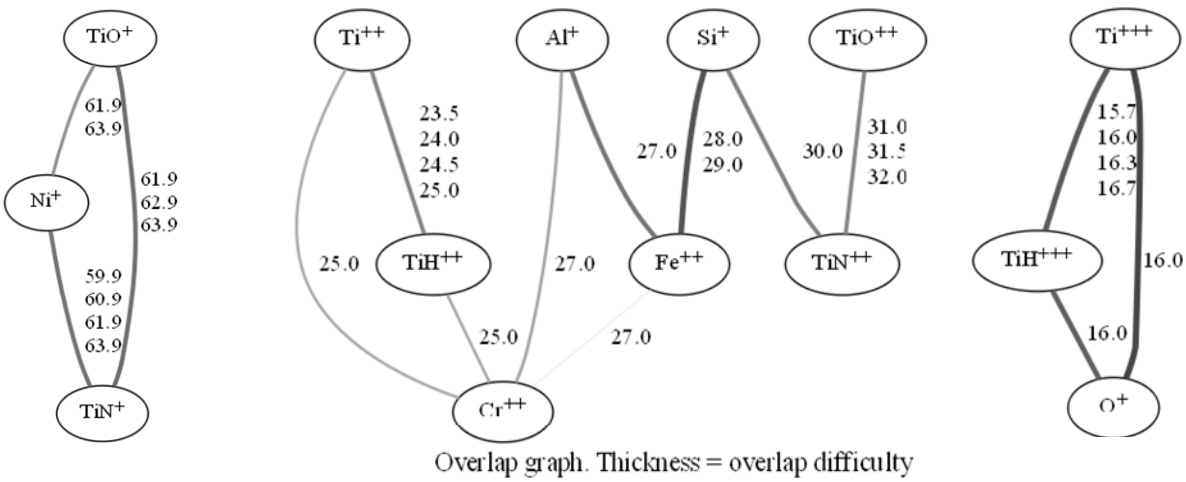


Figure 3.10: Bubble diagrams illustrating the mass spectrum peak overlaps involving oxygen in Ti-7Al + 2500 wppm O, 49 day aged.

Of the mass spectrum overlaps present in Ti-64, the overlap between Fe++, Si+ and N_2+ is of particular interest since N_2+ is the main ionic species contributing to the overall nitrogen

concentration. The other nitrogen-containing species (N+, Ti_2N+++, TiN+, TiN++) are in lower concentration.

For each dataset, deconvolution of mass spectrum peak overlaps was performed, based on the candidate ionic species inputted, using the method described by London [184]. The level of agreement between the heights of the peaks in the overlap-solved mass spectrum and the original mass spectrum was used to aid peak identification; combinations of species that led to good agreement were selected. The Akaike Information Criteria was also used to assist with peak identification by minimising over-fitting, as described by London [184].

3.3.4.1 Proximity histograms and line profiles

When studying the α_2 precipitates, proximity histograms [179] were created from the aluminium isoconcentration surfaces to track change in composition across the α_2 precipitate-matrix interface. The proximity histogram was created using a range file in which each mass spectrum peak was assigned its own unique identity, to allow peak overlap solving. The aluminium peaks were selected to create the isoconcentration surface for the proximity histogram since they do not overlap with other peaks, and the precipitates are enriched in aluminium. The mass spectrum peaks contributing to each proximity histogram bin were then deconvolved using custom Matlab code following the method established by London [184], to provide an accurate composition measurement by accounting for the changing nature of the local mass spectrum as relative position is varied across the interface.

A similar approach of solving mass spectrum overlaps on a bin-by-bin basis has also been used to generate line concentration profiles to quantify the change in concentration of species across phase/ grain boundaries. 95% confidence intervals are reported as error bars on these profiles and proximity histograms, and are a measure of the uncertainty in the composition, which was determined using the maximum likelihood estimation when mass spectrum peak overlaps were present. Both counting error and uncertainty from solving the peak overlaps can contribute to the

overall uncertainty in composition. When no peak overlaps are present, the uncertainty is given by the counting error. Further details of the sources of uncertainty can be found in work by London [184].

3.3.5 Identifying and extracting precipitates

Detection and extraction of small precipitates is challenging, and several approaches have been taken in the literature, a summary of which can be found here [185]. One of the most common approaches involves using a density-based cluster searching algorithm, known as the maximum separation method. For density-based methods, groups of solute atoms that are spatially closer together than they would be in a randomly distributed solid solution are defined as clusters [186]. However, since the feathering effect, described in section 3.3.3, produces density artefacts, the maximum separation method cannot be used to identify small clusters for this material. An alternative method of precipitate identification is local concentration filtering [187]. Instead of using density to identify precipitates, the local concentration of each atom in the dataset is calculated, and atoms with a local concentration above a user-defined threshold are identified as belonging to precipitates. While this was effective in identifying precipitates, the computational time required to achieve the filtering was prohibitive.

Isoconcentration surfaces are also a concentration-based selection method and are not affected by density fluctuations. They are quick to render, allowing parameter sweeps to be made to select the optimum isoconcentration surface value. Aluminium isoconcentration surfaces were generated within the reconstructed APT data to identify the α_2 precipitates. The level of aluminium concentration defining such surfaces was initially varied, and the value which produced the proximity histogram with the narrowest interface width was selected, an approach previously developed by Homma et al. [188]. This was to minimise blurring of the data due to shape misrepresentation. Ions contained within the chosen isoconcentration surface were then extracted as precipitates.

A drawback of using isoconcentration surfaces is that they are limited in spatial resolution, which is determined by the voxel size used to create them, and the delocalisation applied. The method of isoconcentration value selection described by Homma et al. [5] requires that the concentration plateaus within the precipitates so that the interface width can be well-defined by a sigmoid function. This is not possible if the voxel size is approaching the feature size, as the data is insufficiently spatially sampled to recover robust shape information. This defines the spatial resolution limit for identifying precipitates using isoconcentration methods.

During an APT experiment, evaporation artefacts can also cause density fluctuations. The mass-to-charge values of the data points in each of the APT datasets were randomly exchanged to distinguish between these artefacts and chemical clustering. Any clusters identified in the randomised dataset were deemed to be a result of density fluctuations and were referred to as random precipitates. For all of the datasets studied, the isoconcentration value selected resulted in only a small number of random precipitates, such that their contribution was deemed negligible.

The composition of the extracted precipitates was calculated using a MATLAB mass spectrum peak deconvolution tool [182]. Precipitate volume fraction was estimated by dividing the total number of ions within the precipitates by the total number of ranged ions in the whole APT dataset.

3.3.6 Precipitate morphology

To analyse precipitate morphology, precipitates were identified and extracted using isoconcentration surfaces as described in section 3.3.5. Precipitates that intersected the edge of the APT dataset were then excluded. Once extracted, a d_{max} cluster search was performed on the precipitates, since this indexes each precipitate, counts the number of ions per precipitate and measures the dimensions of each precipitate. The cluster search parameters (d_{max} and N_{min}) were selected by varying these parameters until the number of clusters identified matched the number

of precipitates extracted using the isoconcentration surface. It should be noted that the purpose of the cluster search was not to identify precipitates but rather to index them. Once indexed, an ellipsoid was fitted to each precipitate, thus identifying the three principal axes, L_1, L_2 and L_3, where $L_1 > L_2 > L_3$. The relative length of the principal axes was used to categorise the precipitates as discs ($L_1 = L_2$, $L_2 > L_3$), spheres ($L_1=L_2=L_3$), laths ($L_1>L_2>L_3$) or rods ($L_2 = L_3$, $L_1>L_2$), as illustrated in Figure 3.11.

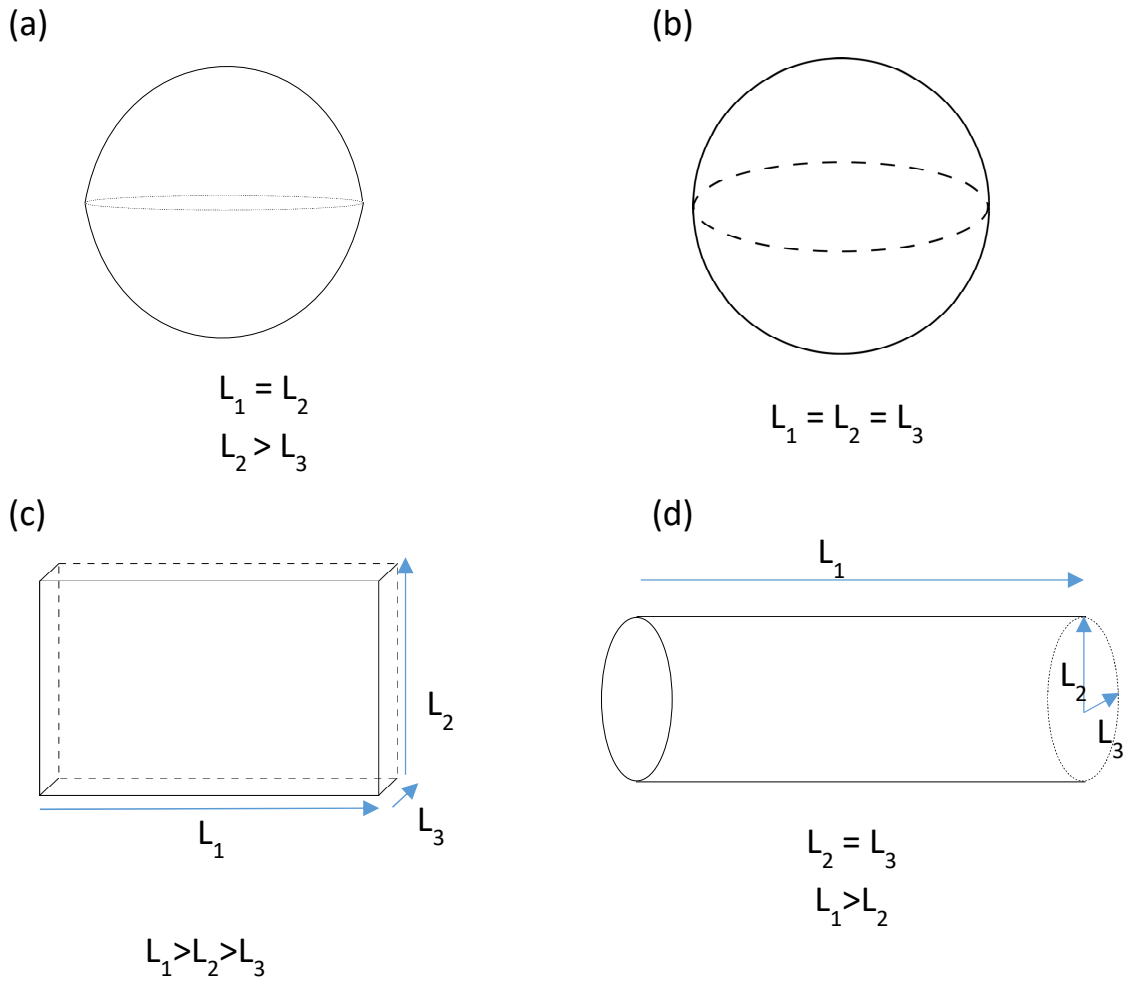


Figure 3.11: Schematic showing the four precipitate morphology categories; (a) disc, (b) sphere, (c) lath and (d) rod.

3.4 Electron Probe Microanalysis (EPMA)

3.4.1 Principles

Electron probe microanalysis (EPMA) is an electron beam-based analytical technique that makes use of a focussed electron beam to generate characteristic X-rays from the sample of interest. Detection and measurement of the energy of these X-rays identifies the elements present in the sample. EPMA can perform wavelength dispersive spectroscopy (WDS) and EDS simultaneously. WDS separates the characteristic X-rays by their wavelength while EDS separates them by energy. EDS is limited in its count rates for individual X-ray peaks as it is collecting all X-ray channels and, since the detector can only process one X-ray at a time, there is a substantial loss of signal. On the other hand, WDS only allows one single X-ray to be diffracted onto the detector, meaning that there is no loss of signal from competing X-rays. Furthermore, WDS is advantageous since it has a higher spectral resolution, as seen in Figure 3.12, which allows peaks that would overlap in EDS to be resolved. However, the downside of WDS over EDS is that the number of elements that can be analysed simultaneously is limited by the number of WDS detectors that the instrument has.

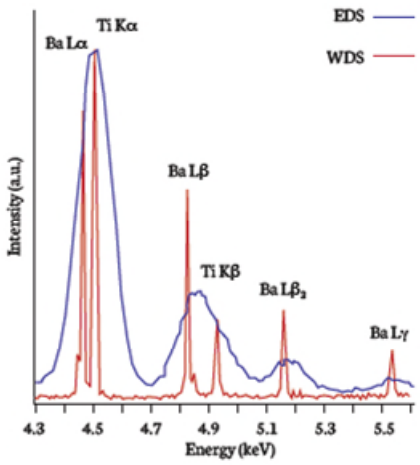


Figure 3.12: X-ray spectra of the same kinetic energy region taken with EDS and WDS, highlighting the higher spatial resolution of WDS [189].

The electron microprobe used in this study was a CAMECA SX5-FE EPMA in the Department of Earth Sciences, University of Oxford. It has five spectrometers, three of which are equipped with four crystals, and two of which are equipped with two crystals. A schematic showing the system and diffracting crystals can be seen in Figure 3.13. Details of the available crystals are given in Table 3.3. Each spectrometer is set up with one crystal designed to analyse a specific element, and therefore a particular wavelength. Each crystal is optimised to measure a specific range of wavelengths, and thus the choice of crystal depends partly on the wavelength of the characteristic X-rays emitted by the element of interest. However, other factors must be considered, and these are discussed in section 3.4.3.

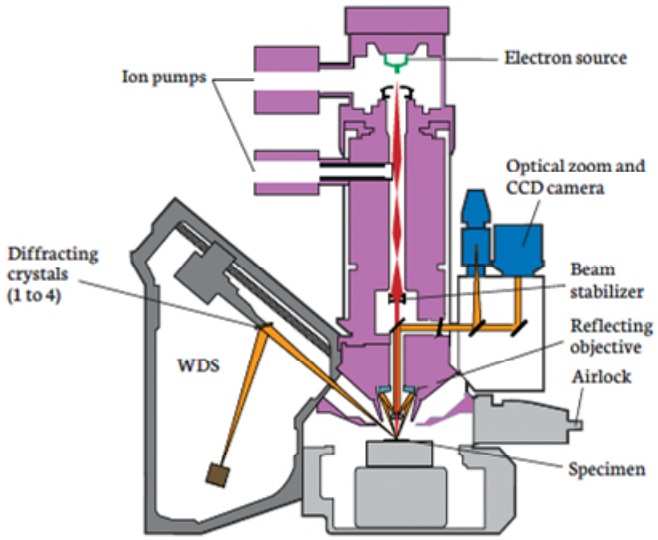


Figure 3.13: Schematic cross-section illustrating the setup of the electron microprobe, courtesy of Marion Chopin at CAMECA instruments [189].

Quantitative analysis can be performed using WDS by comparing the intensity of the X-rays measured from the sample to the intensity of X-rays measured from a known standard material. Standard corrections can be applied to correct for differences in atomic number, absorption of X-rays and fluorescence. Wavescans are performed to provide accurate estimates of background counts to improve background subtraction.

Table 3.3: Details of available spectrometer crystals.

Crystal	Name	Wavelength range (Å)
LIF	Lithium fluoride (LiF)	0.9-3.3
PET	Pentaerythritol ($C(CH_2OH)_4$)	2.2-7.1
TAP	Thallium acid phthalate ($TlHC_8H_4O_4$)	6.5-20
PC0	Pseudocrystal (W-Si)	11.0-36.0
PC1	Pseudocrystal (W-Si)	15-48
PC2	Pseudocrystal (Ni-C)	25-80

3.4.2 Sample requirements

X-ray emission is very sensitive to the sample surface condition because electron scattering is affected by surface geometry [190]. Thus, a flat sample, without surface relief due to polishing, and without edge bevels, is required. To achieve this, careful sample preparation must be carried out. Samples were mounted in conductive resin, ground and polished from 600 – 2500 grit, then polished from 3 µm to 1 µm diamond. The final polishing stage made use of neutralised colloidal silica solution. This was necessary to give the surface finish required for subsequent EBSD. Since the colloidal silica solution was neutralised, the surface relief after polishing was minimal, and therefore suitable for EPMA too. During all grinding and polishing stages, polishing was carried out such that the edge of interest was always at the trailing edge to minimise sample bevel, as illustrated in Figure 3.14.

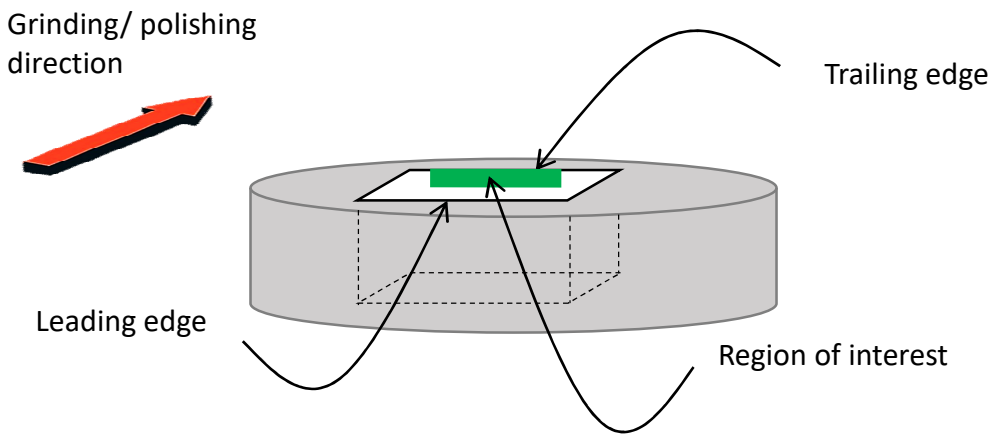


Figure 3.14: Schematic to show the polishing setup that was used to minimise sample bevel.

Additionally, the electron microprobe was set up such that the spectrometer measuring oxygen was positioned behind the surface of interest. This ensured that the position of the spectrometer mitigated any enhancement of the oxygen signal if there was any slight bevel present, as shown

in Figure 3.15. The compressor disc sample was mounted in conductive resin to maximise conductivity, which was essential to prevent charging as a result of the high beam current used for collecting data. Copper tape was used to provide a conductive pathway from the sample to the sample holder to aid conductivity.

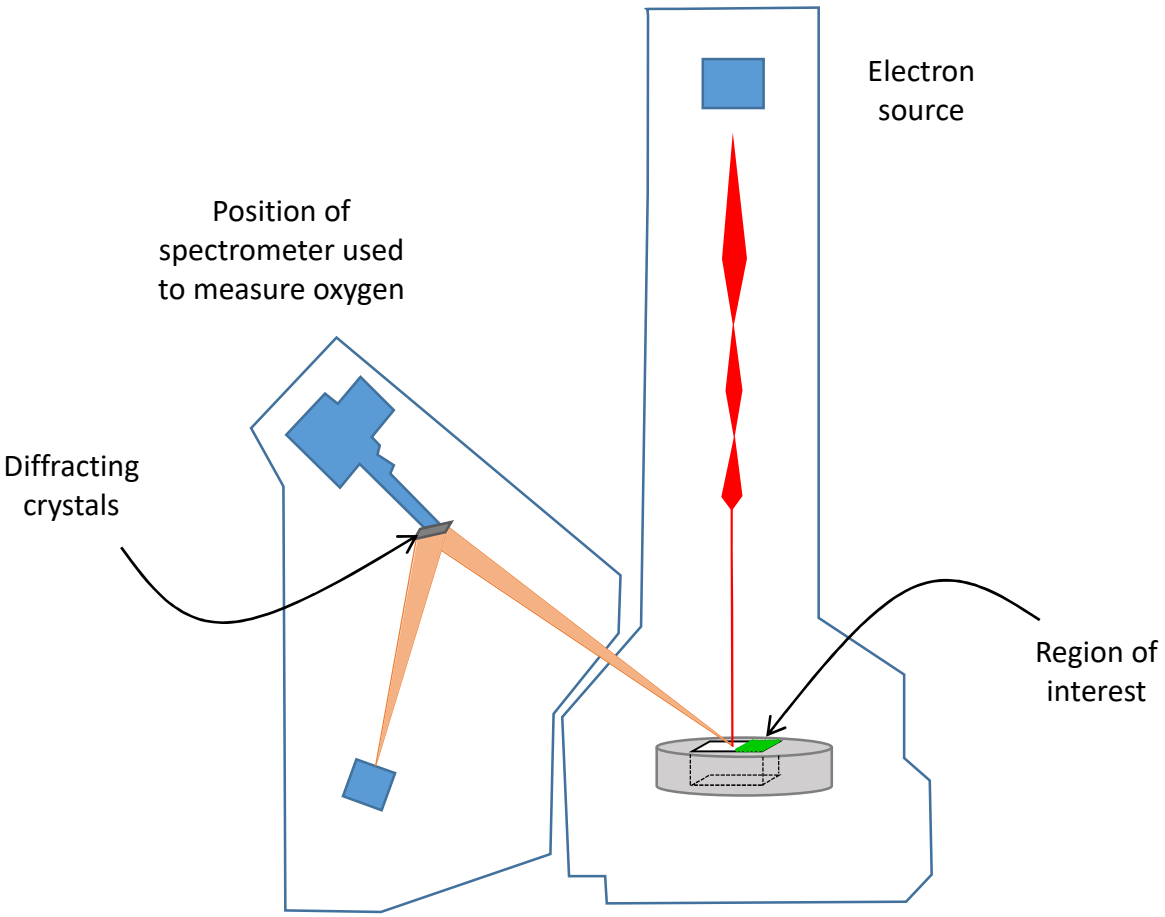


Figure 3.15: Schematic of the electron microprobe setup showing the position of the spectrometer used to measure oxygen, selected in order to mitigate enhancement of the oxygen signal.

3.4.3 Selection of EPMA analysis conditions

When choosing appropriate analysis conditions, a range of interdependent factors must be considered including choice of X-ray line, choice of spectrometer crystal, accelerating voltage and probe current.

When choosing the appropriate X-ray line, the accelerating voltage, atomic number of elements present and spatial resolution must be considered. The accelerating voltage must be sufficient to

excite the characteristic X-rays. A metric used to determine this is the overvoltage, which is given by electron accelerating voltage divided by X-ray excitation energy. Overvoltage should have a value of at least four to achieve sufficient signal intensity and peak-to-background ratio [191]. However, there is a trade-off between overvoltage (intensity) and reduced fluorescence yield. Also, increasing accelerating voltage decreases the spatial resolution [192].

For mapping oxygen, an accelerating voltage of 10 keV was used. The Kα X-ray line for oxygen has an energy of 0.525 keV, giving an overvoltage of ~19. This high overvoltage has the advantage of increasing the signal to background ratio, since the intensity of the continuum signal increases at a slower rate than the peak intensity, as the voltage is increased [192]. It should be borne in mind that for soft X-rays that are easily absorbed, such as oxygen, self-absorption can reduce signal intensity above a certain voltage, and can reduce the accuracy of the absorption correction applied. A beam current of 10 nA with 0.05 second per pixel dwell time was used to give sufficient counting statistics while minimising damage and carbon deposition on the sample. For all elements of interest, α lines were chosen over β lines due to their higher intensity.

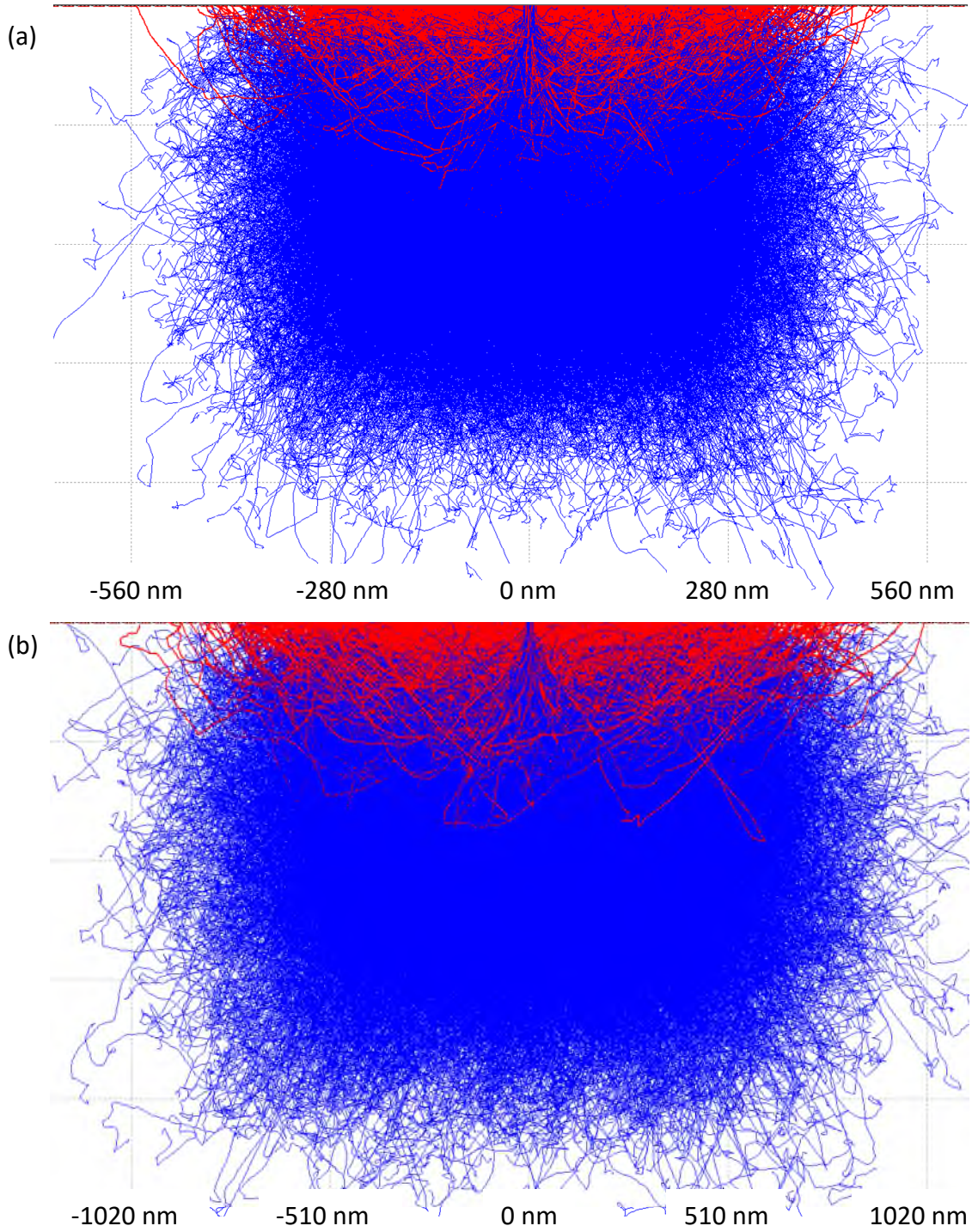


Figure 3.16: Monte Carlo simulation of the interaction volumes of a (a) 10 keV and (b) 15 keV incident electron beam in titanium using CASINO software [193].

Lateral spatial resolution is also governed by accelerating voltage. The higher the accelerating voltage, the larger the interaction volume and the lower the lateral spatial resolution. For the surface line profiles, an accelerating voltage of 15 keV was used to maximise oxygen signal, but

the spatial resolution was compromised, as it was less critical for the surface profiles. The maximum width of the estimated interaction volume at 15 keV was 1.85 µm, as can be seen in Figure 3.16 (a). However, higher spatial resolution was required for the oxygen maps at the surface since it was necessary to determine if the fine microstructural features (on the order of tens of nanometres) were affecting oxygen ingress. Thus, an accelerating voltage of 10 keV was used for the maps. The maximum width of the estimated interaction volume was 950 nm, as can be seen in Figure 3.16 (b).

Spectrometer crystals are each optimised for a specific range of atomic numbers (wavelengths) and intensities. In some cases, the wavelength ranges for different spectrometer crystals overlap, meaning there is a choice of crystal that can be used to measure an element. Generally, the spectrometer crystal with the larger plane spacing will be selected since this will give a higher peak intensity. However, sometimes it is necessary to choose the crystal with smaller plane spacing when there are overlaps, since this provides higher spectral resolution.

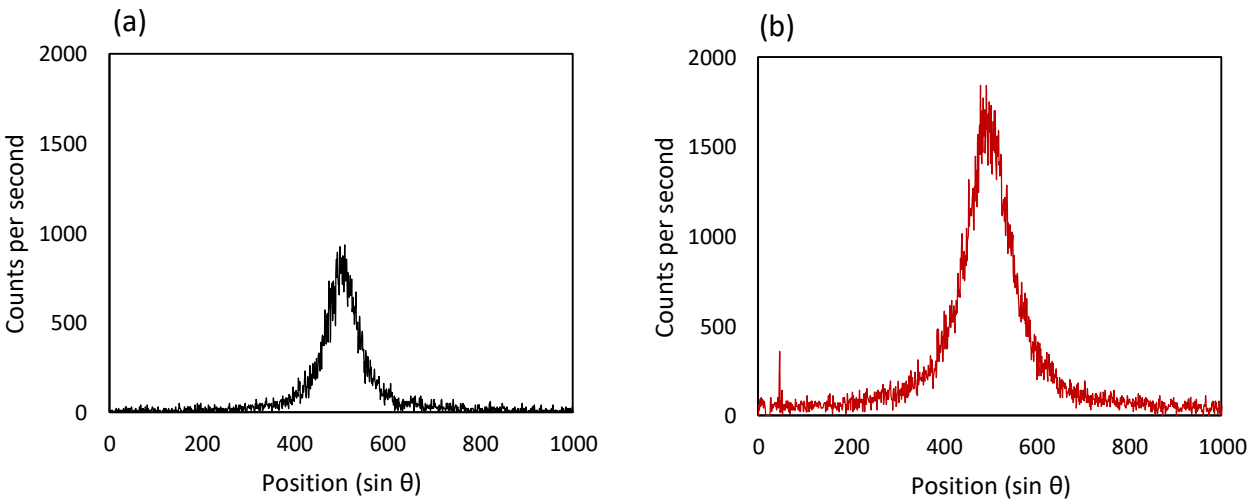


Figure 3.17: Wavescans of the oxygen Kα peak, measured on a TiO_2 standard sample, using the crystal (a) PC0 and (b) PC1.

For example, Figure 3.17 shows wavescans of the oxygen Kα peak, measured on a TiO_2 standard sample, using two different crystals; PC0 and PC1. PC1 was chosen initially to measure oxygen for the surface line profiles since it has a larger plane spacing and therefore gives higher counts.

However, PC0 was used to measure the oxygen for the surface map analyses, in order to try and resolve the Ti Lβ and O Kα peak overlap by making use of the superior spectral resolution of PC0. Details of the spectrometers used to measure different elements can be found in Table 3.4.

Table 3.4: Spectrometer information for surface oxygen maps/ surface line profiles on compressor disc

Spectrometer	1	2	3	4	5
Crystal	PC0 (surface map)/ PC1 (surface line profile)	TAP	LPET	PC2	LPET
X-ray line	O Kα	Al Kα	Zr Lα	N Kα	V Kα

Overlapping peaks in the wavelength spectrum can often be identified and accounted for if appropriate standards are available. However, it is generally best to avoid peak overlaps wherever possible, perhaps by selecting a lower intensity but non-overlapping β X-ray line in favour of an α line. This is because overlaps result in increased effective background, and there is also uncertainty associated with solving a peak overlap [192]. In the material being studied, a particularly relevant overlap at both 10 and 15 kV was between Ti Lβ (3 and 4) and O Kα. Despite the Ti lines being less intense β lines, the overlap was still problematic because titanium was the major component of the material.

A standard material containing pure titanium and no oxygen is required to solve the peak overlap in the wavelength spectrum. The peak overlap could be solved by taking a measurement on a pure titanium standard, and subtracting the resulting peak from the combined titanium and oxygen peak in the wavelength spectrum of the compressor disc sample. However, titanium has a very high affinity for oxygen, and so it is challenging to obtain a suitable standard; an appropriate standard could not be sourced for this study due to the presence of an oxide film on all samples on which this was attempted.

Thus, it was not possible to quantify the EPMA-measured oxygen and, as a result, the background-corrected counts have been used, and the oxygen measurements should be regarded as semi-quantitative. This means confidence can be placed in the measurement of relative changes in EPMA-measured oxygen content since the strength of the overlap between titanium and oxygen can be assumed to be constant, but absolute values should not be relied upon. It was possible to pin the EPMA surface oxygen profiles using fully quantified APT measurements.

In the case of the surface oxygen line profiles, background passes were made with a background offset, determined by a wavescan, for each peak position. For each spectrometer, a range of wavelengths either side of the characteristic X-ray of interest were scanned. This enabled checking of the spectrum for any peak overlaps and identification of suitable continuum background wavelengths either side of the central peak. Background correction was performed by subtracting the background signal from the peak spectrum.

Making multiple measurements on the same area increases the carbon deposition and chance of high beam current damage to the sample. Furthermore, the background corrections applied to the line profiles were noted to be small. Therefore, a background measurement was not made for the surface oxygen maps.

Background-corrected X-ray line profiles were acquired on five randomly selected points on the surface of the compressor disc. These profiles were acquired using a 15 keV and 10 nA electron beam. A relatively long dwell time of 0.1 s per pixel was employed to improve the counting statistics. Surface maps were acquired using the same instrument with a 10 keV accelerating voltage, 10 nA beam current and 0.05 s dwell time.

3.5 NANOINDENTATION

3.5.1 Principles

Nanoindentation is a micromechanics technique that uses the interaction between a probing indenter tip and a material of interest to inform about localised material properties on the nanoscale. A known force is applied, and displacement is measured using a capacitance gauge. The determination of mechanical properties from indentation relies on the contact mechanics being well-understood. Oliver, Pharr and Brotzen [194] used data from Sneddon [195] to show that, for axisymmetric tip shapes, the relationship between contact stiffness, contact area and elastic modulus can be described by a simple expression, which is independent of tip geometry

$$\frac{dP}{dh} = \frac{2}{\sqrt{\pi}}\sqrt{A}E_r \qquad \textit{Equation 3.2}$$

where $\frac{dP}{dh}$ is the contact stiffness, A is the contact area and E_r is the reduced elastic modulus (which is necessary when the deformation of the indenter contributes to the measured displacement). Thus, the initial slope of the load-displacement curve during unloading ($\frac{dP}{dh}$) can be used to extract the contact area and elastic modulus. This calculation does not depend on geometry for axisymmetric tips and can be extended to include non-axisymmetric tips, such as the diamond Berkovich tip used in this study, through the multiplication of Equation 3.2 by a geometric factor, β. During an experiment, the indentation depth, *h*, and applied load, *P*, are measured, and then the area of the tip that was in contact during the indentation, *A,* is calculated. *A* is a function of contact depth, h_c, where $h_c = h - \varepsilon \frac{P}{dP/dh}$. The function used to calculate the contact area assumes that the tip is sharp; tip blunting over time can lead to inaccurate contact area calculations. This can be mitigated by regularly calibrating the tip to take into account geometric changes [196]. The contact area, *A*, is used to calculate the hardness, *H*, and modulus, *E*, of the material, using Equation 3.3 and Equation 3.4.

$$H = \frac{P}{A(h)} \qquad \textit{Equation 3.3}$$

$$E = \frac{\sqrt{\pi}}{2} \frac{dP/dh}{A(h)} \qquad \textit{Equation 3.4}$$

An extension to the quasi-static loading-unloading method described above is the continuous stiffness measurement (CSM) method [194,197,198]. By applying a high-frequency dynamic load in addition to the static indentation load, the stiffness can be measured continuously rather than just obtaining a single stiffness measurement when the material is unloaded. This enables the measurement of depth-dependent properties in a single experiment, and the measured stiffness can be used to obtain hardness and modulus as a function of depth.

3.5.2 Experimental details

Nanoindentation was performed on all Ti-7Al + O and Ti-64 +N samples, as well as the TIMETAL 834 compressor disc sample. All samples were ground using 600-4000 grit SiC paper, polished with 3 µm to 1 µm diamond suspension and then polished with colloidal silica solution neutralised with hydrogen peroxide. For the Ti-7Al and Ti-64 samples, arrays of 2 µm deep indents were created within the bulk material. Two indent arrays were made at the surface of the compressor disc, one of ten by five indents, and one of six by six indents. Indents were 250 nm deep to allow for close spacing (4 µm) such that multiple measurements could be made within the oxygen-rich subsurface region without overlapping indent plastic zones. The shallow indent depth also improved sensitivity to the fine microstructural features within TIMETAL 834. A NanoIndenterXP (MTS) was used with a diamond Berkovich indenter. The contact stiffness was continually measured (2 nm amplitude, 50 Hz oscillation) and was used to assess the quality of the indentation data. All indents used in this thesis have a near-linear depth vs load/stiffness, which indicates suitable sample mounting and good contact between tip and surface. Hardness values reported are derived from the CSM data and averaged between depths of 1250-1750 nm and 100-200 nm for the shallow indents.

3.5.2.1 Express indent arrays

An express indent array of area 350 µm by 50 µm was created to produce hardness maps for the material at the surface of the exposed compressor disc. Indents were performed on the Agilent Nano indentor G200 using a diamond Berkovich tip and 200 nm deep indents at a spacing of 1 µm. Further details of the Express indentation mapping can be found in Chapter 7.

3.6 ELECTRON MICROSCOPY BASED TECHNIQUES

EBSD and EDS was carried out using a Zeiss Crossbeam 540 Focussed Ion Beam/ Scanning Electron Microscope (FIB/SEM) instrument equipped with Oxford Instruments XmaxN 150 EDS detector and Oxford Instruments Nordlys Max EBSD detector. A probe current of 15 nA, an aperture size of 120 mm and an accelerating voltage of 30 kV were used for EBSD, while an accelerating voltage of 20 keV was used for EDS. EDS was not used to measure oxygen for reasons outlined in section 3.4, but was useful for mapping segregation of heavier elements on the micron lengthscale. Analysis of EBSD and EDS data was carried out using Oxford Instruments Aztec software.

Multiple EBSD maps were taken of the indents in the bulk compressor disc material, with step sizes of 0.5 µm, and the maps were subsequently stitched. Each indent was defined as having an interaction radius of 2 µm. For each indent that did not interact with a grain/ phase boundary, the orientation of the indented grain was determined. EBSD maps were also taken at the surface of the compressor disc sample and the *lab-controlled* sample, using the conditions described above.

Transmission Kikuchi Diffraction (TKD) was used to identify and select grain boundaries for study with APT. Samples were prepared using the focussed ion beam using the novel technique described by Jenkins et al. [178]. The thinned trapezia were mounted on top of standard Si flat-top coupons in a 45-degree pre-tilt holder, which was then tilted 35 degrees, giving a total tilt angle of 80 degrees. The thinned trapezia were imaged with a beam current of 3 nA and an accelerating voltage of 30 kV at a working distance of 12.5 mm. The TKD image was used to

inform the shaping of the APT tip, using the FIB, so that the grain boundary was located within the top 100 nm of the tip. A second TKD image was taken to confirm the location of the grain boundary in the tip, before the final polishing stage in the FIB. No TKD was performed after the final polishing stage to minimise carbon deposition on the tip before analysis in the atom probe.

4 MAPPING OXYGEN AND NITROGEN WITHIN THE MICROSTRUCTURE OF TITANIUM ALLOYS

4.1 INTRODUCTION

As discussed in section 2.7 of the Literature Review, oxygen and nitrogen can embrittle titanium and its alloys at room temperature [85]. The high diffusivity of both oxygen and nitrogen in titanium, combined with the strong affinity of these interstitial elements for titanium means that native oxide forms on the surface of a titanium component within a matter of hours, and this is accompanied by their diffusion into the surface regions of the material [39,146].

However, oxygen is typically hard to map and quantify within titanium alloys for a number of reasons. As an element with a relatively low atomic mass, oxygen is hard to detect within the microstructure using conventional X-ray spectroscopy techniques, since the lower energy X-rays produced by oxygen are easily absorbed before detection, resulting in low signal. In addition, the relationship between desired spatial resolution and counting statistics is problematic. More details of the challenges facing oxygen quantification by EPMA and EDS are outlined in section 3.2 of the Materials and Methods section. Much of the microstructural change effected by oxygen occurs on the micron or nanometre scale, yet the low energy electron beam required to study fine microstructural features results in low oxygen signal. However, the combined high spatial resolution and chemical sensitivity of APT can overcome these problems by allowing mapping and quantification of oxygen on the nanoscale, with site specific sample preparation being used to map oxygen concentrations over larger area.

The embrittling nature of oxygen is well known [66,79,85] and is of particular concern from an engineering perspective, yet the embrittling mechanisms are not well understood. Mapping the distribution of oxygen within the microstructure can help develop a deeper understanding of the mechanical behaviour of titanium alloy components, allowing assessment of products and processes, and highlighting potential improvements.

4.2 MAPPING OXYGEN AT GRAIN BOUNDARIES

Grain boundaries play a critical role in controlling the mechanical properties of a wide range of polycrystalline materials [199,200]. In particular, segregation of species to grain boundaries can have a beneficial or detrimental effect on fracture toughness and yield strength. This idea can be exploited through grain boundary segregation engineering [201]. Thus, mapping segregation at grain boundaries is a crucial step to enable a full understanding of the mechanical response of a material.

Transmission Kikuchi diffraction (TKD) was used in conjunction with APT to identify, position, and characterise α / α grain boundaries in the model alloy Ti-7Al, as described in section 3.6 of the Materials and Methods section. APT was used for mapping to allow quantification of oxygen on the nanoscale.

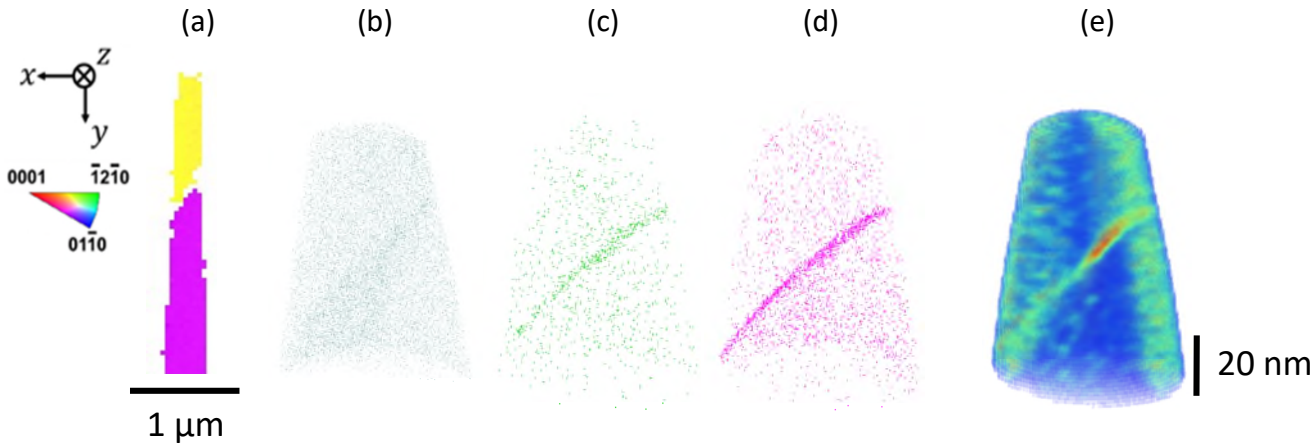


Figure 4.1 (a) TKD map of Ti-7Al + 2500 wppm O sample that contains a grain boundary. Atom map showing the segregation of (b) TiO ions (c) Ni and (d) Fe to a grain boundary. (e) Density map showing an increase in density at a grain boundary, at the same location as the segregation.

Figure 4.1 (a) shows a TKD map of an α / α boundary contained within an APT needle. The FIB was subsequently used to polish the needle such that the boundary was positioned in the top 100 nm of the APT needle-shaped specimen. The boundary was characterised, as described by Jenkins et al. [202], as having a misorientation angle of 51.7°, with a grain boundary rotation axis of

[2 3 $\bar{5}$ $\bar{8}$], and the grain boundary normals in each of the grains on either side of the boundary were found to be (10 8 $\overline{18}$ 1) and ($\bar{5}$ 5 0 6). These directions are very close to the (1 1 $\bar{2}$ 0) and ($\bar{1}$ 1 0 1) directions, respectively.

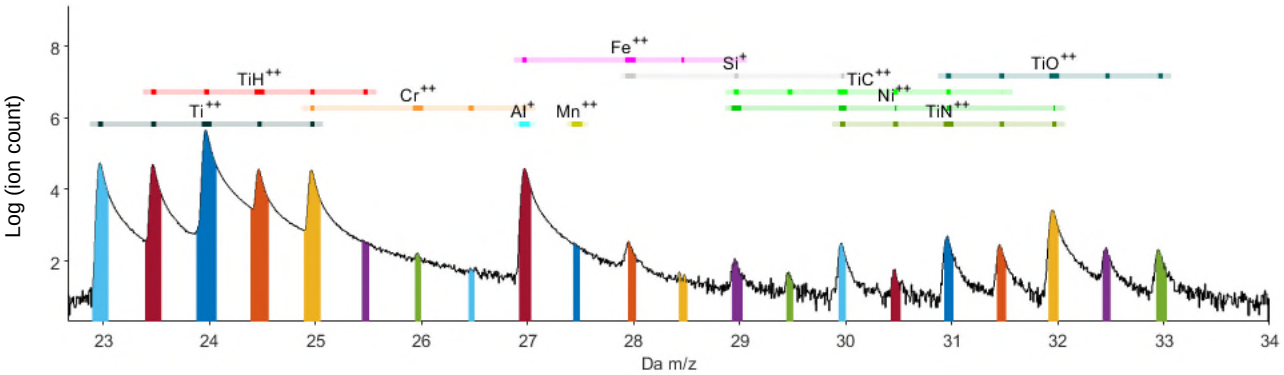


Figure 4.2: Section of mass spectrum showing the overlaps involving iron and nickel.

The atom map in Figure 4.1 (b) shows some inhomogeneity in the distribution of TiO ions. Segregation of nickel and iron to the boundary can be seen clearly in the atom maps in Figure 4.1 (c) and (d). The fast diffusion rate of β eutectoid elements, such as Ni and Fe [203–205], means they are likely to segregate to grain boundaries from the recrystallizing α phase. However, this is the first time that this has been observed experimentally.

Mass spectrum peak overlaps involving TiO++ and TiO+ ions occur in the range 31-32 Da and 62-64 Da, respectively. Overlaps involving iron and nickel occur in the range 23-33 Da, which can be seen in Figure 4.2 along with the TiO++ overlap. Solving these mass spectrum overlaps enabled each mass spectrum peak to be labelled as the dominant species contributing to that peak. The ions displayed in (b) and (c) result from identifying Fe++ as the dominant species contributing to the peak at 28 and 28.5 Da, Ni++ as the dominant species contributing to the peak at 29 Da, TiO++ as the dominant species at 31, 31.5, 32, 62, 63 and 64 Da.

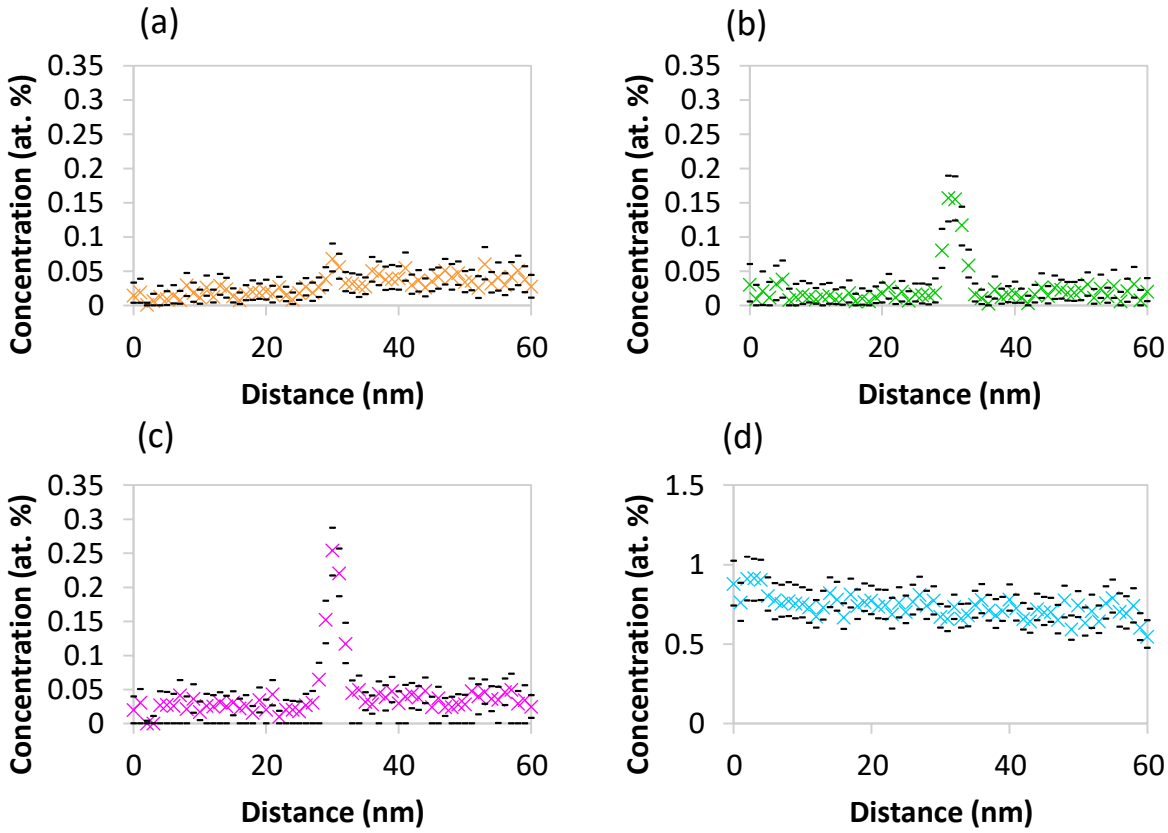


Figure 4.3: Mass spectrum peak overlap-solved 1D-concentration profiles across the grain boundary showing concentration of (a) Cr, (b) Ni, (c) Fe, (d) O.

To quantify the change in concentration of species across the boundary, line concentration profiles were created, in which the mass spectrum overlaps were solved on a bin-by-bin basis. These can be found in Figure 4.3 along with 95% confidence intervals, determined using the method reported in [184]. It can be seen from Figure 4.3 that oxygen does not segregate to the grain boundary, while Cr segregation occurs in addition to Fe and Ni at this grain boundary. The same segregation behaviour was observed in APT analysis of a second α - α grain boundary.

4.3 OXYGEN AND THE α_2 PHASE

Understanding the location of oxygen within the quenched Ti-7Al model alloy, as described above, is a first step to mapping oxygen within the microstructure of titanium aerospace alloys. After

quenching, samples of the model alloy were then aged for 10 days and 49 days at 550°C to form α_2 precipitates, adding another layer of complexity.

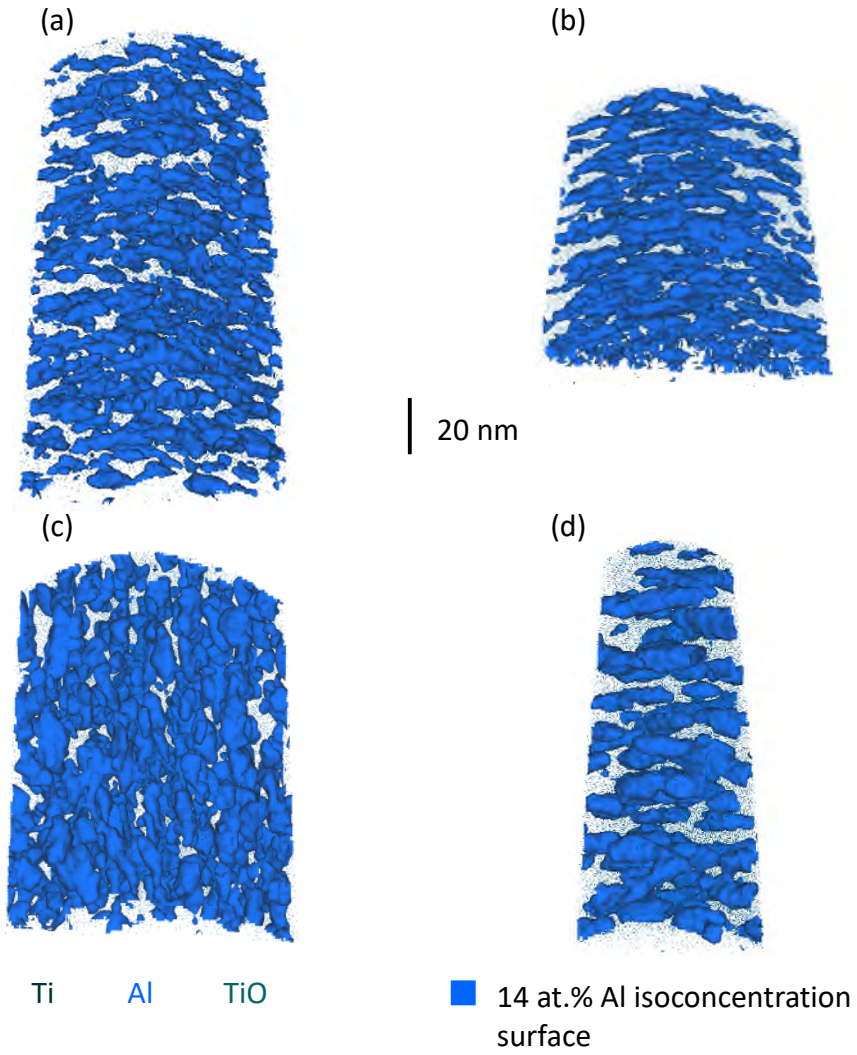


Figure 4.4: APT atom maps with 14 at.% Al isoconcentration surfaces highlighting α_2 precipitates in (a) Ti-7Al + 500 wppm O, 10 day aged, (b) Ti-7Al + 500 wppm O, 49 day aged, (c) Ti-7Al + 2500 wppm O, 10 day aged and (d) Ti-7Al + 2500 wppm O, 49 day aged. All samples aged at 550°C.

APT reconstructions for each of the aged samples in the Ti-7Al+O series are displayed in Figure 4.4; precipitates were found in these aged samples only. The Ti-Al binary phase diagram [49] does not predict the formation of α_2 for Ti-7Al at 550°C, but the effect of oxygen on the $\alpha/\ \alpha + \alpha_2$ boundary must not be neglected. It is known that oxygen reduces the solubility of aluminium in α-Ti, causing the $\alpha/\ \alpha + \alpha_2$ boundary to shift to lower aluminium concentrations [79,111,206–208]. This can be seen more clearly from the Ti-Al-O ternary phase diagram in Figure 4.5, which predicts formation of

α_2 in Ti-7Al with both 500 wppm O and 2500 wppm O. Comparison of the binary and ternary phase diagram emphasises that both ageing and the addition of oxygen are required to form α_2 in Ti-7Al.

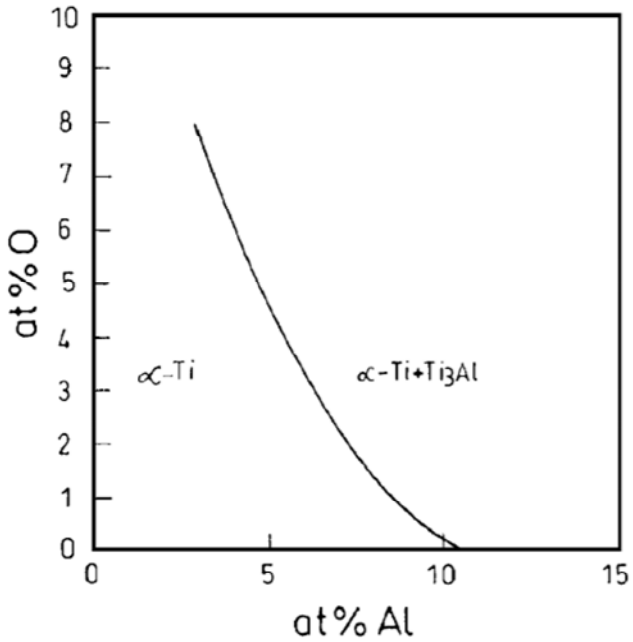


Figure 4.5: Calculated isothermal section (Ti rich regions) of the Ti-Al-O ternary system at 500 °C [67].

Aluminium isoconcentration surfaces were generated within the reconstructed APT data to identify the α_2 precipitates. The level of aluminium concentration defining such surfaces was selected using an approach previously developed by Homma et al. [188]. Ions contained within the chosen isoconcentration surface were then extracted as precipitates. The concentration of the extracted precipitates was calculated using a MATLAB mass spectrum peak deconvolution tool [182]. Precipitate volume fraction was calculated, using the Lever rule [209], from precipitate, matrix and bulk APT-measured compositions.

Proximity histograms [179] were created from the aluminium isoconcentration surfaces to track changes in composition across the precipitate-matrix interface, using custom Matlab code to solve peak overlaps on a bin-by-bin basis [184]. The APT atom maps show that the precipitates formed upon ageing are rich in aluminium, and precipitate compositions are reported in Table 4.1. The composition of aluminium in the α_2 precipitates lies within the region of the ternary phase diagram where $\alpha + \alpha_2$ two-phase field is stable [210]. Considering the precipitate composition in conjunction

with the fact that the Ti-7Al was aged within the α_2 region of the TTT curve [104] provides confidence that the precipitates formed upon ageing are α_2.

Table 4.1: APT-measured concentrations of bulk, precipitates and matrix in each of the Ti-7Al + 500 wppm O and Ti-7Al + 2500 wppm O samples.

	Ti-7Al + 500 wppm O							Ti-7Al + 2500 wppm O						
Element	IWQ	10 day			49 day			IWQ	10 day			49 day		
	Bulk (at. %)	Bulk	α_2	α	Bulk	α_2	α	Bulk	Bulk	α_2	α	Bulk	α_2	α
Al	9.35	9.97	16.04	9.32	10.16	14.75	8.98	10.60	10.17	16.58	9.64	9.40	15.27	8.15
Ti	90.05	89.49	83.42	90.14	89.32	84.75	90.49	88.25	88.71	82.43	89.23	88.79	83.14	90.02
O	0.19	0.16	0.13	0.16	0.18	0.15	0.18	0.69	0.72	0.58	0.74	1.12	0.86	1.17
N	0.05	0.02	0.02	0.02	0.04	0.04	0.04	0.06	0.06	0.06	0.06	0.08	0.08	0.08

Proximity histograms across the precipitate-matrix interfaces in the aged Ti-7Al reveal that oxygen partitions away from the precipitates to the matrix for both oxygen contents and at all ageing times, as can be seen in Figure 4.6. While oxygen has been observed to partition to the α_2 phase in titanium aluminide ($\gamma+\alpha_2$) alloys [109], Figure 4.6 indicates that the partitioning preference switches for the $\alpha+\alpha_2$ alloy systems that are found at the lower aluminium end of the Ti-Al phase diagram. It is possible that mechanical property changes that have been previously attributed to microstructure, including microstructural length scale, morphology and crystallography, may actually be driven by chemistry and nanoscale features.

α_2

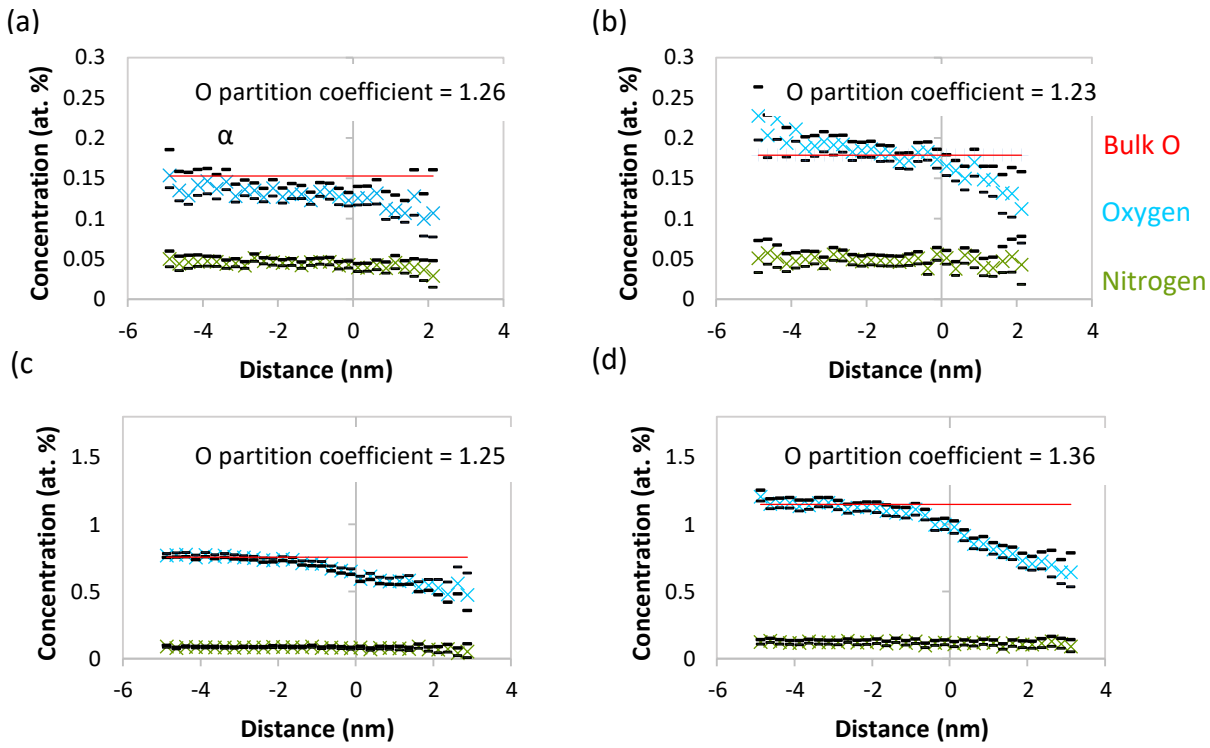


Figure 4.6: Proximity histograms showing oxygen and nitrogen concentration across the α/ α_2 interface in (a) Ti-7Al + 500 wppm O, 10 day aged, (b) Ti-7Al + 500 wppm O, 49 day aged, (c) Ti-7Al + 2500 wppm O, 10 day aged and (d) Ti-7Al + 2500 wppm O, 49 day aged.

Despite oxygen partitioning away from the α_2 phase, it is important to note that oxygen actually promotes α_2 formation. For example, the α_2 volume fractions in Figure 4.7 (a) are consistent with the trend of increasing volume fraction with increasing oxygen content reported in the literature for other low aluminium Ti-alloys [18,104].

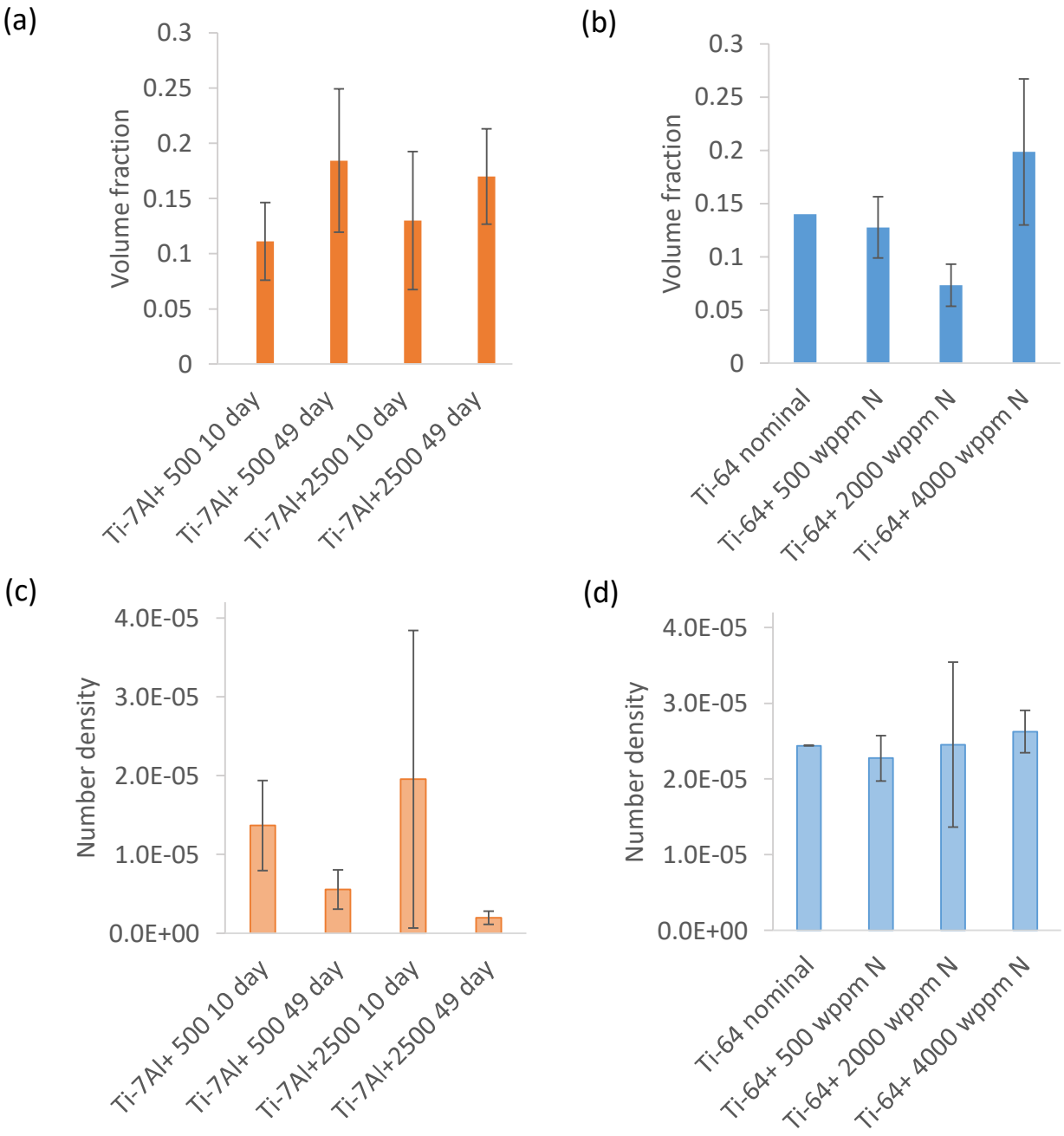


Figure 4.7: Plot of (a) precipitate volume fraction and (c) precipitate number density as a function of oxygen content in Ti-7Al, and (b) precipitate volume fraction and (d) precipitate number density as a function of nitrogen content in Ti-64. Precipitate number density is defined as the number of precipitates in the dataset divided by the total number of ions in the dataset.

The small volume of material analysed (of the order of $1x10^{-28}$ m^3 per APT sample) may explain the large standard deviations associated with the measurements. The average α_2 volume fraction in the Ti-7Al + 500 wppm O, 49 day aged sample appears particularly high. The significant scatter in the data contributing to this point could be due to an unknown additional factor, such as increased

density of nucleation centres due to lattice defects, increasing α_2 volume fraction. Nevertheless, the broad trend of increasing α_2 volume fraction with oxygen content agrees with previous observations [18,104] that oxygen encourages α_2 formation.

Figure 4.7 (c) shows that increased oxygen content increases precipitate number density for the 10 day aged samples, but that in the 49 day aged samples, precipitate number density decreases with increased oxygen content. Again, the error bars are large, especially for the Ti-7Al + 2500 wppm O, 10 day aged sample, so trends here should be interpreted with caution. It should be noted that only two samples contributed to this measurement; further data would help identify any possible outliers.

4.4 MAPPING NITROGEN

The commercially available alloy Ti-64 was selected to study the role of nitrogen in titanium alloys. This material is widely used in jet engines to make fan blades, amongst other components.

Table 4.2: APT-measured concentrations of bulk, precipitates and matrix in the Ti-64 as-received sample and each of the Ti-64 aged samples.

Element	As-received	Nominal N, 49 day aged			500 wppm N, 49 day aged			2000 wppm N, 49 day aged			4000 wppm N, 49 day aged		
	Bulk (at.%)	Bulk	α_2	α	Bulk	α_2	α	Bulk	α_2	α	Bulk	α_2	α
Al	10.5	12.0	17.5	11.1	10.7	16.7	9.8	10.9	17.9	10.6	11.1	15.4	10.1
Ti	83.1	84.3	79.1	85.1	80.3	75.0	81.0	82.7	76.6	83.0	80.8	77.4	81.7
O	0.67	0.74	0.59	0.77	2.3	1.8	2.3	0.94	0.73	0.95	0.73	0.61	0.76
V	4.47	2.10	1.88	2.15	2.19	1.94	2.22	2.00	1.75	2.02	2.01	1.85	2.05
N	0.08	0.03	0.02	0.03	0.11	0.11	0.11	0.55	0.48	0.55	0.72	0.64	0.73

APT atoms maps for the aged samples are shown in Figure 4.8; it can be seen that α_2 precipitates form at all levels of nitrogen concentration during ageing. In general, the partitioning trends of nitrogen in Figure 4.9 are less clear than that of oxygen in Figure 4.6. However, the partition coefficients displayed Figure 4.9 are all greater than 1 showing that, in all cases, nitrogen does

partition preferentially to the matrix. The partitioning of nitrogen is most clearly seen in Figure 4.9 (c) for the sample containing 2000 wppm N.

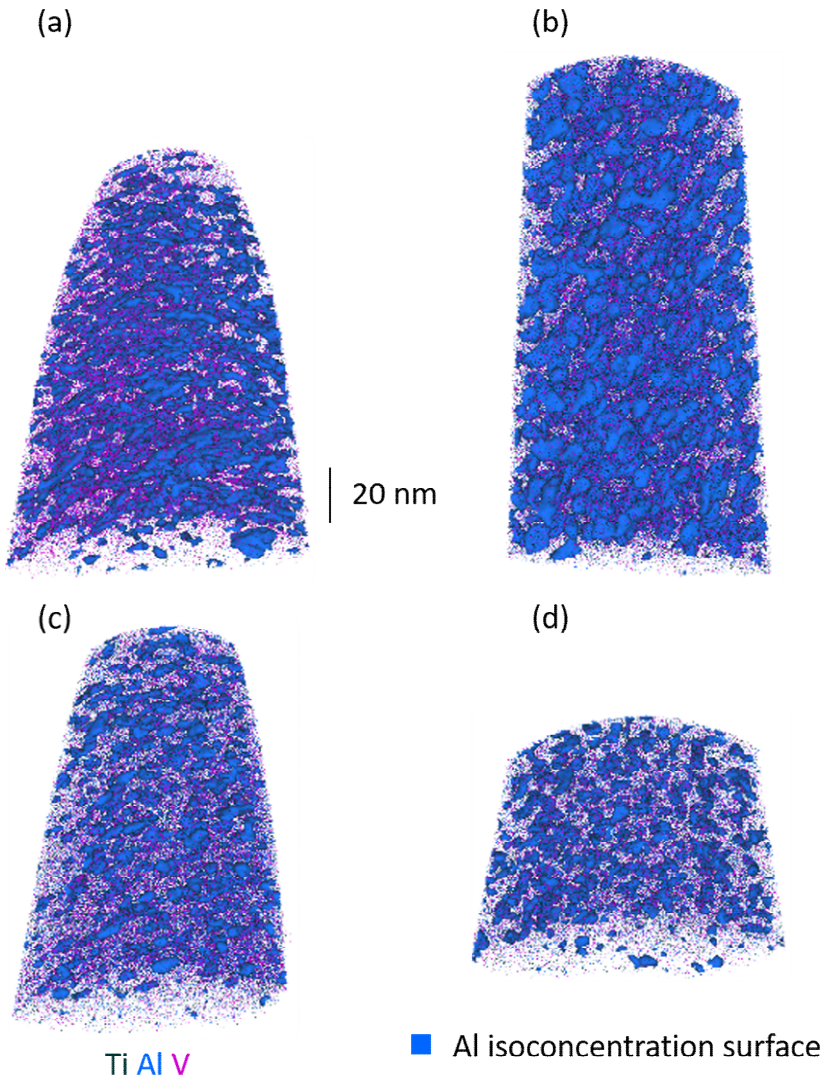


Figure 4.8: APT atom maps with Al isoconcentration surfaces highlighting α_2 precipitates in (a) Ti-64 + nominal N, (b) Ti-64 + 500 wppm N, (c) Ti-64 + 2000 wppm N and (d) Ti-64 + 4000 wppm N, all aged for 49 days at 550°C.

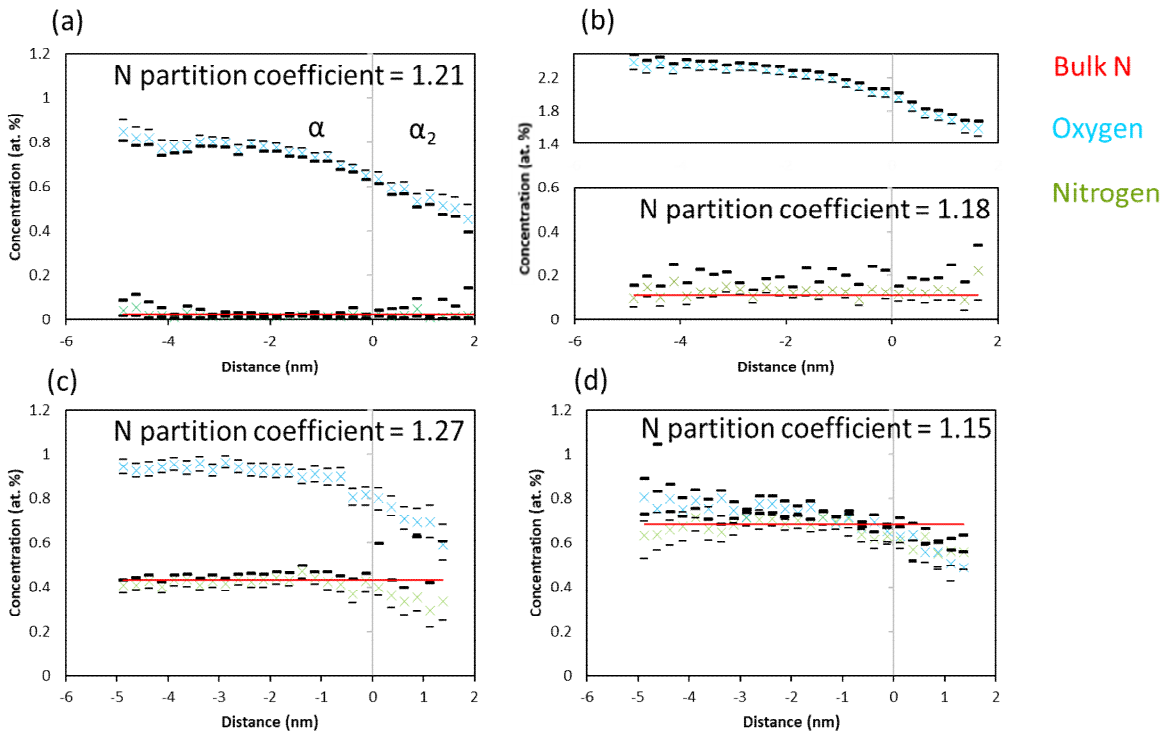


Figure 4.9: Proximity histograms showing oxygen and nitrogen concentration across the α/ α_2 interface in (a) Ti-64 + nominal N, (b) Ti-64 + 500 wppm N, (c) Ti-64 + 2000 wppm N and (d) Ti-64 + 4000 wppm N, all aged for 49 days at 550°C.

Figure 4.7 (b) shows that the α_2 precipitate volume fraction does not depend strongly on nitrogen content. The volume fraction in the sample containing 2000 wppm N is low. The reason for this is unclear. Looking at Table 4.2, we can see that the bulk composition of vanadium and oxygen in the Ti-64 + 2000 wppm N sample is not significantly different to the other samples, and that the nitrogen value is close to the nominal value. It is possible that unseen microstructural features, such as dislocations or grain boundaries, outside the small APT sample volume are providing preferential sites for α_2 formation. The precipitate number density in Figure 4.7 (d) is also independent of nitrogen content.

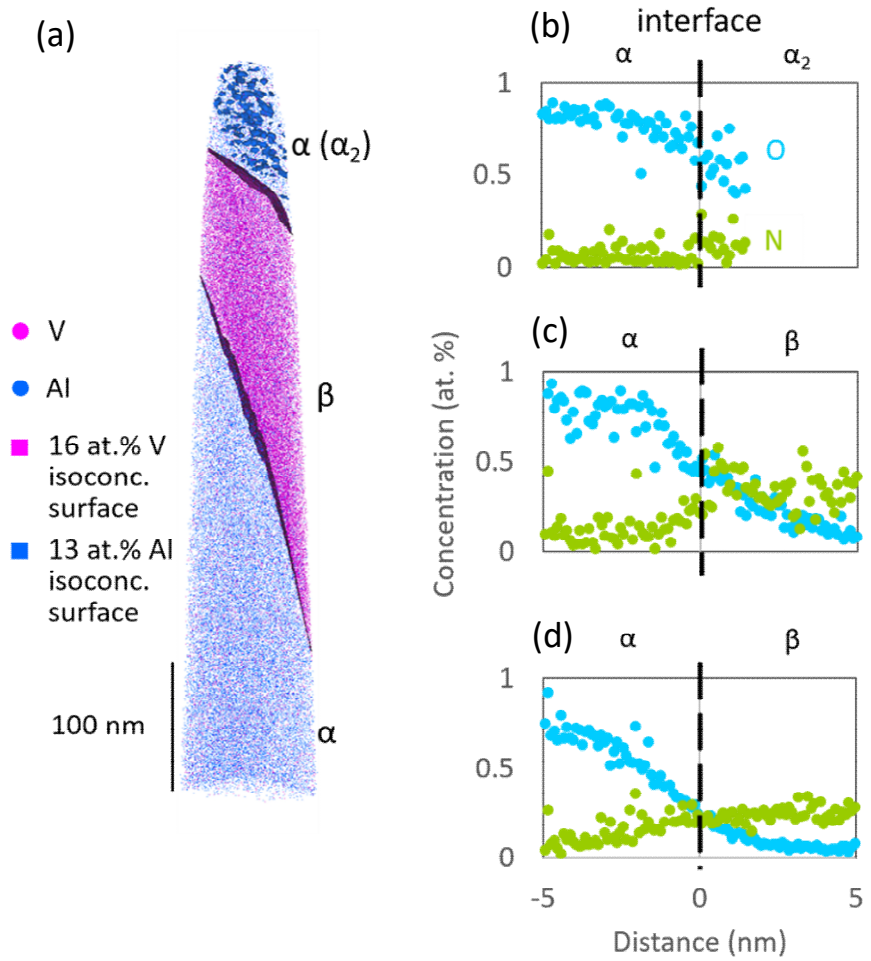


Figure 4.10: (a) APT atom map showing a sample of Ti-64 containing a β grain between two α grains. The uppermost α grain contains α_2 precipitates, highlighted by a dark blue 13 at.% isoconcentration surface, whereas the lower α grain does not. Proximity histograms showing oxygen and nitrogen concentration across the (b) α/ α_2 interface, (c) uppermost α / β interface and (d) lower α / β interface.

Oxygen and nitrogen both partition away from the α_2 phase. In Figure 4.10, the behaviour of oxygen and nitrogen is mapped on a wider length scale. It can be seen that oxygen partitions to the α phase, in agreement with literature reports. However, nitrogen shows the opposite partitioning behaviour, and partitions to the β phase. This is surprising given that nitrogen is usually reported as an α stabiliser [85]. The behaviour of nitrogen across α - β interfaces in other samples of Ti-64, with different levels of nitrogen, is shown in Figure 4.11.

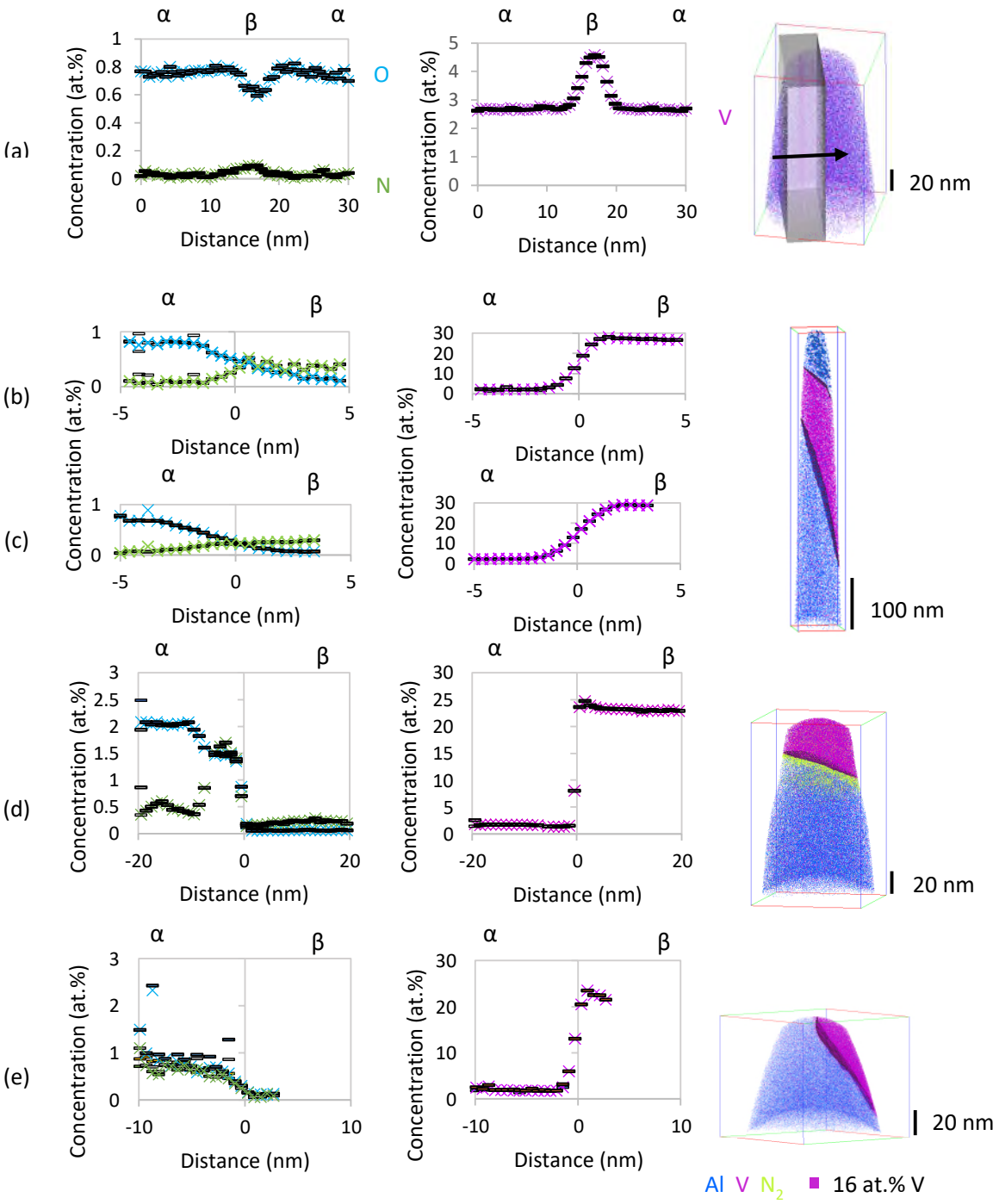


Figure 4.11: (a) Line profiles and APT atom maps across a vanadium-rich region in Ti-64, as-received material. The box on the atom map shows the region from which the line profile was calculated and the arrow shows the direction in which the line profile was measured. Proximity histograms across α - β interfaces in (b) Ti-64 nominal N, 49 day aged (small interface), (c) Ti-64 nominal N, 49 day aged (large interface), (d) Ti-64 + 500 wppm N, 49 day aged and (e) Ti-64 + 4000 wppm N, 49 day aged.

It can be seen in Figure 4.11 (a) and (b)/ (c) that for the unaged and aged sample with nominal (~70 wppm) nitrogen, nitrogen partitions to the vanadium-rich regions. However, for the aged samples containing 500 wppm N and 4000 wppm N in Figure 4.11 (d) and (e), the nitrogen partitions ahead of the interface and to the α phase, respectively.

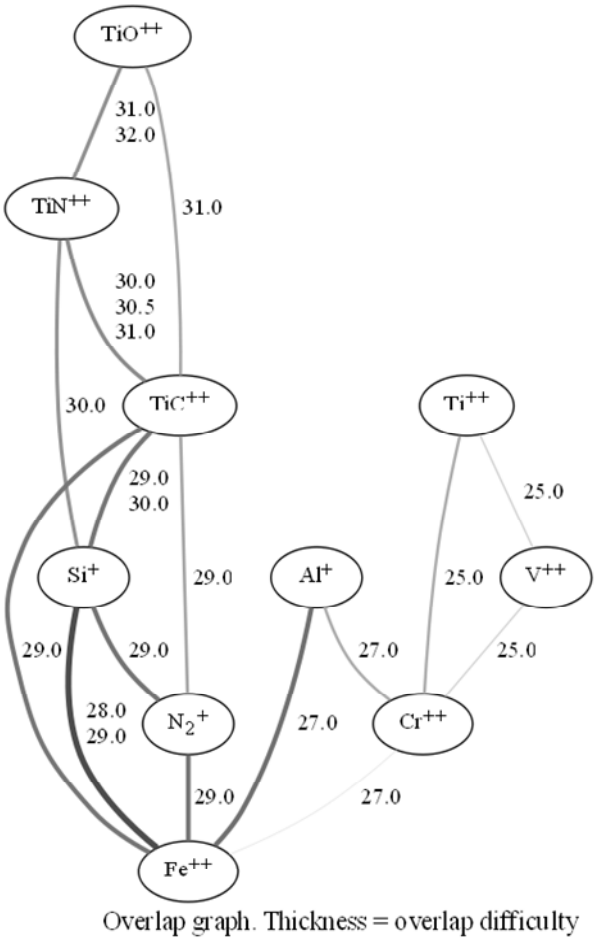


Figure 4.12: Schematic of the overlapping species in the section of the mass spectrum for Ti-64 nominal N, as-received, between 24 and 33 Da. Lines represent a mass spectrum peak overlap, and the number on the line represents the Da value at which it occurs.

There is a mass spectrum overlap between Fe++, Si+ and N_2+, which is drawn schematically in Figure 4.12. However, the mass spectrum peak overlaps contributing to the proximity histograms reported in Figure 4.10 (c) and (d) have been solved, as described in section 3.3.4 of the Materials and Methods chapter. Thus, the overlap-solved concentration profiles and proximity histograms in Figure 4.10 and Figure 4.11 can be considered a good measurement of the behaviour of nitrogen across the α - β interfaces.

4.5 DISCUSSION

4.5.1 Segregation at $\alpha - \alpha$ grain boundaries

When interpreting the experimental results presented in section 4.2, it is useful to consider the underpinning theory. DFT calculations predict attraction of oxygen to symmetric twin boundaries, owing to the symmetry of the octahedral voids at this type of boundary which make it favourable for oxygen to segregate there. However, DFT predicts repulsion of oxygen from general, non-symmetrical grain boundaries since the lower symmetry voids make segregation at these boundaries less favourable [211,212].

The high aluminium content (7 wt.%) of the Ti-7Al alloy used in this study means that twinning is suppressed [39]. Common HCP twin boundary types include $(\bar{1}012)$, $(\bar{1}011)$, $(\bar{2}112)$ and $(\bar{2}111)$. The grain boundary in Figure 4.1 has been characterised as having a rotation axis of $[2\ 3\ \bar{5}\ \bar{8}]$, which is not close to any of the common twin boundary planes. In addition, the grain boundary normal in each of the grains on either side of the boundary are not equivalent. All of this suggests the boundary imaged is non-symmetrical. Thus the APT findings in Figure 4.3 experimentally confirm the theoretical calculations of Aksyonov [213], Ghazisaeidi [212] and Semenova [172], supporting the DFT calculations that suggest oxygen does not segregate to non-symmetrical boundaries. Furthermore, the APT shows that it is favourable for iron and nickel to segregate to non-symmetrical boundaries, in line with DFT calculations by Aksyonov et al. [214] that predict segregation of iron at grain boundaries in CP-Ti. This reduces the grain boundary energy, leading to higher thermal stability of CP-Ti containing iron [214].

4.5.2 Role of oxygen in the formation of the α_2 phase

When considered in the context of the current literature, the findings in section 4.3 point towards a difference in oxygen partitioning behaviour with respect to α_2 in the $\alpha + \alpha_2$ system compared to the the $\gamma + \alpha_2$ system. For high aluminium concentrations (greater than ~ 37 at.% Al) the $\gamma + \alpha_2$ system is stable whereas at lower aluminium concentrations, the $\alpha + \alpha_2$ system is stable. The solubility limit of

oxygen is highest in the α phase at ~34 at.% [49], dropping to 10-14 at.% in the α_2 phase [94,215] and ~800 at. ppm in the γ phase [95]. Oxygen prefers to occupy octahedral interstitial sites that are surrounded by titanium atoms, known as [OTi6] sites, which can be seen in Figure 4.13 [80,94–97].

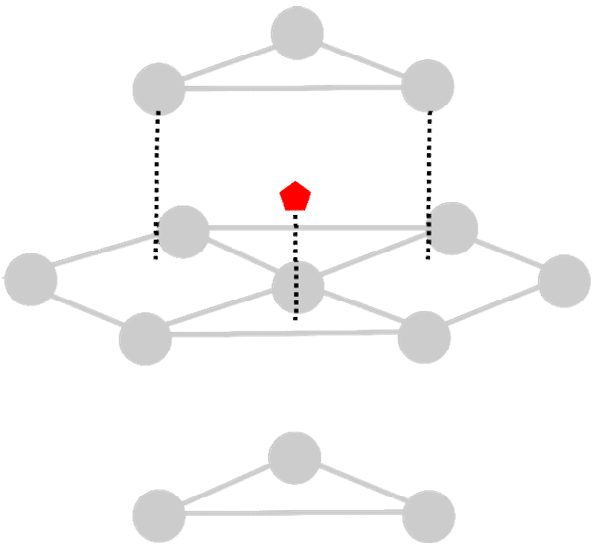


Figure 4.13: Diagram showing the location of the octahedral interstitial site (red pentagon) within the hexagonal close packed structure of α-Ti [97].

Consideration of the number of [OTi6] sites present in each phase can explain the difference in solubility between the γ, α_2 and α phases. One [OTi6] site exists per atom in the α phase. However, there is only one [OTi6] site per every four atoms in the α_2 phase because, unlike in the α phase, α_2 substitutional sites are not all equivalent due to chemical ordering [95]. Substitution of excess aluminium on the α_2 titanium sites further reduces the number of [OTi6] sites [94]. Oxygen has been observed to fill more interstitial sites than the 50% occupancy that gives rise to maximum configurational entropy, yet fills fewer than the total predicted number of available interstitial sites [94]. This suggests that, as oxygen concentration in the α_2 phase increases, interaction between the interstitial atoms leads to ordering of oxygen on the interstitial sites, reducing the number of filled [OTi6] sites and limiting the solubility of oxygen in the α_2 phase [94]. For γ phase of equiatomic composition, no [OTi6] sites exist, but with weak titanium excess, a few are present; hence, the solubility limit of oxygen in the γ phase is meagre. In the high aluminium γ + α_2 system, oxygen is much more soluble in the α_2 phase than the γ phase and therefore partitions to the α_2. In contrast, in

the α + α_2 system, oxygen solubility is higher in the α phase and so oxygen partitions away from the α_2. This is despite the α_2 [OTi6] sites being slightly larger than in α [108]; the effect of the higher number of [OTi6] sites in α outweighs the impact of the [OTi6] site size. Thus, the difference in solubility of oxygen in the phases present is the driving force for oxygen partitioning.

Jones et al. [94] suggest that occupation of interstitial sites by oxygen also forces non-random occupation of the titanium sites by excess aluminium atoms; dissolved oxygen encourages ordering of excess aluminium. Furthermore, Ti-Al and Ti-Ti bonds aligned close to the c-axis direction are weakened as oxygen content is increased [94].

In light of this, a possible mechanism outlining how oxygen promotes α_2 formation can be proposed. As oxygen is added to the α phase, it is possible that local aluminium clustering and oxygen-induced ordering of aluminium occurs. Aluminium clustering maximises oxygen solubility by increasing the number of [OTi6] sites, and aluminium ordering increases stability of the system. This, aided by the weakening of the existing Ti-Al and Ti-Ti bonds by the increased oxygen content, leads to formation of the α_2 phase. Thus, oxygen reduces the solubility of aluminium in α-Ti, in line with the ternary Ti-Al-O phase diagram. However, the oxygen is still more soluble in the α phase than the α_2 phase, and so oxygen partitions to the α phase, away from the α_2 phase. The proposed mechanism is consistent with the conditional spinodal mechanism for α_2 formation proposed by Wood et al. [116]. The result in section 4.5.1 of this thesis that oxygen does not partition to the imaged α-α boundary also support the proposed mechanism, since it supports the idea that availability of interstitial sites in the α phase is the dominant factor driving the behaviour of oxygen. Further work is required to verify the proposed mechanism. For example, measurement of the number of [OTi6] sites as a function of oxygen content for α+α_2 alloy systems could be carried out using neutron diffraction. Use of resonant ultrasound spectroscopy to determine oxygen site occupancy could also be explored.

4.5.3 Comparison of the behaviour of oxygen and nitrogen with respect to α_2

Like oxygen, nitrogen is also known to occupy the octahedral interstitial sites of titanium alloys [97]. Therefore, the partitioning of nitrogen away from the α_2 phase to the α phase suggests that nitrogen also prefers to occupy octahedral interstitial sites surrounded by titanium atoms ([NTi6] sites), since there are a greater number of [NTi6] sites available in the α phase compared to the α_2 phase. Thus, it seems possible that nitrogen could promote α_2 formation by the same mechanism as described for oxygen in section 4.5.2.

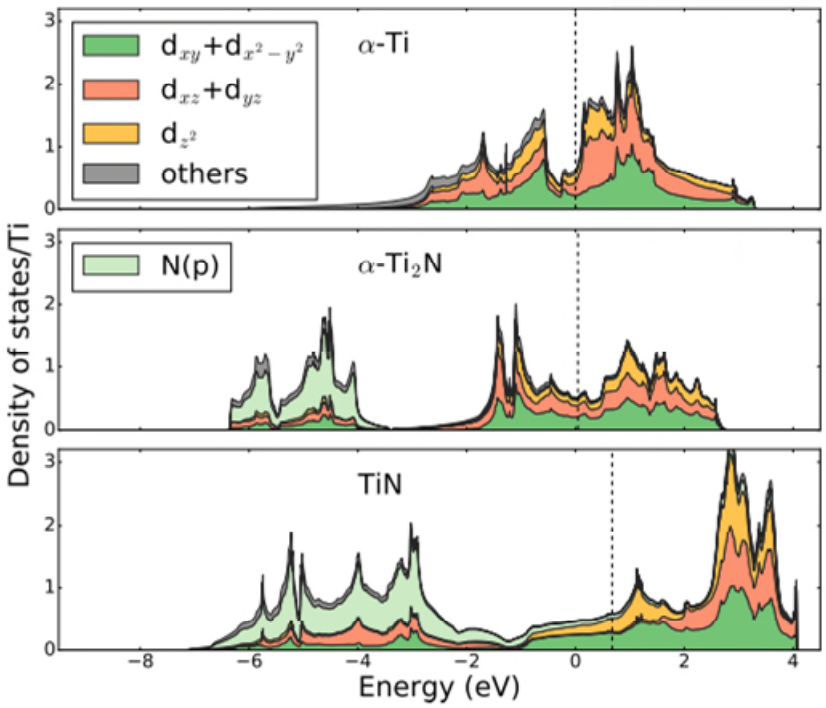


Figure 4.14: Projected density of states of α-Ti, the α-Ti_2N ground state, and metastable HCP TiN, reproduced from [98].

The weaker partitioning of nitrogen away from α_2 compared to oxygen may be explained by considering electronic structure. Insertion of interstitial elements into the octahedral sites of α-Ti introduces p states below the Fermi level in the density of states diagram, as can be seen in Figure 4.14. The p states of nitrogen are at a higher energy level than oxygen owing to the lower nuclear charge of nitrogen [98]. Thus, the thermodynamic driving force to occupy octahedral interstitial sites in α-Ti is lesser for nitrogen than for oxygen. This means that the difference in the number of

available [XTi6] sites between the α and α_2 phase is of less importance for nitrogen than oxygen. This could contribute to the observed weaker partitioning behaviour of nitrogen compared to oxygen.

Comparison of Figure 4.7 (c) and (d) shows that oxygen affects the number density of α_2 precipitates, whereas nitrogen does not. This could again be related to the fact that it is more favourable for oxygen to occupy the octahedral interstitial sites than nitrogen. Thus, according to the mechanism proposed in section 4.5.2, the presence of oxygen will provide a stronger driving force for clustering of Al in order to maximise the number of [OTi6] octahedral sites.

4.5.4 Partitioning behaviour of nitrogen with respect to β phase

Figure 4.11 shows that nitrogen sometimes partitions to the β phase, and not always to the α phase as previously thought [85,216]. In Figure 4.11 (a), (b) and (c), nitrogen is clearly seen to partition to the same location as the vanadium.

When considering the behaviour of nitrogen in BCC vanadium metal, we find that nitrogen is most stable in the octahedral interstitial sites. The binding of nitrogen located on the octahedral interstitial site of vanadium metal is very strong; -2.55 eV/ atom [217]. However, it is weakened by the presence of Mo [217], so it is possible that the binding energy of nitrogen in the β phase is lowered by the presence of multiple alloying elements. As an approximate comparison, the formation energy of a nitrogen atom located at an octahedral interstitial site in HCP Ti is -1.789 eV/ supercell [96], which is much less favourable than the vanadium octahedral interstitial site.

Location of nitrogen at the vanadium octahedral interstitial site causes displacement and distortion of the surrounding lattice, meaning occupation of nearby interstitial sites by additional nitrogen atoms is not favourable [217]. This suggests that the solubility limit of nitrogen in BCC vanadium is controlled, at least in part, by the number of octahedral interstitial sites available.

A potential mechanism to explain the changing partitioning behaviour of nitrogen with respect to the β phase is proposed below. It is possible that, at relatively low nitrogen concentrations, nitrogen

occupies the octahedral interstitial sites in the BCC β phase, owing to the favourable binding energy of nitrogen and vanadium. However, the resulting lattice distortion means the solubility of nitrogen in the β phase is low. Thus, at higher nitrogen concentrations (Figure 4.11 suggests between ~70 wppm and 500 wppm), nitrogen is no longer soluble in the β phase, and so partitions to the α phase instead.

4.6 CONCLUSIONS

Oxygen and nitrogen have been mapped within the microstructure of Ti-7Al and Ti-64. Oxygen has not been observed to segregate to α-α grain boundaries, but nickel and iron have increased in concentration at the boundary by five times and ten times the bulk concentration, respectively, in agreement with DFT predictions. Volume fraction measurements confirm that oxygen promotes α_2 formation. Use of APT to map oxygen partitioning across the α – α_2 phase boundary reveals oxygen partitions away from the α_2 phase, despite encouraging its formation. This has led to proposal of a mechanism for α_2 formation. Further work on the level of oxygen needed to form aluminium clusters in the α matrix would help confirm and clarify the mechanism of formation.

Nitrogen has also been shown to partition away from the α_2 phase, although volume fraction measurements suggest that the role of nitrogen in promoting α_2 formation is less significant than that of oxygen. APT-mapping of nitrogen across the α - β phase boundary in Ti-64 shows that for low nitrogen concentrations, nitrogen partitions to the β phase and thus shows opposing behaviour to oxygen, which partitions to the α phase.

5 CHARACTERISATION OF THE α_2 PHASE AND ITS EFFECT ON MECHANICAL PROPERTIES

5.1 INTRODUCTION

As discussed in Chapter 4, interstitial elements prefer to reside in the octahedral interstitial sites in α-Ti [218]. Occupation of the octahedral interstitial sites by oxygen or nitrogen results in a greater change in lattice strain in the c-axis compared to the a-axis, increasing the c/a ratio [93]. However, as discussed in section 2.7.2.1 of the Literature Review, Yu et al. [99] report that elastic interactions between the lattice strains of interstitial atoms and lattice strains of dislocations is not the dominant hardening mechanism. Rather, interstitial solid solution hardening originates from strong interactions between interstitial solutes and the core of screw dislocations [99].

Whilst interstitial hardening can occur at both room temperature and higher temperatures, other hardening mechanisms are also activated at raised temperatures. One such mechanism is hardening and embrittlement through α_2 formation, which is encouraged by the presence of oxygen [18].

During service, Ti-64 fan blades remain at low temperatures since the air drawn into the engine by the fan blades acts to cool them. This means that α_2 formation in fan blades during service is unlikely. However, fan blades are processed at temperatures close to 700°C for a combined age and stress relief treatment. In this temperature regime, α_2 precipitates can form. Thus, there is a possibility of α_2 precipitates being present in *in-service* engine components, encouraging strain localisation and making the alloy more susceptible to low cycle fatigue, notch high cycle fatigue and cold dwell fatigue [60]. Consequently, it is important to understand the evolution of the precipitates during ageing, and their effect on mechanical properties.

5.2 CHARACTERISATION OF THE α_2 PHASE

The work in Chapter 4 shows that oxygen encourages α_2 formation, as evidenced by the general trend of a greater volume fraction of α_2 as oxygen is added, and that nitrogen appears to have a less

significant effect on encouraging α_2 formation. The composition and morphology of the α_2 precipitates, and their effect on mechanical properties, will be studied in this Chapter.

5.2.1 Composition

The ratio of titanium to aluminium in the α_2 precipitates, shown in Figure 5.1, remains constant as a function of ageing time and nominal oxygen/ nitrogen concentration in both the Ti-7Al and Ti-64 material.

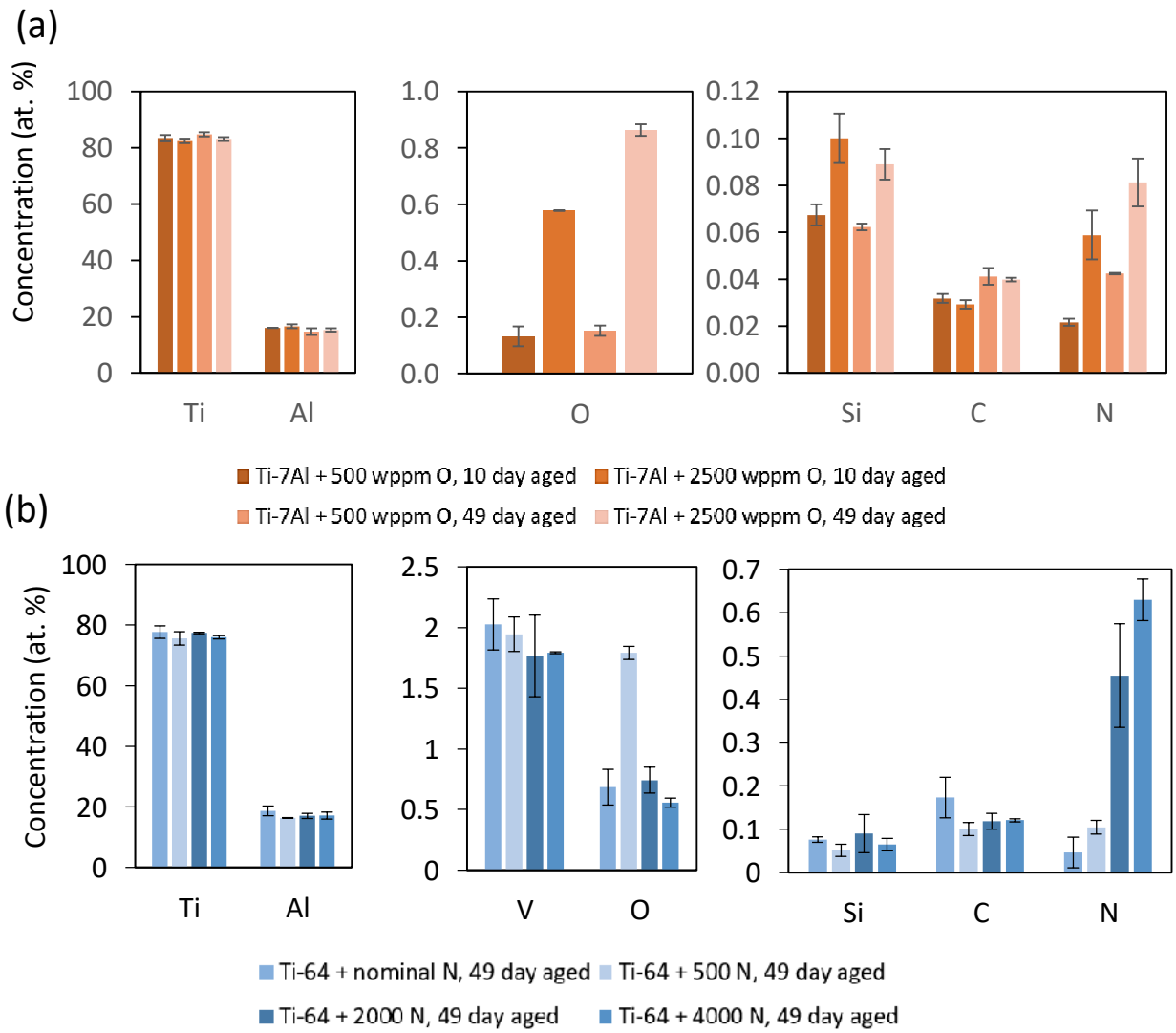


Figure 5.1: Composition of α_2 precipitates in (a) Ti-7Al and (b) Ti-64 as a function of ageing time and oxygen/ nitrogen composition. Error bars show the standard deviation between multiple samples measured.

DFT calculations suggest that transition metal elements, such as V, occupy the Ti sublattice in α_2 , whilst Si occupies the Al sublattice [219,220]. Assuming this to be true for the current study, the α_2

precipitates formed in Ti-64 have been calculated to have the stoichiometry $Ti_{4.5}Al$ and precipitates in Ti-7Al have the stoichiometry $Ti_{4.8}Al$. Often, a range of compositions are reported in literature for Ti_3Al, since both the Ti and Al sublattice can be defective [95]. For example, Donachie [88] reports that α_2 alloys typically contain 23-25 at.% Al, whereas Jones et al. [94] report a composition of 22.5-39 at.% Al. It should be noted that these reported compositions are both for the $\gamma - \alpha_2$ system, which can be found at the high aluminium end of the titanium-aluminium phase diagram (~ 35- 50 at.% Al on Figure 5.2). However, the system under study in this work is at the lower end of the Ti-Al phase diagram, at ~ 10-20 at.% Al. It is acknowledged that the binary phase diagram in Figure 5.2 should be used only as a guide; oxygen is known to shift the $\alpha + \alpha_2$ phase boundary to lower aluminium concentrations, as illustrated by the ternary phase diagram in [210]. Taking into consideration that the material in this study is at the low aluminium end of the Ti-Al binary phase diagram, the APT-measured compositions, displayed in Figure 5.1, are within the ranges expected.

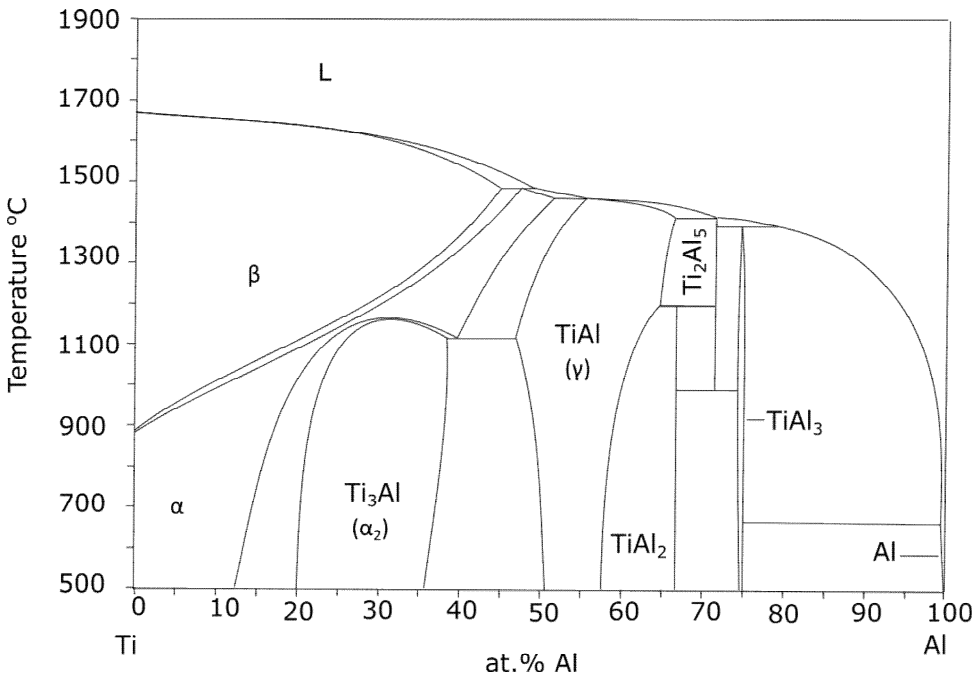


Figure 5.2: Calculated Ti-Al binary phase diagram, re-drawn from [61].

5.2.1.1 Ti-7Al

As might be expected, Figure 5.1 (a) shows that the oxygen concentration within the precipitates increases as nominal oxygen content within the alloy is increased. The oxygen content of the

precipitates in the Ti-7Al + 2500 O, 49 day aged samples is significantly higher than for the other material conditions. This is likely because the bulk Ti-7Al + 2500 wppm O, 49 day aged material contained more oxygen than intended; 0.4 wt.% instead of 0.25 wt.%. The behaviour of nitrogen increases with nominal oxygen content.

The silicon content of the precipitates is higher in the material with greater oxygen content. Carbon content increases with ageing time, although the difference in carbon content between the four datasets is small.

5.2.1.2 Ti-64

Taking the error bars on Figure 5.1 (b) into consideration, the level of vanadium in the precipitates remains constant as a function of nitrogen content, as does the concentration of silicon and carbon. The oxygen content is constant, with the exception of the Ti-64 + 500 wppm N sample, for which it is assumed there was some oxygen contamination. Thus, nitrogen is the only element within the precipitates that varies, increasing as a function of nominal nitrogen content. A summary of the changes in composition of the α_2 precipitates in Ti-7Al and Ti-64, as a function of oxygen and nitrogen, respectively, can be found in Table 5.1.

Table 5.1: Summary of the change in composition of α_2 precipitates with increasing oxygen (Ti-7Al) and nitrogen (Ti-64).

	Ti-7Al	**Ti-64**
O	↑	Constant
N	↑	↑
Si	↑	Constant
C	Constant	Constant
V	Constant	Constant

5.2.2 Morphology

The morphology of the precipitates in Ti-7Al changes with increased ageing time. To analyse this, the precipitates were extracted using isoconcentration surfaces following the method described in section 3.3.5 of the Materials and Methods chapter. An example of the isoconcentration surfaces

used to extract precipitates in the Ti-7Al + 2500 wppm O, 49 day aged sample can be seen in Figure 5.3 (a). The indexed, non-edge precipitates for the same sample can be seen in Figure 5.3 (b). Once indexed, an ellipsoid was fitted to each precipitate, thus identifying the three principal axes, L_1, L_2 and L_3, where $L_1 > L_2 > L_3$. Figure 5.3 (c) shows the principal axes for the indexed precipitates in the Ti-7Al + 2500 wppm O, 49 aged sample.

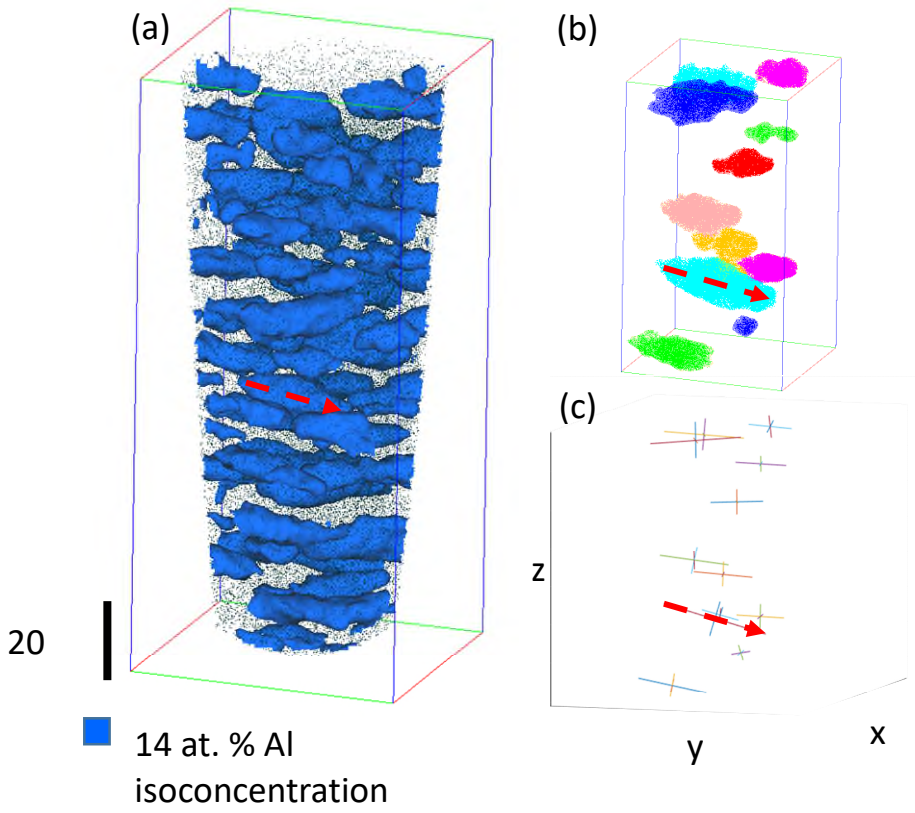


Figure 5.3: (a) 14 at.% Al isoconcentration surfaces used to highlight the α_2 precipitates in the Ti-7Al + 2500 wppm O, 49 day aged sample. (b) shows the same dataset with all edge precipitates removed, and each precipitate individually identified using d_{max} cluster searching. In (c), the fitted axes for each of the precipitates identified in (b) are displayed. The red dotted arrow indicates the major axis of the same precipitate across all three figures.

The relative length of the principal axes was used to categorise the precipitates as discs ($L_1 = L_2$, $L_2 > L_3$), spheres ($L_1=L_2=L_3$), laths ($L_1>L_2>L_3$) or rods ($L_2 = L_3$, $L_1>L_2$). Each categorised precipitate is represented as a circle on the morphology plots seen in Figure 5.4 and Figure 5.5. The size of the circle represents the number of ions contained within the precipitate. The morphology plots were all

created using APT datasets of equal volume such that comparisons can be drawn between datasets. Examination of Figure 5.4 shows that the morphology of the α_2 precipitates in the Ti-7Al samples changes from spherical to more rod-like as ageing progresses. It should be noted that the lines at 0.5 in Figure 5.4 and Figure 5.5 are entirely arbitrary, and are included only as a guide to the eye.

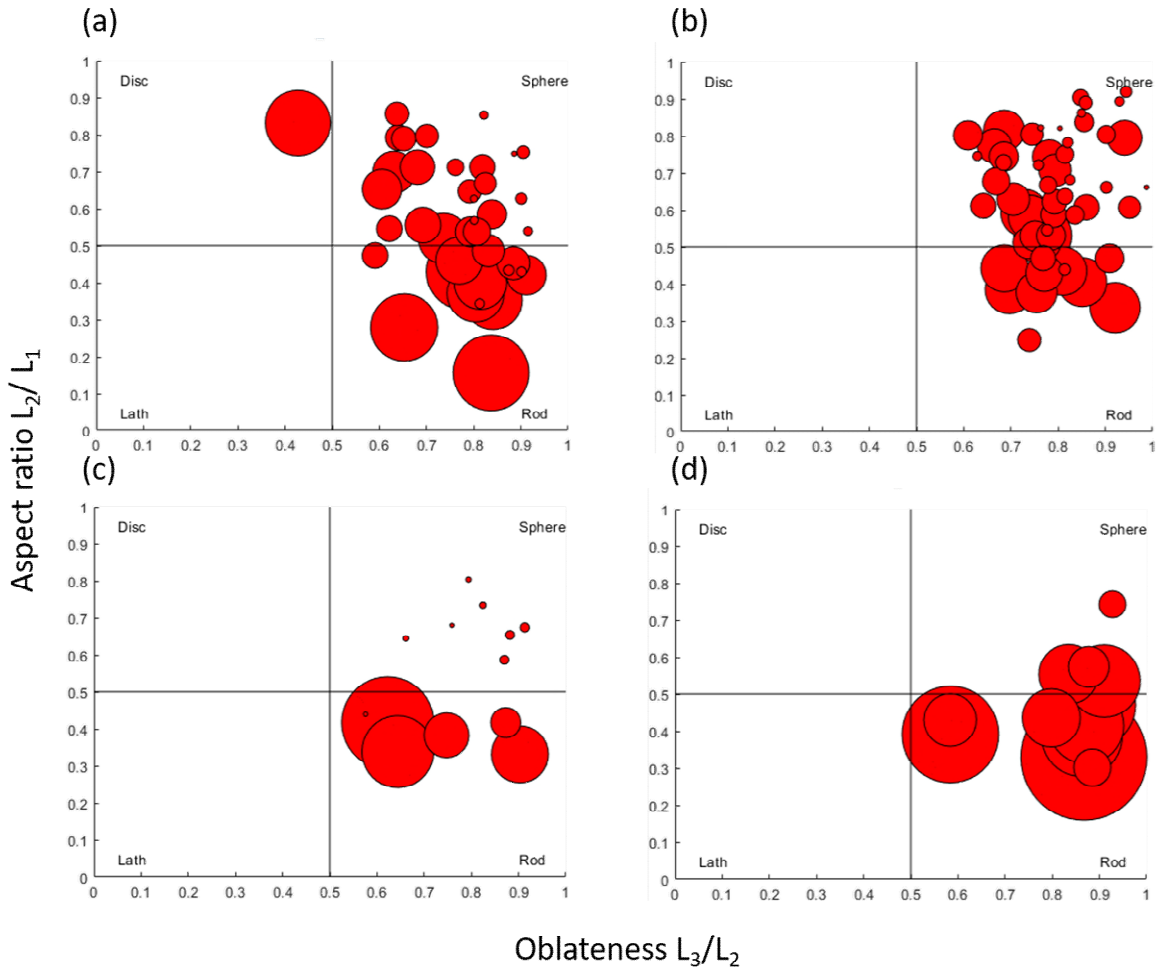


Figure 5.4: Plots of precipitate aspect ratio vs oblateness for the samples aged for (a) Ti-7Al + 500 wppm O, 10 day aged (b) Ti-7Al + 2500 wppm O, 10 day aged, (c) Ti-7Al + 500 wppm O, 49 day aged and (d) Ti-7Al + 2500 wppm O, 49 day aged to indicate change in precipitate morphology. L_1, L_2, and L_3 are the three axes of the precipitate, where $L_1>L_2>L_3$. A circle is plotted for each precipitate, and the circle area is proportional to the number of ions contained in the precipitate.

This is consistent with reports elsewhere in literature [46,59,112], and results from strain energy considerations [39]. The decrease in number of precipitates and increase in size of precipitates with ageing time can be seen clearly on Figure 5.4 and is consistent with coarsening of the precipitates.

Figure 5.5 shows that, as nitrogen content in increased, the α_2 precipitates in the Ti-64 samples do not show a marked change in morphology.

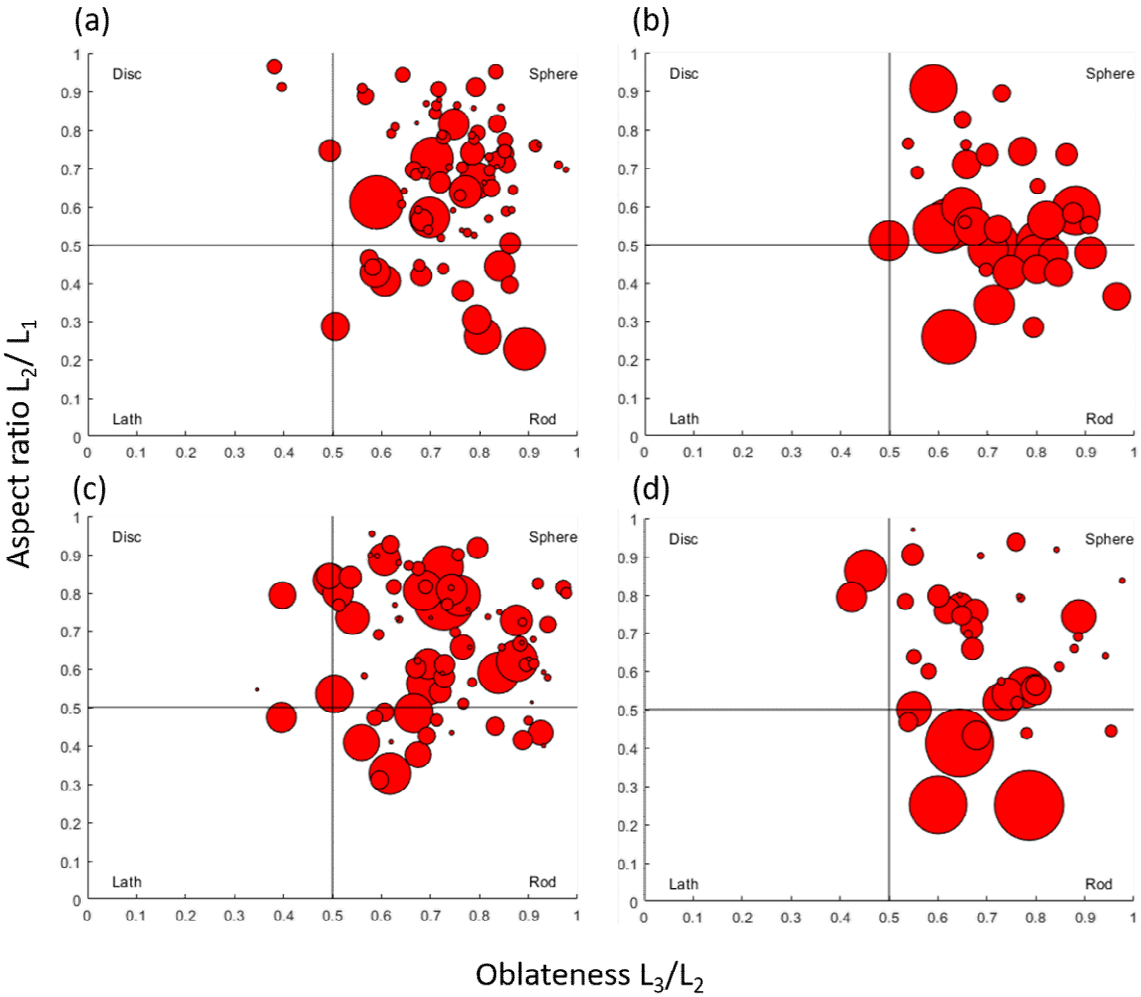


Figure 5.5: Plots of precipitate aspect ratio vs oblateness for the samples aged for (a) Ti-64 + nominal N, 49 day aged (b) Ti-64 + 500 N, 49 day aged, (c) Ti-64 + 2000 N, 49 day aged and (d) Ti-64 + 4000 N, 49 day aged to indicate change in precipitate morphology. L_1, L_2, and L_3 are the three axes of the precipitate, where $L_1>L_2>L_3$. A circle is plotted for each precipitate, and the circle area is proportional to the number of ions contained in the precipitate.

However, the precipitates formed in the Ti-64 are more spherical than the precipitates in the Ti-7Al samples, on average. This can be seen more clearly in Figure 5.6, where the percentage of spheres, rods, laths and discs present in both the Ti-64 and Ti-7Al samples is plotted.

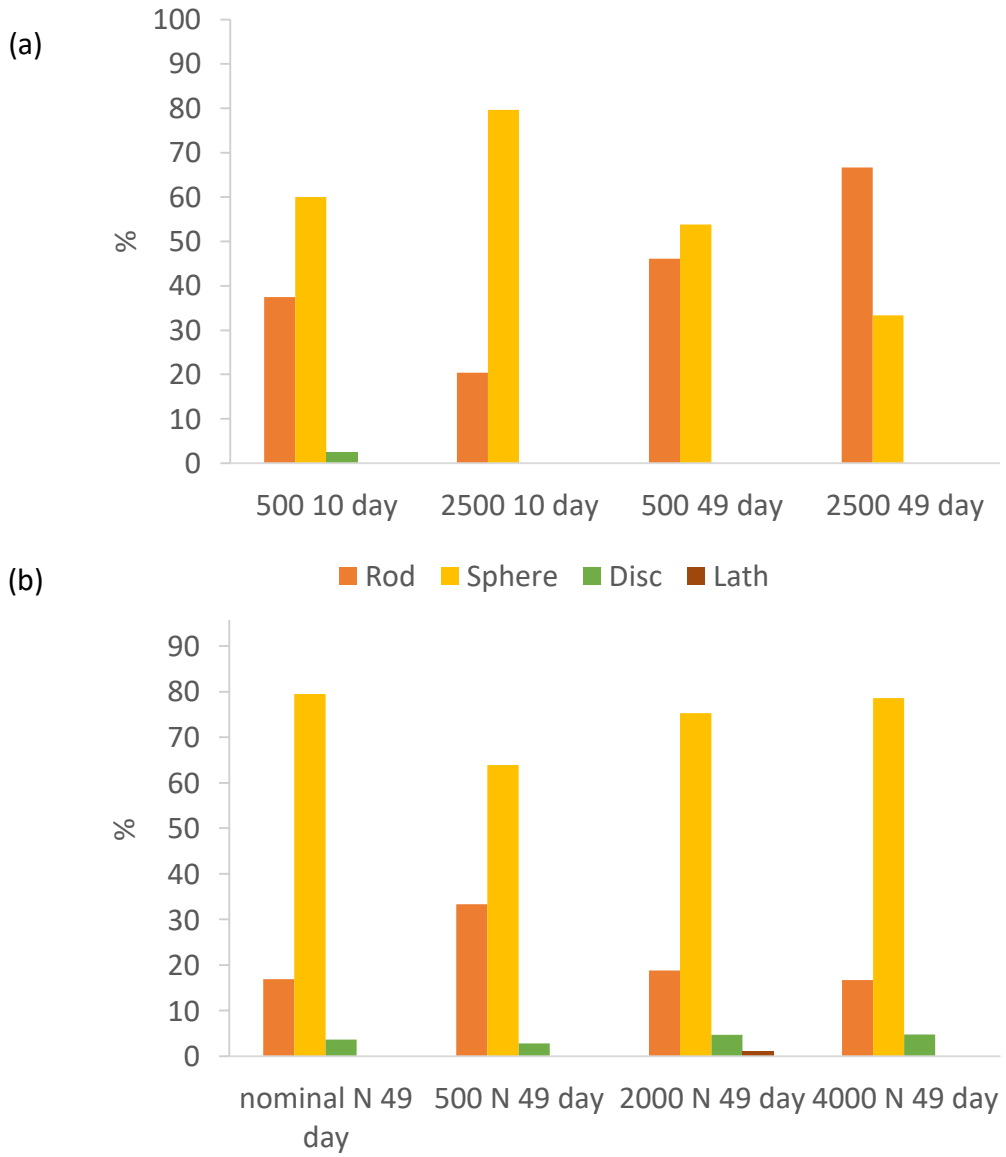


Figure 5.6: Plot of precipitate morphology as a function of (a) oxygen content and ageing time in Ti-7Al and (b) nitrogen content in Ti-64.

The orientation of the long axes of the precipitates with respect to the x, y, z axes of the APT dataset can be plotted on a stereographic projection to highlight common directions and thus show if precipitates are aligned along common axes. The stereographic projections for the Ti-7Al and Ti-64 samples are seen in Figure 5.7 and Figure 5.8, respectively.

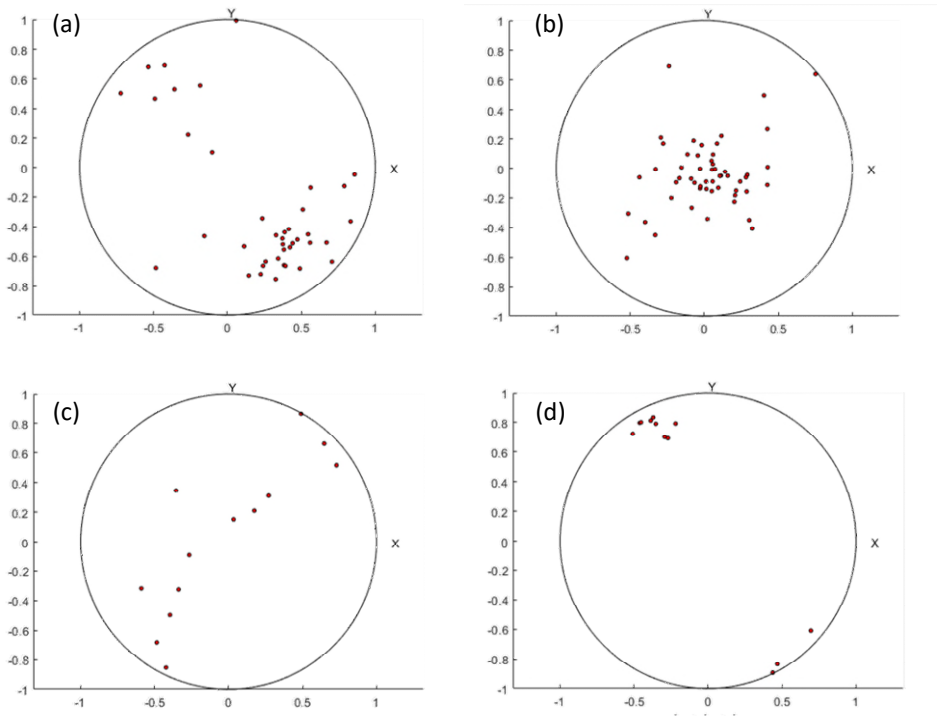


Figure 5.7: Stereographic projection of axis vectors for (a) Ti-7Al + 500 wppm O, 10 day aged (b) Ti-7Al + 2500 wppm O, 10 day aged, (c) Ti-7Al + 500 wppm O, 49 day aged and (d) Ti-7Al + 2500 wppm O, 49 day aged.

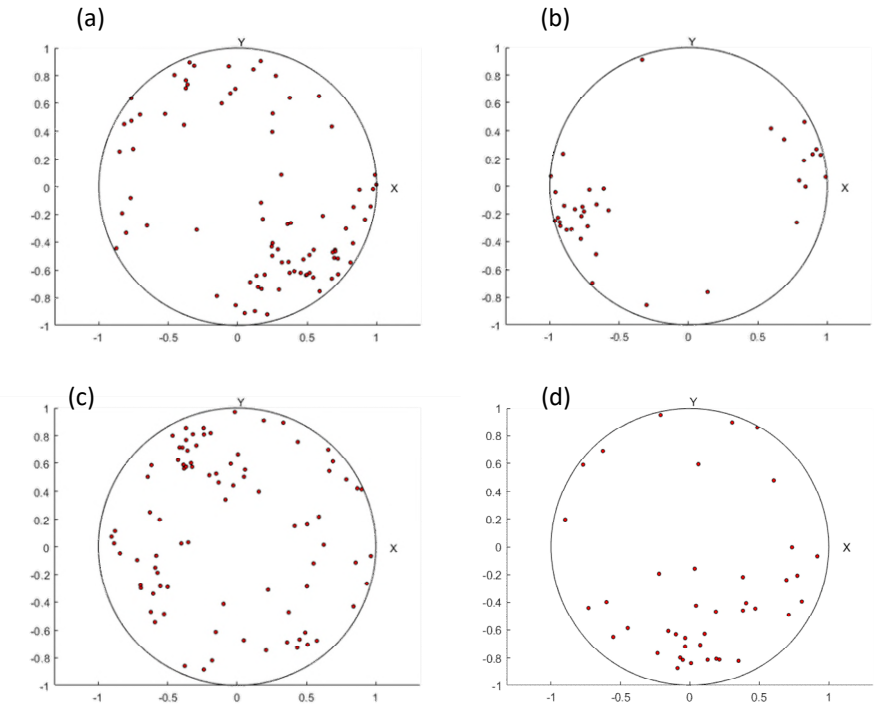


Figure 5.8: Stereographic projection of axis vectors for (a) Ti-64 + nominal N, 49 day aged (b) Ti-64 + 500 N, 49 day aged, (c) Ti-64 + 2000 N, 49 day aged and (d) Ti-64 + 4000 N, 49 day aged.

Figure 5.7 (a), (c) and (d) shows alignment of the long axis of the precipitates in the x-y plane of the APT dataset, perpendicular to the APT analysis direction (z direction). Figure 5.7 (b) shows alignment of the precipitates parallel to the APT analysis direction. The x, y, z axes of the APT dataset are arbitrarily oriented with respect to the HCP crystal, since APT liftouts sites were randomly selected from different grains. Thus, the difference between precipitates being oriented perpendicular and parallel to the APT analysis direction is not meaningful; alignment parallel to the APT analysis direction in one dataset could be crystallographically equivalent to alignment perpendicular to the APT analysis direction in another dataset, depending on the orientation of the grain from which each sample was taken. However, it does suggest that precipitate alignment is unlikely to be an APT artefact since precipitates are observed to be aligned both parallel and perpendicular to the APT analysis direction.

Of key importance is that Figure 5.7 shows precipitate alignment in all Ti-7Al samples. By contrast, the stereographic projections in Figure 5.8 show that there is no clear alignment of precipitates in the Ti-64 samples, with the exception of Ti-64 + 500 wppm N in Figure 5.8 (b). The lack of alignment agrees with the observation that the Ti-64 precipitates are generally more spherical, since spherical precipitates do not have a long axis that can be aligned.

5.3 HARDNESS AS A FUNCTION OF AGEING TIME AND INTERSTITIAL CONTENT

Micromechanical testing is commonly used to inform about the effect of microstructure on mechanical properties [77,171,221]. Nanohardness measurements are used in this study to investigate the material response to ageing and changes in interstitial content.

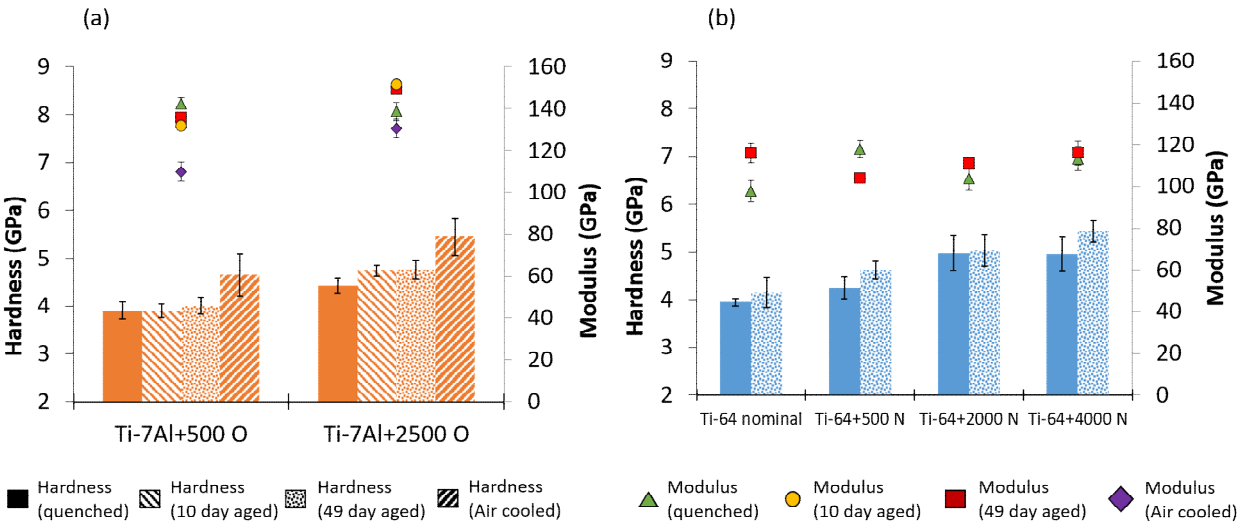


Figure 5.9: Hardness as a function of ageing time and (a) oxygen content in Ti-7Al, (b) nitrogen content in Ti-64.

By looking at the hardness of the quenched Ti-7Al samples in Figure 5.9 (a), it can be seen that as oxygen concentration increases, hardness also increases. Hardness increases with nitrogen content in the Ti-64 quenched samples. Comparing Figure 5.9 (a) and (b), it can be seen that nitrogen has a greater hardening effect than oxygen, per wt.% added.

Figure 5.9 (a) shows that there is a hardness increase between the ice water quenched and air-cooled Ti-7Al samples. A custom FIB sample preparation procedure was developed to produce APT samples from directly beneath a specific nanoindent, such that the composition and microstructure contributing to the nanohardness measurement could be analysed. The preparation method is shown in Figure 5.10 , and it can be seen from the atom map in Figure 5.10 (d) that there are no precipitates present in the air-cooled sample. Multiple APT samples were analysed, and none were found to contain precipitates.

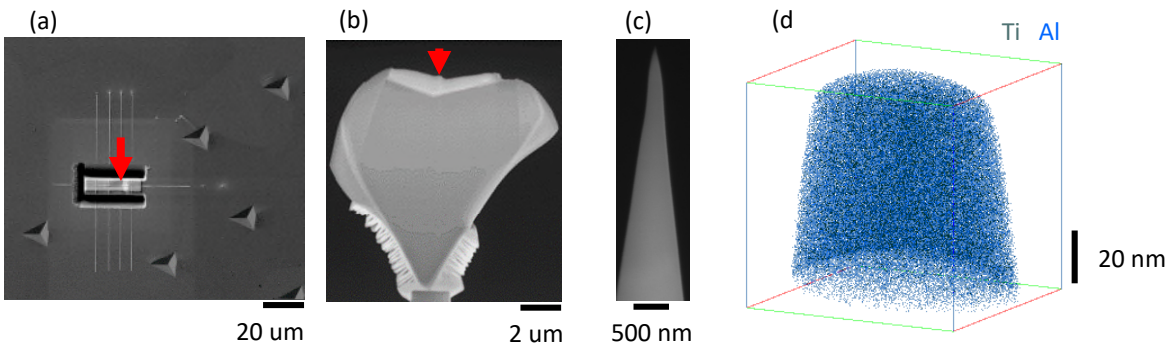


Figure 5.10: The stages of sample preparation and analysis involved in analysing the material directly below a nanoindent. (a) shows the location of the FIB-milled lift-out bar within the indent array. (b) shows the indented material mounted on top of a pre-sharpened silicon post. (c) Shows the indented material sharpened into an APT sample and (d) shows the material analysed in atom probe. Red arrows indicate the same location on the liftout bar and on the mounted sample.

Considering the aged samples, Figure 5.9 shows no statistically significant hardness change between the Ti-7Al + 500 wppm O quenched sample and either of the Ti-7Al + 500 wppm O aged samples. However, in Figure 4.4 of Chapter 4, APT shows that α_2 have formed in both the 10 day and 49 day aged Ti-7Al + 500 wppm O samples. Similarly, Figure 4.8 of Chapter 4 shows that both the 10 day and 49 day aged Ti-7Al + 2500 wppm O samples contain α_2 precipitates. However, unlike the Ti-7Al + 500 wppm O samples, the Ti-7Al + 2500 wppm O samples do harden upon ageing.

To directly study the material that was contributing to the hardness increase in the Ti-7Al+2500 wppm O 10 day aged sample, a FIB lift-out was performed from beneath an indent, as shown in Figure 5.11. The atom map in Figure 5.11 (d) confirms that there are α_2 precipitates present directly below the indent.

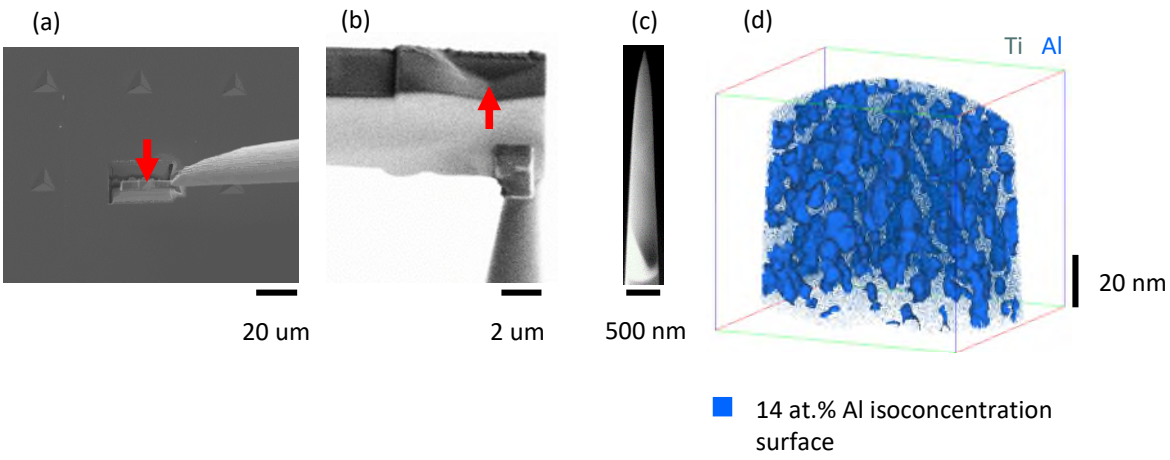


Figure 5.11: The stages of sample preparation and analysis involved in analysing the material directly below a nanoindent. (a) shows the location of the FIB-milled lift-out bar within the indent array. (b) shows the indented material mounted on top of a pre-sharpened silicon post. (c) Shows the indented material sharpened into an APT sample and (d) shows the material analysed in atom probe, containing α_2 precipitates highlighted with 14 at.% Al isoconcentration surfaces. Red arrows indicate the same location on the liftout bar and on the mounted sample.

5.3.1 Effect of crystal orientation on hardness

It has been reported in literature that, for CP-Ti, there is a strong dependence of hardness on orientation of the crystal c-axis relative to the indentation direction. Grains with c-axis parallel to the indentation direction are hardest [77]. Figure 5.12 shows the hardness of the Ti-7Al+ 2500 wppm O, air-cooled sample as a function of declination angle. Grains with a small declination angle have their c-axis oriented close to the indentation direction. An array of indents was made, and indents whose plastic zone interacted with a grain boundary were excluded. The orientation of remaining indented grains was measured using EBSD, and the second Euler angle (equal to the declination angle), was recorded. Hardness for each indent was then plotted with the corresponding declination angle, as seen in Figure 5.12. This confirms that, like for CP-Ti, the hardness of α-Ti decreases with increasing declination angle; increasing the declination angle from 16 to 85° decreases hardness by 1.6 GPa.

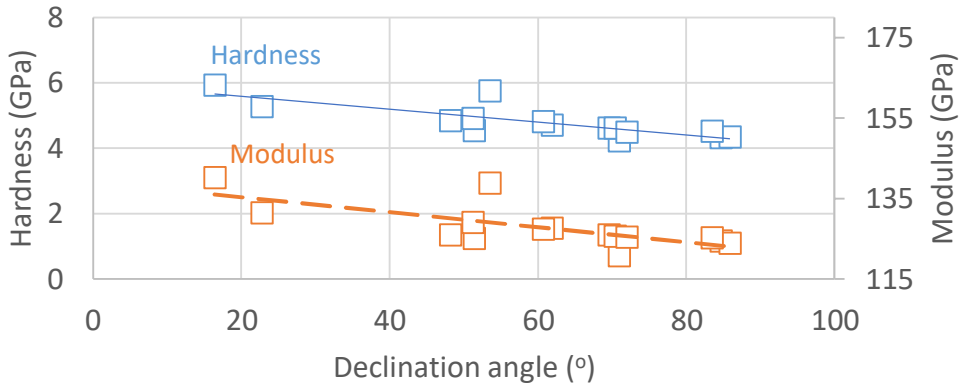


Figure 5.12: Hardness and modulus as a function of declination angle in the Ti-7Al + 2500 wppm O, air-cooled sample.

5.4 Discussion

5.4.1 Characterisation of the α_2 phase

Apart from the expected increase in oxygen/ nitrogen concentration, the only significant change in precipitate composition with interstitial content is the increase in Si with nominal oxygen content seen in the aged Ti-7Al material. As mentioned above, Si is predicted to occupy the Al sublattice. Si is known to improve creep resistance in titanium alloys through enhancing interstitial dynamic strain ageing. It is thought that introduction of Si atoms into HCP Ti alloys may cause loss of spherical symmetry of an oxygen-occupied octahedral interstitial site. This introduces a shear component to the associated lattice distortion, which enables interaction with the screw components of dislocations, causing hardening [222,223]. Although the effect of silicon on the mechanical properties of the ordered α_2 phase is not known, it is possible that the silicon may have a similar effect on the strain field surrounding the interstitial sites; further investigation is required.

Precipitates are more spherical in the Ti-64 + N materials and morphology is independent of nitrogen concentration. For shorter ageing times, increasing the oxygen content increases the number of spherical precipitates. This is in line with the proposed α_2 formation mechanism in Chapter 4 since, as oxygen content is increased, clustering of aluminium is favoured and more spherical α_2

precipitates form. For longer ageing times, increasing the oxygen content decreases the number of spherical precipitates and increases the number of rods.

This could indicate the existence of two regimes. At short ageing times it seems oxygen is encouraging precipitate formation whereas at longer ageing times, oxygen encourages precipitate elongation. This is in agreement with the findings of Ardakani et al. [104]. They propose that increasing oxygen content leads to an increase in precipitate misfit perpendicular to the [0001] direction, which is the direction along which α_2 precipitates are observed to elongate during growth, due to strain energy considerations.

Jones et al. [94] use neutron diffraction studies to provide an explanation for the change in α_2 precipitate misfit that is caused by oxygen. They measure an increase in bond length of Ti-Al bonds aligned close to the [0001] direction as interstitial oxygen content is increased.

At shorter ageing times, the α_2 precipitates are not large enough for precipitate misfit to be significant. Thus changing the oxygen content does not have a further significant effect on misfit. However, at longer ageing times the precipitates grow larger and so the difference in lattice misfit strain energy perpendicular and parallel to the [0001] direction becomes more significant, causing the precipitates to elongate along the [0001] direction. For example, Figure 5.6 shows that, when oxygen concentration is held constant, increasing the ageing time increases the proportion of rod shaped precipitates. However, if oxygen content is increased for the 49 day aged samples, which contain larger, elongated precipitates, it is proposed that the increased oxygen causes further elongation along the [0001] direction. This is because oxygen further increases the lattice misfit perpendicular to the [0001], making elongation parallel to the [0001] more favourable.

5.4.2 Evaluation of hardening mechanisms

When trying to understand the processes giving rise to the hardness changes between the Ti-7Al samples, the available hardening mechanisms should be considered. In their work on alloys with similar compositions to Ti-64, Liu and Welsch [79] report that α_2 precipitation and intrinsic lattice

flow stress have a minor contribution to hardening of the α phase, with solid solution hardening (including solid solution hardening due to interstitial oxygen), work hardening and boundary hardening providing major hardness contributions. At low temperature, ordering of interstitial oxygen atoms can occur [79–81], leading to hardening. However, ordering is lost at temperatures above 427-577^{o}C [80].

Grain size is comparable across all the samples in this study. The indent size was very much smaller than the grain size, and the indent spacing of 50 µm ensured multiple grains were indented and contributed to the hardness measurement. All samples were recrystallised so should contain very few dislocations. Thus, any contributions from work hardening and boundary hardening will be minimal and can be neglected. The maximum variation in hardness due to crystal orientation in Ti-7Al has been measured in section 5.3.1 to be 1.6 GPa. However, all the material used has a random texture, and multiple grains were indented in all cases meaning the overall effect of crystal orientation on the average hardness of each sample will be negligible.

Table 5.2: Hardness of the Ti-7Al samples.

	Hardness (GPa)	
	500 wppm O	**2500 wppm O**
IWQ	3.91±0.18	4.43±0.15
10 day	3.90±0.14	4.74±0.11
49 day	4.01±0.18	4.77±0.20
Air-cooled	4.65±0.44	5.46±0.39

The hardness of the Ti-7Al samples is displayed in Table 5.2, while the corresponding oxygen concentration of these samples is reported in Table 5.3.

Table 5.3: APT-measured oxygen concentration in the Ti-7Al samples.

	Oxygen concentration (at.%)					
	500 wppm O			**2500 wppm O**		
	Bulk	**α_2**	**α**	**Bulk**	**α_2**	**α**
IWQ	0.177±0.01	/	/	0.737±0.2	/	/
10 day	0.193±0.05	0.156±0.04	0.197±0.04	0.739±0.02	0.599±4x10^{-4}	0.750±0.003
49 day	0.185±0.009	0.156±0.02	0.192±0.01	1.109±0.05	0.853±0.02	1.16±0.06
Air-cooled	0.156±0.003	/	/	0.710±0.03	/	/

There is a 10% hardness increase as oxygen concentration is increased from 500 wppm to 2500 wppm in the ice water quenched samples. This can be explained by considering the lattice strain caused by the increased number of oxygen atoms located at the interstitial sites. It is unlikely that oxygen ordering is occurring on the oxygen interstitial sublattice, since ordering of interstitial oxygen in CP-Ti typically occurs at temperatures below 550°C and at oxygen concentrations very much higher than 2000 wppm O [98]. The presence of aluminium in the alloy will change the ordering behaviour, since all interstitial sites are no longer equivalent. However, the quenching process will not give time for the oxygen atoms to order; rather they are likely to be "frozen" in the disordered arrangement that they are in at 980°C. Thus, the hardness increase with oxygen content in the ice water quenched samples is thought to be primarily due to solid solution hardening; interstitial ordering is not thought to contribute.

In order to study the effect of oxygen concentration on the hardness changes between the Ti-7Al samples, each hardness change was normalised by the change in oxygen, and is reported in Table 5.4. Each arrow in Table 5.4 denotes a hardness change, and the number on the arrow represents the magnitude of the hardness change normalised by the change in oxygen concentration (oxygen-normalised hardness change.) When precipitates are present, only the oxygen concentration of the matrix is considered.

Table 5.4: Changes in hardness between the Ti-7Al samples normalised to changes in oxygen concentration. Numbers in red indicate small values of oxygen-normalised hardness that indicate interstitial hardening.

	$\frac{\Delta\lvert\text{Hardness}\rvert}{\Delta\lvert\text{oxygen concentration}\rvert}$ (GPa/ at. % O)	
	500 wppm O	2500 wppm O
IWQ	0.5 → 0.9	24
10 day	35, 7	38, 0.8
49 day		
Air cooled		

We can assume that the hardness change between the two ice water quenched (IWQ) samples is due solely to interstitial solid solution hardening, as discussed above. Thus, the small value of oxygen-normalised hardness change between the IWQ samples is taken to be representative of interstitial solid solution hardening, and is used as a baseline against which the other values in Table 5.4 can be compared. All small values of oxygen-normalised hardness are shown in red. Larger values of oxygen-normalised hardness change point to a greater change in in hardness per at.% O. This suggests that another hardness mechanism, in addition to interstitial hardening, is at work in the samples associated with large values of oxygen-normalised hardness change; specifically both air-cooled samples, and the Ti-7Al + 2500 wppm O, 10 day aged sample.

To better understand what is contributing to the hardness increase in the air-cooled samples, we can look at the processing conditions experienced by the sample. After recrystallization at 980^{o}C, samples were ice water quenched and then aged for 40 minutes at 550^{o}C before being air-cooled. Air-cooling from 550^{o}C gives time for ordering of interstitial oxygen, which could provide the increase in hardness.

There is a significant increase in hardness upon ageing for the high oxygen samples, which is in contrast to the low oxygen samples. α_2 precipitation hardening and interstitial solid solution hardening in the matrix are possible mechanisms acting to cause the hardness change upon ageing. Given the lack of significant hardness increase upon α_2 formation in the low oxygen samples, and that Liu et al. [79] have reported that α_2 precipitation has a minor hardening contribution, it is assumed that an alternative hardening mechanism (other than α_2 formation) is operating in the Ti-7Al + 2500 wppm O aged samples.

It is interesting to note that the change in oxygen-normalised hardness between the Ti-7Al + 2500 wppm O, IWQ and Ti-7Al + 2500 wppm O, 49 day aged samples is particularly small, and close in value to the change between the two IWQ samples. The same is true for the change in oxygen-normalised hardness between Ti-7Al + 500 wppm O, IWQ and Ti-7Al + 500 wppm O, 10 day aged

samples. This is interpreted as showing that interstitial hardening is providing significant hardening in the Ti-7Al + 2500 wppm O, 49 day aged sample, and the Ti-7Al + 500 wppm O, 10 day aged sample. We can see that the bulk oxygen concentration in the Ti-7Al + 2500 wppm O, 49 day aged sample, reported in Table 5.3, is higher than the nominal value of 2500 wppm O (~0.7 at.% O). As discussed previously, this is thought to be a result of oxygen diffusion into the sample during heat treatment. Table 5.3 also shows that the bulk oxygen content is slightly higher for the Ti-7Al + 500 wppm O, 10 day aged sample. Thus, inward oxygen diffusion could be providing the interstitial hardening that is indicated by the small value of oxygen-normalised hardness change for these samples in Table 5.4.

The Ti-7Al + 2500 wppm O, 10 day aged sample has a relatively large value of oxygen-normalised hardness, suggesting another hardening mechanism is operating, in addition to interstitial hardening. As discussed above, α_2 precipitation hardening is not deemed to be providing a significant contribution. Thus, additional mechanisms must be considered. Since the aged samples were all air-cooled after heat treatment, and the rate of cooling was controlled, it is possible that some order hardening is occurring in this sample due to a slower air-cooling rate; further investigation is needed.

Nitrogen causes a greater hardness increase per wt.% interstitial added compared to oxygen. In their investigations into the origins of interstitial oxygen solid solution strengthening in titanium, Yu et al. [99] report that it is the short range interactions between screw dislocation cores and interstitial oxygen that give rise to strengthening. These interactions result, in part, from the reduction in interstitial site volume that occurs during slip displacement. The author anticipates that the greater hardening effect of nitrogen compared to oxygen in titanium may result from the larger atomic radius of nitrogen; occupation of the smaller interstitial sites, that form during slip, by the larger nitrogen atom is expected to be less energetically favourable than occupation by oxygen.

5.5 CONCLUSIONS

Characterisation of the α_2 phase using APT revealed that the ratio of titanium to aluminium remained constant as a function of oxygen content and ageing time in Ti-7Al, and nitrogen content in Ti-64, suggesting that the precipitates have reached a stable stoichiometry. Silicon concentration in the α_2 precipitates increased with oxygen concentration, which could provide additional hardening; further investigation is needed into the role of silicon. Increased oxygen concentration has been observed to favour further precipitate elongation in 49 day aged samples. By contrast, increasing oxygen concentration in the shorter-term aged samples seems to promote α_2 precipitate formation, in line with the proposed α_2 formation mechanism in Chapter 4.

This work highlights that careful control of interstitial oxygen in titanium alloys is still necessary since interstitial oxygen plays a significant role in the hardening, and therefore embrittlement, of titanium alloys. Evaluation of the hardening mechanisms acting in the Ti-7Al suggests that interstitial solid solution hardening and oxygen order hardening provide a greater contribution than α_2 precipitation hardening. The rate of cooling of the alloy after heat treatment is of particular importance. Fast cooling rates are necessary to prevent oxygen ordering, which this study suggests can cause up to a 23% hardness increase.

6 CHARACTERISATION OF THE *OXYGEN-RICH LAYER*

6.1 INTRODUCTION

Titanium alloys are used for multiple safety-critical jet engine components including fan blades and compressor discs. However, greater use of titanium alloys in compressor discs is currently temperature-limited since above ~480°C, oxygen can start to diffuse through the surface oxide layer on components [5]. This leads to the detrimental formation of a brittle, high oxygen content surface layer that contains up to 8 times the oxygen concentration of the bulk. This starts to limit use by promoting crack formation when components are operated at temperatures approaching 600°C under cyclic loading conditions over thousands of hours [39,216].

As discussed in section 2.10 of the Literature Review, the term *α case* is often broadly used in industry as an umbrella term for both the surface layers formed during processing and *in-service*. However, this study will use the specific definitions of *oxygen-rich layer* for the *in-service* layer and *α case* for the processing layer, as defined by Satko et al. [11].

A fundamental understanding of the underlying mechanisms that govern formation of *oxygen-rich layer*s will ultimately improve component life predictions. Improved life length predictions enable components to safely operate for longer times at higher temperatures, decreasing the required inspection frequency and the costs associated with replacement components.

6.2 CHARACTERISATION OF BULK TIMETAL 834 MATERIAL

Characterisation of bulk TIMETAL 834 material was necessary to provide a comparison point for the *in-service*, oxygen-affected material. To this end, a region of representative microstructure away from the surface of the compressor disc that was unaffected by oxygen ingress was analysed using EDS. The larger atomic number of the β stabilising elements gives rise to lighter contrast on the SEM image. In Figure 6.1 (a), the long, thin areas of lighter contrast are identified as β phase, based on both their morphology and composition, while the darker material is α

phase. It can be seen from Figure 6.1 (b) that aluminium partitions away from the β phase, while all other elements in Figure 6.1 (c) – (e) appear to segregate to it. Mo and Nb are known β stabilisers whereas Zr is generally considered a neutral element with no strong partitioning preference [66]. However, Figure 6.1 (c) shows partitioning of Zr to the β phase.

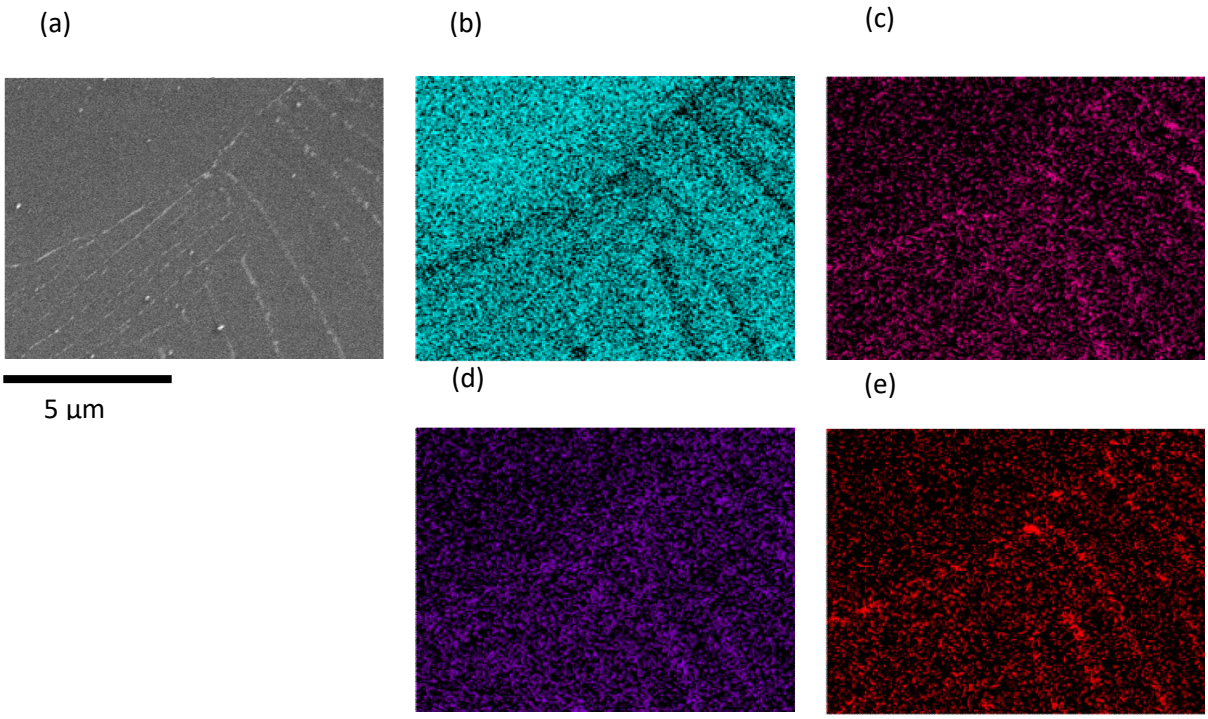


Figure 6.1: EDS maps of a representative, bulk region of TIMETAL 834 in-service compressor disc, away from the oxygen-affected surface material. A secondary electron image of the region of interest can be seen in (a), and elemental segregation of (b) Al, (c), Zr, (d) Nb and (e) Mo.

APT was used to measure the concentration of a bulk piece of unused TIMETAL 834, which can be found in Table 6.1. The corresponding atom maps, displaying elemental segregation, can be seen in Figure 6.2. Mo and Nb clearly partition to the β phase whereas Zr and Si segregate to a particle on the grain boundary. The composition of this particle is shown in Table 6.1, and is consistent with a $(Ti,Zr)_6Si_3$ silicide. These precipitates are intentionally formed within TIMETAL 834 in order to improve strength by pinning grain boundaries [224].

Table 6.1: APT-measured compositions of the α phase, β phase and silicide in Figure 6.2.

	Comp (at.%)		
Element	**α**	**β**	**Silicide**
Ti	89.6	80.6	39.3
Sn	1.7	1.9	1.8
Zr	2.1	1.9	27.2
Al	6.6	2.1	0.7
Mo	-	10	0.5
Nb	-	3.5	0.8
As	-	-	0.3
Si	-	-	28.6

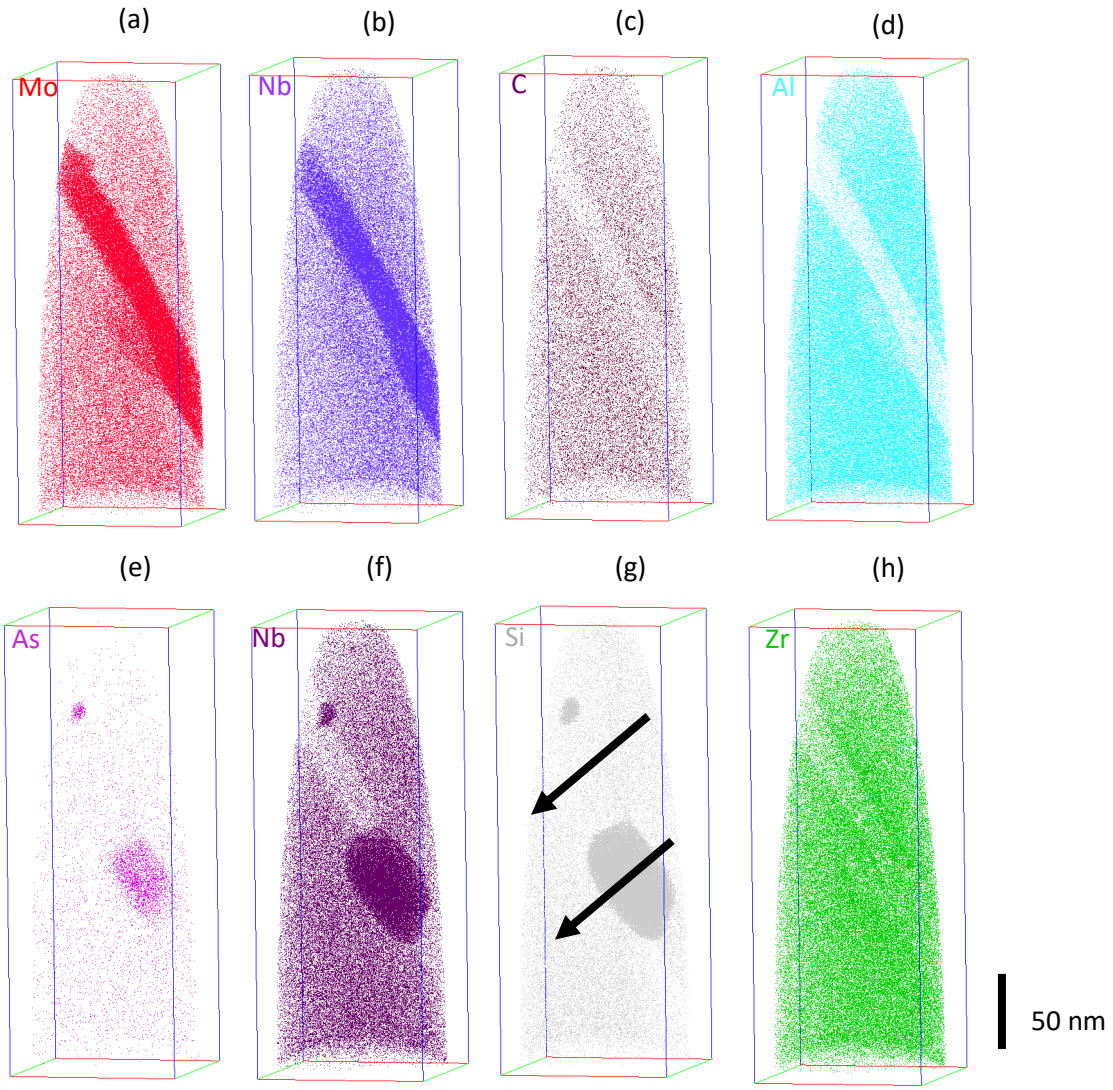


Figure 6.2: APT maps of an α - β interface in an unused sample of TIMETAL 834. Elemental segregation of (a) Mo, (b) Nb, (c) C, (d), Al (e) As, (f) Zr, (g) Si and (h) Sn can be seen. The arrows in (g) indicates the direction of the two 1D concentration profiles.

To investigate the behaviour of Zr with respect to the β phase, a 1D concentration profile was created across the boundary (excluding the silicide), and can be seen in Figure 6.3 (a). The profiles displayed in Figure 6.3 are all mass-spectrum overlap solved. While Nb and Mo segregate to the β phase, it seems that Zr segregates ahead of the α - β interface instead. The APT analysis provides higher resolution than the SEM-EDS maps, since a combination of large interaction volume on the order of a cubic micron and mechanical drift across the EDS scan have led to a reduction in spatial resolution of the β phase imaged in Figure 6.1. Figure 6.3 (b) shows the concentration change through the silicide. The silicide is enriched in Mo, Zr, Nb and Si, as would be expected for a $(Ti,Zr)_6Si_3$ silicide.

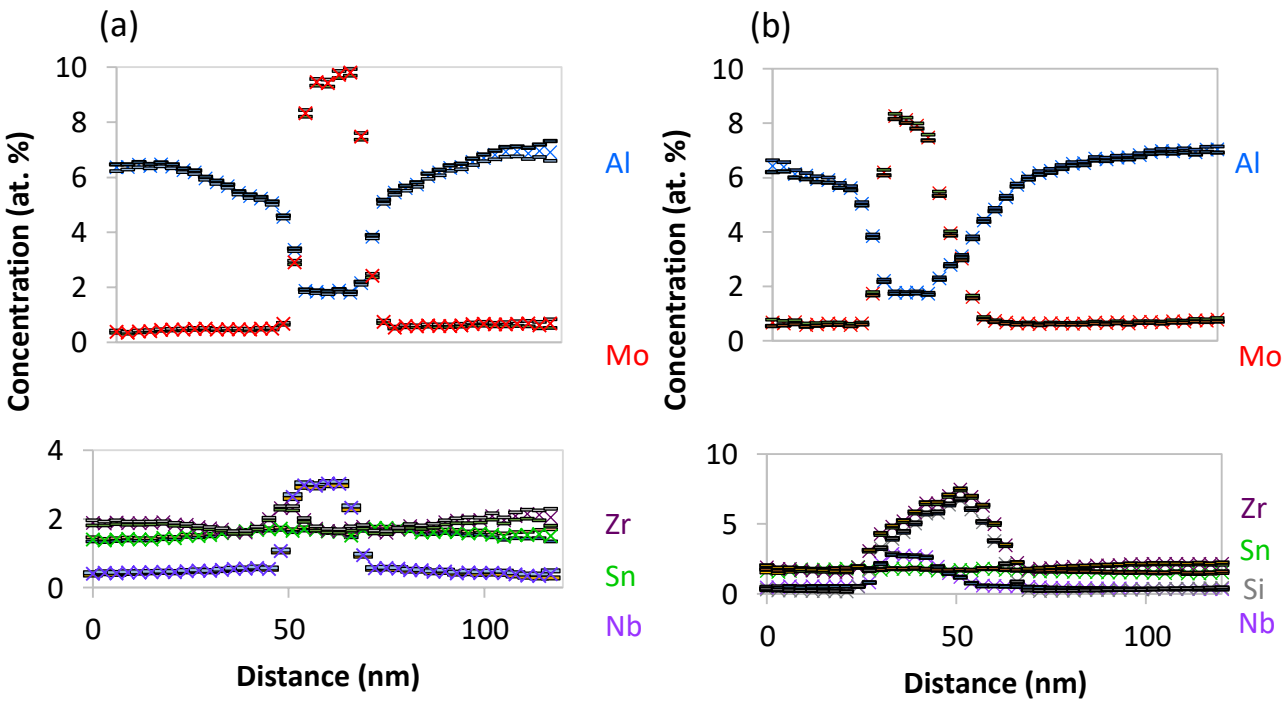


Figure 6.3: 1D concentration profiles across (a) the α - β interface and (b) the silicide particle.

6.3 *IN-SERVICE* COMPRESSOR DISC

A schematic overview of the analysis carried out on the *in-service* sample is shown in Figure 3.4.

6.3.1 Oxygen concentration

To study the effects of oxygen on the *in-service* compressor disc, it was necessary to map the extent to which oxygen had penetrated.

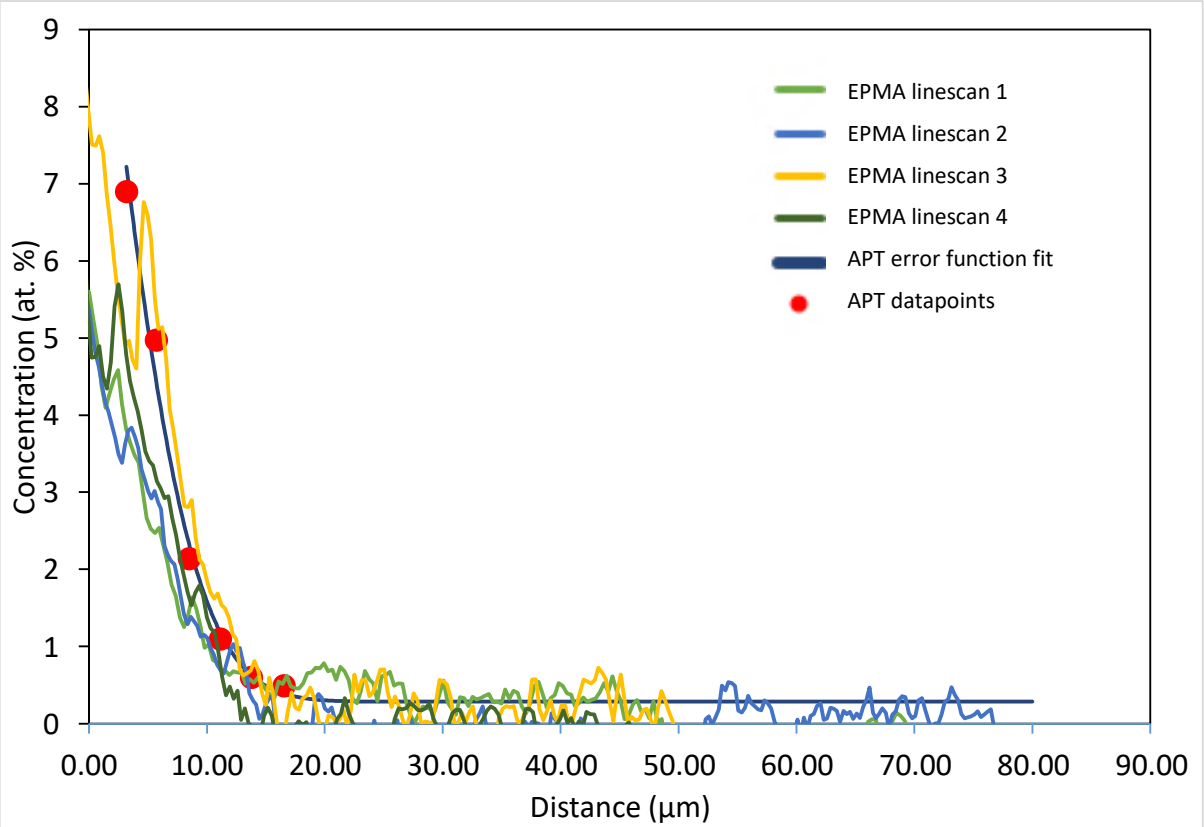


Figure 6.4: Overlay of the averaged EPMA profiles and the fully quantitative oxygen measurements taken using APT at the surface of the in-service compressor disc. Dark blue line shows error function fit to the APT data points.

Four EPMA profiles, taken to measure the oxygen concentration from the surface inwards on the *in-service* sample, are presented in Figure 6.4. The location on the surface at which the profiles were taken was chosen at random, yet the shape of the profile was found to be very similar for all four separate measurements. This is not surprising given the uniform temperature distribution experienced by the component *in-service*.

It was not possible to quantify the EPMA-measured oxygen because of a peak overlap between the K α oxygen and L β titanium X-ray lines in the WDS spectrum, which requires a standardised titanium sample containing no oxygen to deconvolve. A suitable oxygen free Ti metal standard for this could not be obtained due to the presence of an oxide film on all samples this was attempted on. Thus the background-corrected counts have been used, and the oxygen measurements should be regarded as semi-quantitative. This means confidence can be placed in the measurement of relative changes in EPMA-measured oxygen content, but absolute values should not be relied upon.

To overcome this issue and directly quantify the oxygen within the subsurface region, a series of APT samples were made at increasing depth from the compressor disc surface, and the total oxygen content of each APT sample measured. In Figure 6.4, these APT-measured oxygen concentrations (red circles) have been overlaid with the EPMA profile. A correction shift in the EPMA y-axis (oxygen concentration) was necessary to fully overlay the EPMA and APT profiles, but no shift was required in the x-axis (depth beneath sample surface). Thus we demonstrate how direct measurement of oxygen with APT can be used to calibrate EPMA profiles, with both techniques combining in a highly-complementary manner which adds confidence to their interpretation.

Figure 6.4 also shows the complementary error function, which has been fitted to the APT data. Diffusion of oxygen into the surface of the component is a form of non-steady state diffusion and can be described by a specific solution of Fick's second law [159]

$$C(x,t) = C_s - (C_s - C_0)erf(\frac{x}{2\sqrt{Dt}}) \qquad \textit{Equation 6.1}$$

where C_s is the concentration of oxygen at the surface of the material, C_0 is the concentration of oxygen in the bulk material, x is the diffusion depth, D is the diffusion coefficient and t is time. Equation 6.1 is reached by applying the following boundary conditions:

1. $C(x=\infty, t) = C_0$
2. $C(x=0, t) = C_s$

Table 6.2 shows the fitting parameters for the error function in Equation 6.1. The APT data was fitted to the model described by Equation 6.1 using orthogonal distance regression. The first row of Table 6.2 displays the values of C_s, C_0 and D that were obtained when all three of these parameters were allowed to vary. The standard error for each parameter and the sum of squares error for the fit are also displayed. Row 2 and row 3 of Table 6.2 show the values of C_o and D that result when C_s is fixed at 66 at. % (concentration of oxygen in the TiO_2 surface oxide layer) and 33 at. % (solubility limit of oxygen in the α phase). These two fixed values of C_s were chosen as two different approximations for the oxygen concentration at the exposed component surface, and the resulting fits were used as comparison points for fit 1. Fit 1 results in the smallest sum of squares error and has therefore been selected as fit that best describes the APT data. Thus the optimised values of C_s, C_o and D are 11.5 at. % O, 0.28 at. % O and 3.1E-07 μm^2/ s, respectively.

Table 6.2: Values of the fitting parameters C_s, C_0 and D in Equation 6.1 for the APT-measured oxygen profile at the surface of the in-service *sample. Red numbers indicate values of parameters that have been fixed; parameters in black have been allowed to vary freely.*

	C_s (at. %)	C_s standard error	C_0 (at. %)	C_0 standard error	D (μm^2/ s)	D standard error	Sum of squares error
Fit 1	11.5	1.13	0.28	0.29	3.1E-07	7.1E-08	0.24
Fit 2	**66**	-	1.07	0.48	5.1E-08	1.6E-08	3.61
Fit 3	**33**	-	0.94	0.45	8.7E-08	2.2E-08	2.68

Although the overall shape and depth of the EPMA profiles is consistent, subtle variations can be seen in some individual profiles. For example, in Figure 6.5 (a), a slight increase in oxygen concentration is seen at a depth of 21-51 µm. From looking at the corresponding SEM micrograph in Figure 6.5 (b) of the area profiled, it can be seen that these depths correspond to a large, equiaxed α grain, indicating dependence of oxygen concentration on microstructure.

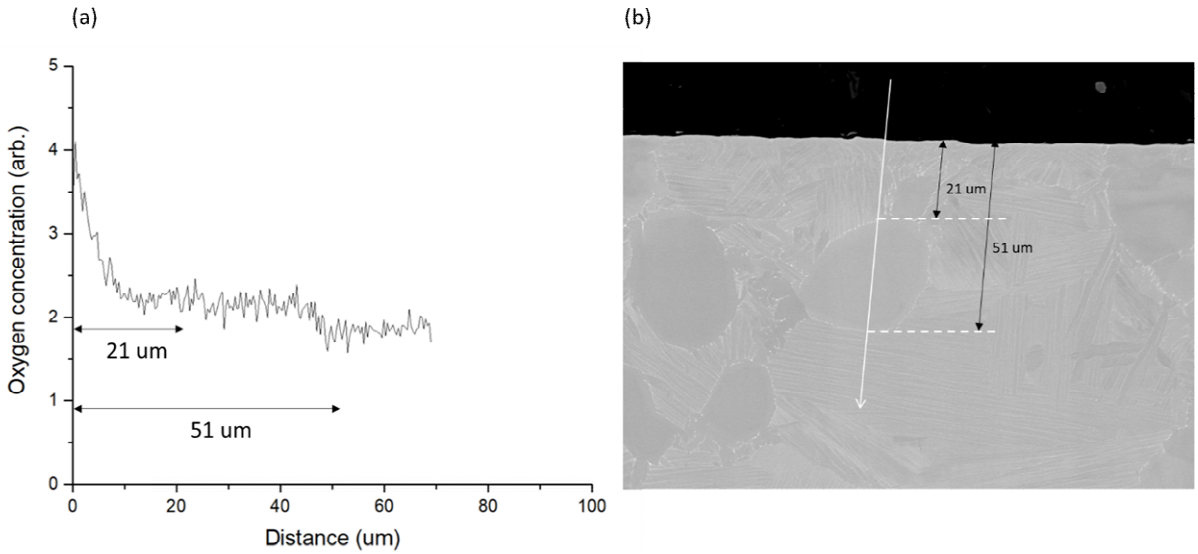


Figure 6.5: (a) EPMA- measured oxygen concentration profile and (b) corresponding SEM image indicating the microstructure over which the profile was taken. Taken at the surface of the in-service compressor disc.

6.3.2 Nanohardness measurements

Once the oxygen concentration at the surface had been mapped, it was also necessary to determine how the mechanical properties, specifically hardness, were changing as a function of depth from the surface.

Two indent arrays, also taken at randomly chosen points on the surface, give rise to the hardness profiles at two separate locations labelled *site A* (black circles) and *site B* (red squares) shown in Figure 6.6.

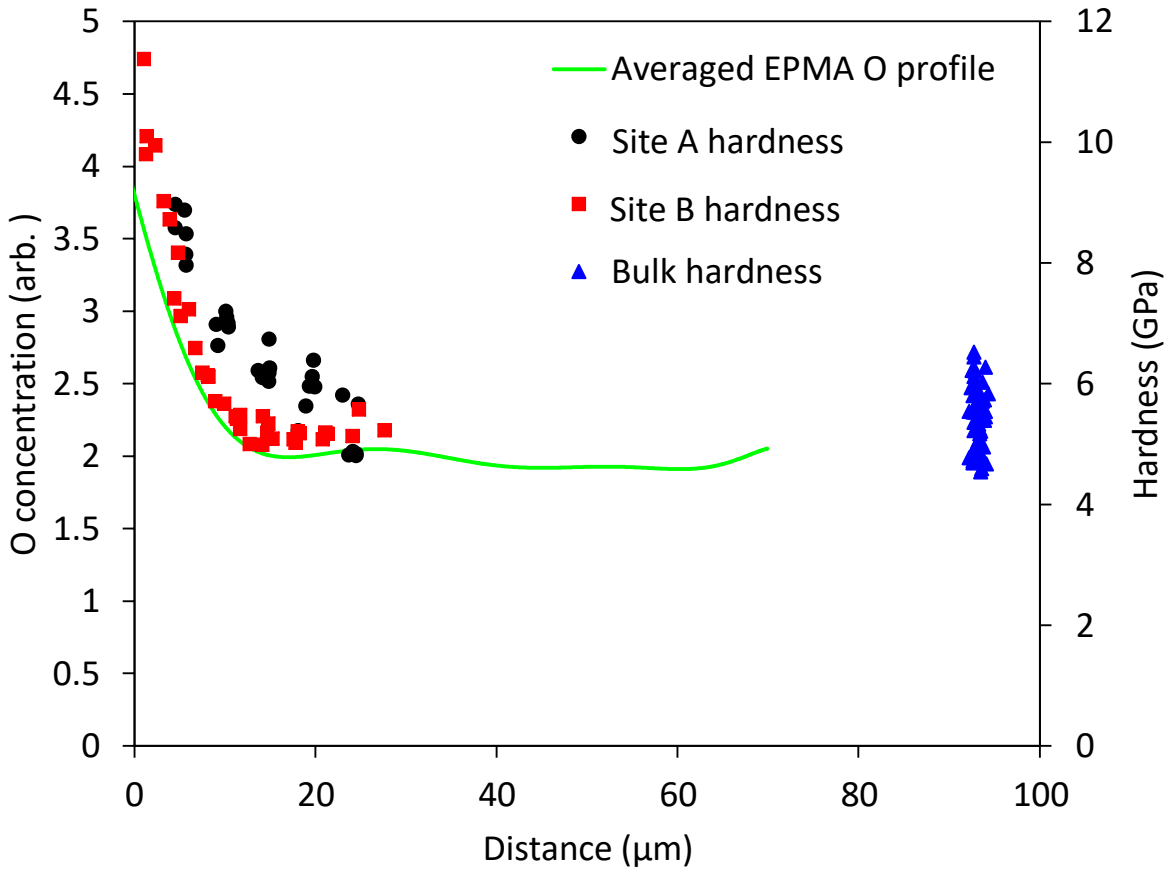


Figure 6.6: Overlay of the averaged EPMA profiles at the surface of the in-service compressor disc (green) and the two surface hardness arrays (black and red). In blue are the hardness measurements taken from the bulk indents at a constant depth of 95 µm from the surface.

The hardness profile from *site A* is the same shape as that at *site B*, but the hardness at *site A* is consistently slightly higher. To further explore the cause of this hardness difference, and to investigate if it was related to microstructure and crystal orientation, a set of indents were made in the bulk of the compressor disc material. Indents were made at a constant depth of 95 µm from the surface, well away from the influence of the oxygen profile. The hardness values from this can be seen in Figure 6.6 (blue triangles), and the results are presented in more depth in Figure 6.7 (a). The microstructure of the region indented can be seen clearly in the backscattered

electron image in Figure 6.7 (b). The EPMA line scan in Figure 6.7 (c) shows that oxygen concentration measured adjacent to the bulk indents does not vary significantly. Grain orientation information was obtained from the IPF Z map of the indented region in Figure 6.7 (d), and the second Euler angle was extracted for each indented grain, which is equal to the declination angle in the hexagonal α-Ti crystal system [225]. The declination angle is the angle between the crystal c-axis and the indent loading direction, and was combined with the hardness measurement for each indent that did not interact with a grain/ phase boundary. The results of this are presented in Figure 6.8, which shows that grains that have a small angle between their c-axis and the sample surface normal are harder, in good agreement with trends measured in the literature [77,226].

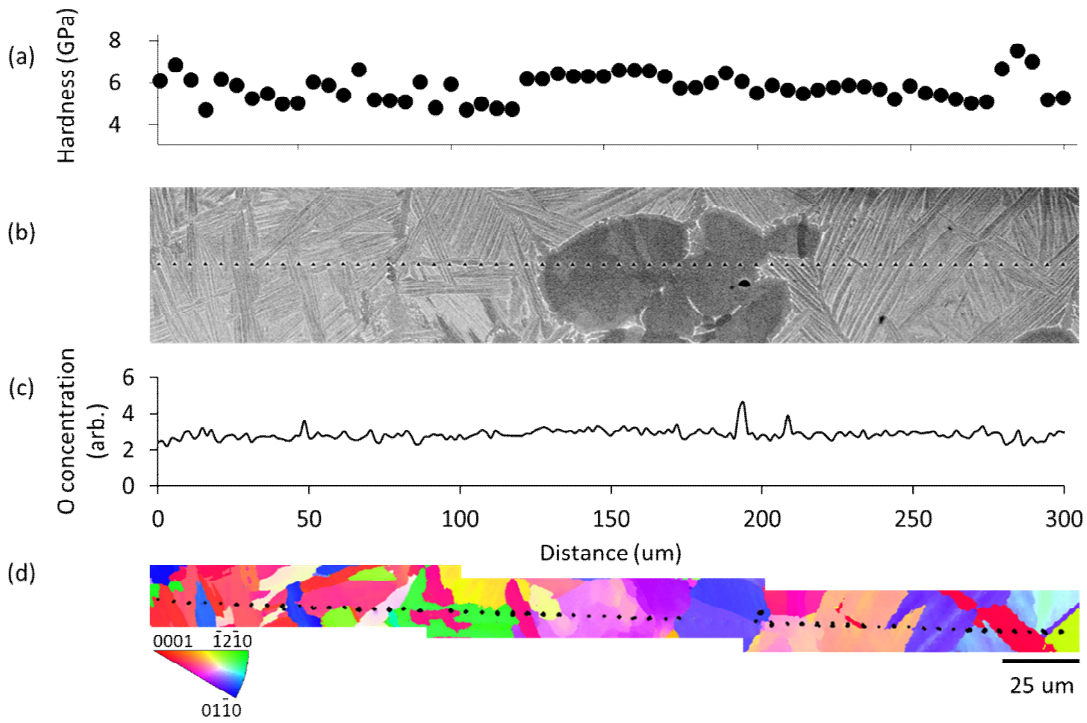


Figure 6.7: (a) Hardness plotted along the length of the indent profile. (b) BSE image showing the microstructure of the region indented. Contrast between the large α grain in the middle of the image and the surrounding α / β laths can be seen. (c) EPMA-measured oxygen line profile measured adjacent to the indent profile, showing the oxygen concentration is relatively constant. (d) IPF Z map showing the orientation of the indented grains in the bulk material at a constant depth of 95 µm from the surface.

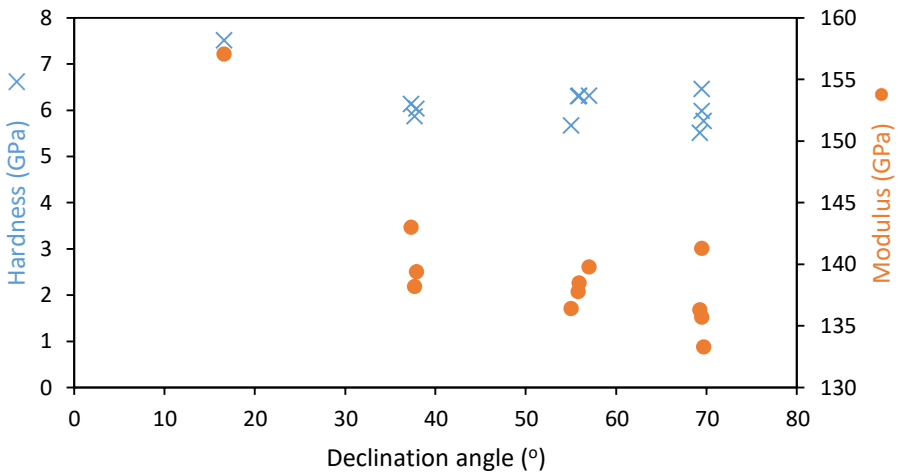


Figure 6.8: Hardness and modulus of the bulk TIMETAL 834 compressor disc sample plotted as a function of grain declination angle.

6.4 *LAB-CONTROLLED* SAMPLE

Since the environmental conditions that the compressor disc was exposed to cannot be well defined, a piece of TIMETAL 834 was heated in air for 1000 hours at 550°C to form an *oxygen-rich layer* under controlled conditions, referred to as the *lab-controlled* sample. APT samples were taken at increasing depth from the surface of the sample to measure the oxygen concentration profile from the surface inwards. The EDS maps, EBSD pattern quality map and IPF X map in Figure 6.9 (b)-(i), (j) and (k), respectively, show the microstructure and elemental segregation within the region from which APT samples were made. It can be seen from Figure 6.9 (a) that the section of the APT liftout bar nearest the sample surface contains an α/ β lath region. Figure 6.9 (e), (f) and (i) show segregation of Nb, Mo and Zr to the β phase in this lath region. The two grains that make up the majority of the APT liftout bar can be seen in Figure 6.9 (k) to be of similar crystallographic orientation, despite having different microstructure morphologies. The Si and O rich particle in Figure 6.9 is a piece of surface contamination.

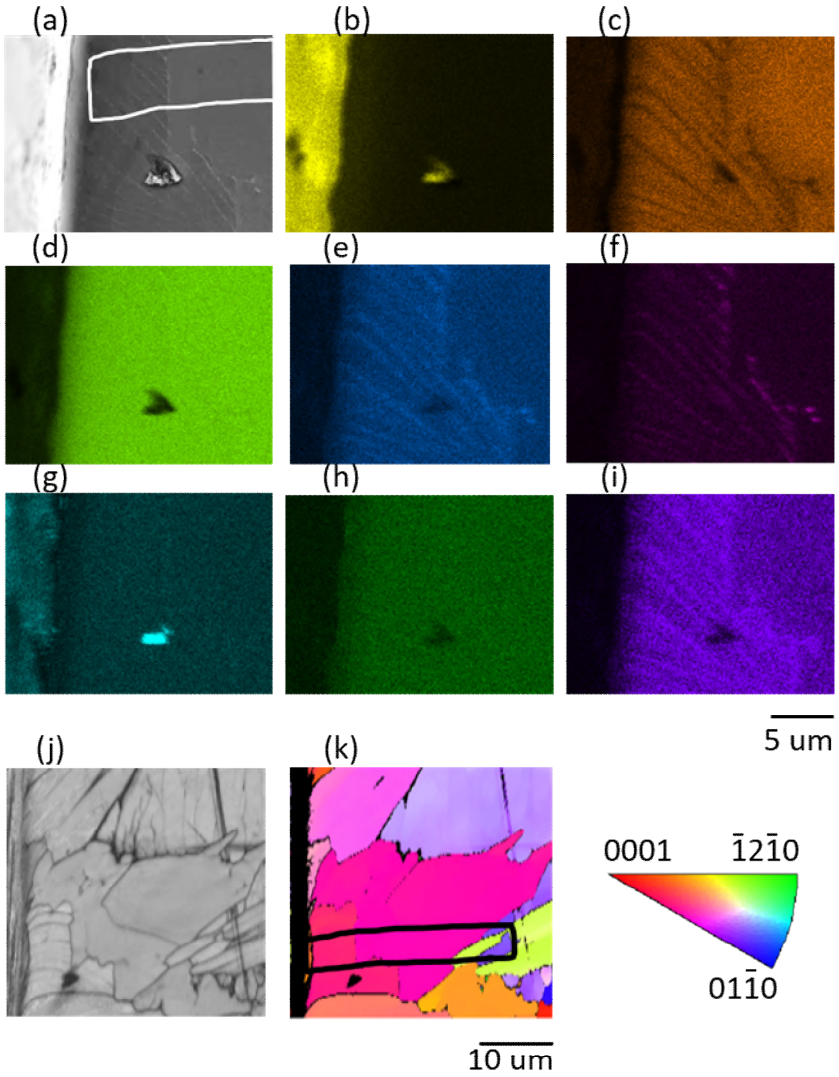


Figure 6.9: (a) SEM image and corresponding EDS maps for (b) O, (c) Al (d) Ti, (e) Nb, (f) Mo, (g) Si, (h) Sn and (i) Zr showing distribution of elements within the region from which APT samples were prepared in the TIMETAL 834 lab-controlled sample. (j) EBSD pattern quality map and (k) IPF X image the microstructure and the grain orientation of the region from which the APT liftout was created. Boxes on (a) and (k) indicate regions from which the APT liftout bar was created.

Figure 6.10 shows the fitted oxygen concentration profile for both the *in-service* and *lab-controlled* sample, for comparison. As for the *in-service* sample, the data was fitted using orthogonal distance regression. Fit 1 in Table 6.3 was selected and plotted for the *lab-controlled* sample since this resulted in the smallest sum of squares error. The optimised values of C_s, C_0 and D for the *lab-controlled* sample are 11 at. % O, 0.35 at. % and 1.4E-06 μm^2/ s, respectively.

Table 6.3: Values of the fitting parameters C_s, C_0 and D in Equation 6.1 for the APT-measured oxygen profile at the surface of the lab-controlled *sample. Red numbers indicate values of parameters that have been fixed; parameters in black have been allowed to vary freely.*

	C_s (at. %)	C_s standard error	C_0 (at. %)	C_0 standard error	D (μm²/s)	D standard error	Sum of squares error
Fit 1	11.0	0.21	0.35	0.02	1.4E-06	5.5E-08	0.01
Fit 2	**66**	-	0.58	0.21	5.7E-08	5.8E-08	1.28
Fit 3	**33**	-	0.58	0.21	1.0E-07	1.0E-07	1.28

The activation energy for formation of the *oxygen-rich layer* can be calculated from this value of diffusion coefficient using

$$D = D_0 e^{-\frac{Q}{RT}} \quad [159] \qquad \textit{Equation 6.2}$$

where D_0 is the diffusivity, Q is the activation energy for *oxygen-rich layer* formation, R is the gas constant and T is temperature.

Table 6.4: Literature values of D_0 for diffusion of oxygen in α-Ti and some titanium alloys.

Material	D_o (m²/s)	Method used	Reference
α-Ti	2±1E-07	Calculated from ^{18}O depth profiles at 623–873 K that were measured using nuclear resonance techniques	[227]
α-Ti	2.04E-06	Calculated using kinetic Monte Carlo methods	[97]
α-Ti	4.97E-11	Calculated from O depth profile measured using Auger electron spectroscopy between 773 and 823 K	[228]
α-Ti	4.08E-05	Calculated from mass gain measurements during oxidation experiments between 923-1148 K	[229]
α-Ti	4.50E-05	Calculated from ^{16}O depth profiles at 733–973 K that were measured using nuclear microanalysis	[230]
TIMETAL 834	1.00E-05	Calculated from hardness profiles at 873- 1173 K	[231]
Ti-6242	6.54E-07	Calculated from hardness profiles (confirmed by EPMA oxygen depth profiles) at 773-973 K	[162]

The activation energy, *Q,* can be calculated from Equation 6.2, using the fitted value of *D* in row 1 of Table 6.3 and a value of D_0 from the literature. Table 6.4 shows the range of values of D_0 for oxygen in titanium that are reported in the literature, and calculating *Q* using each of these literature values of D_0 gives a range of activation energies from 119-213 kJ mol^{-1}. The literature value of D_0 of 1E-5 m^2/s [231] was selected since it was determined using material of similar composition and microstructure to the TIMETAL 834 in this study; the resultant calculated *Q* value is 203 kJ mol^{-1}. This is higher than reported activation energy for *α case* formation in α + β TIMETAL 834 (160-184 kJ mol^{-1}) [154,156,231], but is of the same order of magnitude. For comparison, the activation energy for *α case* formation in β solution treated TIMETAL 834 was reported to be 223 kJ mol^{-1} [156]. Thus it seems activation energy is sensitive to β volume fraction, and it is possible that the β volume fraction in the material in this study is higher than usual.

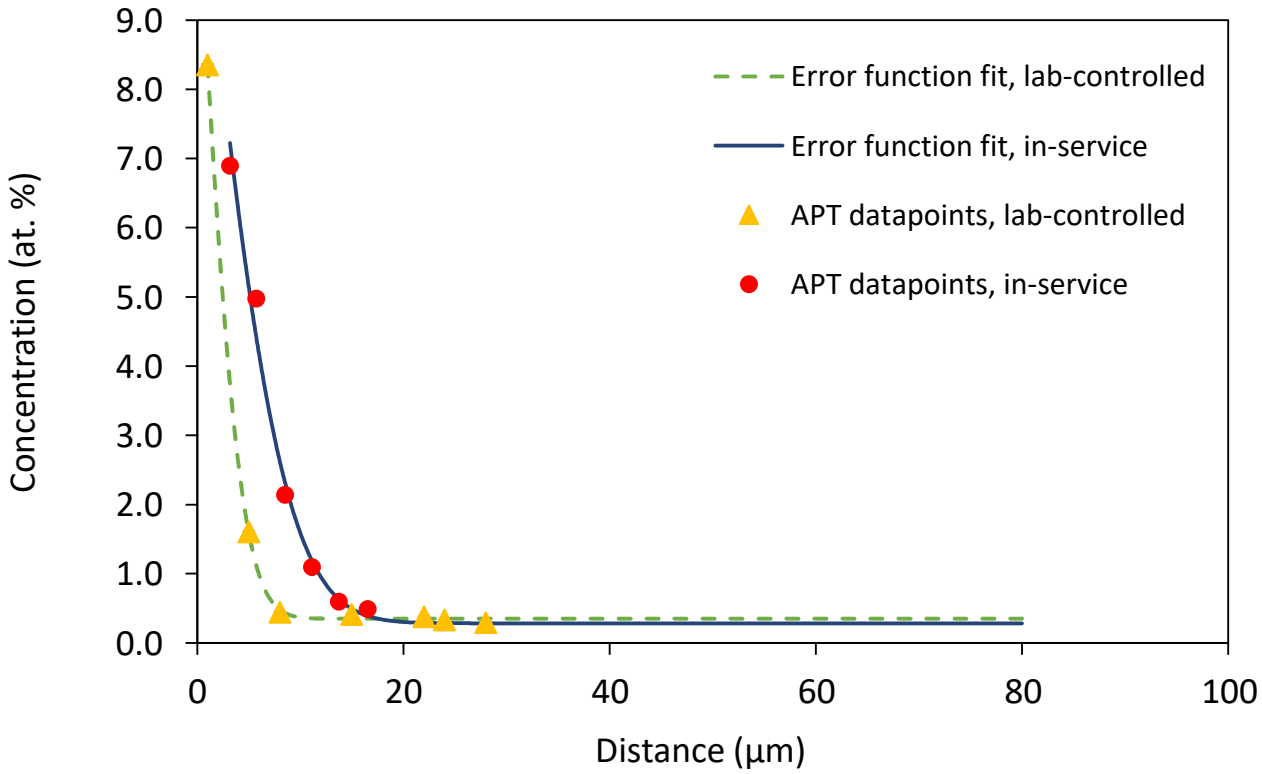


Figure 6.10: APT-measured oxygen concentration profiles and fitted error function in the in-service component and lab-controlled sample.

Taking *Q* to be the value calculated for the *lab-controlled* sample, and D_o to be 1E-5 m^2/s [231], we can use Equation 2.4 to calculate a representative operating temperature experienced by the

component. The temperature calculated is 510°C, which is within the operating temperature window of the component.

Figure 6.11 shows APT atom maps for the sample that was taken from nearest the surface, which has the highest oxygen concentration. Within the needle, a Mo-rich phase can be seen. Leading away from this phase is a region enriched with Sn, Nb and TiO, and depleted in Al and Zr, as shown by the isoconcentration surfaces in Figure 6.11. While the isoconcentration surfaces are used qualitatively to visually demarcate the phases, for quantitative analysis, an overlap-solved proximity histogram was created across the Al isoconcentration surface, indicated in Figure 6.12. The Mo-rich phase was isolated using a 2.0 at. % isoconcentration surface, and found to be of composition Ti0.64-Mo0.23-Al0.02-Nb0.07.

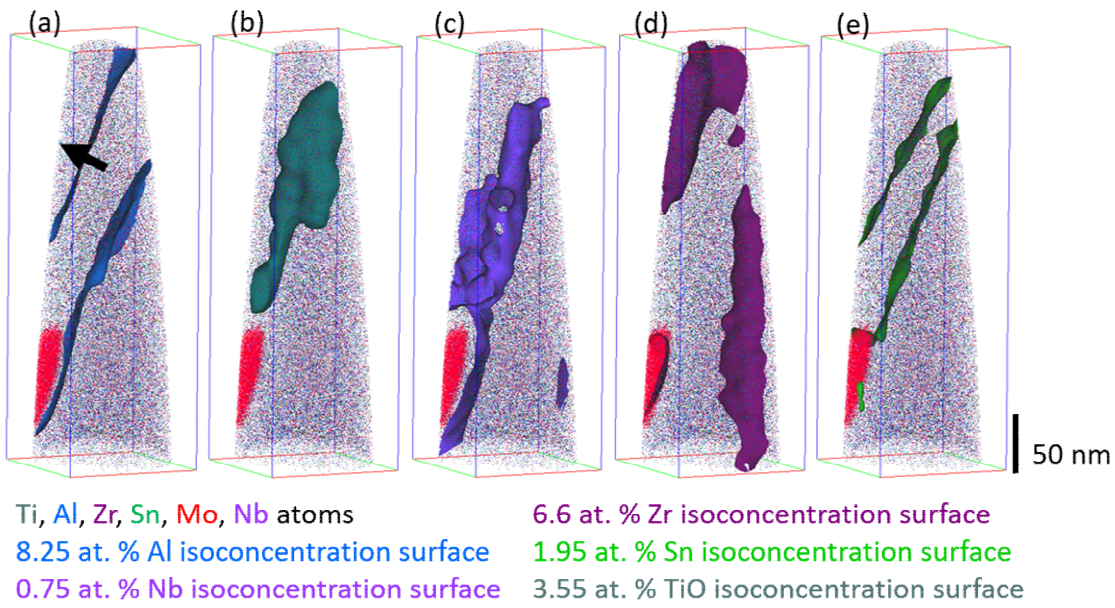


Figure 6.11: APT atom maps with isoconcentration surfaces showing the segregation of (a) Al and(d) Zr away from a possible α -β boundary and segregation of (c), Nb,(b) TiO and (e) Sn along a possible α / β phase boundary in the lab-controlled sample. Black arrow indicates the Al isoconcentration surface across which the proximity histogram in Figure 10 are calculated.

The *lab-controlled* sample was heat treated at 550°C with the aim of forming α_2. The temperature was selected based on supporting calculations carried out using Thermo-Calc 2017a with the ThermoTech Ti-based Alloys Database (v3) ,which showed α_2 formation within the range 400-562°C. As no clear α_2 regions were visually apparent in the atom maps, it was decided to employ a

more sensitive statistical approach to look for these. For this, in each APT dataset the deviation of the distribution of aluminium atoms from a random solid solution was measured by calculating the Pearson coefficient, μ, for aluminium [232]. Some deviation from random in the distribution of aluminium was observed for the three samples nearer the surface (see Table 6.5). However, no aluminium-rich precipitates could be identified using isoconcentration surfaces for voxels of side length 0.5-2 nm, and delocalisation of 1-3 nm.

Table 6.5: Calculated values of Pearson coefficient (μ) for APT samples taken at increasing depth from the surface of the compressor disc.

Distance from surface (μm)	$\mu_{measured}$	μ_{random}
3.18	0.0482	0.0054
5.71	0.0179	0.0055
8.49	0.0096	0.0041
11.12	0.006	0.0017
13.75	0.0054	0.0017
16.53	0.0031	0.0017

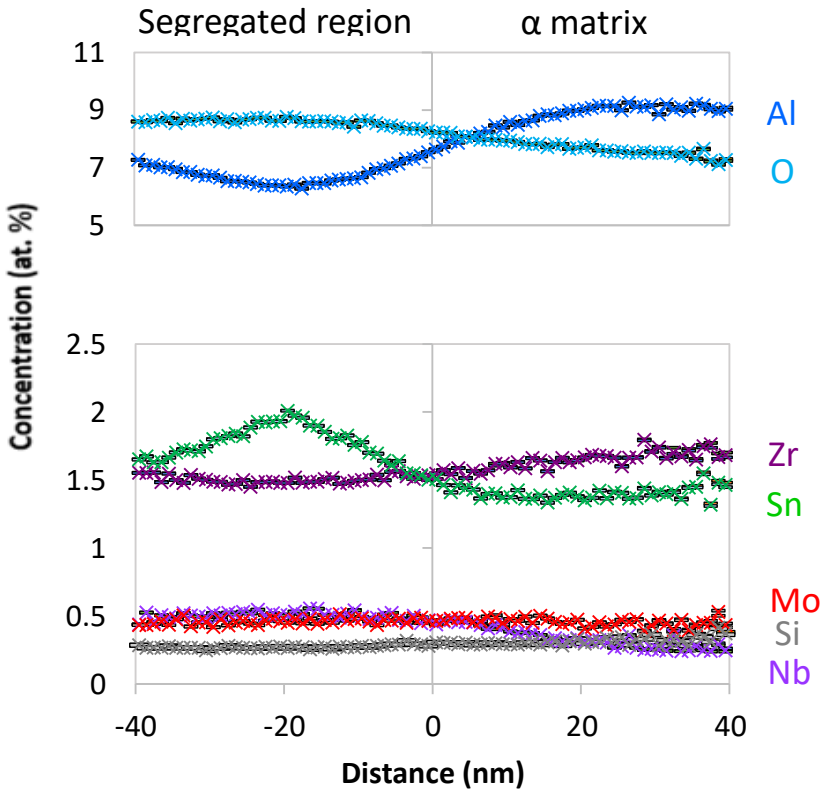


Figure 6.12: Overlap-solved proximity histograms calculated across the Al isoconcentration surface indicated by the black arrow in Figure 9 (a). The proximity histograms quantify the enrichment of O, Sn and Nb, and the depletion of Al and Zr, in the segregated region. Measurements taken in the lab-controlled sample.

6.5 Discussion

Excellent agreement between the shapes of the EPMA- and APT-measured oxygen profiles, as seen in Figure 6.4 , validates the use of APT to produce fully quantitative oxygen profiles from a set of discrete measurements. This is of particular importance since accurate quantitative oxygen measurements in titanium are challenging to obtain with other techniques on this length scale.

Figure 6.5 shows that oxygen concentration within the *oxygen-rich layer* has some dependence on microstructure; there is a clear drop in oxygen concentration from the large equiaxed α grain to the fine α / β lamellar structure. A number of factors are known to affect oxygen diffusivity, and thus penetration depth, in near-α-Ti alloy. Leyens et al. [139] observed that the depth of the oxygen diffusion zone is greater for bimodal microstructures compared to lamellar microstructures. They attribute this to the larger number of phase boundaries available in the

bimodal microstructure, which can act as fast diffusion paths for oxygen. However, more recent work by Satko et al. [11] shows the opposite trend; the *oxygen-rich layer* is deeper for the lamellar microstructure. This can be explained by considering the dependence of oxygen penetration on the alignment of interfaces relative to the oxygen-exposed surface; α / β phase boundaries perpendicular to the sample surface increase oxygen ingress [10] and thus it is possible that a large proportion of boundaries in the Leyens lamellar microstructure were unfavourably oriented. The α/ β laths across which oxygen concentration was measured in Figure 6.5 (b) are oriented almost parallel to the oxygen-exposed surface. This unfavourable orientation of the α / β phase boundaries results in lower oxygen diffusivity, which could account for the lower oxygen concentration in the α/ β lath region compared to the equiaxed α grain.

Hardness has been directly measured as a function of depth from the component surface and found to independently agree with the shape and depth of the oxygen profiles, as can be seen in Figure 6.6. This supports the idea that interstitial oxygen alone is causing the hardening, and that there is no β denudation, in line with the definition of *oxygen-rich layer* introduced by Satko et al. [11]. The lack of evidence for α_2 precipitates also corroborates the idea that interstitial solid solution hardening is dominant in this surface region.

Analysis of bulk indents shows that grains with a small declination angle are harder, and thus the crystal orientation has an effect on the measured hardness. The oxygen EPMA profile in Figure 6.7 (c) shows no significant change in oxygen concentration along the length of the bulk indents, meaning oxygen can be discounted as a variable affecting relative hardness changes in the bulk material. However, it is likely that microstructure is playing a role in the observed variation in bulk hardness, seen in Figure 6.7 (a). Ghamarian et al. [84] report that equiaxed α grains are the softest microstructural components in α + β alloys, such as TIMETAL 834. When Figure 6.7 (a) and (b) are compared, it can be seen that some lower hardness regions correspond to areas where there are large α grains. The relatively small area of microstructure sampled in Figure 6.7 makes it

difficult to distinguish the contributions of microstructure and grain orientation to bulk hardness. Further work is needed to study a greater region of material that includes a higher volume fraction of both equiaxed α grains and α / β lath regions, and this is explored in Chapter 7. However, we can conclude that both microstructure and grain orientation are giving rise to the variation in the bulk hardness measurements in Figure 6.7 (a). This likewise also leads to the suggestion that grain orientation and microstructure are contributing to the variation in the height of the surface hardness profiles at *sites A* and *B*, in Figure 6.6.

Since interstitial oxygen is the dominant hardening mechanism, the varying oxygen concentration within the *oxygen-rich layer* will contribute to hardness changes, in addition to the hardness contributions from crystal orientation and microstructure. Furthermore, the diffusion of oxygen from the surface of the component is affected by the microstructure, as evidenced by Figure 6.5. This in turn will dictate how the hardness changes as a function of depth. Further work involving a careful study of a range of microstructures, textures and oxygen contents is needed to determine the relative contributions to hardness of these factors. However, from this work we can already see that changes in hardness due to crystal orientation and microstructure, as outlined in Figure 6.5 and Figure 6.7, are minor compared to the change in hardness as a function of depth due to oxygen ingress.

The extent of oxygen penetration was determined by calculating the depth at which the gradient of the fitted oxygen concentration profiles, in Figure 6.10, was less than 1 ppm O/micrometre. The oxygen penetration depths were found to be 27.6 µm and 14.3 µm for the *in-service* and *lab-controlled* sample, respectively. The deeper oxygen penetration depth for the *in-service* sample is expected since the exposure time for an *in-service* component is typically much longer than 1000 hours, and the flight cycles experienced are more complex and will have had higher temperature exposure than the isothermal treatment at 550^{o}C given to the *lab-controlled* sample. Lack of microstructural change (β denudation) observed in the *lab-controlled* and *in-service* material also

points towards both samples having experienced similar temperatures that are below the β transus locally.

The APT dataset taken from nearest the surface of the *lab-controlled* sample, seen in Figure 6.11, contains a small piece of Mo-rich phase. The composition measured, Ti0.64-Mo0.23-Al0.02-Nb0.07, is consistent with that of the ordered intermetallic Ti_2(Al, X) phase, where X= Nb, Mo [233].

The isoconcentration surfaces in Figure 6.11 show tin and niobium segregate in a plane ahead of the molybdenum-rich phase, and aluminium segregates strongly away from this plane. This is supported by the proximity histograms in Figure 6.12, which are calculated across the aluminium isoconcentration surface indicated by the arrow in Figure 6.11 (a).

The 1D concentration profile across the unexposed α-β interface in Figure 6.3 (a) shows segregation of aluminium away from the β phase, and segregation of niobium towards the β phase. Niobium and aluminium exhibit similar behaviour in the segregated region, shown on Figure 6.12. Molybdenum also strongly segregates to the β phase in Figure 6.3(a), whereas it shows no strong preference in Figure 6.12. However, the presence of the molybdenum-rich phase, seen in Figure 6.11 , may have depleted the segregated region of molybdenum. The similarities in segregation behaviour between the unexposed α-β interface in Figure 6.3(a) and the segregated region in Figure 6.12 suggest that the plane ahead of the molybdenum-rich phase is a piece of β phase that is depleted in β stabilising elements as a result of formation of the molybdenum-rich phase. When examined in context of the SEM and EDS images in Figure 6.9, it can be seen that the region nearest the surface from which this APT sample was taken contains α / β laths, with niobium partitioning to the β phase, and α-stabilising aluminium partitioning away from β phase. The laths are oriented at an acute angle to the oxygen-exposed surface, and thus favourably oriented to act as fast diffusion paths for oxygen. Inspection of the APT maps corresponding to this surface sample in Figure 6.11 does indeed reveal segregation of TiO ahead

of the molybdenum-rich phase. Thus it seems that Figure 6.11 (b) shows oxygen diffusing preferentially along an α / β boundary that is acting as a fast diffusion path, ahead of a molybdenum-rich phase.

6.6 CONCLUSIONS

A detailed, multi-technique approach was taken to characterise the *oxygen-rich layer* on a Ti-alloy compressor disc that has experienced *in-service* civil aerospace gas-turbine engine conditions. Oxygen concentration was directly measured and quantified as a function of depth from the surface using Atom Probe Tomography, and the resultant oxygen diffusion profile obeys Fick's second law. Fitting the APT-measured oxygen profile using the complementary error function yields an activation energy for formation of the *oxygen-rich layer* of 214 kJ mol^{-1}, which is consistent with literature values [154,156,231].

The oxygen ingress depth was found to be 21.3 µm and 13.7 µm for the *in-service* and *lab-controlled* sample, respectively. Since the conditions experienced by both these samples was equivalent to the intermediate *in-service* temperatures described by Satko et al. [11], no β denudation was observed and the oxygen ingress depth is considered to be the depth to which the mechanical properties are detrimentally affected.

The shape of the APT- and EPMA-measured oxygen profiles agree, as do the surface hardness profiles, indicating that interstitial oxygen is the main hardening mechanism within the *oxygen-rich layer*. The contributions of microstructure and crystal orientation to the hardness measurements have been qualitatively studied, but further work is needed to quantify the relative contributions. However, oxygen content as a function of depth has a greater impact on hardness than microstructure and crystal orientation, highlighting the importance of using APT to accurately quantify oxygen concentration. Moreover, oxygen ingress has been shown to be affected by microstructure on both the micron-scale, using EPMA, and on the nanoscale, through

use of APT. Both of these techniques underline the effect of α/ β interfaces on oxygen ingress. This information could pave the way for modifications in alloy processing to control the proportion and orientation of α / β interfaces present in the surface region. This has the potential to reduce oxygen ingress and ultimately increase component lifetimes.

7 UNDERSTANDING THE RELATIONSHIP BETWEEN CRYSTAL ORIENTATION, MICROSTRUCTURE, OXYGEN INGRESS AND HARDNESS

7.1 INTRODUCTION

In Chapter 6, characterisation of the *oxygen-rich layer* formed *in-service* on a compressor disc component revealed that crystal orientation and microstructure have a role to play in dictating the hardness of titanium alloys. However, oxygen ingress was found to be the major contributor to the hardness change as a function of depth in the material. This Chapter studies the relative contributions of crystal orientation, microstructure and oxygen ingress to hardness changes at the surface of the compressor disc in closer detail.

The study of the interdependence of crystal orientation, microstructure, oxygen ingress and hardness in Chapter 6 was performed on a small region of a cross section of the compressor disc surface, approximately 300 x 10 µm in area. To sample a more representative area of microstructure, a surface region of area 350 x 50 µm was mapped here, using a combination of EPMA, EBSD, BSE imaging and nanoindentation.

7.2 DATA COLLECTION AND PROCESSING

To better understand how the hardness is changing throughout the microstructure, a hardness mapping technique was used. This makes use of the Express Test mapping option on the Nano Indenter G200 setup, which performs 1 indent per second compared to 1 indent per 3 seconds, allowing maps of tens of thousands of indents to be made in a matter of hours. The fast rate at which indents can be performed, and the accurate positioning of shallow indents at relatively small spacing (1 µm), enables the hardness of large areas to be mapped. Hardness maps can, as a consequence, be more easily correlated with complementary EBSD and EPMA maps than indentation line profiles or smaller, discrete indent arrays. For this sample, this may allow the deconvolution of the effect of composition and crystallographic effects on hardness. This study

aims to set up the analysis procedure for combining these analytical techniques as a proof of concept that can be further developed in the future.

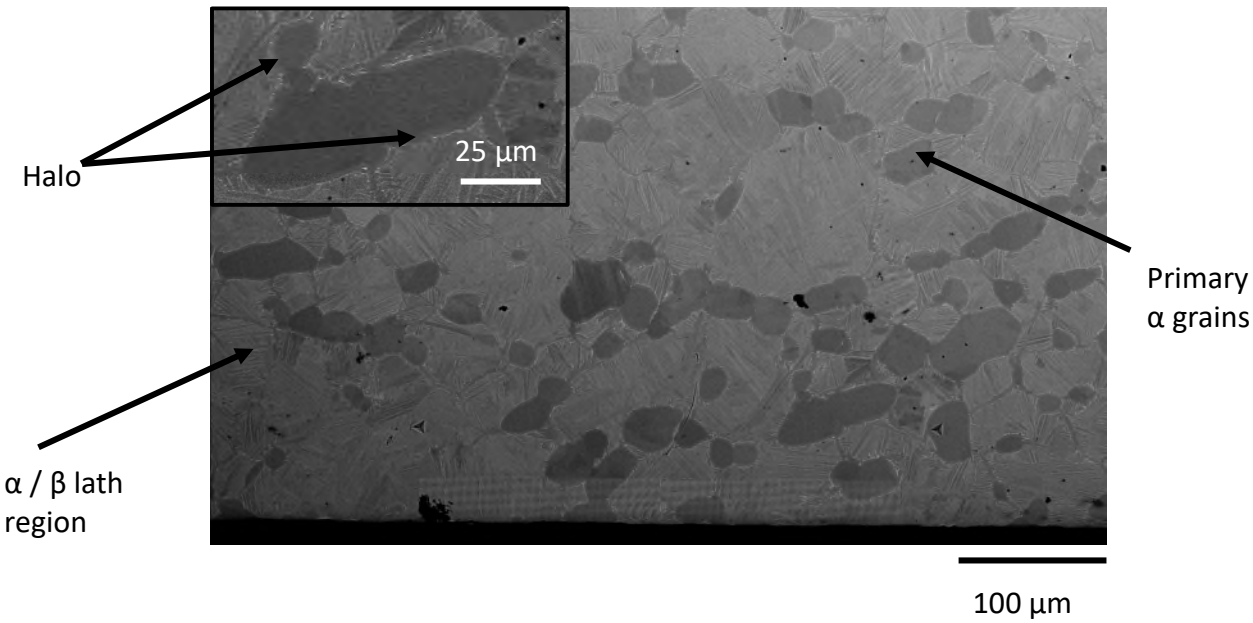


Figure 7.1: Overview backscattered electron image showing the microstructure of the TIMETAL 834 compressor disc. The indented region of interest is at the bottom of the image, which is the surface of the compressor disc; the top of the image is the bulk of the compressor disc. Inset shows an example of an α grain halo.

Figure 7.1 shows the heterogeneous distribution of the α grains. Additionally, it can be seen that there is some structure within the α grains; they are clearly non-uniform. In particular, there is a 'halo' that can be seen on the BSE image around the edge of the α grains. This points to increased concentrations of heavier, β stabilising elements at the edge of the grain compared to the centre, which is in agreement with the observations of Dichtl et al. [234] on the same alloy. The primary α has mainly formed at the intersection of multiple transformed β grains and, in some cases, along prior β grain boundaries. This is the expected microstructure for this alloy, under the standard processing conditions.

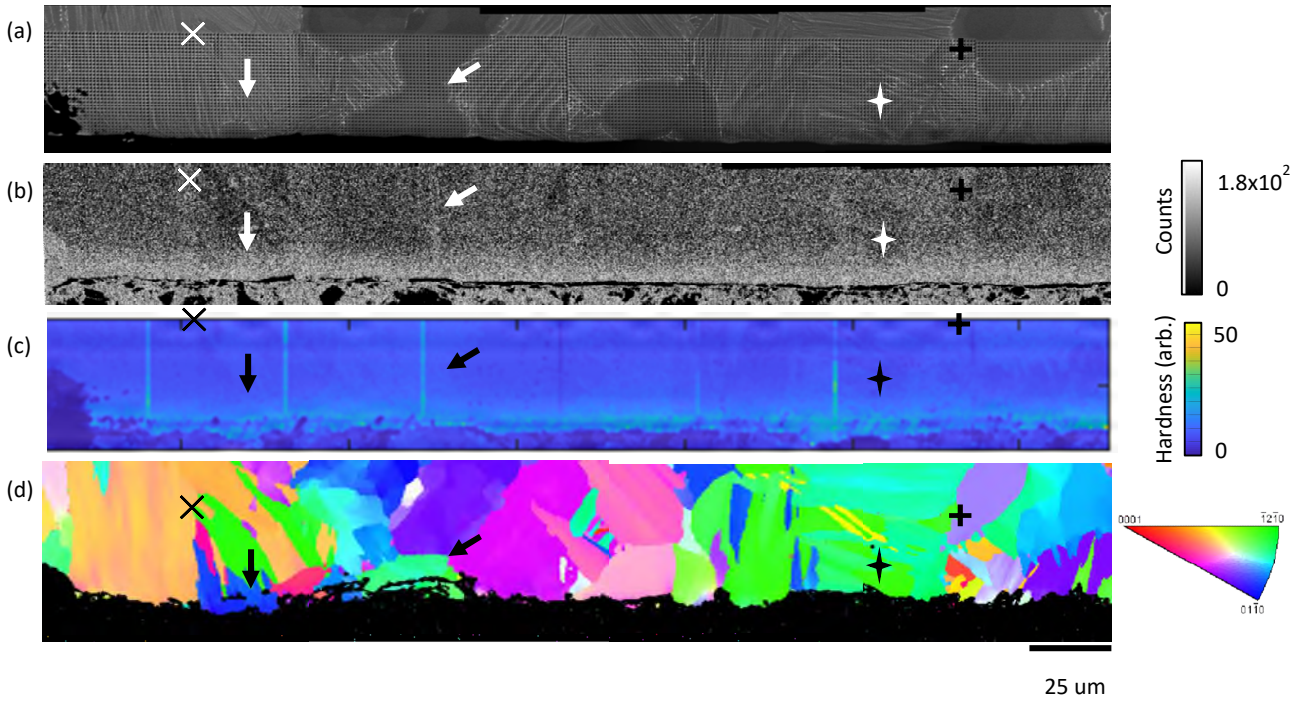
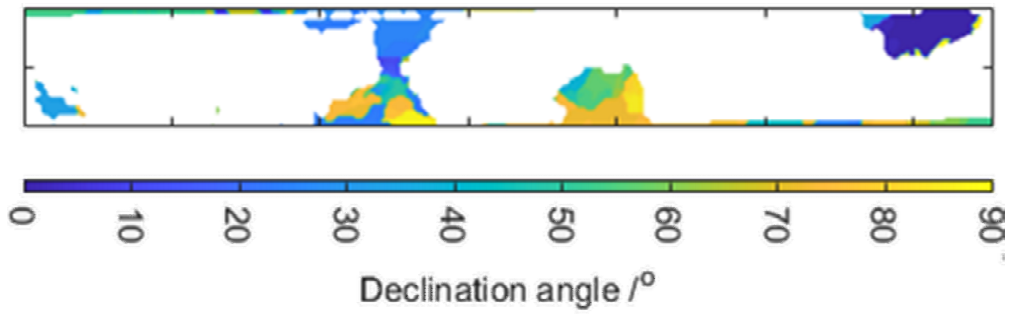


Figure 7.2: (a) shows the backscattered electron image of the indented region of interest. (b) shows the electron probe microanalysis oxygen map (c) shows the hardness map and (d) shows the IPF Z map, all of the same region of interest. The five sets of symbols indicate examples of common features on each of the maps.

Figure 7.2 (a) examines more closely the surface region of interest. β stabilisers that partition to the β phase, such as Mo and Nb, have a higher atomic number than typical α phase stabilisers, such as Al. Thus, the β phase can be seen more clearly as white, high contrast regions around the edge of the large α grains, as well as in the α / β lath regions. Comparing Figure 7.2 (a) and Figure 7.2 (d) reveals that some of the large α grains contain multiple regions of different orientations. In Figure 7.2 (b) the oxygen EPMA map reveals some variation in oxygen content with microstructure, while some grains and lath features can be seen on the hardness map in Figure 7.2 (c). Figure 7.2 (d) shows the change in grain orientation between different regions of microstructure. These independent maps of oxygen content, hardness and grain orientation are all useful separately, but overlaying the data enables trends and relationships to be analysed in much greater depth. Figure 7.2 (c) was created by tiling eight hardness arrays. The vertical lines are from where two adjacent hardness arrays have overlapped slightly, due to the limited precision in the stage movement of the nanoindentor. Minimal pile-up of material was observed

around the indent marks, but any pile-up would be likely to increase the measured hardness [235].

(a)



(b)

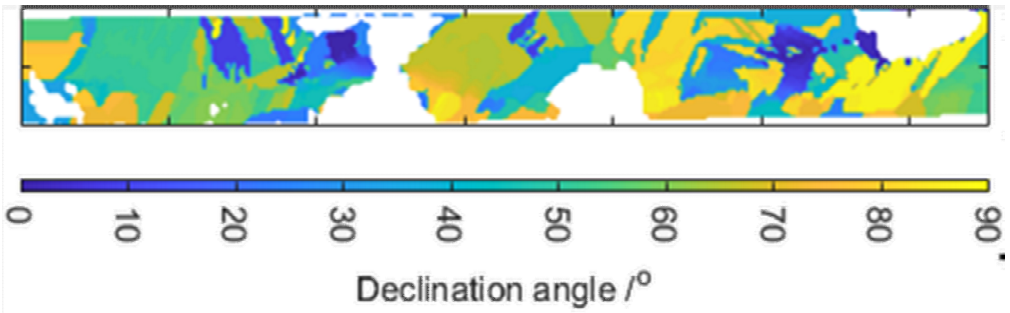


Figure 7.3: Map of the phi angle showing the extracted regions of microstructure corresponding to the (a) α grains and (b) lath regions.

The array of hardness measurements was used as the reference grid to which all other map data was aligned. Pairs of control points, distinct features that were identifiable on both the BSE image and the hardness map, were manually selected and used to infer a geometric transform that would overlay the two sets of data. Features used as control points include grain boundaries and phase interfaces, and five sets of control points are represented with symbols on Figure 7.2, as an example. The EPMA and EBSD data was overlaid with the hardness data in the same way. The BSE image was used to segment the area studied into α grains and transformed β lath regions by making use of the lower contrast of the α grains compared to the lath regions. This enabled

hardness, declination angle of the α phase (mined from the EBSD data) and oxygen content measurements to be extracted separately for the lath regions and α grains. For example, the grain orientation maps corresponding to the α grain and lath regions can be seen in Figure 7.3. A hardness threshold was selected such that data below 4.5 GPa, mainly corresponding to the indents in the Bakelite mounting material, was discarded. Figure 7.4 shows the hardness data that was retained.

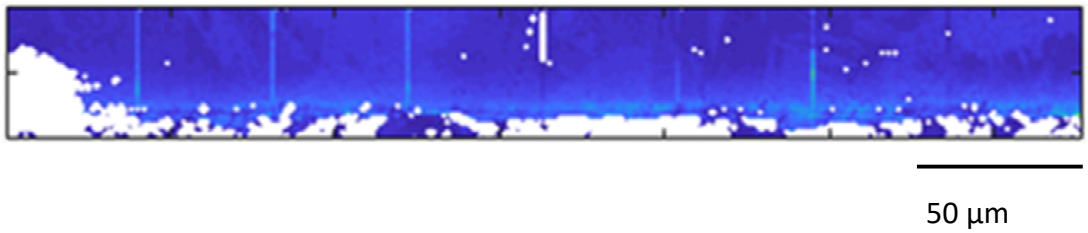


Figure 7.4: Hardness map showing the data retained after filtering out hardness values below 4.5 GPa.

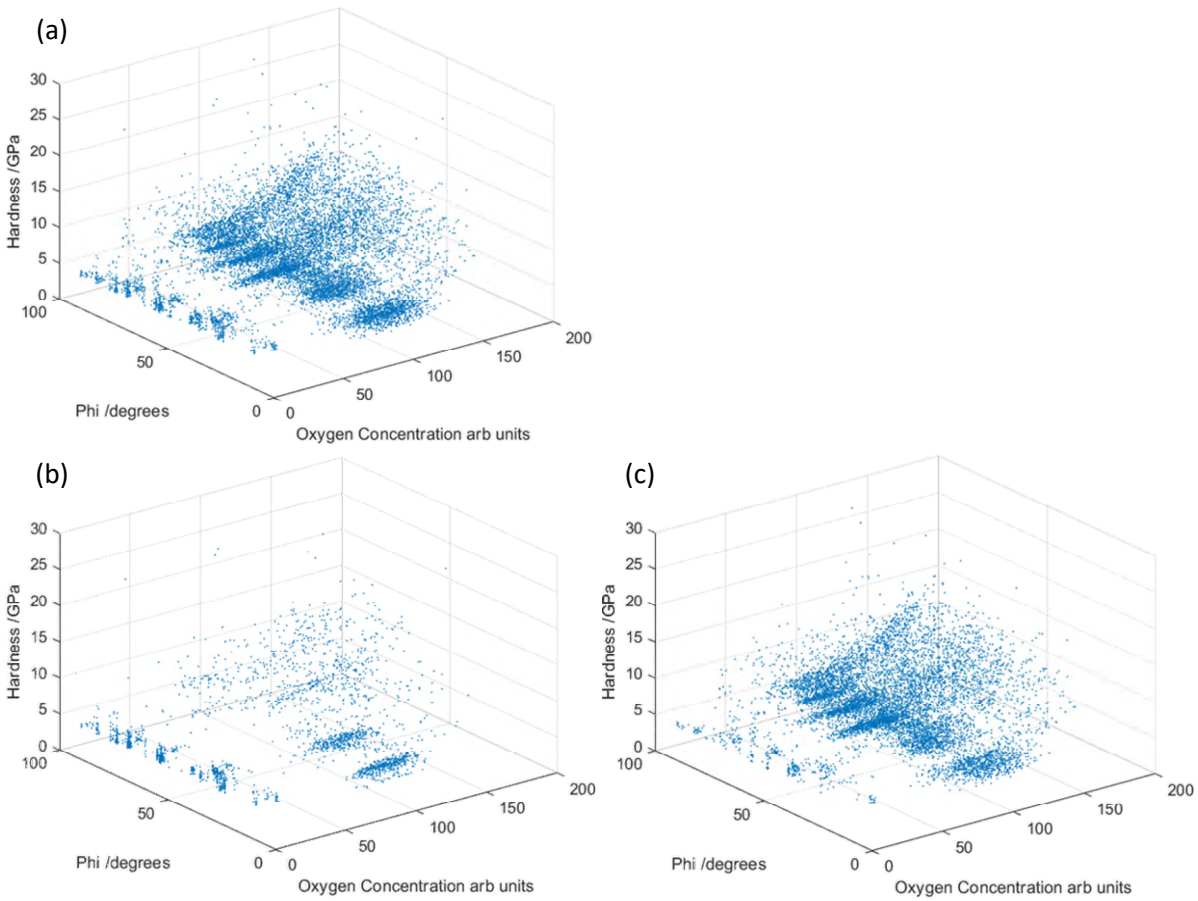


Figure 7.5: Three-dimensional plots showing the relationship between hardness, oxygen concentration and grain orientation for (a) all regions of microstructure, (b) primary α grains only and (c) laths regions only.

In Figure 7.5, hardness is plotted as a function of phi (declination angle) and oxygen content, for the laths, α grains and all regions of microstructure combined. Clearer trends can be seen in the plot for the extracted α grain data. The hardness vs declination angle trends were examined as a function of oxygen content and microstructure (α grains vs laths), which can be seen in . A linear fit and 95% confidence bounds have been fitted to all the plots. The trends are marginal overall, with considerable scatter. However, it can still be seen that the gradient of the fit is negative for the low oxygen, α grains plot shown in (a), but positive for the other plots.

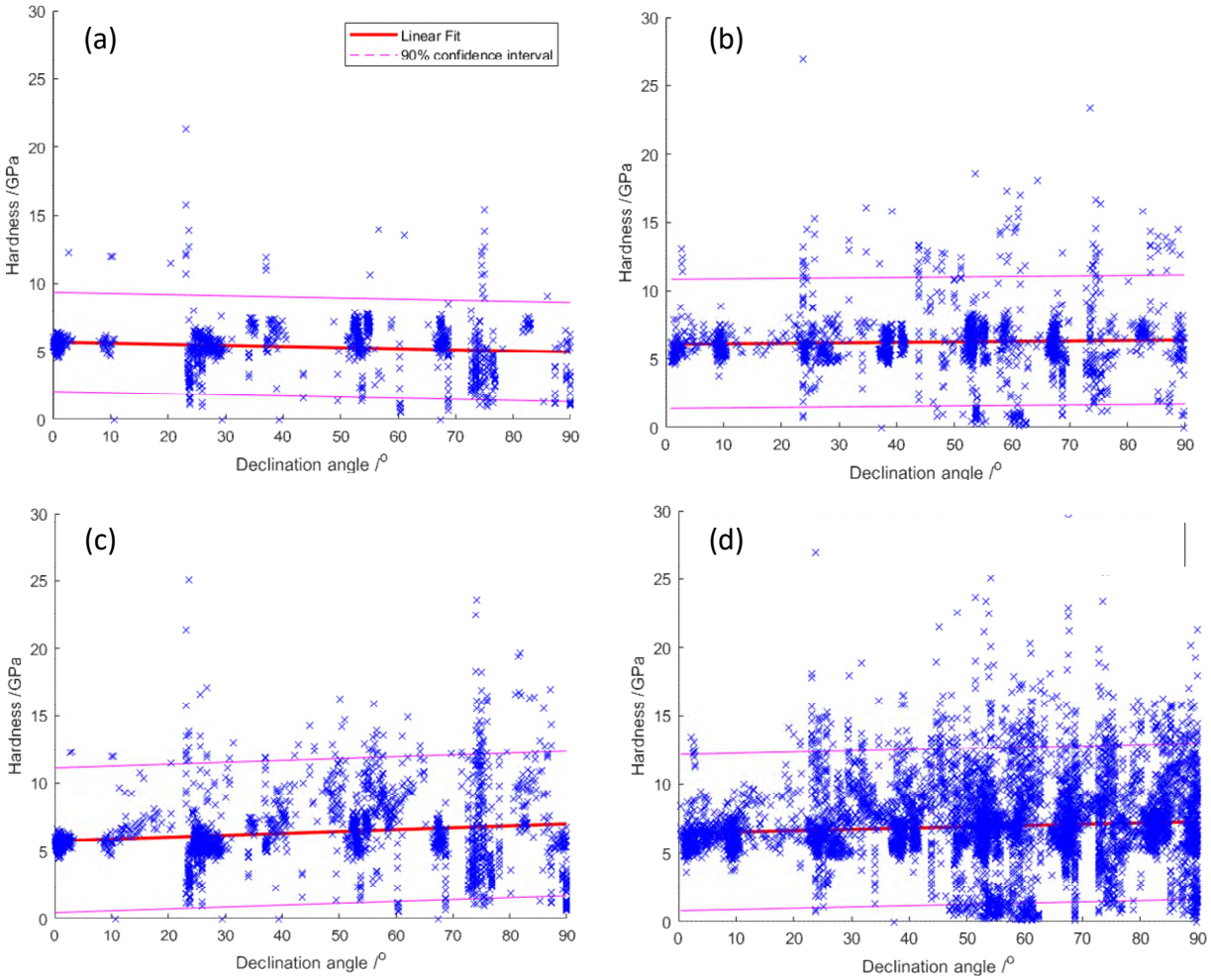


Figure 7.6: Plots of hardness as a function of declination angle, with 95% confidence intervals and a linear trend line for (a) low oxygen α grains, (b) low oxygen lath regions, (c) all α grains and (d) all laths.

Figure 5.12 of Chapter 5 shows that, for α-Ti, hardness is expected to increase with decreasing declination angle, phi. However, this trend is only seen in (a) suggesting that, at high oxygen

contents and when β phase is present, factors other than α grain orientation have a greater effect on hardness.

Figure 7.7 shows the measured oxygen concentration as a function of declination angle for the region of interest at the surface of the compressor disc. It can be seen that there are regions of similar declination angle but varying oxygen content that have been highlighted with red rectangles on Figure 7.7. Points within a single grain will have similar declination angles, and thus the regions marked by rectangles on Figure 7.7 correspond to single grains, or small groups of grains with similar crystallographic orientation. To illustrate this, the regions of microstructure corresponding to each range of declination angles on Figure 7.7 have been extracted, and can be seen in Figure 7.8. The average declination angle of each extracted region increases from (a) to (i). The colour scale on Figure 7.8 indicates the hardness of these regions; the extracted regions nearer the surface are harder, owing to the higher oxygen content at the surface. Figure 7.9 quantifies the effect of oxygen on hardness for each of these extracted regions, with the aim of investigating the effect of different microstructure morphologies (α grains or laths) on hardness.

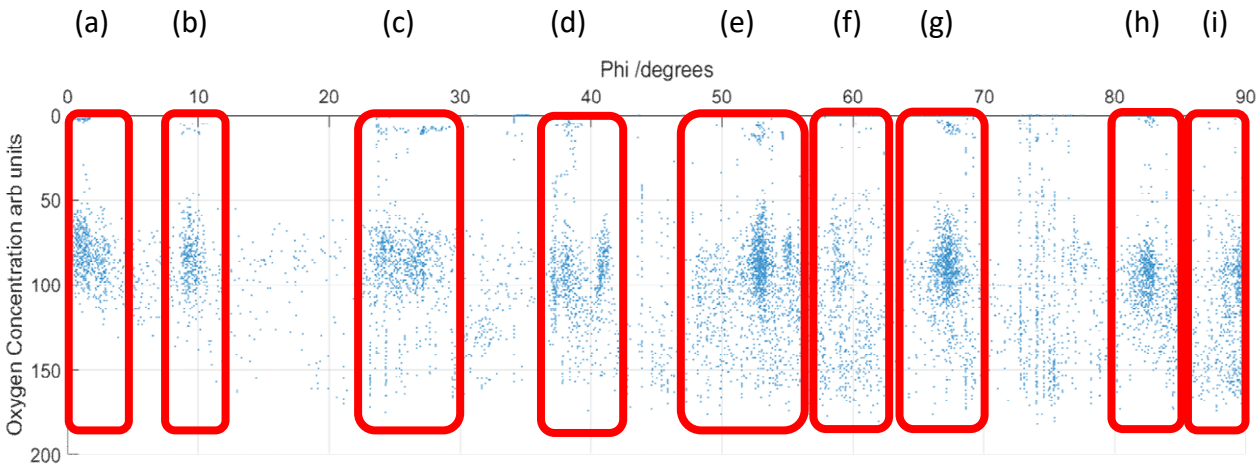


Figure 7.7: Measured oxygen content is plotted as a function of declination angle with respect to the sample polished surface for the region of interest at the surface of the compressor disc. Red boxes, labelled (a)-(j), show how the data has been divided up into regions of similar declination angle.

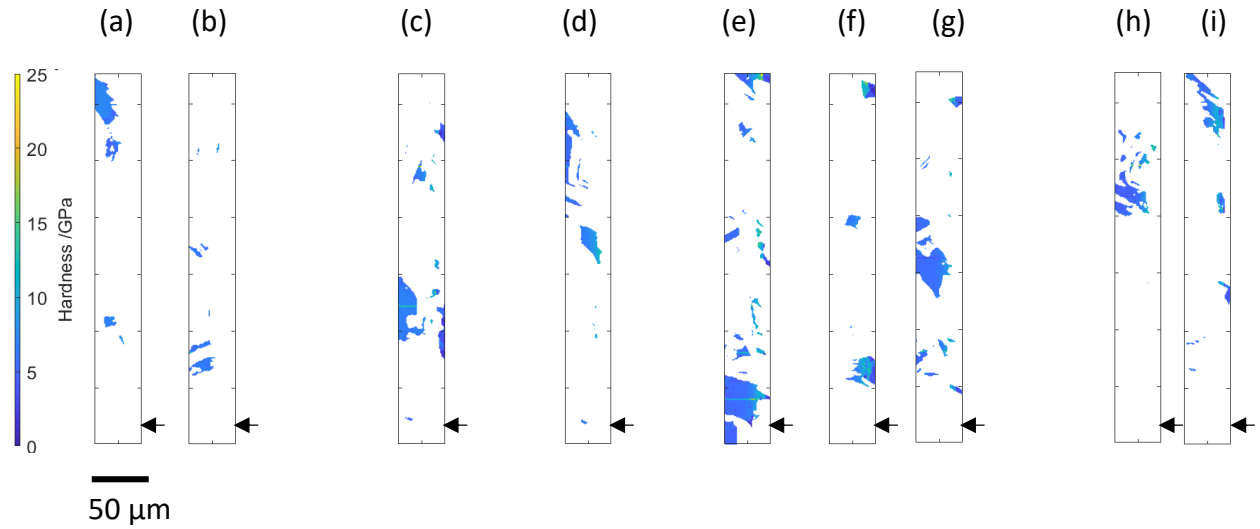


Figure 7.8: The grains and regions of microstructure that correspond to each of the declination angle ranges defined in Figure 7.7; (a) 0-5°, (b) 8-11°, (c) 22-30°, (d) 36-42°, (e)46-56°, (f) 58-63°, (g) 64-70°, (h) 81-85°, (i) 86-90°. The colour scale shows the hardness variation within each of the extracted regions. In each case, the oxygen-exposed surface corresponds to the right hand side of the rectangle, as indicated by the black arrow.

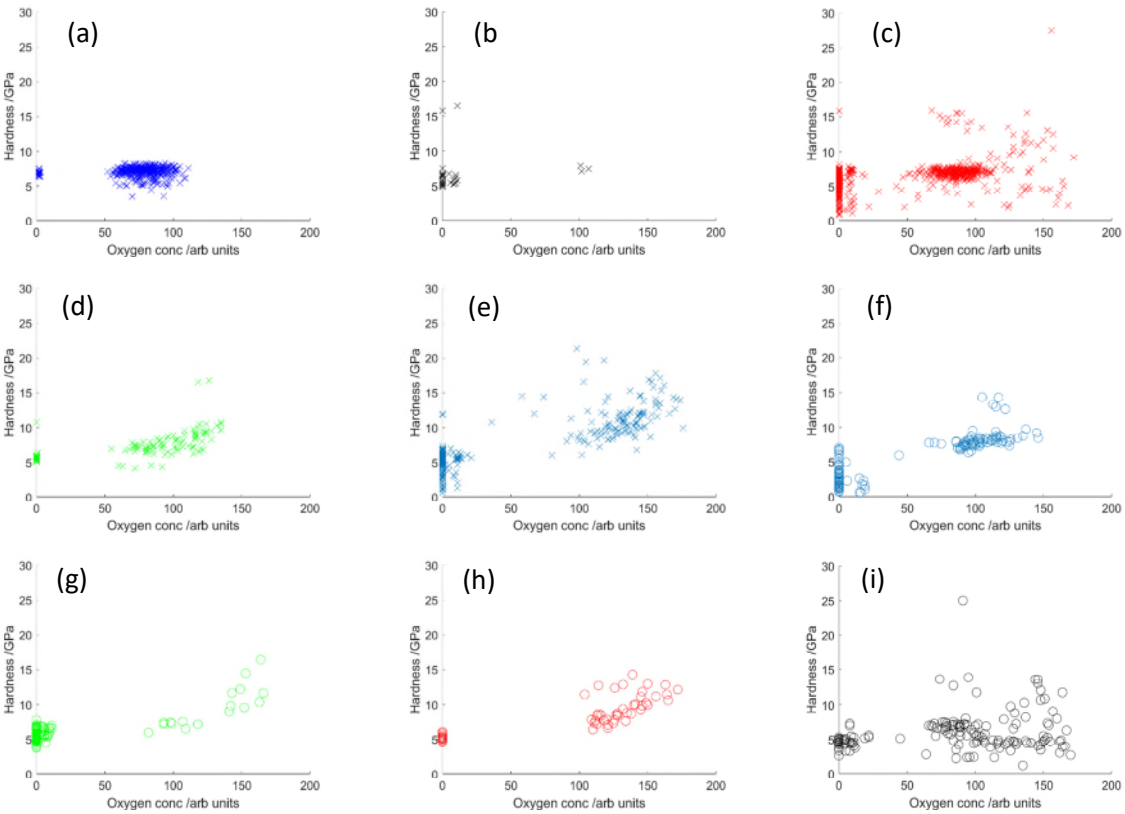


Figure 7.9: (a) - (i) show the plots of hardness as a function of oxygen concentration for each of the extracted regions of microstructure highlighted in Figure 7.8.

7.3 Discussion

When examining the factors that affect hardness at the surface of the compressor disc, it is useful first to consider the more straightforward case of the factors affecting hardness in the bulk, which are illustrated schematically in Figure 7.10 (a). The oxygen concentration is regarded as constant in the bulk such that microstructure and crystal orientation are the only main factors affecting hardness to be considered. Chapter 6 studies the effect of crystal orientation and microstructure on bulk hardness in TIMETAL 834, and the approximate contributions of these factors are recorded in Table 7.1.

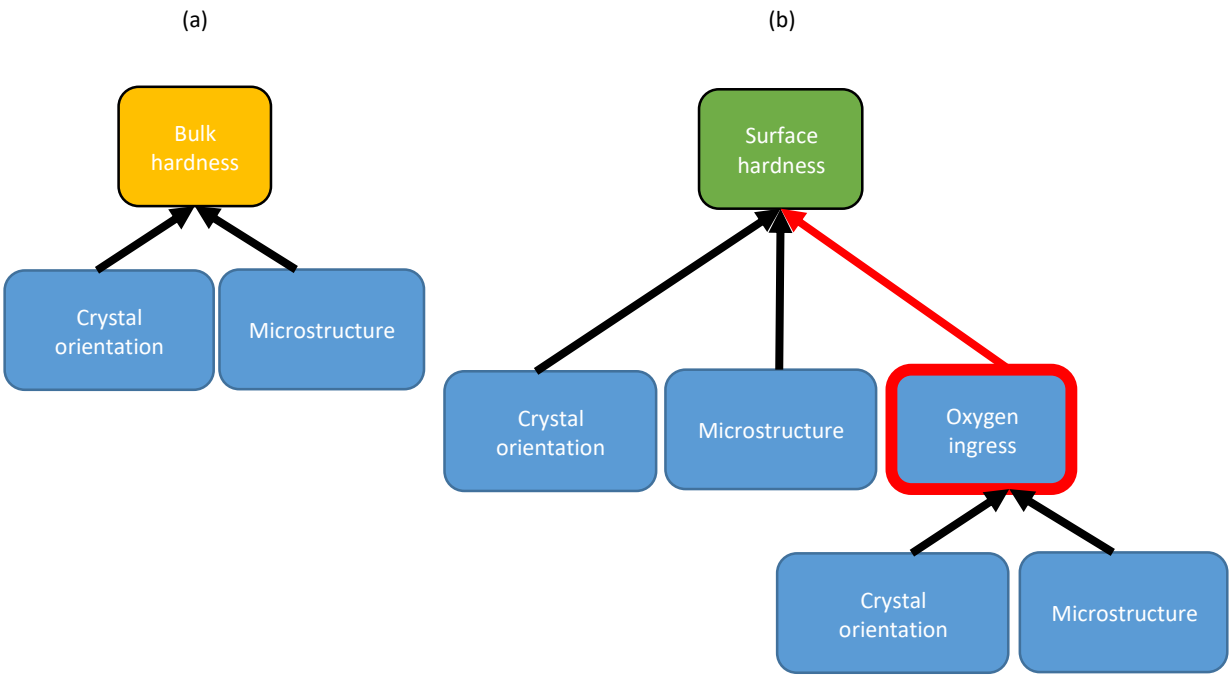


Figure 7.10: Schematic indicating the factors affecting hardness (a) in the bulk of the compressor disc and (b) at the surface of the compressor disc.

Microstructure and crystal orientation still affect the hardness at the surface of the compressor disc. However, Table 7.1 shows that oxygen ingress results in an order of magnitude greater change in hardness than crystal orientation or microstructure, as represented by the red outline in Figure 7.10 (b).

Table 7.1: Summary of approximate hardness contributions calculated from the hardness line profiles and maps.

	Hardness contribution (GPa)	
	Hardness line profile (Ch. 3)	**Surface hardness map**
Crystal orientation	2 (bulk)	0.8
Microstructure	1 (bulk)	1
Max. oxygen ingress	10 (surface)	13

7.3.1 Mechanisms underpinning hardness changes

It is important to consider the possible mechanisms underpinning the different contributions to the hardness change at the surface of the compressor disc.

7.3.1.1 Crystal orientation

As discussed in section 2.6 of the Literature Review, the dependence of hardness on crystal orientation for HCP α-Ti stems from the difference in critical resolved shear stress on each of the slip systems involved in the deformation. The critical resolved shear stress is higher on the <c+a> type slip systems, meaning the material is harder when indented closer to the c-axis [77,78].

7.3.1.2 Microstructure

In Chapter 6, it was noted that α grains are typically softer than regions containing α + β laths [84]. This may be partly because mobile dislocations can travel further in the α grains without being impeded by grain/ phase boundaries. However, lath regions are made up of a series of α colonies, which are approximately the same size as the α grains (20 – 50 μm), as can be seen in Figure 7.1. Within a colony, all the laths are oriented in the same direction, meaning that if slip occurs in one lath, it is easily transmitted to neighbouring laths of the same orientation. Thus colony size is a more important factor in governing slip length and, by extension, hardness in bimodal microstructures [66]. Figure 7.2 (a) shows that difference in size of α grains and colonies is small, which could explain why there are small differences in hardness between laths and non-laths, illustrated in (a) and (b).

7.3.1.3 Oxygen content

It is the interaction of oxygen atoms with dislocation cores that produce interstitial hardening. When considering the total dislocation energy, the dislocation core interactions usually make a lesser contribution than the diffuse elastic interactions of the dislocation. However, oxygen in titanium provides exceptional levels of solid solution hardening, which is described in detail by Yu et al. [99]. The strengthening originates from a strong interaction between the oxygen atom and screw dislocation cores. The strong interaction is caused by a combination of strong repulsion of the dislocation by the oxygen solute, a high energy barrier to rearrangement of oxygen atoms within the core and cross slip induced by the oxygen atoms [99].

7.3.2 Interplay between crystal orientation, microstructure, oxygen content, and hardness

Declination angle is expected to only have an effect on hardness for the HCP α phase, because the β phase has cubic symmetry and therefore does not have the highly anisotropic properties of the HCP α phase. Despite the small volume fraction of β phase present (~ 5 volume % [39]) , there is a high concentration of α/ β boundaries in the lath regions. Therefore, when indenting lath regions, any trends in hardness as a function of crystal orientation that are plotted on (c) and (d) are made less clear by the contributions of the cubic β phase and the inevitably large number of lath boundary interactions.

Very shallow (200 nm deep) indents were used to create the hardness map. This gives an approximate plastic zone size of 3 µm. The indents were spaced 1 µm apart to obtain sufficient spatial resolution on the hardness maps, meaning the plastic zones of neighbouring indents overlap. This means the maps cannot be used to report absolute values of hardness, but comparisons of relative hardness changes remain valid. The size of the plastic zone is such that multiple laths will be indented at one time, which will also have a blurring effect.

Nevertheless, we can mitigate the grain boundary and β phase blurring effects described above by extracting the data corresponding to the lath regions and the α grains and analysing them

separately. Figure 7.5 (b) and Figure 7.5 (c) show that segmenting the data in this way reveals more apparent trends in hardness as a function of declination angle. This is further emphasised by looking at (a) and (b). Thus it appears the β phase and presence of high density of grain boundaries in the lath regions are altering the observed trend in declination angle.

Comparison of (a) and (c) shows that oxygen is affecting the observed trend in hardness as a function of declination angle. In α-type titanium, hardness is expected to increase as the declination angle decreases [77]. However, this is only observed in the α grain regions when the high oxygen contributions (greater than 80 arbitrary units) are filtered out. At higher oxygen concentrations, it seems that the effect of interstitial oxygen solid solution hardening is dominant. Thus the effects of microstructure and crystal orientation are only significant when the oxygen content is low, i.e. further away from the surface.

7.3.2.1 Relative contributions of crystal orientation, microstructure and oxygen to hardness

Although crystal orientation can make slip challenging to initiate, the barrier to dislocation motion is small in comparison to the barrier to dislocation motion presented by oxygen. Likewise, the type of microstructure (lath region or α grain) has minimal effect on hardness since the lath regions and α grains are of comparable size, leading to similar slip lengths. The unusually strong, local dislocation core- interstitial interaction [99] dominates over the long-range, weaker, elastic interaction of dislocations with grain boundaries/ phase boundaries. This explains why interstitial hardening dominates except at low oxygen concentrations.

7.3.3 Effect of crystal orientation and microstructure on oxygen ingress

The effect of crystal orientation and microstructure on oxygen ingress can be explored using data from Figure 7.5. It should be noted that, as discussed in Chapter 2 section 2.10, oxygen does not change the microstructure in the temperature and time regimes considered in this study. Thus the arrow on the schematic diagram in Figure 7.10 connecting oxygen ingress and microstructure is only one directional.

Figure 7.9 was created to study changes in oxygen ingress as a function of crystal orientation and microstructure. However, it is difficult to compare the oxygen ingress in the lath regions with ingress within the α grains since the number of α grains sampled is small. The two largest α grains detected, seen in Figure 7.9(a) and Figure 7.9 (c), are not at the surface and so would not be expected to show the steepest oxygen concentration profile. The aim of this study was to set up the analysis procedure for combining multiple analytical techniques as a proof of concept, so a more extensive investigation is beyond the scope of this thesis. This study paves the way for further development of this method. For example, to study the effect of microstructure on oxygen ingress, a larger region of microstructure should be sampled, with multiple α grains and multiple lath regions at the surface. This would also enable a more quantitative study of the effect of lath orientation relative to the ingress direction on oxygen ingress.

The minimal number of α grains sampled in this region of interest means that no clear relationship between declination angle and oxygen ingress can be determined. The two α grains that were extracted have phi angles in the range of 0-5 degrees and 22-30 degrees, and both have similar oxygen concentrations. However, this may be a result of their location at a similar depth from the surface. This work has defined the analysis procedure and highlights factors that need to be taken into consideration for future work. For example, a further study on a larger area should be carried out, in which only surface α grains are studied, to remove the dependence of oxygen concentration on depth from exposed surface.

7.4 CONCLUSIONS

Development of a new analysis method has allowed the overlay of hardness maps, EBSD maps and EPMA oxygen maps, bringing deeper insights into the relative effects of crystal orientation, microstructure and oxygen content on hardness. Oxygen interstitial solid solution strengthening has been observed to dominate other hardness contributions by up to an order of magnitude, except for very low oxygen concentrations, where microstructural and crystallographic effects can

be observed. This is thought to be a result of the strong interaction between dislocation cores and oxygen interstitials [99].

8 SUMMARY AND CONCLUSIONS

8.1 INTRODUCTION

Safe operation of jet engines running at maximum efficiency relies on a fundamental understanding of the behaviour of the materials they are made from. Titanium alloys are used to make jet engine components, such as fan blades and compressor discs, owing to their high specific fatigue strength. Two of the key challenges facing titanium components are cold dwell fatigue and oxidation of compressor discs. These both reduce component *in-service* life, and component oxidation prevents use of titanium in hotter parts of the engine, ultimately increasing total engine weight. However, the mechanisms underpinning these processes are not fully understood. Much of the activity driving these mechanisms occurs on the nanoscale, and thus atom probe tomography is one of the few analytical techniques that has sufficient combined spatial resolution and chemical sensitivity to provide insight into these processes. When coupled with larger length scale techniques for mapping oxygen, such as EPMA, and when combined with nanohardness measurements to relate changes in composition to mechanical properties, this approach has the power to provide a holistic overview of the processes. This Chapter will summarise the findings of this thesis and show how this work addresses the initial research questions: where do oxygen and nitrogen sit within the microstructure of titanium alloys?; what is the role of oxygen and nitrogen in α_2 formation?; what is the effect of oxygen, nitrogen and α_2 on mechanical properties?; how do crystal orientation, microstructure and oxygen content affect hardness?

8.2 CONCLUSIONS

APT measurements show that oxygen partitions away from the α_2 phase, despite promoting its formation. This is contrary to assumptions made previously in the literature. Nitrogen also

partitions away from the α_2 phase, but less strongly. This has led to the proposal of a mechanism for α_2 formation. Combined TKD and APT analysis revealed that oxygen was found not to partition to a non-symmetric α-α grain boundary. This experimentally confirms DFT calculations of segregation behaviour at α- α grain boundaries [236], and is consistent with the proposed α_2 formation mechanism. These findings are of importance for academia, since the directly measured partitioning behaviour of oxygen with α_2 is opposite to the assumed behaviour in the current literature, but also for industry, as the proposed mechanism contributes to an improved understanding of how α_2 formation can be controlled.

Oxygen and nitrogen were mapped through other regions of the microstructure, and oxygen was observed to partition preferentially to the α phase over the β phase. By contrast, nitrogen sometimes partitioned to the β phase, which has not been observed previously.

During evaluation of the active hardening mechanisms, interstitial solid solution hardening dominated over α_2 precipitation hardening. This further quantifies the observations of Liu and Welsch that α_2 precipitation provides a minor hardening contribution [79]. Post heat treatment cooling rates should be carefully controlled to avoid oxygen ordering, which this study suggests causes significant hardening.

Oxygen ingress has been shown to be affected by microstructure on both the micron and nano scale. Many current models for *α case* depth prediction do not routinely account for microstructure, and so the findings of this work support the work of Tiley et al. [10] in highlighting the importance of orientation of α/ β interfaces on oxygen ingress.

Chapter 6 quantifies the effect of microstructure and crystal orientation on hardness, showing that their effect on hardness is an order of magnitude less than the hardening effect of oxygen ingress. Chapter 7 explores the relative contributions of microstructure, crystal orientation and oxygen to hardness effects, and shows that the hardening effects of microstructure and crystal

orientation are only significant at very low oxygen concentrations. Interstitial solid solution hardening dominates by an order of magnitude for higher oxygen concentrations.

8.3 FUTURE WORK

The results and conclusions presented in this thesis highlight areas of research that warrant further study, but could not be investigated due to time constraints. These are outlined below:

- Experimental verification of the proposed α_2 formation mechanism. This could be achieved through measurement of the number of [OTi6] sites as a function of oxygen content in low titanium alloys using neutron diffraction. The level of oxygen needed to form aluminium clusters in the α matrix could also be investigated through creation of a Ti-Al alloy series in which aluminium content is varied.
- Investigation of the effect of silicon on the mechanical properties of the α_2 phase, through creation of a series of Ti-Al alloys with varying silicon content.
- Controlled study of the effect of air-cooling on hardness, through use of nanoindentation and APT to examine oxygen ordering.
- Study of a range of bimodal microstructures, textures and oxygen contents in TIMETAL 834 to understand the contributions of crystal orientation, microstructure and oxygen concentration on hardness. This can be combined with further development of the hardness mapping analysis method outlined in Chapter 7, which is already in progress.

8.4 CONCLUDING REMARKS

The goal of this study was to improve fundamental understanding of the role of oxygen and nitrogen in titanium alloys for aerospace through use of both model alloys and *in-service* components. A multi technique approach, spanning length scales, has been taken in order to provide new insights into factors affecting cold dwell fatigue and compressor disc oxidation. Careful characterisation of the interaction of oxygen with the α_2 phase has led to the proposal of

a mechanism for α_2 formation. Further mapping of both trace and high levels of oxygen and nitrogen throughout the microstructure of model alloys and industrially used alloys has provided insight into the dominant hardening mechanisms and the interplay of factors controlling oxygen ingress. A new analysis method has been established to relate complementary techniques to mapped hardness data, paving the way for future studies on the relationship between composition, crystal orientation and mechanical properties on the nanoscale.

9 REFERENCES

1. Brien P, Rhodes C. The aerospace industry : statistics and policy [Internet]. House of Commons Library Standard Note. 2017.
2. ACARE 2050 Flightpath targets [Internet]. 2011. Available from: www.acare4europe.org/sria/flightpath-2050-goals/protecting-environment-and-energy-supply-0
3. Rugg D, Dixon M, Burrows J. High-temperature application of titanium alloys in gas turbines. Material life cycle opportunities and threats – an industrial perspective. Mater High Temp [Internet]. 2016;33(4–5):536–41.
4. McReynolds KS, Tamirisakandala S. A study on alpha-case depth in Ti-6Al-2Sn-4Zr-2Mo. Metall Mater Trans A Phys Metall Mater Sci. 2011;42(7):1732–6.
5. Gaddam R, Sefer B, Pederson R, Antti M-L. Study of alpha-case depth in Ti-6Al-2Sn-4Zr-2Mo and Ti-6Al-4V. IOP Conf Ser Mater Sci Eng [Internet]. 2013;48:012002.
6. Shamblen CE, Redden TK. Air Contamination and Embrittlement of Titanium Alloys. Jaffee RI, Promise NE, editors. Sci. Technol. Appl. Titan. Pergamon Press; 1970. 199–208 p.
7. Chan KS, Koike M, Johnson BW, Okabe T. Modeling of alpha-case formation and its effects on the mechanical properties of titanium alloy castings. Metall Mater Trans A Phys Metall Mater Sci. 2008;39(1):171–80.
8. Parthasarathy TA, Porter WJ, Boone S, John R, Martin P. Life prediction under tension of titanium alloys that develop an oxygenated brittle case during use. Scr Mater [Internet]. 2011;65(5):420–3.
9. Oskay C, Haney M. Computational modeling of titanium structures subjected to thermo-chemo-mechanical environment. Int J Solids Struct [Internet]. 2010;47(24):3341–51.
10. Tiley J, Shaffer J, Shiveley A, Pilchak A, Salem A. The effect of lath orientations on oxygen ingress in titanium alloys. Metall Mater Trans A Phys Metall Mater Sci. 2014;45(2):1041–8.
11. Satko DP, Shaffer JB, Tiley JS, Semiatin SL, Pilchak AL, Kalidindi SR, et al. Effect of microstructure on oxygen rich layer evolution and its impact on fatigue life during high-temperature application of α/β titanium. Acta Mater [Internet]. 2016;107:377–89.
12. Sutton A, Rugg D. CECAM Workshop Scientific Report Cold Dwell Fatigue in Titanium Alloys [Internet]. 2014.
13. Hasija V, Ghosh S, Mills MJ, Joseph DS. Deformation and creep modeling in polycrystalline Ti-6Al alloys. Acta Mater. 2003;51(15):4533–49.
14. Suri S, Neeraj T, Daehn GS, Hou DH, Scott JM, Hayes RW, et al. Mechanisms of primary creep in α/β titanium alloys at lower temperatures. Mater Sci Eng A. 1997;234–236:996–9.
15. Neeraj T, Holc DH, Daehn GS, Mills MJ. Phenomenological and microstructural analysis of room temperature creep in titanium alloys. Acta Mater. 2000;48(6):1225–38.
16. Cuddihy MA, Stapleton A, Williams S, Dunne FPE. On cold dwell facet fatigue in titanium alloy aero-engine components. Int J Fatigue [Internet]. 2017;97:177–89.
17. Neeraj T, Mills MJ. Short-range order (SRO) and its effect on the primary creep behavior of a Ti-6wt.%Al alloy. Mater Sci Eng A [Internet]. 2001;319–321:415–9.

18. Lim JY. The effect of Oxygen on the structure and mechanical behaviour of aged Ti-8 wt% Al. Metall Trans A. 1976;7(1):139–44.

19. IATA Financial Forecasts [Internet]. Available from: http://www.iata.org/whatwedo/Documents/economics/Industry-Outlook-Dec2012.pdf;

20. IATA - IATA Forecasts Passenger Demand to Double Over 20 Years [Internet]. Available from: http://www.iata.org/pressroom/pr/Pages/2016-10-18-02.aspx

21. 34,000 Planes Required in Next 20 Years to Meet Passenger Demand [Internet]. Available from: http://www.globaltravelerusa.com/34000-planes-required-in-next-20-years-to-meet-passenger-demand/

22. Schulte D. Estimating Maintenance Reserves. Boeing Aero. 2013;13:4–11.

23. IATA. Airline Maintenance Cost Executive Commentary. IATA Maintenance Cost Task Force. 2013;

24. Aainsqatsi K. Bypass Ratio (Image) [Internet]. Available from: https://en.wikipedia.org/wiki/Bypass_ratio

25. FAA. Airplane Flying Handbook (FAA-H-8083-38). 2016.

26. Strobridge TR, Moulder JC, Clark AF. Report on Titanium combustion in turbine engines. Titanium combustion in turbine engines. 1979.

27. Marsh G. Aero engines lose weight thanks to composites. Reinf Plast. 2012;56(6):32–5.

28. Liu L, Luo G, Chen W, Zhao Z, Huang X. Dynamic Behavior and Damage Mechanism of 3D Braided Composite Fan Blade under Bird Impact. Int J Aerosp Eng [Internet]. 2018;

29. Cervenka M. The Rolls-Royce trent engine (www.msm.cam.ac.uk/phase-trans/mphil/Trent1) Date accessed: 2017-03-08. Online. 2000.

30. Ready AJ, Haynes PD, Grabowski B, Rugg D, Sutton A. The role of molybdenum in suppressing cold dwell fatigue in titanium alloys. Proc R Soc A. 2017;45(13):6075–87.

31. Sutton A, Rugg D. CECAM Workshop Cold dwell fatigue in titanium alloys [Internet]. 2014. Available from: https://www.cecam.org/workshop-1019.html

32. ATAG. Beginner's Guide to Aviation Efficiency [Internet]. 2010. Available from: http://large.stanford.edu/courses/2017/ph240/chhoa1/docs/atag-nov10.pdf

33. Reed RC. The superalloys : fundamentals and applications [Internet]. Cambridge University Press; 2006.

34. Banerjee D, Williams JC. Perspectives on Titanium Science and Technology. Acta Mater [Internet]. 2013;61(3):844–79.

35. Niinomi M. Mechanical properties of biomedical titanium alloys. Mater Sci Eng A [Internet]. 1998;243(1–2):231–6.

36. Gorynin I. Titanium alloys for marine application. Mater Sci Eng A [Internet]. 1999;263(2):112–6.

37. Bedinger GM. Titanium and titanium dioxide. USGS Miner Commod Summ. 2015;1(703):2015–6.

38. Talbot D, Talbot J. Corrosion science and technology [Internet]. CRC Press, Taylor & Francis Group; 2007.

39. Lutjering G, Williams JC. Titanium. First Edit. Springer; 2003.

40. Zhang W, Zhu Z, Cheng CY. A literature review of titanium metallurgical processes. Hydrometallurgy [Internet]. 2011;108(3–4):177–88.

41. Liew HJ. [Thesis] Short range order and phase separation in Ti-rich Ti-Al alloys. University of Oxford; 1999.

42. Stainless Steel - High Temperature Resistance [Internet]. Available from: https://www.azom.com/article.aspx?ArticleID=1175

43. Metals and Alloys - Melting Temperatures [Internet]. Available from: https://www.engineeringtoolbox.com/melting-temperature-metals-d_860.html

44. Steels, General Properties [Internet]. Available from: http://www.matweb.com/search/datasheet.aspx?bassnum=MS0001&ckck=1

45. Properties: Titanium Alloys - Ti6Al4V Grade 5 [Internet]. Available from: https://www.azom.com/properties.aspx?ArticleID=1547

46. Blackburn MJ. The Ordering Transformation in Titanium:Aluminium Alloys Containing up to 25 at. pct Aluminium. Trans Metall Soc AIME. 1967;239:1200–8.

47. Clark D, Jepson K, Lewis G. A Study of Titanium-Aluminium System up to 40 at.% Aluminium. J Inst Met. 1963;6(197).

48. Ence E, Margolin H. Phase relations in the Titanium-Aluminium System. Trans Metall Soc AIME. 1961;221(1):151–7.

49. Murray JL. Phase diagrams of binary titanium alloys [Internet]. ASM International; 1987. 345 p.

50. Shull R, McAllister A, Reno R. Phase Equilibria in the Titanium-Aluminum System. In: Lutjering G, Zwicker U, Bunk W, editors. Proceedings of the 5th International Conference on Titanium. 1985. p. 1459.

51. Massalski T, Murray J. Binary phase diagrams. ASM Int [Internet]. 1990;

52. Valencia JJ, McCullough C, Levi CG, Mehrabian R. Microstructure evolution during conventional and rapid solidification of a Ti-50at%Al alloy. Scr Metall. 1987;21(10):1341–6.

53. Kainuma R, Palm M, Inden G. Solid-phase equilibria in the Ti-rich part of the Ti-Al system. Intermetallics [Internet]. 1994;2(4):321–32.

54. McCullough C, Valencia JJ, Levi CG, Mehrabian R. Phase Equilibria and Solidification in Ti-Al alloys. Acta Metall. 1989;37(5):1321–36.

55. Okamoto H. Al-Ti (aluminum-titanium). J Phase Equilibria [Internet]. 1993;14(1):120–1.

56. Radecka A. [Thesis] Ordering and the deformation mechanisms of Ti-Al alloys. 2015.

57. Mahan GD. Crystal [Internet]. Encyclopædia Britannica, inc. 2016. Available from: https://www.britannica.com/science/crystal#ref506252

58. Swartzendruber L, Bennett L, Ives L, Shull R. The Ti-Al Phase Diagram: the α-α2 Phase Boundary. Mater Sci Eng. 1981;51:1–9.

59. Namboodhiri TKG. On the Ti-Al phase diagram. Mater Sci Eng. 1983;57(1):21–2.

60. Radecka A, Coakley J, Jones IP, Rugg D, Lindley TC, Dye D. Ordering and the

micromechanics of Ti-7Al. Mater Sci Eng A [Internet]. 2016;650:28–37.

61. Kattner UR, Lin JC, Chang YA. Thermodynamic assessment and calculation of the Ti-Al System. Metall Trans A. 1992;23(8):2081–90.

62. McCullough C, Valencia JJ, Mateos H, Levi CG, Mehrabian R, Barbara S, et al. The High Temperature alpha Field in the Titanium-Aluminium Phase Diagram. Scr Metall. 1988;22:1131–6.

63. Watkins GR. [Thesis] Development of a High Temperature Titanium Alloy for Gas Turbine Applications. The University of Sheffield; 2015.

64. Correa DRN, Vicente FB, Araújo RO, Lourenço ML, Kuroda PAB, Buzalaf MAR, et al. Effect of the substitutional elements on the microstructure of the Ti-15Mo-Zr and Ti-15Zr-Mo systems alloys. J Mater Res Technol. 2015;4(2):180–5.

65. Weiss I, Semiatin SL. Thermomechanical processing of alpha titanium alloys - an overview. Mater Sci Eng A [Internet]. 1999;263:243–56.

66. Lütjering G, Williams JC, Gysler A. MICROSTRUCTURE AND MECHANICAL PROPERTIES OF TITANIUM ALLOYS. In: Microstructure and Properties of Materials [Internet]. WORLD SCIENTIFIC; 2000. p. 1–77.

67. Maeda T. [Thesis] Phase Equilibrium and Beta Stability in Ti-Rich Ti-V-Al Alloys. University of London; 1988.

68. Mouritz AP. Titanium alloys for aerospace structures and engines. In: Mouritz AP, editor. Introduction to Aerospace Materials. Woodhead Publishing; 2012. p. 202–23.

69. Paton NE, Mahoney MW. Creep of titanium-silicon alloys. Metall Trans A [Internet]. 1976;7(11):1685–94.

70. Mahoney MW, Paton NE, Parris WM. Report on the Effect of Minor Alloying Elements on the Mechanical Properties of Titanium Alloys. Ohio, USA; 1976.

71. Seagle SR, Hall GS, Bomberger HB. High temperature properties of Ti--6Al--2Sn--4Zr--2Mo--0.09Si. Met Eng Q, v 15, no 1, pp 48-54 [Internet]. 1975;

72. Eylon D, Fujishiro S, Postans PJ, Froes F. H. High-Temperature titanium alloys- a review. J Met. 1984;(November):55–6.

73. Ogden HR, Maykuth DJ, Finlay WL, Jaffee RI. Mechanical properties of High purity Ti-Al alloys. J Met. 1953;(February):267–72.

74. Cottrell A. An Introduction to Metallurgy. The Institute of Materials; 1995. 264 p.

75. Zhang Z, Eakins DE, Dunne FPE. On the formation of adiabatic shear bands in textured HCP polycrystals. Int J Plast [Internet]. 2016;79:196–216.

76. Churchman AT. The slip modes of titanium and the effect of purity on their occurance during tensile deformation of single crystals. Proc R Soc A. 1954;226(1165):216.

77. Britton TB, Liang H, Dunne FPE, Wilkinson AJ. The effect of crystal orientation on the indentation response of commercially pure titanium: experiments and simulations. Proc R Soc A Math Phys Eng Sci [Internet]. 2010;466(2115):695–719.

78. Britton TB, Dunne FPE, Wilkinson AJ. On the mechanistic basis of deformation at the microscale in hexagonal close-packed metals. Proc R Soc A Math Phys Eng Sci [Internet]. 2015;471(2178):20140881–20140881.

79. Liu Z, Welsch G. Effects of oxygen and heat treatment on the mechanical properties of alpha and beta titanium alloys. Metall Trans A. 1988;19(3):527–42.

80. Ruban A V., Baykov VI, Johansson B, Dmitriev V V., Blanter MS. Oxygen and nitrogen interstitial ordering in hcp Ti, Zr, and Hf: An ab initio study. Phys Rev B [Internet]. 2010;82(13):134110.

81. Williams JC, Sommer AW, Tung PP. The influence of oxygen concentration on the internal stress and dislocation arrangements in alpha titanium. Metall Trans. 1972;3(11):2979–84.

82. Hall EO. The Deformation and Ageing of Mild Steel: III Discussion of Results. Proc Phys Soc Sect B. 1951;64(9):747.

83. Petch NJ. The Cleavage Strength of Polycrystals. J Iron Steel Inst. 1953;173(5).

84. Ghamarian I, Hayes B, Samimi P, Welk BA, Fraser HL, Collins PC. Developing a phenomenological equation to predict yield strength from composition and microstructure in β processed Ti-6Al-4V. Mater Sci Eng A. 2016;660:172–80.

85. Ogden HR, Jaffee RI. The effects of carbon, oxygen and nitrogen on the mechanical properties of titanium and titanium alloys. Titan Metall Lab [Internet]. 1955;XXXIII(2):81–7.

86. Jaffee RI, Ogden HR, Maykuth DJ. Alloys of Titanium with Carbon, Oxygen, and Nitrogen. Trans Metall Soc AIME. 1950;188:1261.

87. Choudhury A, Hengsberger E. Electron beam melting and refining of metals and alloys. ISIJ Int. 1992;32(5):673–81.

88. Donachie MJ. Titanium : a technical guide [Internet]. ASM International; 2000. 381 p.

89. Shimojo M, Myeong TH, Higo Y, Iguchi R. The entering behavior of environmental gases into the plastic zone around fatigue crack tips in titanium. Metall Mater Trans A. 1997;28(June):1341–6.

90. Bhadeshia HKDH. Titanium & its Alloys -Lecture notes [Internet]. 2000. p. 1–13. Available from: http://www.msm.cam.ac.uk/phase-trans/2000/C9/lecture3.pdf

91. Wasz ML, Brotzen FR, McLellan RB, Griffin a. J. Effect of oxygen and hydrogen on mechanical properties of commercial purity titanium. Int Mater Rev. 1996;41(1):1–12.

92. Conrad H. Effect of interstitial solutes on the strength and ductility of titanium. Prog Mater Sci [Internet]. 1981;26(2–4):123–403.

93. Montanari R, Costanza G, Tata ME, Testani C. Lattice expansion of Ti-6Al-4V by nitrogen and oxygen absorption. Mater Charact. 2008;59(3):334–7.

94. Jones CY, Luecke WE, Copland E. Neutron diffraction study of oxygen dissolution in α2-Ti3Al. Intermetallics. 2006;14(1):54–60.

95. Lefebvre W, Loiseau A, Thomas M, Menand A. Influence of oxygen on the α → γ massive transformation in a Ti-48 at.% Al alloy. Phil Mag A. 2002;82:2341–55.

96. Nayak SK, Hung CJ, Sharma V, Alpay SP, Dongare AM, Brindley WJ, et al. Insight into point defects and impurities in titanium from first principles. npj Comput Mater [Internet]. 2018;4(1).

97. Scotti L, Mottura A. Interstitial diffusion of O , N , and C in α -Ti from first-principles : Analytical model and kinetic Monte Carlo simulations. J Chem Phys [Internet]. 2016;144.

98. Gunda NSH, Van der Ven A. First-principles insights on phase stability of titanium interstitial alloys. Phys Rev Mater [Internet]. 2018;2(8):083602.

99. Yu Q, Traylor R, Rugg D, Asta M, Chrzan DC, Minor AM. Origin of dramatic oxygen solute strengthening effect in titanium. Science (80-). 2015;347(6222):635–40.

100. McKinley TD. Effect of Impurities on the Hardness of Titanium. J Electrochem Soc [Internet]. 1956;103(10):561.

101. Rausch JJ. Solid Solution Hardening of Alpha and Beta Titanium, Summary report on Contract DA-11-022-ORD-1439. Chicago; 1954.

102. Jaffee RI, Holden FC, Ogden HR. Mechanical Properties of Alpha Titanium as Affected by Structure and Composition. J Met. 1954;6:1282.

103. Finlay WL, Snyder JA. Effect of Three Interstitials (C, O, and N) on Mechanical Properties of Alpha Titanium. J Met. 1950;2:277.

104. Ardakani, Shollock, Flower. The effect of Oxygen on microstructure of α and α2 phase in titanium-rich alloys. In: Titanium ’95: Science and Technology. 1995.

105. Yan M, Dargusch MS, Ebel T, Qian M. A transmission electron microscopy and three-dimensional atom probe study of the oxygen-induced fine microstructural features in as-sintered Ti–6Al–4V and their impacts on ductility. Acta Mater [Internet]. 2014;68:196–206.

106. Ando T, Nakashima K, Tsuchiyama T, Takaki S. Microstructure and mechanical properties of a high nitrogen titanium alloy. Mater Sci Eng A [Internet]. 2008;486(1–2):228–34.

107. Byeeong-Joo L, Saunders N. Thermodynamic evaluation of the Ti-O-Al ternary system. Zeitschrift für Met. 1997;88(2):152–61.

108. Gehlen. The crystallographic structure of Ti3Al. In: Jaffee RI, editor. The Science, Technology and Application of Titanium. Pergamon Press; 1970.

109. Menand A, Huguet A, Nérac-Partaix A. Interstitial solubility in γ and α2 phases of TiAl-based alloys. Acta Mater [Internet]. 1996;44(12):4729–37.

110. Radecka A, Coakley J, Vorontsov VA, Martin TL, Bagot PAJ, Moody MP, et al. Precipitation of the ordered α2 phase in a near-α titanium alloy. Scr Mater [Internet]. 2016;117:81–5.

111. Namboodhiri TKG, McMahon CJ, Herman HJ. Decomposition of alpha phase in Titanium-rich Ti-Al alloys. Metall Trans. 1973;4:1323.

112. Radecka A, Bagot PAJ, Martin TL, Coakley J, Vorontsov VA, Moody MP, et al. The formation of ordered clusters in Ti–7Al and Ti–6Al–4V. Acta Mater [Internet]. 2016;112:141–9.

113. Williams JC. Titanium Technology. Froes FH, Eylon D, Bomberger HB, editors. 1984;57.

114. Radecka A, Vorontsov VA, Coakley J, Rahman KM, Bagot PAJ, Martin TL, et al. Ordering in Titanium Alloys. In: Proceedings of the 13th World Conference on Titanium. 2016. p. 971–8.

115. Lenssen LA. [Thesis] FIM/Atom Probe Study of a Titanium Alloy. University of Oxford; 1987.

116. Wood H, Smith GDW, Cerezo A. Short range order and phase separation in Ti-Al alloys. Mater Sci Eng A [Internet]. 1998;250(1):83–7.

117. Gleiter H, Hornbogen E. Theorie der Wechselwirkung von Versetzungen mit koh??renten

geordneten Zonen (I). Phys Status Solidi. 1965;12(1):235–50.

118. Kelly A. Strengthening methods in crystals. Nicholson RB, Kelly A, editors. Amsterdam, New York: Elsevier; 1971.

119. Lutjering G, Weissmann S. Mechanical properties of age-hardened titanium-aluminium alloys. Acta Metall. 1970;18(7):785–95.

120. Zhang J, Li D. Preferred precipitation of ordered α2 phase at dislocations and boundaries in near-α titanium alloys. Mater Sci Eng A. 2003;341(1–2):229–35.

121. Sasano H, Tsujimoto T, Kimura H. On the Quenched Structure and Aging Process of Ti-8~15.8 wt.% Al Alloy. In: Jaffee RI, Burke HM, editors. Titanium '72: Science and Technology, Volume 3. Metallurgical Society of AIME; 1972. p. 1635.

122. Goold D. DIFFUSION OF ALUMINIUM, TIN, VANADIUM, MOLYBDENUM, AND MANGANESE IN TITANIUM. J Inst Met. 1960;88(10):444–8.

123. Shewmon PG. Diffusion in solids. McGraw-Hill; 1963.

124. Sircar S, Narasimhan K, Mukherjee K. An investigation of the ordered DO19 phase formation in the Ti-Al system. J Mater Sci. 1986;21(12):4143–6.

125. Donlon WT, Allison JE, Lasecki JV. The influence of thermal exposure on properties and microstructure of elevated temperature titanium alloys. In: Titanium '92: Science and Technology. 1992. p. 295.

126. Wagner C. Theorie Der Alterung Von Niederschlagen Durch Umlosen (Ostwald-Reifung). Zeitschrift für Elektrochemie. 1961;65(7–8):581–91.

127. Neeraj T, Mills M. Short-range order (SRO) and its effect on the primary creep behavior of a Ti–6wt.%Al alloy. Mater Sci Eng A [Internet]. 2001;319–321:415–9.

128. Wu Z, Qiu C, Venkatesh V, Fraser HL, Williams REA, Viswanathan GB, et al. The influence of precipitation of alpha2 on properties and microstructure in TIMETAL 6-4. Metall Mater Trans A Phys Metall Mater Sci. 2013;44(4):1706–13.

129. Evans WJ. The influence of microstructure on dwell sensitive fatigue in a near alpha titanium alloy. Scr Metall. 1987;21(4):469–74.

130. McBagonluri F, Akpan E, Mercer C, Shen W, Soboyejo WO. An investigation of the effects of microstructure on dwell fatigue crack growth in Ti-6242. Mater Sci Eng A. 2005;405(1–2):111–34.

131. Shen W, Soboyejo WO, Soboyejo ABO. An investigation on fatigue and dwell-fatigue crack growth in Ti-6Al-2Sn-4Zr-2Mo-0.1Si. Mech Mater. 2004;36(1–2):117–40.

132. Shen W, Soboyejo a. BO, Soboyejo WO. Microstructural Effects on Fatigue and Dwell-Fatigue Crack Growth in α/β Ti-6Al-2Sn-4Zr-2Mo-0 . 1Si. Metall Mater Trans A. 2004;35(January):163–87.

133. Bache MR. A review of dwell sensitive fatigue in titanium alloys: The role of microstructure, texture and operating conditions. Int J Fatigue. 2003;25(9–11):1079–87.

134. Ozturk D, Shahba A, Ghosh S. Crystal plasticity FE study of the effect of thermo-mechanical loading on fatigue crack nucleation in titanium alloys. Fatigue Fract Eng Mater Struct. 2016;39(6):752–69.

135. Shahba A, Ghosh S. Crystal plasticity FE modeling of Ti alloys for a range of strain-rates.

Part I: A unified constitutive model and flow rule. Int J Plast [Internet]. 2016;87:48–68.

136. Schneiker T, Forsberg K. Process Chemistry and Acid Management for Titanium Pickling Processes. Stockholm; 2014.

137. Shenoy RN, Unnam J, Clark RK. Oxidation and embrittlement of Ti-6Al-2Sn-4Zr-2Mo alloy. Oxid Met. 1986;26(1–2):105–24.

138. Pilchak AL, Porter WJ, John R. Room temperature fracture processes of a near-alpha titanium alloy following elevated temperature exposure. J Mater Sci. 2012;47(20):7235–53.

139. Leyens C, Peters M, Weinem D, Kaysser WA. Influence of long-term annealing on tensile properties and fracture of near-α titanium alloy Ti-6Al-2.75Sn-4Zr-0.4Mo-0.45Si. Metall Mater Trans A [Internet]. 1996;27(6):1709–17.

140. Jia W, Zeng W, Liu J, Zhou Y, Wang Q. Influence of thermal exposure on the tensile properties and microstructures of Ti60 titanium alloy. Mater Sci Eng A [Internet]. 2011;530(1):511–8.

141. Gaddam R, Antti M-LL, Pederson R. Influence of alpha-case layer on the low cycle fatigue properties of Ti-6Al-2Sn-4Zr-2Mo alloy. Mater Sci Eng A [Internet]. 2014;599:51–6.

142. Abdallah Z, Perkins K, Williams S. Alpha-case kinetics and surface crack growth in the high-temperature alloy Timetal 834 under creep conditions. Metall Mater Trans A Phys Metall Mater Sci. 2012;43(12):4647–54.

143. Gaddam R, Sefer B, Pederson R, Antti M-L. Oxidation and alpha-case formation in Ti–6Al–2Sn–4Zr–2Mo alloy. Mater Charact [Internet]. 2015;99:166–74.

144. Birks N, Meier GH. High Temperature Oxidation of Metals. Edward Arnold (Publishers) Ltd; 1983.

145. Kumar S, Narayanan TSNS, Sundara SG, Seshadri SK. Thermal oxidation of Ti6Al4V alloy : Microstructural and electrochemical characterization. 2010;119:337–46.

146. Guleryuz H, Cimenoglu H. Oxidation of Ti – 6Al – 4V alloy. J Alloys Compd. 2009;472:241–6.

147. Kofstad P. High temperature corrosion [Internet]. Elsevier Applied Science; 1988. 558 p.

148. Stringer J. Oxidation of titanium in oxygen at high temperatures. Acta Metall. 1960;8(11):758–66.

149. Wagner C. Beitrag zur Theorie des Anlaufvorgangs. Zeitschrift fur Phys Chemie [Internet]. 1933;21B(1):25–41.

150. Chaze AM, Coddet C. Influence of Aluminium on the oxidation of titanium between 550 and 750°C. J Less-Common Met. 1990;157:55–70.

151. Kofstad P. High-temperature oxidation of metals. John Wiley {&} Sons. Inc; 1966.

152. Du HL, Datta PK, Lewis DB, Burnell-Gray JS. Air oxidation behaviour of Ti6Al4V alloy between 650 and 850°C. Corros Sci. 1994;36(4):631–42.

153. Pitt F, Ramulu M. Influence of grain size and microstructure on oxidation rates in titanium alloy Ti-6Al-4V under superplastic forming conditions. J Mater Eng Perform. 2004;13(6):727–34.

154. Evans RW, Hull RJ, Wilshire B. The effects of alpha-case formation on the creep fracture

properties of the high-temperature titanium alloy IMI834. J Mater Process Technol [Internet]. 1996;56(1–4):492–501.

155. Gurrappa I. On the mechanism of degradation of titanium alloy IMI 834 in an oxidizing atmosphere at elevated temperatures. Corros Prev Control [Internet]. 2002;49(2):79–84.

156. Srinadh KVS, Singh V. Oxidation behaviour of the near α-titanium alloy IMI 834. Bull Mater Sci. 2004;27(4):347–54.

157. Chaze AM, Coddet C. The role of nitrogen in the oxidation behaviour of titanium and some binary alloys. J Less-Common Met. 1986;124(1–2):73–84.

158. Perez P. Influence of nitriding on the oxidation behaviour of titanium alloys at 700 C. Surf Coatings Technol. 2005;191:293–302.

159. Shewmon P. Diffusion in Solids [Internet]. Second Edi. Shewmon P, editor. Springer International Publishing; 2016. 9–51 p.

160. Kofstad P. High-temperature oxidation of titanium. J Less Common Met [Internet]. 1967;12(6):449–64.

161. Liu Z, Welsch G. Literature Survey on Diffusivities of Oxygen, Aluminium and Vanadium in alpha-Titanium, beta-Titanium and in Rutile. Metall Trans A. 1988;19A.

162. Sefer B. [Thesis] Oxidation and Alpha–Case Phenomena in Titanium Alloys used in Aerospace Industry: Ti–6Al–2Sn–4Zr–2Mo and Ti–6Al–4V. 2014. 112 p.

163. Dobeson R, Petrazoller N, Dargusch M, McDonald S. Effect of thermal exposure on the room temperature tensile properties of Grade 2 titanium. Mater Sci Eng A. 2011;528(10–11):3925–9.

164. Richards G. [Thesis] The formation and tensile behaviour of α -case in fine-grained Ti-6Al-4V. University of Sheffield; 2018.

165. Bagot PAJ, Radecka A, Magyar AP, Gong Y, Bell DC, Smith GDW, et al. The effect of oxidation on the subsurface microstructure of a Ti-6Al-4V alloy. Scr Mater. 2018;148.

166. Schneider CA, Rasband WS, Eliceiri KW. NIH Image to ImageJ: 25 years of image analysis. Nat Methods. 2012;9(7):671–5.

167. Thomas M, Lindley T, Jackson M. The microstructural response of a peened near-α titanium alloy to thermal exposure. Scr Mater. 2009;60(2):108–11.

168. Gaddam R, Sefer B, Pederson R, Antti ML. Oxidation and alpha-case formation in Ti-6Al-2Sn-4Zr-2Mo alloy. Mater Charact [Internet]. 2015;99:166–74.

169. Thomas M, Jackson M, Hutson G, Chater RJ. Focused ion beam-SIMS oxygen assay of the surface of titanium alloys prepared by the shot peening process. Surf Interface Anal [Internet]. 2013;45(1):575–8.

170. Bagot PAJ, Radecka A, Magyar AP, Gong Y, Bell DC, Smith GDW, et al. The effect of oxidation on the subsurface microstructure of a Ti-6Al-4V alloy. Scr Mater [Internet]. 2018;148:24–8.

171. Rugg D, Britton TB, Gong J, Wilkinson AJ, Bagot PAJ. In-service materials support for safety critical applications - A case study of a high strength Ti-alloy using advanced experimental and modelling techniques. Mater Sci Eng A [Internet]. 2014;599:166–73.

172. Semenova I, Salimgareeva G, Da Costa G, Lefebvre W, Valiev R. Enhanced strength and

ductility of ultrafine-grained Ti processed by severe plastic deformation. Adv Eng Mater. 2010;12(8):803–7.

173. Coakley J, Vorontsov VA, Jones NG, Radecka A, Bagot PAJ, Littrell KC, et al. Precipitation processes in the Beta-Titanium alloy Ti–5Al–5Mo–5V–3Cr. J Alloys Compd [Internet]. 2015;646:946–53.

174. Kolli RP, Herzing AA, Ankem S. Characterization of yttrium-rich precipitates in a titanium alloy weld. Mater Charact [Internet]. 2016;122:30–5.

175. Kelly TF. Atom-probe tomography. In: Springer Handbooks. Springer; 2019. p. 715–63.

176. Gault B, Moody MP, De Geuser F, La Fontaine A, Stephenson LT, Haley D, et al. Spatial Resolution in Atom Probe Tomography. Microsc Microanal [Internet]. 2010;16(1):99–110.

177. Thompson K, Lawrence D, Larson DJJ, Olson JDD, Kelly TFF, Gorman B. In situ site-specific specimen preparation for atom probe tomography. Ultramicroscopy [Internet]. 2007;107(2–3):131–9.

178. Jenkins BM, Douglas JO, Gardner HM, Tweddle D, Kareer A, Karamched PS, et al. A more holistic characterisation of internal interfaces in a variety of materials via complementary use of transmission Kikuchi diffraction and Atom probe tomography. Appl Surf Sci [Internet]. 2020;528:147011.

179. Gault B, Moody MP, Cairney JM, Ringer SP. Atom Probe Microscopy. Hull R, Jagadish C, Osgood RM, Parisi J, Wang ZM, editors. Springer; 2012.

180. Pedrazzini S, London AJ, Gault B, Saxey D, Speller S, Grovenor CRM, et al. Nanoscale Stoichiometric Analysis of a High-Temperature Superconductor by Atom Probe Tomography. Microsc Microanal [Internet]. 2017;1(11).

181. Haley D. threedepict.sourceforge.net. threedepict.sourceforge.net, version 0021. 2010;

182. London A. sourceforge.net/projects/atomprobelab. Matlab Code, sourceforge.net/projects/atomprobelab. 2019;

183. Haley D, Choi P, Raabe D. Guided mass spectrum labelling in atom probe tomography. Ultramicroscopy [Internet]. 2015;159 Pt 2:338–45.

184. London AJ. Quantifying Uncertainty from Mass-Peak Overlaps in Atom Probe Microscopy. Microsc Microanal. 2019;25(2):378–88.

185. Marquis EA, Hyde JM. Applications of atom-probe tomography to the characterisation of solute behaviours. Mater Sci Eng R Reports [Internet]. 2010;69(4–5):37–62.

186. Marquis EA, Araullo-Peters V, Dong Y, Etienne A, Fedotova S, Fujii K, et al. On the Use of Density-Based Algorithms for the Analysis of Solute Clustering in Atom Probe Tomography Data. In: Jackson J, Paraventi D, Wright M, editors. Proceedings of the 18th International Conference on Environmental Degradation of Materials in Nuclear Power Systems – Water Reactors The Minerals, Metals & Materials Series [Internet]. Springer, Cham; 2019. p. 2097–113.

187. Chen Y, Chou PH, Marquis EA. Quantitative atom probe tomography characterization of microstructures in a proton irradiated 304 stainless steel. J Nucl Mater [Internet]. 2014;451(1–3):130–6.

188. Homma T, Arafah A, Haley D, Nakai M, Niinomi M, Moody MP. Effect of alloying elements on microstructural evolution in oxygen content controlled Ti-29Nb-13Ta-4.6Zr (wt%) alloys

for biomedical applications during aging. Mater Sci Eng A [Internet]. 2018;709(October 2017):312–21.

189. Heath J, Taylor N. Electron probe microanalysis. Essential Knowledge Briefing, Microscopy and Microanalysis. First edit. 2015;

190. Newbury DE. Quantitative electron probe microanalysis of rough targets: Testing the peak-to-local background method. Scanning. 2004;26(3):103–14.

191. Chatterjee N. Electron Microprobe Analysis Lecture notes [Internet]. 2012.

192. Reed SJB. Optimization of wavelength dispersive x-ray spectrometry analysis conditions. J Res Natl Inst Stand Technol. 2002;107(6):497–502.

193. Drouin D, R'eal Couture A, Joly D, Tastet X, Aimez V, Gauvin R. CASINO V2 . 42 — A Fast and Easy-to-use Modeling Tool for Scanning Electron Microscopy and Microanalysis Users. Scanning. 2007;29:92–101.

194. Pharr GM, Oliver WC, Brotzen FR. On the generality of the relationship among contact stiffness, contact area, and elastic modulus during indentation. J Mater Res. 1992;7(3):613–7.

195. Sneddon IN. The relation between load and penetration in the axisymmetric boussinesq problem for a punch of arbitrary profile. Int J Eng Sci. 1965;

196. Jamal M, Morgan MN. Materials characterization part I: contact area of the Berkovich indenter for nanoindentation tests. Int J Adv Manuf Technol. 2017;92(1–4):361–70.

197. Asif SAS, Wahl KJ, Colton RJ. Nanoindentation and contact stiffness measurement using force modulation with a capacitive load-displacement transducer. Rev Sci Instrum. 1999;70(5):2408–13.

198. Li X, Bhushan B. A review of nanoindentation continuous stiffness measurement technique and its applications. Mater Charact. 2002;48(1):11–36.

199. McLean D. Grain boundaries in Metals. Oxford: Clarendon Press; 1957.

200. Sutton AP, Ballauffi W. Interfaces in Crystalline Materials. New York, NY: Oxford University Press; 2007.

201. Raabe D, Herbig M, Sandlöbes S, Li Y, Tytko D, Kuzmina M, et al. Grain boundary segregation engineering in metallic alloys: A pathway to the design of interfaces. Curr Opin Solid State Mater Sci. 2014;18(4):253–61.

202. Jenkins BM, Douglas JO, Gardner HM, Tweddle D, Kareer A, Karamached PS, et al. Complementary Use Of Transmission Kikuchi Diffraction and Atom Probe Tomography To Provide A More Holistic Characterisation Of Internal Interfaces In A Variety of Materials. Submitt to Appl Surf Sci. 2019;

203. Zhang LJ, Chen ZY, Hu QM, Yang R. On the abnormal fast diffusion of solute atoms in α-Ti: A first-principles investigation. J Alloys Compd. 2018;740:156–66.

204. Nakajima H, Koiwa M. Diffusion of iron, cobalt and nickel in alpha-titanium. Titanium--Science Technol. 1984;3:1759–66.

205. Nakajima H, Koiwa1 M. Diffusion in Titanium. Vol. 31, ISIJ International.

206. Truax DJ, McMahon CJ. Plastic behavior of titanium-aluminum alloys. Mater Sci Eng. 1974;13(2):125–39.

207. Vavilova VV, Brynza AP, Mnuskin IP. Phase-Diagram and Electrochemical Properties of Alloys in System Titanium-Aluminum-Oxygen. J Appl Chem USSR. 1975;48(7):1523–5.

208. Saunders N. Modelling of phase equilibria in Ti-alloys. In: Titanium ’95: Science and Technology. 1996. p. 2167.

209. Porter DA, Easterling KE. Phase transformations in metals and alloys. 2nd ed. Nelson Thornes Ltd; 1992. 514 p.

210. Villars P (Pierre), Prince A, Okamoto H (Hiroaki). Handbook of ternary alloy phase diagrams: Volume 4. ASM International; 1995.

211. Aksyonov DA, Hickel T, Neugebauer J, Lipnitskii AG. The impact of carbon and oxygen in alpha-titanium: Ab initio study of solution enthalpies and grain boundary segregation. J Phys Condens Matter. 2016;28(38).

212. Ghazisaeidi M, Trinkle DR. Interaction of oxygen interstitials with lattice faults in Ti. Acta Mater [Internet]. 2014;76:82–6.

213. Aksyonov DA, Hickel T, Lipnitskii AG, Neugebauer J. The impact of carbon and oxygen in alpha-titanium : Ab initio study of solution enthalpies and grain boundary segregation. J Phys Condens Matter [Internet]. 2016;385001:1–23.

214. Aksyonov DA, Lipnitskii AG. Solubility and grain boundary segregation of iron in hcp titanium: A computational study. Comput Mater Sci [Internet]. 2017;137:266–72.

215. Das K, Choudhury P, Das S. The Al-O-Ti (Aluminum-Oxygen-Titanium) System. J Phase Equilibria [Internet]. 2002;23(6):525–36.

216. Polmear IJ. Light alloys : from traditional alloys to nanocrystals [Internet]. Elsevier/Butterworth-Heinemann; 2006. 421 p.

217. Lee K, Liguori S, Psarras P, Wilcox J. Theoretical Study of Nitrogen Absorption in Metals. J Phys Chem C. 2017;121(31):17016–28.

218. Fromm E, Hörz G. Hydrogen, nitrogen, oxygen, and carbon in metals. Int Met Rev. 1980;25(1):269–307.

219. Holec D, Reddy RK, Klein T, Clemens H. Preferential site occupancy of alloying elements in TiAl-based phases. J Appl Phys [Internet]. 2016;119(20).

220. Benedek R, Van De Walle A, Gerstl SSA, Asta M, Seidman DN, Woodward C. Partitioning of solutes in multiphase Ti-Al alloys. Phys Rev B - Condens Matter Mater Phys. 2005;71(9):1–12.

221. Armstrong DEJ, Rogers ME, Roberts SG. Micromechanical testing of stress corrosion cracking of individual grain boundaries. Scr Mater. 2009;61(7):741–3.

222. Winstone MR, Rawlings RD, West DRF. Dynamic strain ageing in some titanium-silicon alloys. J Less-Common Met. 1973;31(1):143–50.

223. Winstone MR, Rawlings RD, West DRF. The creep behaviour of some silicon-containing titanium alloys. J Less-Common Met. 1975;39(2):205–17.

224. Ramachandra C, Singh AK, Sarma GMK. Microstructural characterisation of near-α titanium alloy Ti-6Al-4Sn-4Zr-0.70Nb-0.50Mo-0.40Si. Metall Trans A. 1993;24(6):1273–80.

225. Weaver JS, Priddy MW, McDowell DL, Kalidindi SR. On capturing the grain-scale elastic and plastic anisotropy of alpha-Ti with spherical nanoindentation and electron back-scattered

diffraction. Acta Mater. 2016;117:23–34.

226. Fitzner A, Palmer J, Gardner B, Thomas M, Preuss M, da Fonseca JQ. On the work hardening of titanium: new insights from nanoindentation. J Mater Sci [Internet]. 2019;54(10):7961–74.

227. Bregolin FL, Behar M, Dyment F. Diffusion study of 18O implanted into α-Ti using the nuclear resonance technique. Appl Phys A Mater Sci Process. 2007;86(4):481–4.

228. Wittberg, Wolf, Keil, Wang. Low-temperature oxygen diffusion in alpha titanium characterized by Auger sputter profiling. 1982;1(June):475–8.

229. Deschamps, Lehr. On the oxidation of α titanium in an oxygen atmosphere: the role of oxidized layer and mechanism of oxidation,. J Less-Common Met. 1977;56:193–207.

230. David D, Beranger G, Garcia EA. A Study of the Diffusion of Oxygen in α-Titanium Oxidized in the Temperature Range 460°–700°C. J Electrochem Soc. 1983;130(6):1423.

231. Johnson TJ, Loretto MH, Kearns MW. Oxidation of High Temperature Titanium Alloys. Titan '92 Sci Technol. 1993;2035–42.

232. Moody MP, Stephenson LT, Ceguerra A V., Ringer SP. Quantitative binomial distribution analyses of nanoscale like-solute atom clustering and segregation in atom probe tomography data. Microsc Res Tech. 2008;71(7):542–50.

233. Sikora T, Hug G, Jaouen M, Flank AM. EXAFS study of the local atomic order in Ti2AlX (X=Nb, Mo) B2 intermetallic compounds. J Phys IV JP. 1996;6(2).

234. Dichtl C, Zhang Z, Gardner HM, Bagot P, Radecka A, Dye D, et al. Element segregation and α2 formation in primary α of a near-α Ti-alloy. Mater Charact. 2020;164:110327.

235. Bolshakov A, Pharr GM. Influences of pileup on the measurement of mechanical properties by load and depth sensing indentation techniques. J Mater Res [Internet]. 1998;13(4):1049–58.

236. Aksyonov D a, Lipnitskii a G, Kolobov YR. Grain boundary segregation of C, N and O in hexagonal close-packed titanium from first principles. Model Simul Mater Sci Eng. 2013;21(7):75009.

237. von Mises R. Mechanik der plastischen Formanderung von Kristallen. Zeitschrift Angew Math und Mech. 1928;8(3):161–85.

238. Pineau A, Pardoen T. 2.06 - Failure of Metals. In: Comprehensive Structural Integrity. Elsevier Ltd; 2007. p. 684–797.